Isotopic Systematics and Mass Transfer

in Amphibolite-Grade Mylonites

by

David Matthew Wayne

Dissertation submitted to the Faculty of the

Virginia Polytechnic Institute and State University

in partial fulfillment of the requirements for the degree of

Doctor of Philosophy

in

Geology

APPROVED:

A. Krishna Sinha, Chairperson

David A Hewitt

J. Donald Rimstidt

Paul H. Ribbe

Susan C. Eriksson

June, 1990

Blacksburg, Virginia

Isotopic Systematics and Mass Transfer

in Amphibolite-Grade Mylonites

by

David Matthew Wayne

A. Krishna Sinha, Chairperson

Geology

(ABSTRACT)

Alleghanian-aged deformation and grain size reduction of quartzofeldspathic and mafic rocks of the Late Precambrian Ponaganset Gneiss proceeded at amphibolite grade conditions (600°C, 4-6 kb), and were accompanied by considerable mobility of Si, Na, K, Ca, Fe and Mg. Fluids present during and after ductile deformation facilitated hydration reactions within a narrow (> 10 cm), foliation-parallel mafic layer composed largely of clinopyroxene and albitic plagioclase (An_3). The final product of these reactions was a K-feldspar/plagioclase (An_9)-rich amphibolite. Mass balance relations show that the amphibolite-forming reactions required an influx of Fe^{2+} and Mg^{2+} cations, and expulsion of Na^{+} into the surrounding gneisses. The source for Fe^{2+} and Mg^{2+} was probably the adjacent, actively-deforming quartzofeldspathic mylonite which, with reference to the protolith gneisses less than 30 cm from the gneiss-amphibolite contact, is reduced by 60% of its original concentration of these elements. Where no amphibolite layer is present, quartzofeldspathic mylonites display a similar depletion in Fe and Mg, but also carry textural and geochemical evidence for fluid flow on a millimeter to centimeter scale (e.g. foliation-parallel quartz veins walled by monomineralic layers of plagioclase or K-feldspar, and pronounced cm scale gradients in whole rock K, Na and Si concentrations).

Despite the evidence in favor of fluid flow, reaction progress calculations in the amphibolite layer suggest that minimum volumetric fluid-rock ratios never exceeded 0.05 liters H_2O/liter of rock. The local presence of strained clinopyroxene microporphyroclasts and laminae of clinopyroxene-albite mylonite in the amphibolite layer suggest that hydration reactions did not go to completion. The presence of biotite in the amphibolite layer elsewhere at the outcrop suggests that fluid-rock ratios were not uniform during, or shortly after, deformation. Post deformational metamorphic re-

actions in the amphibolite resulted in the formation of actinolitic rims on amphibole grains which continued to grow at the expense of adjacent, strained clinopyroxene microporphyroclasts. Textural relationships indicate that the actinolitic rims grew via diffusive processes in the presence of an intergranular fluid film.

The ability of the zircon U-Pb system to yield useful geochronologic information on the timing of deformational events is a complex function of the degree of metamictization of the zircons, the chemistry and mineralogy of the enclosing rock, the P-T conditions of metamorphism and the presence and composition of metamorphic fluids. The possible effects of dynamic metamorphism on the isotopic ages obtained from zircons range from no apparent Pb loss to complete resetting of the isotopic "clock". The two examples presented here represent the two extremes: the mid-Paleozoic, greenschist-grade Rockfish Valley Fault Zone, and the Pennsylvanian-Permian amphibolite-grade Hope Valley Shear Zone. In the mylonites of the Rockfish Valley Fault Zone, zircons underwent brittle failure and were comminuted in the ductilely deforming matrix. Comparative U-Pb isotopic studies of zircons from the mylonites and from the Grenville-aged charnockitic protolith demonstrate that no appreciable Pb loss occurred as the result of intense mylonitization, despite the presence of aqueous fluids during deformation which affected the hydration of the mylonitic mineral assemblages.

A detailed U-Pb isotopic study of a single outcrop of the late Precambrian Ponaganset gneiss was also undertaken. Amphibolite-grade mylonitization associated with movement along the Hope Valley Shear Zone caused some grain size reduction ofthe zircons in the mylonite zones. However, the primary cause of isotopic disturbance in these zircons is the extensive growth of U-rich metamorphic zircon during, or shortly after, metamorphism. Corrosion of pre-existing zircon also occurred during metamorphism/deformation, but it is difficult to quantify its effects on U-Pb systematics. The lower intercept ages of 289± 24 m.y. and 265± 62 m.y. from the pink gneiss and gray gneiss, respectively, both fall within the range of other published age estimates (e.g. Zartman et al. 1988) for Alleghanian deformation and metamorphism in southeastern New England.

Acknowledgements

Acknowledgements are not meant to be mere lists of names, and if this brief note of thanks sounds more like a roll call...please attribute that to my lack of writing skills, rather than a lack of sincerity. The past six years have been both turbulent and wonderful, and I have been incredibly lucky to have found such great people to spend them with. So - there you have it...the greatest reward of being here at Virginia Tech is the friends I have made. I wouldn't have it any other way!!

I would first like to thank my parents, Roger C. and Marian L. Wayne, for their unfaltering support. I truly could not have done any of this without them. My best friend, Christine Hastings, has been a constant source of laughs, insight, good food and good times, and is basically the gal I want to spend the rest of my life with. My colleagues and friends in Lab Central: John Hogan, Karen Hogan, Charlotte Allen, Rob Badger, Joe Jurinski, Diana Solie, Russell Guy, Hal Pendrak and Janet Schweitzer (the "new kid") all made substantial contributions to my ability to "do science" by showing me how isotopes, mylonites and computers work. These great folks, and their spouses, also provided all kinds of pleasant distractions and diversions throughout the years. The same could also be said of Jean Cline, Matt Nyman, Bill Hames, Ron Sheets, John Groen, Mike Sterner, Carolyn Rebbert, Carl Kirby, Tom Armstrong, Randy Cumbest, Kurt Bartelmehs, Laura Davis, Jeff Foley, Don Hall, Maya Elrick, Rich Gibson, Alan Hubbard, Fred Sundberg, Dave Jacobs, Brett Bennington, Isabel Montanez, Dave Osleger, and Mike Wizevich, all of whom provided intense, probing scientific insights and comic relief (sometimes both simultaneously!!). I am well aware of my good fortune in meeting, working with, and hanging out with such great group of people.

Huge dollops of thanks are also owed to Linda Bland, Dean Hefner, Belinda Pauley, Carolyn Williams, Karen Hunt, Dan Smith, Don Bodell, Jim Light, Llyn Sharp, Sharon Chaing, Ethel Schrader, Ada Simmons, Pat Morris, Hersha Evans-Wardell and Margie Strickler. If I had a nickel for all the times you all "dropped everything" to answer questions or help me out in some way, I'd be financially secure. Special thanks are due to Mr. Todd Solberg who always maintained high standards in the microprobe lab. Photography was made simpler by the able staff of the L.R.C. Photo Lab. Carlile Price, John Groen and Virginia Viers provided able assistance on the SEM fa-

cilities in the Department of Forestry, the Department of Geology, and the Veterinary School, respectively.

Teaching at V.P.I. has been a tremendous learning experience, and I'd like to thank Dr. D. A. Hewitt, Dr. F. D. Bloss, Dr. R. Tracy , Dr. P.H. Ribbe and Dr. G. V. Gibbs for giving me the opportunity to teach their labs. I'd also like to thank their students for making it all worthwhile. Before I arrived in Blacksburg, my tutelage was in the able, patient and perservering hands of Drs. Skip Simmons, Louis Fernandez, Bill Ranson, Wally Fallaw, Ken Sargent and Jack Garihan. Whether they liked it or not, they took it upon themselves to teach me about geology while putting up with all manner of hijinks. I especially appreciate all the field trips that were organized (and endured) by these folks.

My advisor, Dr. A. K. Sinha, deserves thanks for his patience, wealth of ideas and willingness to listen. The best part of being down in Lab Central was the free exchange of thoughts and ideas, and the diversity of the people thinking them - and Dr. Sinha was responsible for that. The other members of my committee: Dr. D. A. Hewitt, Dr. J. D. Rimstidt, Dr. P.H. Ribbe and Dr. S. C. Eriksson have all provided useful scientific discussions, and helped shape my ideas as the project evolved. I am deeply indebted to Dr. L. Peter Gromet, who took the time to familiarize me with the various structural and tectonic aspects of the Hope Valley Shear Zone. His careful examination of Chapter 3, and extremely helpful criticisms, are greatly appreciated. I'd also like to thank Dr. Jim Carl for his thorough reading of the manuscript, his encouragement and useful comments. Drs. Zell Peterman and Paul Karabinos read, and improved, the original manuscript of Chapter 2, which was published in 'Contributions to Mineralogy and Petrology' in 1988. Debra Stakes, at the University of South Carolina, did the oxygen isotope work on the Ponaganset gneiss, and generously shared some unpublished geothermometric data.

Funding for the research presented in this document was provided by the National Science Foundation (grant number EAR-8416575 to A.K. Sinha and D.A. Hewitt) and the United States Department of Energy, Division of Basic Energy Research (contract number DE-FGO5-88-ER-13951 to A.K Sinha, D.A. Hewitt and P.H. Ribbe). I would also like to thank

the Virginia Tech Graduate Student Association Travel Fund for "picking up the tab" on the trips I took to the Geological Society of America National Conventions to present some of these results.

Finally, I'd like to acknowledge some non-geology types...as I have had the good fortune of being involved in something other than geology, namely music. Playing jazz has been an honor as well as a big slab of fun, and my fellow Jazz Impostors - Jeff Asch, Chris Henson and John Husser, Jr. - have allowed me to add another dimension to my life. Their ability and friendship is unmatched. My friends at WUVT-FM, especially Frank Hiehle, were a constant source of new sounds and new ideas.

Table of Contents

Preface 1

Chapter 1: Whole rock and mineral chemical changes associated with amphibolite-grade ductile deformation zones. 9

Abstract 9

Introduction 11

Regional Geology and Sample Description 12

Petrographic and Microstructural Description of the Transects 22

419 Transect: Gray gneiss 22

Mylonite derived from the Gray Augen Gneiss (419) 23

Amphibolite: 419 Transect 26

Pink granitic gneiss: 419 Transect 31

S-1 Transect: Gray gneiss and mylonite 32

S-1 Transect: Pink gneiss 33

Analytical Techniques 34

Modal Analyses 35

Bulk Chemistry 41

Mineral Chemistry 52
Feldspars - 419 Transect 52
Biotite 56
Amphibole 57
Clinopyroxene 68
Geothermometry and Geobarometry 70
Mass transfer calculations 75
Metamorphic reactions in the amphibolite 82
Reaction progress modelling 82
Amphibole zoning 86
Metamorphic reactions in the mylonites and gneisses 90
Biotite, amphibole and clinopyroxene stability 90
Instability of muscovite and epidote 93
The scale of element transport in the Ponaganset gneiss 94
Conclusions 96
References 99

Chapter 2: Physical and chemical response of zircons to deformation. 106
Abstract 106
Introduction 108
Geologic Setting 109
U-Pb Systematics of Zircons in Shear Zones 109
Analytical Procedures 111
Physical Characterization 114
Fracturing 114
Surface features 120
Microprobe Analyses 122
Crystal chemistry of zircon 122

Behavior of Ca and Fe 123
Behavior of U, Y and P 126
Behavior of Hf 133
Discussion and Conclusions 134
References 142

Chapter 3: The effects of fluids on zircon U-Pb systematics in ductile deformation zones. ... 146
Abstract 146
Introduction 148
U-Pb systematics of zircon in mylonites 150
Geologic setting of study areas 152
The Hope Valley Shear Zone 152
Sample Location 154
Petrography of the Ponaganset gneiss 157
Gray Augen Gneiss 157
Mylonite derived from the Gray Augen Gneiss (UM 419) 158
Pink granitic gneiss 159
Mylonite within the Pink Granitic Gneiss (UM 872) 160
Amphibolite 160
The Rockfish Valley Fault Zone 161
Regional geology, geologic setting and sample locality 161
Analytical techniques 165
Electron Microprobe, SEM 165
Mass Spectrometry 166
Zircon Morphology 169
Ponaganset gneiss 169
Charnockite from the Pedlar massif and related ultramylonites 178
Backscattered electron imaging 181

Electron microprobe analyses 190
Isotopic Analyses 195
Ponaganset Gneisses and Mylonites: Zircon data 195
Ponaganset Gneisses and Mylonites: Feldspar data 201
Rockfish Valley Fault Zone 203
Isotopic stability of zircon in shear zones 207
Summary 215
References 217

Explanation of Appendices 224
Standard Analyses 224
Feldspar Analyses 225
Biotite Analyses 225
Amphibole Analyses 225
Clinopyroxene Analyses 226
Appendix A - MICROPROBE STANDARD ANALYSES 227
Appendix B - PLAGIOCLASE ANALYSES - 419 & S-1 Transects 230
Appendix C - K-FELDSPAR ANALYSES - 419 & S-1 Transects 250
Appendix D - BIOTITE ANALYSES - 419 & S-1 Transects 262
Appendix E - AMPHIBOLE ANALYSES - 419 & S-1 Transects 275
Appendix F - CLINOPYROXENE ANALYSES - 419 Transect 317

Vita 324

List of Illustrations

Figure P.1. Schematic depiction of the development of mineral assemblages within a retrograde shear zone 3

Figure P.2. Schematic depiction of the development of mineral assemblages within an amphibolite-grade shear zone 5

Figure 1.1. Generalized geologic map of southeastern New England 13

Figure 1.2. Schematic scale map of the sample locality 15

Figure 1.3. Field photographs of mylonite zones in the Ponaganset gneiss 16

Figure 1.4. Schematic diagram of the 419 and S-1 transects, showing the slabs cut for bulk chemical analyses. 20

Figure 1.5. Schematic diagram of 419 transect (left) and S-1 transect (right) 21

Figure 1.6. Microstructural features of the gneisses and mylonites 24

Figure 1.7. Microstructural features of the amphibolite layer (419) 28

Figure 1.8. Modal analyses of thin sections from the S-1 transect as a function of distance. 38

Figure 1.9. Modal analyses of thin sections from the 419 transect as a function of distance. 39

Figure 1.10. Bulk chemical analyses of slabs from the 419 transect 43

Figure 1.11. Bulk chemical analyses of slabs from the S-1 transect 44

Figure 1.12. Isocon diagrams of samples from the 419 transect 47

Figure 1.13. Isocon diagrams of samples from the S-1 transect 48

Figure 1.14. Plagioclase composition as a function of distance across the 419 Transect . . . 54

Figure 1.15. Plagioclase composition as a function of distance across the S-1 Transect . . . 55

Figure 1.16. Amphibole composition (as Tr activity) and biotite composition (as F-Phl activity) across the 419 Transect 58

Figure 1.17. Amphibole composition (as Tr activity) and biotite composition (as F-Phl activity) across the S-1 transect 59

Figure 1.18. Variation of $Mg/(Mg+Fe^{+2})$ versus tetrahedral Al (per 22 O + F) in biotite from S-1 and 419 60

Figure 1.19. Variation of $Mg/(Mg+Fe^{+2})$ versus Si content (per 24 O + F) in amphibole . 62

Figure 1.20. Variation of $Mg/(Mg+Fe^{+2})$ versus Si content (per 24 O + F) in amphibole . 63

Figure 1.21. $FeMg_{-1}$ and tschermakite (ts) vectors in amphiboles across the 419 transect . 64

Figure 1.22. Zoned amphiboles from the 419 amphibolite layer 66

Figure 1.23. Variation of $(Mg/Mg+Fe^{+2})$ versus Na (per 6 O) in clinopyroxene from the 419 transect 69

Figure 1.24. Temperature estimates from plagioclase - amphibole pairs (using the method of Blundy and Holland 1990) 70

Figure 1.25. Schematic diagram of mass transfer (constant Al reference frame) across the S-1 transect 80

Figure 1.26. Schematic diagram of chemical mobility (constant Al reference frame) between mylonite and amphibolite 81

Figure 2.1. Scanning electron micrographs of zircons from the Henderson gneiss and mylonites (B8A, B8B, B8C) 116

Figure 2.2. Scanning electron micrographs of polished, HF-etched zircon cross-sections . . 118

Figure 2.3. X-ray emission maps showing the distribution of selected minor elements (Hf, Ca, U, Y) within zircons 124

Figure 2.4. Zr/Hf ratios and distributions of selected trace elements in zircons from electron microprobe analyses 129

Figure 2.5. Zr/Hf ratios and distributions of selected trace elements in zircons from electron microprobe analyses 130

Figure 2.6. Zr/Hf ratios and distributions of selected trace elements in zircons from electron microprobe analyses 131

Figure 2.7. Schematic diagram depicting the mechanisms pertinent to Pb-loss and U-gain of zircons in the Brevard Shear Zone 135

Figure 2.8. Plot of surface area (in μm^2) versus the number of throughgoing fractures . . . 137

Figure 3.1. Generalized geologic map of southeastern New England, adapted from O'Hara and Gromet (1985) 153

Figure 3.2. Schematic scale map of the sample locality for the Ponaganset gneiss 156

Figure 3.3. Geologic map of the central Virginia Blue Ridge (adapted from Pettingill et al. 1984) 163

Figure 3.4. Photomicrographs of zircon separates 171

Figure 3.5. Secondary electron images of zircons from the gray gneiss 173

Figure 3.6. Secondary electron images of zircon from the pink gneiss 176

Figure 3.7. Secondary electron images of zircons 179

Figure 3.8. BSE images of zircons from the Ponaganset gray gneiss. and UM419 182

Figure 3.9. BSE images of zircons from the pink granitic gneiss. 184

Figure 3.10. BSE images of zircons from the charnockite and the Rockfish Valley Fault Zone 187

Figure 3.11. Zircon U-Pb data from the Ponaganset gray gneiss 197

Figure 3.12. Zircon U-Pb data from the Ponaganset pink gneiss 198

Figure 3.13. U and Pb concentrations of zircon separates from the Ponaganset gneiss 199

Figure 3.14. U and Pb concentrations of zircon separates from the charnockite and the Rockfish Valley Fault Zone mylonite 205

Figure 3.15. Zircon U-Pb isotopic data from the Rockfish Valley Fault Zone mylonite and the charnockite protolith 206

Figure 3.16. Idealized chemical potential diagram 210

List of Tables

Table 1.1a. Modal analyses (n = 1000) for samples from the 419 and S-1 transects in volume percent. 36

Table 1.1b. Modal analyses (n = 1000) for samples from the 419 and S-1 transects in moles/liter. 37

Table 1.2. Bulk chemical analyses and densities. (a) 419 transect, (b) S-1 transect. 42

Table 1.3. Results of mass balance calculations for successive slab pairs (in moles/liter); 419 and S-1 transects. 77

Table 1.4. Additive components, exchange components and net transfer reactions for the 419 amphibolite. 84

Table 1.5. Results of reaction progress calculations in the amphibolite, in moles/liter of rock. 87

Table 2.1. X-ray lines, standards, counting times and detection limits for zircon microprobe analyses. 113

Table 2.2a. Microprobe analyses of zircons. Numbers in parentheses denote 1σ standard deviation. 127

Table 2.2b. Microprobe analyses of zircons, continued. 128

Table 2.3. Cell dimensions of zircons from the Henderson Gneiss (HGN) and the Brevard Zone mylonites. 139

Table 3.1. Morphologic characteristics of zircons from the Ponaganset gneiss and the Rockfish Valley Fault Zone. 170

Table 3.2a. Electron microprobe analyses of zircons. 192

Table 3.2b. Electron microprobe analyses of zircons, continued. 193

Table 3.3. U-Pb isotopic data from the Ponaganset gneiss and the Rockfish Valley Fault Zone. 196

Table 3.4. Pb isotopic data for alkali feldspar from the Ponaganset gneiss. 202

Table 3.5. Concentrations (in ppm) of zirconium in whole rock samples from the Ponaganset gneiss. 213

Preface

Mylonite zones provide the only geologic evidence of deep-seated tectonic activity, and data on their distribution, structural and geochemical evolution, and age provide significant constraints on models for the tectonic evolution of the lithosphere. Chemical and isotopic data from several major shear zones (e.g. Sinha et al. 1988; LaTour and Kerrich 1982; LaTour 1981; McCaig 1984 and others) suggest that their evolution is a complicated scenario which involves, through time, different degrees of fluid-rock interaction, over a range of P-T conditions. In some cases, the formation of major retrograde shear zones was preceded by ductile deformation and metamorphism at higher grades (Sinha et al. 1988). Thus, the present-day chemical and isotopic signatures of mylonitic rocks may be a composite of several distinct episodes, and the ability to resolve these events is dependent upon the scale of observation.

Mylonitic rocks often contain mineral assemblages that contrast sharply with those of the immediately adjacent, less deformed protolith. The chemical, mechanical and isotopic signatures of these mineral assemblages contain a wealth of information concerning the P-T conditions of chemical and isotopic re-equilibration, the temporal evolution of the fault system, the nature and amount of fluid flow and the deformational mechanisms attending movement at depth. For example, the phyllosilicate-rich mineral assemblages from retrograde mylonite zones indicate that strain localization and metamorphic re-equilibration took place at comparatively low metamorphic

grade and high P_{fluid}. Moreover, retrograde mineral assemblages often preserve evidence of open-system behavior during deformation and recrystallization (e.g. Sinha et al. 1986, 1988; O'Hara 1989; McCaig 1984 and others). These assemblages are often spatially restricted to narrow zones or conduits of actively deforming rock. The predominance of hydrous minerals (particularly phyllosilicates) in such zones requires both a net addition of H_2O to the system, and the breakdown of pre-existing anhydrous phases (such as K-feldspar) via hydration reactions. Several lines of evidence further suggest that the fluids which drive the hydration reactions are externally-derived, and considerable mobility of alkalies, Si, Ca, etc. accompany mineral reactions, grain size reduction and fabric development (e.g. Kerrich et al. 1984). Fluid-rock ratios on the order of 10^3 have been estimated for many such mylonites, far in excess of the amount of fluid required for the hydration of mineral assemblages alone (Etheridge et al. 1983, 1984). In fluid-rich environments, it has been proposed (Walther and Wood 1984) that the rate of metamorphic re-equilibration is controlled by the kinetics of the hydration reactions, rather than the rate of element transport which is accomplished relatively rapidly via the advective transport of dissolved, mobile components along grain boundaries and fractures. Thus, the chemistry and mineralogy of "open system" mylonites is controlled, largely, by the characteristics of an externally-derived aqueous fluid, which results in a patchy to continuous distribution of a single retrograde assemblage (Figure 1).

Mylonites developed at higher metamorphic grades (e.g. amphibolite grade) often display different textural and chemical characteristics than their lower grade counterparts. In some cases (Beach 1973), open-system behavior is evident from vaious bulk chemical and mineralogic considerations. In other cases (Kerrich et al. 1977; Brodie 1981), grain size reduction and strain accomodation have apparently proceeded isochemically. Conceivably, these two examples represent end-members of a continuous array of distinct chemical and deformational processes operative at relatively high metamorphic grades. Microstructures apparent in amphibolite-grade mylonites suggest that strain-accomodation is accomplished primarily by dislocation creep and grain-boundary sliding (Behrmann and Mainprice 1987; Kerrich et al. 1976, and others). Neither process requires large-scale mass transfer, void formation, or presence of a fluid phase (although fluids may

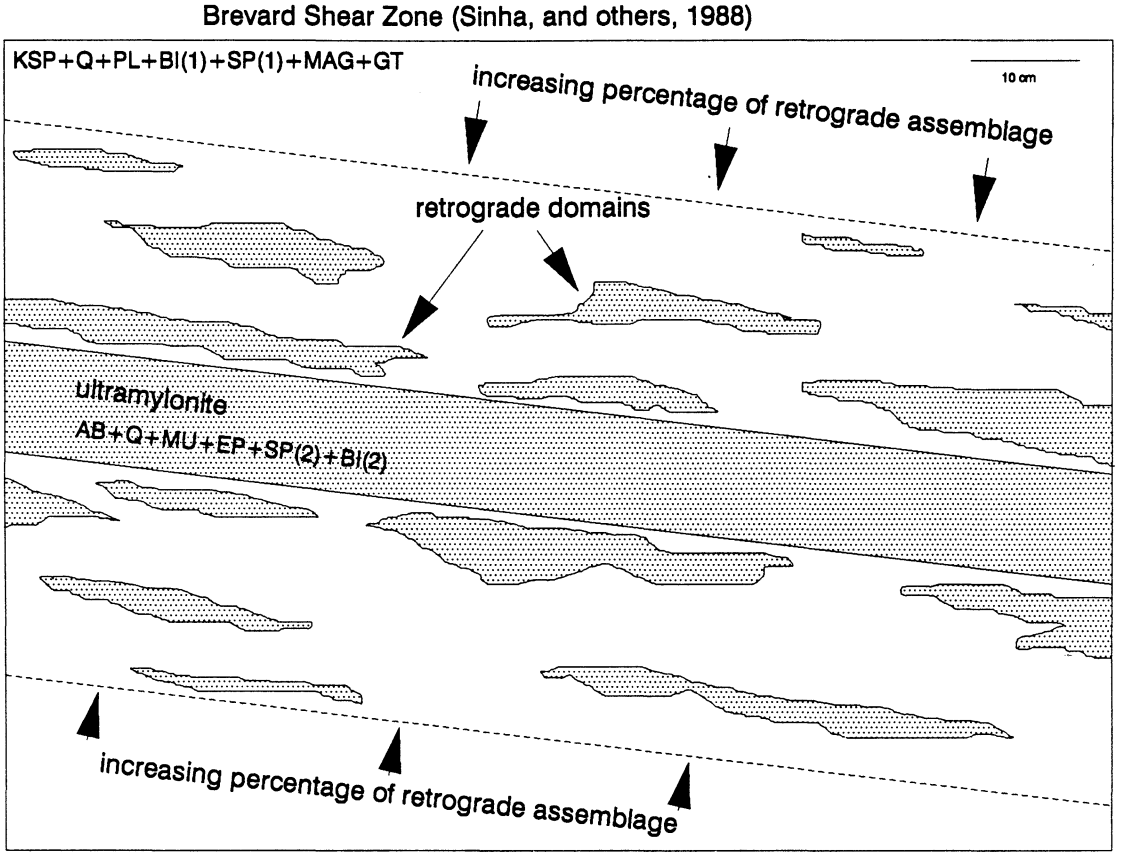


Figure P.1. Schematic depiction of the development of mineral assemblages within a retrograde shear zone: The retrograde mylonitic assemblages are dominated by phyllosilicates and associated with discrete zones of intense brittle and/or ductile deformation. The intensity of the retrogression and deformation in these zones is dependent primarily on the efficiency of hydration reactions which is, in turn, a strong function of the fluid-rock ratio during deformation (see also McCaig 1984). In this case, channelized fluid flow during deformation resulted in the total obliteration of pre-existing mineral assemblages within a narrow dilatant shear zone. Outside of the shear zone, similar retrograde mineral assemblages and mylonitic textures occur in patchily-distributed domains, indicative of a limited degree of fluid-rock interaction.

kinetically enhance strain accomodation mechanisms under any P-T regime), thus mylonitic textures may arise at high metamorphic grades through nearly isochemical processes.

Mylonites are commonly developed at lithologic discontinuities, such as contacts between chemically, mineralogically and, hence, rheologically distinct rocks. Tectonic juxtaposition of such bodies may result in zones of ductile deformation which preserve systematic changes in mineral associations and mineral chemistry related to bulk compositional contrasts, or varying degrees of fluid-rock interaction along the contact. The objective of this study is to obtain a clearer understanding of the processes involved in the mylonitization of quartzofeldspathic and mafic rocks under relatively "dry" (i.e. $P_{fluid} < P_{total}$) conditions at amphibolite grade. Because the process of chemical and isotopic redistribution is inexorably linked to the deformation mechanisms which were active during mylonitization (e.g. diffusive mass transport vs. dislocation creep), patterns may emerge from the data which will offer some insight into how grain size reduction was accomplished, although this is not the primary goal.

Non-isochemical deformation in amphibolite-grade mylonite zones is not necessarily the result of large-scale, open-system processes. Subtle, strain-related mineral-chemical gradients and/or changes in mineral assemblage suggest that mineral reactions may have accompanied grain size reduction, and that a limited amount of fluid (present as a grain boundary film) must have been involved to facilitate mass transfer. Alternatively, deformation and mineral reactions may have been initiated as the consequence of a fluid "pulse" of relatively short duration, and the mineral chemical gradients represent a later, relatively protracted period of diffusional relaxation across once-sharp conduit boundaries (i.e. McCaig and Knipe 1990). In either case, the kinetic limitations of film or grain boundary diffusion will tend to restrict the progress of metamorphic reactions and mass transfer down μ gradients. Thus, an array of mineral associations will be distributed over a relatively small volume of rock (Figure 2) within a given mylonite zone.

Chapter 1 is primarily concerned with the constraints imposed upon the mineralogical and chemical evolution of a mylonite zone at amphibolite grade. Two contrasting examples were chosen: one in which two distinct gneissic units were transposed against each other, and one in which a mafic layer was sandwiched between the two gneisses. Samples were taken as single continuous

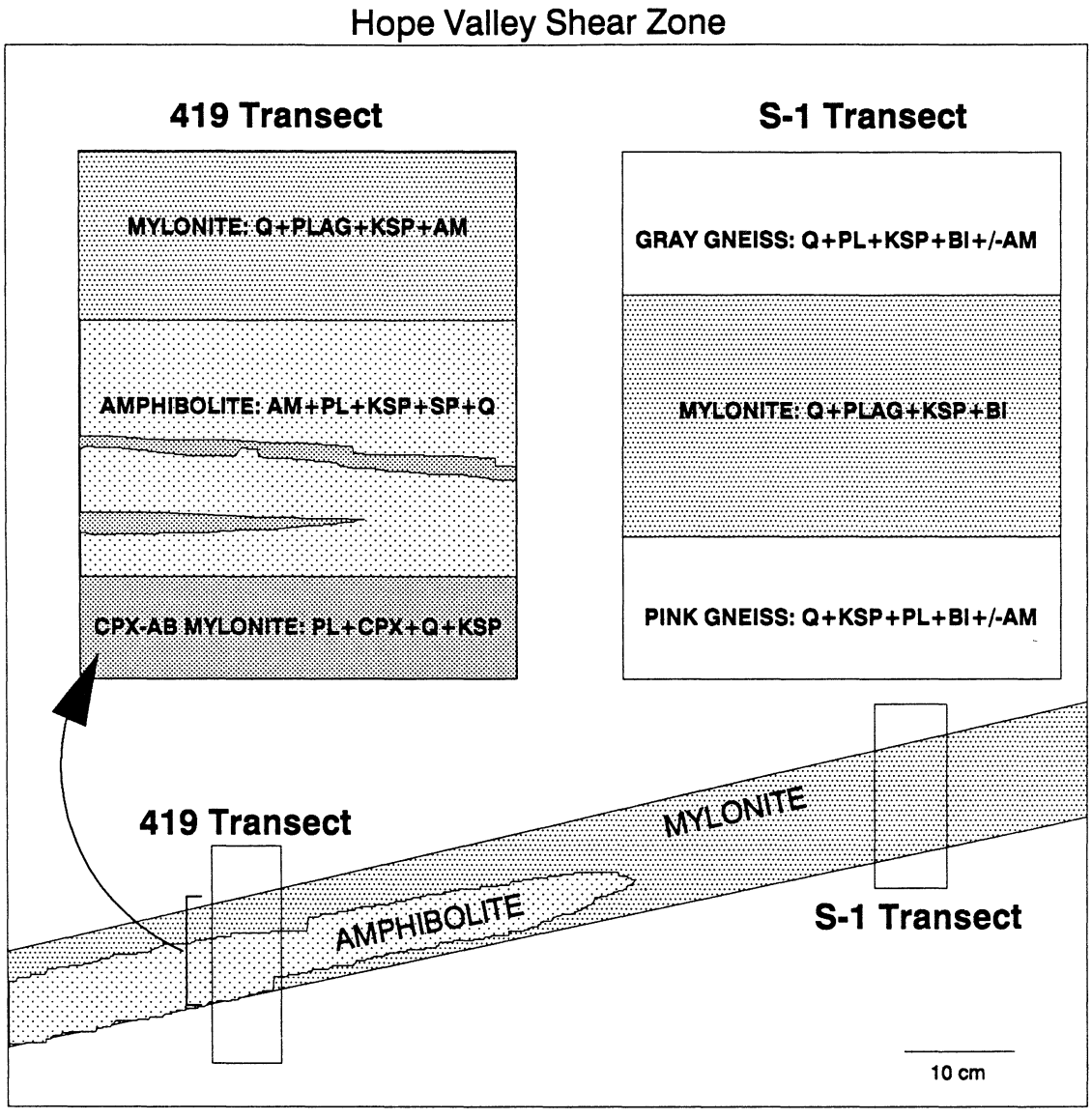


Figure P.2. **Schematic depiction of the development of mineral assemblages within an amphibolite-grade shear zone:** Mineral parageneses within amphibolite-grade ductile deformation zones are distinct from those developed in retrograde shear zones. In this example, mylonitic assemblages lack hydrous phases (except for minor amounts of biotite and/or amphibole) in general, and muscovite in particular, and K-feldspar has remained stable. Stable mineral assemblages and mineral chemistry are strongly influenced by the immediately adjacent lithologies and the diffusion gradients set up across bulk compositional discontinuities. As in the retrograde example, fluid-rock interaction may be localized.

blocks (or transects) from a single outcrop across each lithology, encompassing both gneisses, the mylonitized gneiss at the contact and, if present, the intervening amphibolite layer. Systematic variations in modal mineralogy, bulk chemistry and mineral chemistry across mineral reactions in the amphibolite-present transect are controlled, to a great extent, by hydration reactions which progressed in the mafic layer during, and shortly after, ductile deformation. Specifically, the release of Na and Si from the originally clinopyroxene- and albite-rich mafic layer locally buffered mineral reactions in the surrounding quartzofeldspathic mylonites. In the amphibolite-absent transect, the bulk chemical and modal variations are attributable to the mobility of Si, Na, K, and Ca in response to local pressure gradients set up by fracture-related dilation along the contact during deformation. This is evident from the relative abundance of foliation-parallel quartz veins in the mylonite, and by the preferential movement of Si and K into, and Na out of, the mylonite zone. While the mylonite is enriched in K and Si (as quartz and K-feldspar), the surrounding gneisses contain anomalously small amounts of quartz ($<$ 5% modal) and large amounts of plagioclase ($>$ 50% modal). Thus, on an outcrop scale, the physicochemical processes which accompany ductile deformation and fluid-rock interaction are locally controlled, and are not uniform.

In the second and third chapters, the stability of the zircon U-Pb isotopic system in mylonitic rocks from a variety of metamorphic environments is scrutinized, using mass spectrometry, SEM techniques and chemical analyses obtained from the electron microprobe. Few attempts at utilizing zircon U-Pb systematics as a dating technique have been documented in the literature (see Chapter 3 for a complete summary). The body of work on this topic indicates that the degree of perturbation of the zircon U-Pb isotopic system in rocks that have undergone severe grain size reduction and dynamic recrystallization is extremely variable. The observed effects range from no loss of radiogenic Pb at the time of deformation (e.g. Chase et al. 1983, and Chapter 3) to partial loss (e.g. Lindh and Schoberg 1988)to complete resetting (e.g. Sinha and Glover 1978). The severity of Pb loss is apparently not a simple function of metamorphic grade, as evidenced by numerous instances of magmatically inherited zircons (which preserve the age of source rocks), and by the documentation of partial resetting in middle-amphibolite grade shear zones (Lindh and Schoberg 1988). Chemical and morphological studies of zircons from the Brevard Shear Zone (Chapter 2) suggest

that Pb loss and/or U gain was accomplished during an amphibolite-grade metamorphic event via a multistage process involving 1) preferential microfracturing of α-damaged zircons due to internal stresses imposed by the differential expansion of chemically distinct zircon domains, 2) brittle failure during grain size reduction of the matrix, 3) leaching of radiogenic Pb by fluids associated with amphibolite-grade mylonitization, and 4) development of U-rich overgrowths on zircons via local dissolution-reprecipitation reactions.

An example of the relationship between brittle behavior, fluid-rock interaction and Pb-loss is the perturbation of zircon U-Pb ages in mylonites from the Brevard Shear Zone (Sinha and Glover 1978, see also Chapter 2). Zircons from the mylonite were completely reset during a middle Ordovician amphibolite-grade event, but a later Alleghanian greenschist-grade event had no effect on zircon U-Pb systematics. The reasons for this are twofold, and involve 1) the contrasting mechanical behavior of zircon in a ductilely deforming matrix, and 2) the chemical reactivity of zircon in different metamorphic environments. The likelihood of Pb loss is enhanced when zircons are fractured, thus allowing metamorphic fluids access to easily-leached, α-damaged domains. Fracturing also serves to increase the surface area of zircon available for interaction with potentially corrosive fluids. Fluids provide a medium for the transport and redistribution of Pb (and U) out of the system. Detailed chemical and morphological data presented in Chapter 2 suggest that zircons from the mylonitized rocks were extensively fractured, and that the degree of Pb loss correlated to the observed reduction in matrix grain size. Unlike Pb loss, which occurred in the protomylonites as well as the more severely deformed portions of the shear zone, the growth of U-rich zircon was confined to the most severely deformed mylonite domains. It is particularly interesting that the perturbation of the U-Pb system occurred only during the Ordovician, amphibolite-grade event. The Alleghanian retrograde event produced a large amount of phyllosilicates, which enhanced matrix ductility, thus thwarting further grain size reduction of zircons in the later phase of mylonitization. Additionally, fluids present during the retrograde event may not have been corrosive enough to leach additional Pb from the zircons.

Chapter 3 represents a refinement and an extension of some of the concepts presented in Chapter 2. In this study, zircon morphology, chemistry and U-Pb isotopic systematics are moni-

tored as a function of both lithology and matrix grain size reduction in two distinct quartzofeldspathic orthogneiss units (which comprise the late Precambrian Ponaganset gneiss) which were deformed at middle amphibolite grade along the Alleghanian-aged Hope Valley Shear Zone. These data were compared with isotopic, chemical and morphologic data gathered from zircons in a greenschist-grade ultramylonite: the mid-Paleozoic Rockfish Valley Fault Zone. In the former, perturbation of the zircon U-Pb isotopic system is strongly correlated to lithology, regardless of the strain state, and was accomplished primarily by 1) the dissolution of primary, magmatic zircon and 2) the precipitation of U-rich zircon, both during metamorphism. In one gneiss unit, corrosion-reprecipitation was extensive, regardless of the degree of grain size reduction, while in the other unit no corrosion was observed although U-rich uvergrowths were noted in the mylonitic gneisses derived from it. The unit in which the corrosion-reprecipitation was most extensive also contains abundant accessory fluorite, and it is thought that metamorphic fluids evolved during the Alleghanian deformational-metamorphic episode were locally fluorine-rich. In the latter case, zircons from the greenschist-grade ultramylonites of the Rockfish Valley Fault Zone did not record the late Paleozoic retrograde event, although they are extensively fractured, rounded and comminuted. Zircons from the protolith are strongly zoned, and contain abundant microcracks. These grains, however, did not lose radiogenic Pb as the result of disaggregation and fluid-rock interaction. Thus, the fluids present during mylonitization did not chemically interact with the zircons, despite their accunmulation of relatively high α-dosages. From the present dataset, it appears that the corrosive ability of the metamorphic fluids directly involved in mylonitization and grain size reduction is critical in determining the behavior of the zircon U-Pb system.

Chapter 1: Whole rock and mineral chemical changes associated with amphibolite-grade ductile deformation zones.

Abstract

Alleghanian-aged deformation of quartzofeldspathic and mafic rocks of the Late Precambrian Ponaganset Gneiss proceeded at amphibolite grade conditions (600°C, 4-6 kb), and was accompanied by considerable mobility of Si, Na, K, Ca, Fe and Mg. Fluids present during and after ductile deformation facilitated hydration reactions in a narrow (> 10 cm), foliation-parallel mafic layer composed largely of clinopyroxene and albitic plagioclase (An_3). The final product of these reactions was a K-feldspar/plagioclase (An_9)-rich amphibolite. Mass balance relations show that the amphibolite-forming reactions required an influx of H_2O, plus Fe^{2+} and Mg^{2+} cations, and expulsion of Na^+ into the surrounding gneisses. The source for Fe^{2+} and Mg^{2+} was probably the adjacent, actively-deforming quartzofeldspathic mylonite which, with reference to the protolith gneisses

less than 30 cm from the gneiss-amphibolite contact, is reduced by 60% of its original concentration of these elements. Where no amphibolite layer is present, quartzofeldspathic mylonites display a similar depletion in Fe and Mg, but also carry greater textural and geochemical evidence for fluid flow on a millimeter to centimeter scale, as shown by the presence of foliation-parallel quartz veins walled by monomineralic layers of plagioclase or K-feldspar, and pronounced centimeter-scale gradients in whole rock K, Na and Si concentrations.

Reaction progress calculations in the amphibolite layer suggest that minimum volumetric fluid-rock ratios never exceeded 0.05 liters H_2O/liter of rock. The local presence of strained clinopyroxene microporphyroclasts and laminae of clinopyroxene-albite mylonite in the amphibolite layer suggest that hydration reactions did not go to completion. The presence of biotite in the amphibolite layer elsewhere at the outcrop suggests that fluid-rock ratios were not uniform during, or shortly after, deformation. Post deformational metamorphic reactions in the amphibolite resulted in the formation of actinolitic rims on amphibole grains which continued to grow at the expense of adjacent, strained clinopyroxene microporphyroclasts. Textural relationships indicate that the actinolitic rims grew via diffusive processes in the presence of an intergranular fluid film.

Introduction

The geochemical signature of mylonitization is a complex function of P-T conditions, strain rate, fluid flow and the pre-deformational chemistry of the rock (LaTour 1981; McCaig 1984; Etheridge et al. 1984; and others). At amphibolite grade conditions, mylonites may represent the end-product of an array of essentially isovolumetric and isochemical deformational processes (such as dislocation glide), and locally conservative processes (such as dislocation climb) which require only intergranular diffusive transport of material (e.g. Kerrich et al. 1977; Brodie 1981). Other examples of amphibolite-grade mylonites (e.g. Beach 1973) record an extensive history of fluid flow, mineral reactions and mass transfer which resulted in parageneses distinct from those of the protolith. Still other studies (e.g. Kneller and Leslie 1984) suggest that the amount of fluid channeled through deforming rock at amphibolite grade may be limited, but sufficient to drive hydration reactions along spatially restricted zones. Recently, the possibilty of a protracted history of fluid-rock interaction and movement under a variety of stress regimes, and metamorphic facies, has been proposed for several ductile deformation zones (e.g. LaTour and Kerrich 1983; Kerrich 1986; Sinha et al. 1986 and others). These rocks are characterized by overlapping microstructural, chemical and isotopic features which indicate significant changes in the degree and mode of mass transfer have also taken place during the development of a single mylonite zone.

In order to resolve the metamorphic and geochemical history of mylonites, the processes of mass transfer, mineral reaction and fluid flow must first be understood. Studies of the isotopic, microtextural and chemical consequences of different mass transport mechanisms (e.g. Fletcher and Hoffman 1974; Baker et al. 1990; McCaig and Knipe 1990) require a wide variety of observations of an extremely detailed nature before the information can be generalized into a working model.

This study is primarily concerned with identifying and describing the purely chemical effects of mass transfer, on a centimeter to millimeter scale, associated with the amphibolite-grade mylonitization of interlayered mafic and granitic lithologies of the Ponaganset gneiss in south-central Massachusetts.

Regional Geology and Sample Description

The Hope Valley Shear Zone (Figure 1.1), in southeastern New England, is a major amphibolite-grade ductile shear zone of Alleghanian age (O'Hara and Gromet 1983,1985; Gromet and O'Hara 1984; Wayne and Sinha 1988,1989). In the vicinity of the sample locality, the Hope Valley Shear Zone dips shallowly (10° to 30°) to the west, strikes N-S and cuts a 10 to 15 km wide swath through late Proterozoic and Paleozoic igneous rocks, predominantly of granitic to granodioritic composition (O'Hara and Gromet 1985). O'Hara and Gromet (1985) and Gromet (1989) interpret the Hope Valley Shear Zone as the boundary between two tectonically and petrologically distinct fault-bounded Avalonian fragments: the Hope Valley terrane to the west, and the Esmond-Dedham terrane to the west. The northern segment of the Hope Valley Shear Zone, which extends from south-central Massachusetts to extreme southeastern Connecticut, constitutes the contact between the late Precambrian Ponaganset gneiss to the east and the Hope Valley alaskite gneiss to the west. The Ponaganset gneiss is a variably deformed granitic to granodioritic body of late Precambrian age (Wayne and Sinha 1989; Wayne et al., in review). At its western periphery the Ponaganset gneiss shows progressively greater degrees of ductile deformation in the vicinity of the Hope Valley Shear Zone.

All samples used in this study were taken from a roadcut within the Ponaganset gneiss (Figure 1.2) along Massachusetts route 146, near the town of Auburn (stop 9 in Gromet and O'Hara, 1984).

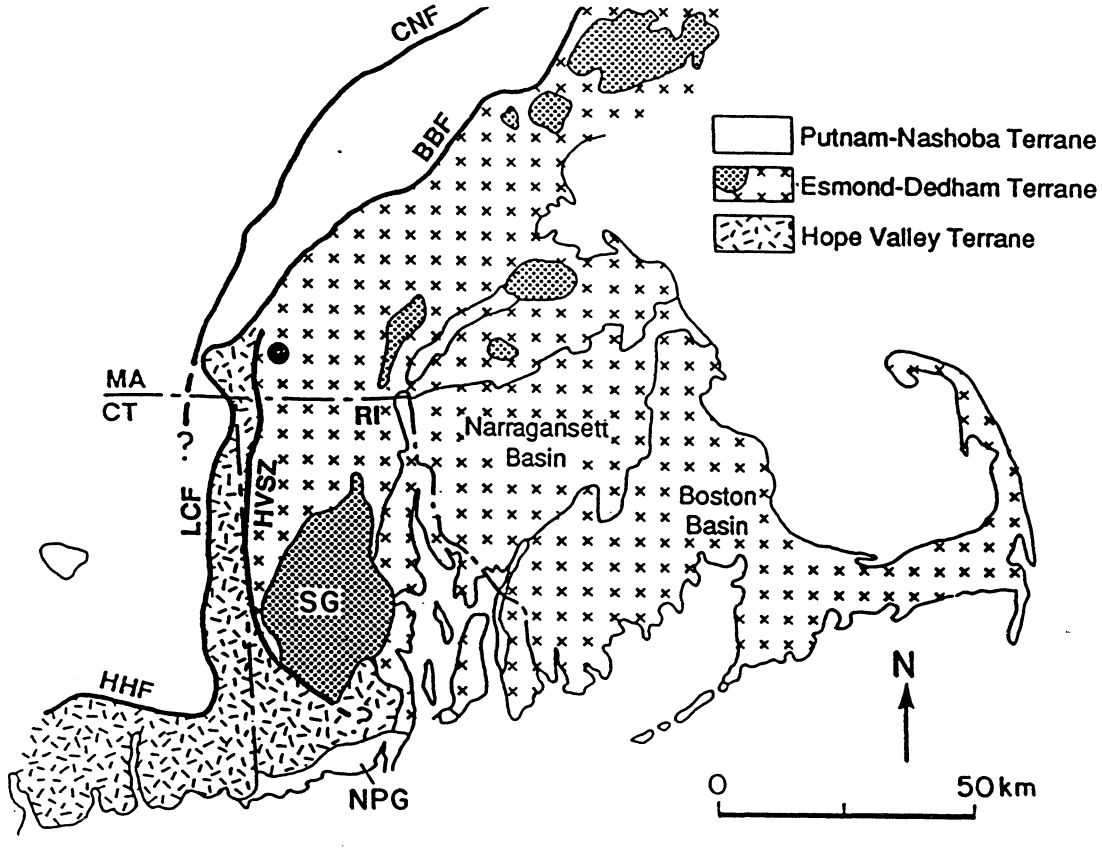


Figure 1.1. Generalized geologic map of southeastern New England: This map, adapted from O'Hara and Gromet (1985) shows the position of terrane boundaries and major fault zones relevant to this study. LCF = Lake Char Fault Zone, HHF = Honey Hill Fault Zone, BBF = Bloody Bluff Fault Zone, HVSZ = Hope Valley Shear Zone.

The outcrop is situated approximately 1.5 km east of the Hope Valley Shear Zone proper, as mapped by O'Hara and Gromet (1985). At the sample locality (also described in Gromet and O'Hara 1985), the Ponaganset gneiss consists of two mineralogically and texturally distinct units: a fine grained, porphyroclastic gray augen gneiss (Pl + Qtz + Ksp + Am + Bi + Tit + Mag), and a fine-to-medium grained pink granitic gneiss (Qtz + Ksp + Pl + Bi + Tit + Mag ± Am ± Gt). These two units occur as discrete alternating tabular bodies, tens of meters thick, often bounded by thin (5-15 cm), attenuated amphibolite layers (Figure 1.2). Typically, the attitudes of the contacts, amphibolite layers, and mylonite zones are similar and parallel the plane of foliation (see also Gromet and O'Hara 1985). The foliation plane strikes nearly perpendicular to the regional strike of the Hope Valley Shear Zone, and asymmetric tails of feldspar augen indicate a southward thrusting direction (Gromet and O'Hara 1985; O'Hara and Gromet 1985). Macroscopic and microscopic structural data (Gromet and O'Hara 1985; O'Hara and Gromet 1985) indicate that the gneissic units were dynamically juxtaposed during amphibolite-grade metamorphism, which resulted in the development of ductile deformation zones. Ductile deformation zones occur both within the tabular gneiss units, and at the contacts between adjacent gneiss units, and are marked by bleaching, appreciable matrix grain size reduction. At the gray gneiss-amphibolite contact, recrystallization and size reduction of K-feldspar augen is evident within approximately 20 cm of the gray gneiss-amphibolite contact (Figure 1.3). Within 10 cm of the contact, intense grain size reduction results in the formation of narrow, sharply bounded, fine grained (50-100 μm) mylonite zones.

The mineralogy of the gneisses, amphibolites and mylonites varies across the outcrop. Most notable is the increasing development of retrograde, phyllosilicate-rich assemblages as a function of increasing proximity to the trace of the Hope Valley Shear Zone (towards the west). Mylonitized gneisses from within the Hope Valley Shear Zone proper are devoid of amphibole, and contain subhedral, foliation-parallel blades of muscovite. With increasing distance from the Hope Valley Shear Zone, muscovite becomes less common in the Ponaganset gneiss., occurring dominantly as patchily-distributed anhedral flakes associated with post-kinematic alteration of feldspars. At the transect sites, mineralogical evidence for the retrogression of the amphibolite-grade

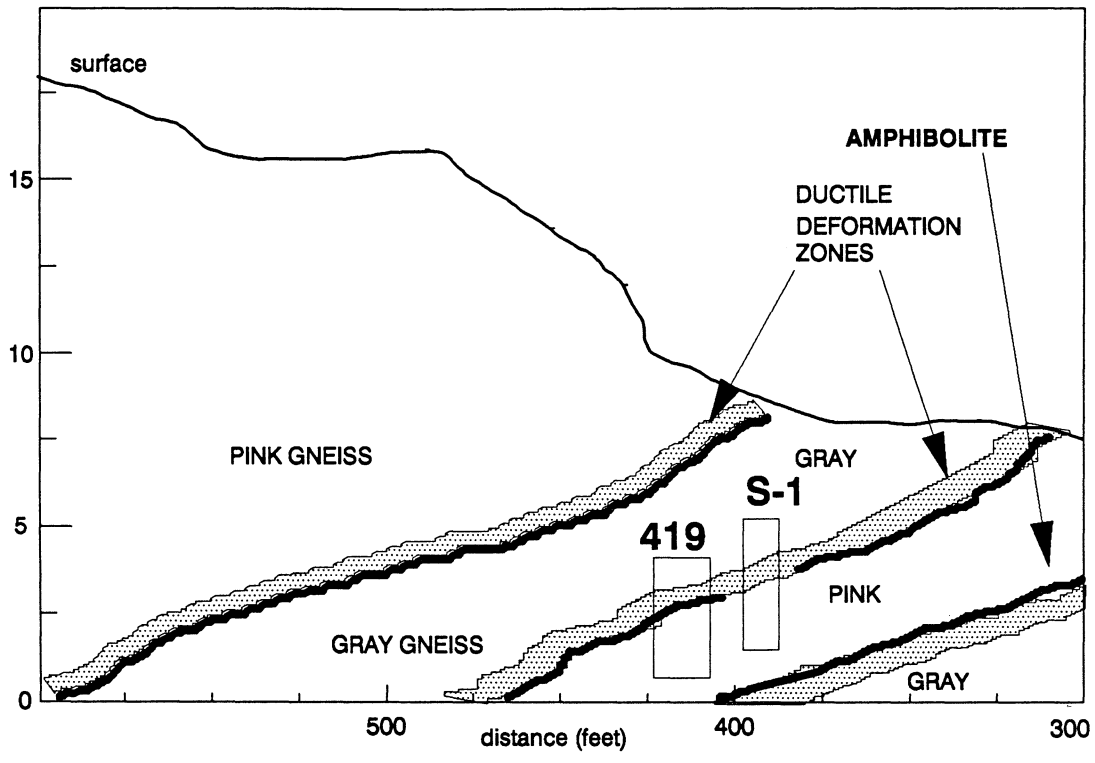


Figure 1.2. **Schematic scale map of the sample locality:** This map shows the general distribution of the major lithologic units (gray augen gneiss, pink granitic gneiss, and amphibolite), ductile deformation zones (DDZ), and the locations of the transects.

Figure 1.3. **Field photographs of mylonite zones in the Ponaganset gneiss:** S-1 Transect (a) without amphibolite layer, and 419 Transect (b) with intervening amphibolite layer. In both examples, the gray gneiss overlays the pink gneiss. Note the sharp amphibolite - mylonite contact.

A
0
5
10 CM
B
0
5
10 CM

mylonitic/metamorphic assemblages is generally lacking, except locally along fractures (which often contain calcite and/or epidote) and along late, locally abundant, crosscutting quartz veins (often surrounded by haloes of stained, altered feldspar).

Of the gneissic units, the gray gneiss is the least variable and retains the assemblage Pl + Ksp + Qtz + Am + Bi across the entire outcrop, although local changes in the modal proportions of these minerals were observed. Also present within the gray gneiss are meter-sized, sheared and deformed pegmatite pods which are mineralogically identical to the surrounding gray gneiss, but often contain a variety of static, late stage alteration products (e.g. epidote, chlorite, etc.). The pink gneiss consists primarily of Qtz + Ksp + Pl + Bi, with locally variable amounts of hornblende, garnet, fluorite and clinopyroxene. The mineralogical diversity of the pink gneiss is related to areas of high strain and extreme grain size reduction. Mylonites within the pink gneiss may also contain macroscopic segregations which consist of plagioclase (An_{24}), spessartine-rich garnet, hastingsitic hornblende, fluorite, magnetite and epidote.

Quartzofeldspathic mylonites derived from the gneisses generally mirror the assemblages of the protolith. In most instances, however, the mylonites lack one of the two ferromagnesian phases that characterize the protolith gneisses. A number of mylonite samples also display systematic millimeter-to-centimeter scale changes in the modal abundance of K-feldspar and plagioclase with increasing proximity to the contact with the amphibolite layer. The mineralogy of the amphibolite layers is extremely variable across the outcrop. For example, the following assemblages were observed in a single amphibolite unit within $\simeq$ 300 meters;

Hbd + Pl + Ksp + Qtz

Hbd + Pl + Ksp + Qtz + Cpx

Pl + Cpx + Ksp + Hbd + Qtz

Bio + Hbd + Qtz + Pl + Ksp.

Other amphibolite layers contain minor amounts (< 1 % modal) of primary epidote and calcite. Like the mylonites, the amphibolites are internally heterogenous on a mm to cm scale.

The physicochemical processes which accompanied the formation of amphibolite-grade ductile deformation zones in the Ponaganset gneiss are best documented over very short (cm scale) distances, due to the sharp transitions between lithologic units and the tendency for the most severe effects of mylonitization to be localized within ≃20 cm of the contacts. Thus, two large samples, each comprising at least two lithologic units and a ductile deformation zone, were selected for detailed study. The two transects are distingushed by the presence (419) or absence (S-1) of an amphibolite layer between the gray gneiss and the pink gneiss (Figure 1.4), and by the development of two distinct successions of mineral assemblages with respect to proximity of a contact (Figure 1.5). The 419 transect consists of a single continuous block (15 cm by 60 cm) with its long axis perpendicular to the foliation. In addition, samples of each gneiss (GG419 and PG419) were collected 30 to 40 cm above and below the vertical extent of the continuous transect. The S-1 transect consists of a single similarly oriented block (30 by 15 cm), approximately 10 m away from the 419 transect across the same contact, which contains no intervening amphibolite layer.

To assess the scale of mass transfer across the ductile deformation zone and describe the relationships between mineral chemistry, modal variations and bulk chemistry, a cm-scale sampling technique was required. To this end, the transects were slabbed parallel to foliation (Figure 1.4), and the 0.5 to 5 kg samples were processed for whole-rock chemical analyses. In general, sample sizes varied as a function of grain size, with the finer grained slabs permitting a representative sampling at smaller sample weights. For the S-1 transect slab thicknesses varied from 1 to 2 cm, with the thinnest slabs cut from the mylonite and the regions immediately surrounding the mylonite (Figure 1.4). Slab thicknesses across the 419 transect were based on microscopic and macroscopic changes in textures and mineral assemblages. As a result, the slab thicknesses vary with respect to their proximity to the ductile deformation zone, with the thinnest slabs cut from the mylonite and the amphibolite. Standard petrographic thin sections, oriented perpendicular to foliation and parallel to the lineation, were also cut from the slabs. Point counts and microprobe analyses were performed on duplicate thin sections.

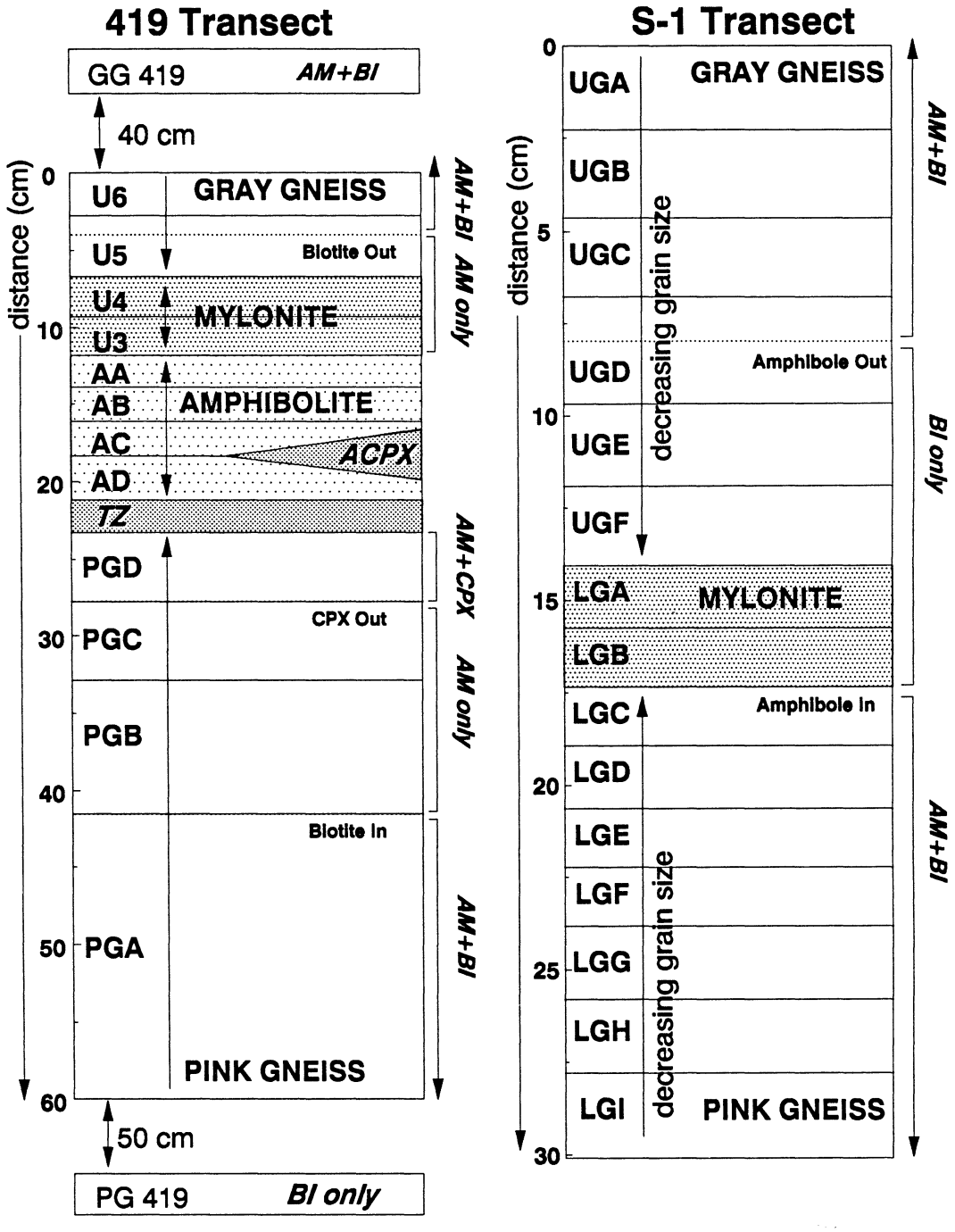


Figure 1.4. Schematic diagram of the 419 and S-1 transects, showing the slabs cut for bulk chemical analyses.

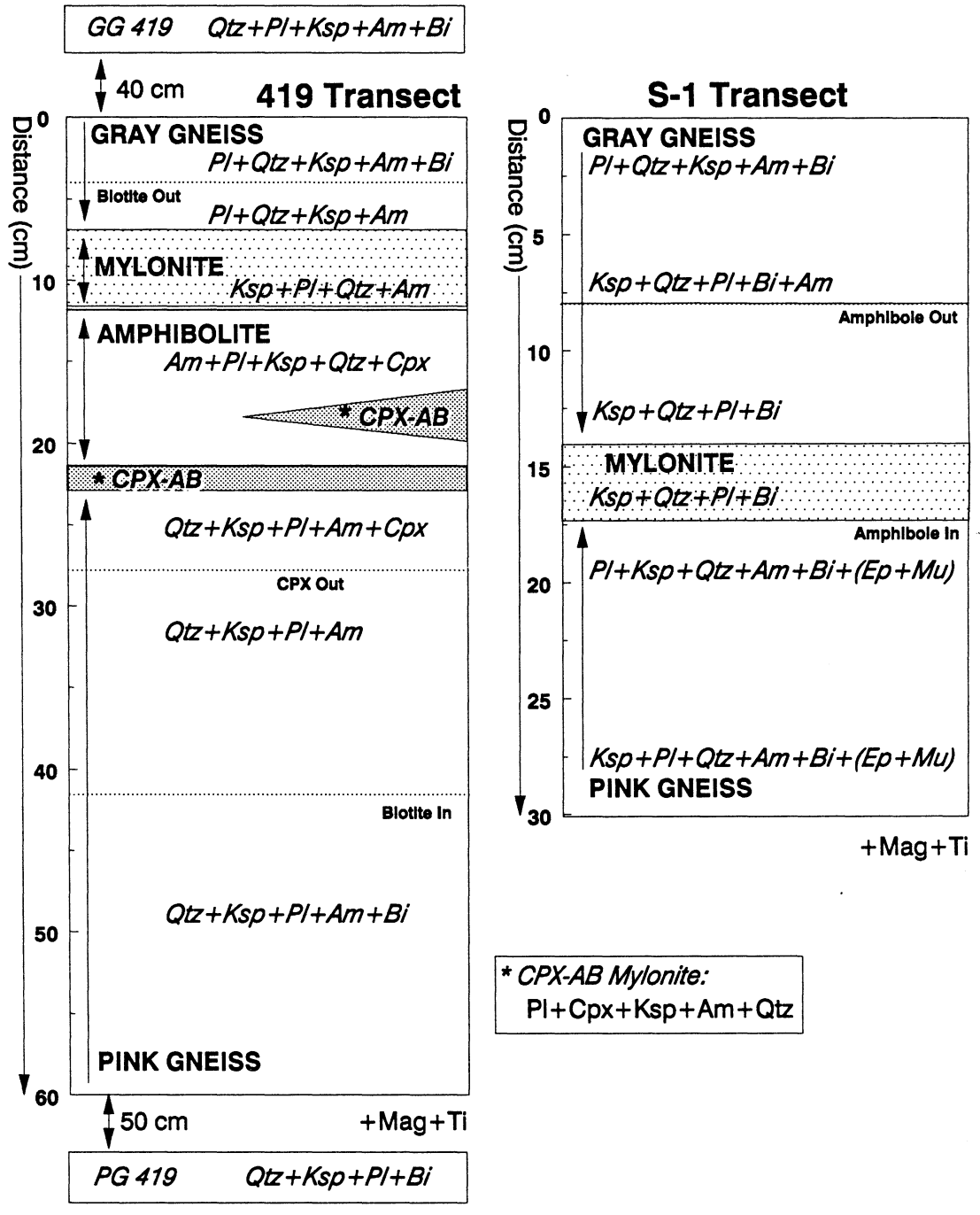


Figure 1.5. Schematic diagram of 419 transect (left) and S-1 transect (right): Note the development of different metamorphic assemblages with increasing strain, and increasing proximity to lithologic discontinuities. Minerals listed in order of decreasing modal abundance.

Petrographic and Microstructural Description of the Transects

419 Transect: Gray gneiss

The gray gneiss is typified by the assemblage plagioclase + quartz + K-feldspar + hornblende ± biotite, with abundant accessory titanite, magnetite, zircon and apatite. Porphyroclastic relict perthite augen are partially recrystallized, and often exhibit myrmekitic rims (Simpson and Wintsch 1989) and/or core and mantle structures. Porphyroclastic plagioclase is rare and occurs as thoroughly recrystallized aggregates of coarse subhedral grains. Hornblende is coarse (up to 1 cm), subhedral and poikiloblastic, with numerous inclusions of titanite, quartz, plagioclase and, rarely, epidote. In the less-deformed samples, euhedral hornblende grains are often surrounded by a "halo" of recrystallized plagioclase. The matrix consists of a polygonal mosaic (~ 100-300 μm) of recrystallized plagioclase, alkali feldspar, quartz and aligned, grain boundary-pinning biotite plates. Accessory titanite, magnetite, and rare allanite euhedra are associated with biotite and hornblende in trains that parallel foliation. Alteration is sparse and consists of static local chloritization of biotite along cleavage planes and sericitization of plagioclase cores. Alkali feldspar augen are often turbid, but rarely contain late muscovite or epidote grains.

Within ≃ 50 cm of the contact with the amphibolite, matrix grain size decreases to ~50-150 μm and polycrystalline quartz eyes with sutured internal grain boundaries become prominent. The cores of perthitic augen are kinked and show slip along the kink planes. The undeformed regions of the augen are bounded by stringers of finely recrystallized microcline, plagioclase (occasionally myrmekite) and quartz, and there is noticeable lattice offset between the various slipped and un-slipped domains. Some of the perthitic augen are extensively recrystallized, and are partially rimmed with coarse (~ 1 mm) quartz, microcline and subhedral twinned plagioclase rather than myrmekite.

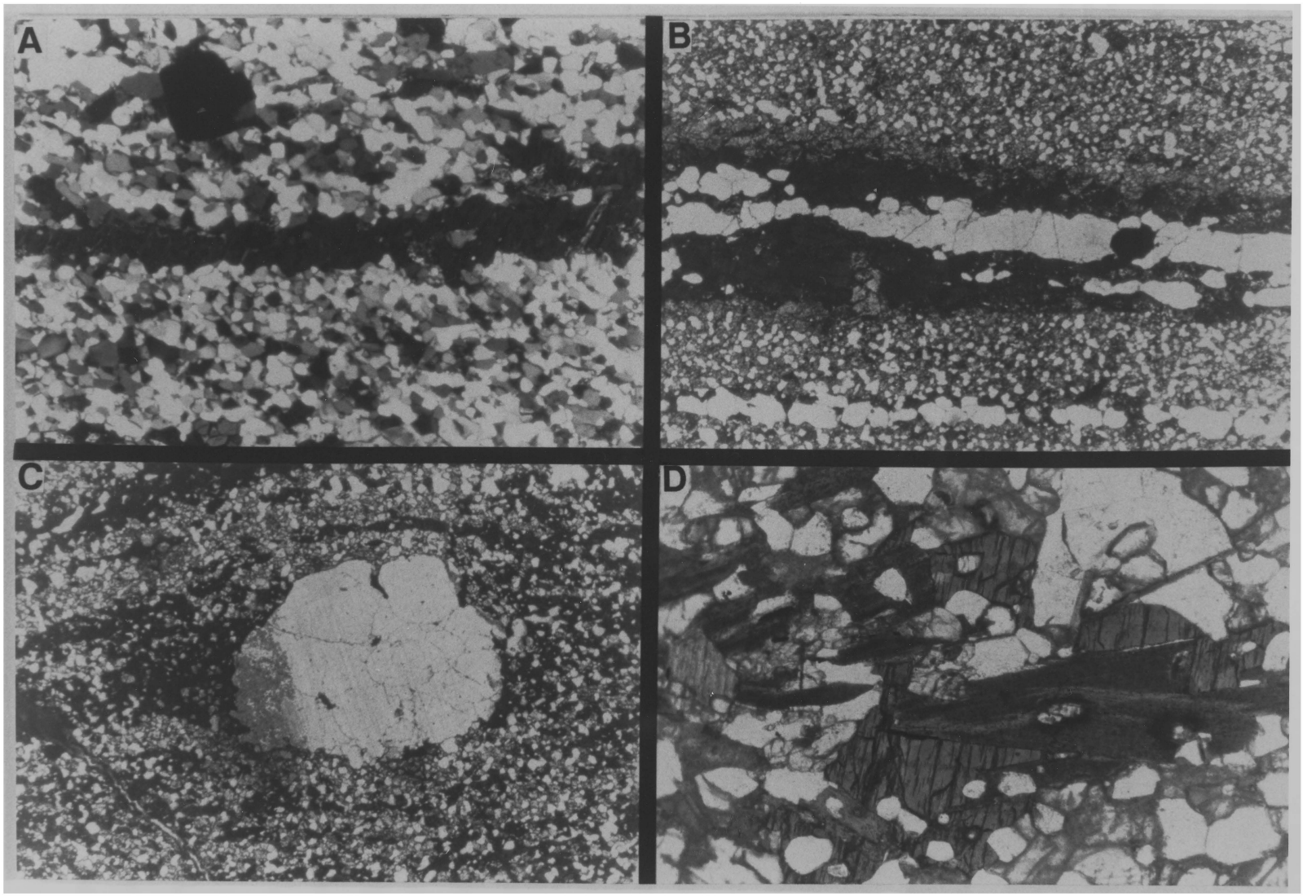
Within $\simeq$ 10 cm of the contact with the amphibolite, quartz eyes increase in abundance and become increasingly stretched (some have aspect ratios >10:1). Hornblende grains also appear to have undergone slip along cleavage planes (see Allison and LaTour 1977) to rotate into foliation and become highly attenuated (Figure 1.6a).

Mylonite derived from the Gray Augen Gneiss (419)

The mylonite derived from the gray gneiss (419) is a thoroughly recrystallized, mosaic-textured aggregate of polygonal 50 to 150 μm plagioclase, K-feldspar and quartz grains, with sparse accessory hornblende and/or biotite and less abundant titanite and magnetite. In general, the mineral assemblages observed in the mylonites are identical to those observed in the central regions of the less-deformed protolith gray gneiss blocks. However, the mineralogy of the mylonites derived from the gray gneiss varies laterally over 10's to 100's of cm, particularly with reference to the modal abundance of feldspars and quartz, and the presence or absence of biotite and amphibole.

Syn-to-post kinematic recrystallization has obscured nearly all evidence of the specific mechanisms that originally affected the grain size reduction. Relatively coarse (< 1 mm in width) quartz ribbons (type 3 of Boullier and Bouchez 1978), with deformation bands normal to the plane of foliation are locally abundant, particularly within 0.5 cm of the contact itself. In some samples, individual quartz ribbons are entirely surrounded by a halo of relatively coarse-grained K-feldspar and/or plagioclase (Figure 1.6b). Fine-grained recrystallized K-feldspar shows textural features similar to those observed in other amphibolite-grade quartzofeldspathic mylonites (e.g. Behrmann and Mainprice 1987), occurring dominantly in streaks and bands that parallel foliation and are deflected by microporphyroclasts (Figure 1.6c), and as pressure shadows (Figure 1.6c) around quartz microporphyroclasts. Recrystallized, stretched and flattened K-feldspar porphyroclasts are rare in the ductile deformation zone. Accessory hornblende occurs both as <400 μm long, prismatic to acicular euhedra with strong grain-shape preferred orientation, and as somewhat larger (< 1 mm)

Figure 1.6. Microstructural features of the gneisses and mylonites: (a) - Attenuated hornblende grain, typical of the protomylonite and mylonite derived from the gray gneiss. Note high angle of cleavage traces to the long dimension of the grain. Crossed nicols. Horizontal field of view = 4.3 mm. (b) - Quartz ribbon enveloped by coarse-grained, strain-free K-feldspar (stained dark) from quartzofeldspathic mylonite. The K-feldspar is, in turn, rimmed by finer-grained plagioclase (light gray). Similar features are common in the mylonite at S-1. Uncrossed nicols. Horizontal field of view = 4.3 mm. (c) - Quartz porphyroclast with K-feldspar-rich pressure shadows (stained dark) from quartzofeldspathic mylonite. Note deflection of K-feldspar stringers around the porphyroclast. Uncrossed nicols. Horizontal field of view = 4.3 mm. (d) - Euhedral biotite replacing resorbed, anhedral hornblende in the gray gneiss $\simeq$ 8 cm above the ductile deformation zone at S-1. Cloudy grains are stained K-feldspar. Horizontal field of view = 2.2 mm.


A
B
C
D

ameboid to subhedral micropoikiloblasts, neither of which show any signs of a previous strain history. Across the S-1 transect, hornblende is apparently unstable in the mylonite and gneiss proximal to the mylonite (Figure 1.6d). Magnetite grains are comminuted and strung out along foliation, and may occur in association with quartz ribbons. Relatively coarse (>200 μm), anhedral titanite is common and appears, in some instances, to overgrow the foliation. The mylonite-amphibolite contacts are sharp (i.e. the transition occurs over a distance < 0.5 mm), and are characterized by persistent quartz ribbons, an abrupt increase in overall grain size and an abrupt modal increase in hornblende. Taken together, textural features such as the thorough recrystallization of feldspars, and mineral assemblages which lack typical hydrated greenschist-grade phases indicate that the formation of ductile deformation zones within the Ponaganset gneiss took place at middle amphibolite grade (~600°C) conditions (see also Simpson and Wintsch 1989; LaTour and Kerrich 1983; and Behrmann and Mainprice 1987).

Amphibolite: 419 Transect

Contacts between the amphibolite layer and the mylonitic gneisses are sharp and non-gradational (e.g. Figure 1.3). The amphibolite layers are generally thin (up to 10 cm) planar, concordant units composed of thinly interlaminated bands of varying mineralogy and texture. Across the 419 transect, these bands fall into three generalized categories: 1) fine grained (100-200 μm), well-foliated Hbd + Pl + Ksp + Qtz ± Cpx. amphibolite, 2) coarser grained (500-1000 μm), microporphyroblastic, poorly foliated amphibolite with a similar assemblage to the finer-grained regions and 3) a fine-grained (50-150 μm), mosaic-textured mylonitic variant composed of Pl + Cpx + Ksp + Am + Qtz (clinopyroxene-albite mylonite). Typically, the finest grained amphibolite domains contain the lowest modal abundances of quartz and clinopyroxene. Accessory titanite is abundant throughout the entire amphibolite, but magnetite is largely restricted to the clinopyroxene-albite mylonite bands.

Boundaries between the coarse and fine grained bands are typically gradational. The clinopyroxene-albite mylonitic bands are often sharply bounded by the fine grained amphibolite, but have a gradational relationship to the coarse-grained amphibolite domains. Variations in grain size and mineralogy within the amphibolite are asymmetrical with respect to the contacts with the gray and pink quartzofeldspathic gneisses. Amphibole and matrix grain size tends to increase systematically with increasing proximity to the gray gneiss-amphibolite contact, while the pink gneiss-amphibolite contact is characterized by the presence of a 0.5 to 1 cm thick layer of clinopyroxene-albite mylonite, which is, itself, bounded by a thin ($\simeq$ 1 to 2 mm) layer of amphibolite at its outermost edge.

In the amphibole-dominated bands, bright green to green-blue pleochroic hornblende euhedra, up to 1 cm long, are set in a fine-grained (100-200 μm) matrix of anhedral, recrystallized plagioclase, K-feldspar and, locally, clinopyroxene. In thin section, individual hornblende grains show no visible evidence of zoning, and often contain inclusions of titanite, apatite and feldspars.

Porphyroclasts in the amphibolite are rare, and consist either of turbid, recrystallized plagioclase, K-feldspar or a composite clinopyroxene-amphibole core and a recrystallized amphibole margin. The evidence for the recrystallization of amphibole in the porphyroclast rim is: 1) abundant subgrains with euhedral outlines showing slight lattice offset, 2) the presence of small euhedral discrete amphibole grains at the porphyroclast margins and in the porphyroclast tail (Figure 1.7a). Clinopyroxene has also undergone recrystallization, as evidenced by the presence of strain-free subhedral clinopyroxene grains within corroded, undulose porphyroclasts. Amphibole and fine-grained clinopyroxene also occur together in the tail regions of the composite porphyroclasts, suggesting that, initially, both phases were stable during deformation. Fine-grained matrix clinopyroxene typically appears strain-free.

The narrow bands of pale green, mosaic-textured, clinopyroxene-albite mylonite consist almost entirely of plagioclase (45 to 70 %) and clinopyroxene (20 to 30%), with minor amounts of K-feldspar, quartz and amphibole, and abundant accessory titanite and magnetite (Figure 1.7b). Magnetite, which is rare in the hornblende-rich regions of the amphibolite, occurs as tiny ($\simeq$50 μm) equant grains with scalloped, irregular margins. Rare, large amphibole grains (up to 1 cm long)

Figure 1.7. Microstructural features of the amphibolite layer (419): (a) - Composite clinopyroxene (light gray) - amphibole (dark gray) porphyroclast from the amphibolite layer. Textural features, such as the presence of fine-grained, recrystallized clinopyroxene in the "tail" region, and the thorough recrystallization of amphibole, suggest deformation took place within the P-T stability field of both minerals. Note especially the polygonal, euhedral nature of subgrains in the amphibole. Uncrossed nicols Horizontal field of view = 4.3 mm. (b) - Typical example of the clinopyroxene-albite mylonite. Clinopyroxene appears light gray. Uncrossed nicols Horizontal field of view = 2.2 mm. (c) - Euhedral amphibole grain (dark) overgrowing corroded clinopyroxene (light gray) in the clinopyroxene-albite mylonite. Other inclusions in the amphibole are titanite. Uncrossed nicols Horizontal field of view = 0.9 mm. (d) - Strained, mechanically twinned clinopyroxene grain from the amphibolite layer. Crossed nicols. Horizontal field of view = 0.9 mm.

A
B
C
D

in the clinopyroxene-rich mylonites are typically euhedral, define a weak lineation and may contain corroded clinopyroxene inclusions (Figure 1.7c). Coarse-grained (up to 2 mm) clinopyroxene, quartz and feldspars occur in the central portions of these layers. Often, the clinopyroxene microporphyroclasts are anhedral, corroded and mechanically twinned (Figure 1.7d), or are variably recrystallized with tails of fine-grained, unstrained matrix clinopyroxene. In addition, narrow (2-3 mm wide) micro-boudins of coarse-grained (500-1000 μm) quartz and strained poikiloblastic clinopyroxene occur locally at the pink gneiss-amphibolite contact Two lines of textural evidence suggest that at least some of the amphibole post-dates the clinopyroxene; 1) anhedral clinopyroxene microporphyroclasts contain ingrown, euhedral amphibole grains, and 2) euhedral amphibole blades may overgrow and envelop corroded clinopyroxene grains (e.g. Figure 1.7c), but the reverse was not observed.

Thin (<5 mm in width) attenuated bands of recrystallized felsic material occur within the amphibolite, and form tight isoclinal internal folds with axes nearly parallel to the foliation. Unlike the clinopyroxene-albite mylonites, these bands consist of recrystallized quartz and feldspars and contain no clinopyroxene. Thus, it appears that the clinopyroxene-albite mylonites do not have a mixing origin.

The origin of the amphibolite layers is somewhat problematic, as they are both compositionally and mineralogically distinct from similar-appearing rocks derived from precursors of broadly basaltic composition. The amphibolite layers within the Ponaganset gneiss contain abundant (up to 20 %) primary K-feldspar, which is not typical of metamorphosed mafic rocks. Bulk and mineral chemical data presented in the following sections also show that the amphibolite layers from the study area are unusually rich in K and Na in comparison to typical basalt-derived amphibolites (e.g. Jan 1988; Weaver et al. 1982). While a mixing origin (c.f. Orville 1972) cannot be completely ruled out, such a model is improbable in light of the igneous origin of the Ponaganset gneiss. An alternate possibility is that the clinopyroxene-albite mylonites represent a lithologic precursor to the amphibolite. This is supported by textural observations which suggest that at least some of the amphibole post-dates the clinopyroxene, and by the fact that the clinopyroxene-albite mylonites contain more Na_2O than any of the other lithologies in the Ponaganset gneiss. Rocks

similar in bulk composition and mineralogy to the clinopyroxene-albite mylonites and Ab-Ksp-rich amphibolites have been reported from the northeastern Adirondacks by Whitney and Olmstead (1988, their 'mafic albite gneisses'), who proposed a high-grade metavolcanic/metavolcaniclastic origin. Thus, it is not implausible that the Ab-Ksp-amphibolites and clinopyroxene-albite mylonites represent the metamorphic equivalent of mafic-to-intermadiate extrusive igneous rocks which had been altered prior to amphibolite-grade metamorphism.

Pink granitic gneiss: 419 Transect

The pink gneiss immediately below the amphibolite layer at 419 is a thoroughly recrystallized, foliated KSP + PLAG + QTZ + HBD + CPX gneiss with accessory sphene, magnetite and allanite. Textures in the pink gneiss below the contact are typified by alternating bands and lenses of fine-grained (50 to 200 μm) mylonitic material, polycrystalline quartz ribbons (Type 3: Boullier and Bouchez 1978) of varying thickness (up to 1 cm across), and bands and lenses of relatively coarse-grained (500 to 1000 μm) material dominated by partially recrystallized, turbid alkali feldspar clasts and rare, completely recrystallized plagioclase porphyroclasts. Transitions between these three textural domains may be gradational, or abrupt and bounded by concentrations of titanite, magnetite and amphibole. Retrograde phases such as muscovite, epidote, calcite and chlorite are present in variable amounts, particularly in the coarse-grained domains. The intensity of this alteration varies on a centimeter scale, but the modal amount of the retrograde minerals never exceeds $\sim$1% of the total rock.

As in the gray gneiss, there appears to be a zonation of ferromagnesian mineral assemblages with increasing distance from the pink gneiss-amphibolite contact The typical pattern is a succession of planar horizons about the amphibolite/ultramylonite layer in which increasingly hydrated ferromagnesian phases are stabilized with increasing distance from the contact. In the pink gneiss, anhedral, resorbed clinopyroxene disappears $<$ 7 cm below the pink gneiss-amphibolite contact

Dark green, subhedral to anhedral, resorbed amphibole is present at the contact between the pink gneiss and the amphibolite, and persists to approximately 70 cm below the contact. Intensely pleochroic green-brown biotite appears, as unoriented anhedral shreds within the coarse feldspar-rich domains, approximately 15 cm below the contact and steadily increases in abundance away from it. In the pink gneiss sample taken ≃2 m below the pink gneiss-amphibolite contact (PG419), the stable assemblage is alkali feldspar, plagioclase, quartz, biotite with accessory sphene and magnetite. The restricted occurrence of amphibole and clinopyroxene in the pink gneiss, and their relationship to the amphibolite layer, suggest a metamorphic origin.

S-1 Transect: Gray gneiss and mylonite

In the amphibolite-absent S-1 Transect, the fabric and mineralogy of the gray gneiss is similar to that of the gray gneiss of the 419 transect. Some differences are apparent in terms of the intensity of post-metamorphic greenschist-grade alteration. The gneisses at S-1 are more pervasively altered than at 419, and the intensity of the alteration tends to decrease in the vicinity of the ductile deformation zone Typically, amphibole and biotite are partially to completely converted to chlorite and/or secondary red-brown biotite. Plagioclase and K-feldspar are often turbid and variably sericitized, and large anhedral shreds of muscovite may appear within partially recrystallized K-feldspar augen. Where alteration is most severe, static retrograde minerals occupy <5% of the total rock volume.

Biotite and amphibole are intimately associated within the gray gneiss at S-1 and, unlike the gneisses at 419, often occur within the same foliation horizon. Biotite blades may penetrate the resorbed, subhedral amphibole grains (e.g. Figure 1.6d). Amphibole disappears altogether ≃5 cm above the ductile deformation zone (see also Figure 1.5). Neither of these textural relationships were observed in the gray gneiss at the 419 transect where biotite and amphibole tend to occur ex-

clusively in separate domains, and biotite disappeared ≃6 cm above the &ggam, while amphibole persisted.

The mylonite at S-1 is texturally and mineralogically similar to the gray gneiss-derived mylonite at 419, except that biotite is the only apparently stable ferromagnesian silicate. Quartz ribbons within the mylonite are surrounded by relatively coarse (≃250 μm) plagioclase grains which, at the quartz-plagioclase interface, are bounded by a thin selvage of K-feldspar. Also present within the mylonite at S-1 are narrow (≃2 mm wide) planar zones of mosaic-textured, fine grained, nearly pure plagioclase and quartz.

S-1 Transect: Pink gneiss

The pink gneiss at S-1 is texturally and mineralogically distinct from pink gneiss at 419. In general, quartz is much less abundant in the S-1 pink gneiss, and quartz ribbons are not developed. The S-1 pink gneiss also lacks "micromylonites", and its grain size is relatively uniform (150 to 350 μm) regardless of proximity to the contact. Porphyroclasts are sparse and completely strain-free. Mineralogically, the S-1 pink gneiss lacks clinopyroxene which was observed adjacent to the amphibolite-pink gneiss contact at 419. Alteration is also more pervasive in the pink gneiss at S-1, and chlorite and muscovite (both coarse and sericitic) are common, although calcite was not observed. Secondary epidote is present within the S-1 pink gneiss as colorless to pale yellow granules concentrated at grain boundaries and within altered feldspar grains. The most severe alteration developed within the pink gneiss at S-1, is restricted to a ≃3 cm band oriented parallel to the foliation 1.5 cm below the mylonitic zone, where retrograde phases comprise ≃1 to 5 volume % of the rock.

Analytical Techniques

Mineral compositions were obtained using a partially automated ARL-SEMQ 9 spectrometer (3 moving, 6 fixed) electron microprobe. Counts were acquired in the wavelength dispersive mode. A version of the QALL analytical scheme (Solberg and Speer 1982), modified to exclude Cr, S and Sr, was used to acquire the data at the standard operating conditions (accelerating potential 15 kV, beam current 20 nA). All minerals were analyzed in point mode (beam diameter $\simeq$ 1 μm), and the raw intensities were corrected using the methods of Bence and Albee (1968) and Albee and Ray (1970). Repeat analyses of several well-characterized standard materials (e.g. Kakanui hornblende, etc.) that were not part of the calibration permitted estimation of analytical bias, the relative precision and accuracy of the analyses over time, and are thought to provide resonable estimates of the uncertainties (2σ/mean) associated with individual analyses. The analyses were recalculated to include estimated H_2O contents using a modified version of SUPERRECAL (Rucklidge 1971). For amphiboles, estimates of of Fe^{3+}, Na^{A} and Na^{M4} were acquired using the 'average' values provided by RECAMP (Spear and Kimball 1984). All microprobe analyses are reported in Appendices A-F. Appendix A is a summary of the standard analyses used to estimate analytical scatter, and Appendices B through F comprise the totality of microprobe analyses of plagioclase, K-feldspar, biotite, amphibole and clinopyroxene (respectively) used in this study.

Backscattered electron images (BSE) were collected on a Camscan Series 2 SEM, at 20 kv accellerating potential.

For the bulk chemical analyses, 0.5 to 5 kg samples were crushed and processed using standard techniques, and the final powders were prepared in a tungsten carbide shatter box. Major element analyses of samples from the S-1 transect were obtained from fused disks, using a Philips 1450 X-ray fluorescence system, following the methods of Norrish and Chappell (1977). Errors in the calibration curves suggest the following uncertainties: 3% - MgO, MnO and Na_2O, < 0.1% - P_2O_5, and 1% for all remaining oxides. Major element analyses for the 419 transect were acquired

using X-ray fluorescence methods performed by Nuclear Activation Services Inc., Ann Arbor, Michigan. Uncertainties associated with instrument stability and sample preparation are below 0.5% for each major oxide, and the overall reliability of these analyses is similar to those performed at Virginia Tech.

Modal Analyses

Thin sections used for modal analyses were stained to facilitate the identification of feldspars. Modal analyses of minerals were made by counting 1000 points (in transmitted light) from entire thin sections or portions of thin sections, cut continuously from each transect, perpendicular to the foliation and parallel to the lineation. No corrections were made for possible systematic errors introduced by the orientation of the mineral grains. For the coarse-grained gneisses and amphibolites, entire thin sections were counted; but for the fine-grained, equigranular mylonitic domains, thin (0.5 to 1 cm wide) strips were counted. Repeat analyses of several samples confirmed reproducibility. The results of the modal analyses are shown in Figures 1.8 and 1.9, and Tables 1.1a and 1.1b. Both transects are characterized by sharp changes in the modal abundance of quartz, K-feldspar and plagioclase. These variations, while not strictly related to the degree of grain size reduction, show marked discontinuities between coarse-grained gneissic units and the mylonitic rocks derived from them.

Across the S-1 transect (Figure 1.8), K-feldspar shows a marked increase in modal abundance from the less-deformed gray gneiss farthest from the ductile deformation zone towards the mylonite. Plagioclase decreases across the same sequence. Quartz remains approximately constant in the gneiss, and a sharp positive deviation in the mylonite is due to the presence of abundant quartz ribbons. Amphibole decreases in abundance with increasing proximity to the ductile deformation

Table 1.1a. Modal analyses (n = 1000) for samples from the 419 and S-1 transects in volume percent.

419 Transect

Sample	QTZ	PLAG	KSP	AMPH	MAG	BI	CPX	TI
452GG	23.9	42.0	25.5	1.0	0.5	6.0	-	0.9
419GG	29.6	37.2	23.1	4.3	0.7	3.5	-	1.5
419U5	26.2	31.8	37.4	4.0	0.7	0.2	-	0.9
431AU2	28.2	34.4	34.1	2.1	1.1	-	-	tr.
431QMA	31.4	29.7	37.0	0.7	0.3	-	-	0.5
419U3	27.2	34.2	37.1	1.3	0.4	-	-	tr.
419u3a	7.9	23.0	19.9	47.3	-	-	0.6	1.4
419U2	0.2	20.0	27.7	50.6	-	-	tr.	1.3
419ACPX2	3.6	47.7	14.5	6.7	2.2	-	23.3	1.7
419L2A	6.8	28.7	9.5	45.3	0.3	-	6.7	2.8
419L2CPX	4.4	46.4	13.7	6.3	1.3	-	25.0	3.2
E3A-CPX	6.9	58.1	6.9	6.9	1.5	-	20.6	2.2
E3A-PG	43.9	23.5	31.3	0.4	0.5	-	tr.	0.2
419L5MY	42.1	32.7	22.7	1.7	0.6	-	tr.	0.2
419L7	43.3	25.7	27.7	1.9	0.2	-	-	0.2
419L9	38.9	22.2	35.2	2.1	0.5	tr.	-	0.6
419L10	34.9	25.2	36.6	2.4	0.1	0.4	-	0.3
419L14	32.7	31.9	31.3	1.5	0.9	1.0	-	0.6
419PG	37.3	31.7	27.8	0.0	0.4	2.7	-	0.2

S-1 Transect

Sample	QTZ	PLAG	KSP	AMPH	MAG	BI	EPI	TI
UG1	31.9	34.4	29.3	2.1	0.7	2.0	0.3	0.6
UG2	35.8	26.3	33.4	1.3	0.4	4.3	tr.	0.9
UG3	33.2	25.4	34.4	tr.	0.5	5.1	tr.	1.4
UG4	28.5	16.1	49.2	-	0.7	5.0	tr.	0.9
LG4	36.4	20.6	40.7	tr.	0.6	1.5	tr.	0.2
LG3	13.9	47.9	32.5	1.3	0.6	0.3	1.4	tr.
LG2	4.2	65.6	26.7	3.1	0.7	0.1	1.2	0.2
LG1	4.2	38.6	52.4	2.0	0.4	1.4	0.1	0.6

Table 1.1b. Modal analyses (n = 1000) for samples from the 419 and S-1 transects in moles/liter.

MINERAL MODES IN MOLES/LITER

419 TRANSECT

GRAY GN.	distance	Q/mol	PL/mol	KSP/mol	AM/mol	MA/mol	BI/mol	CPX/mol	SPH/mol
419GG	0.5	13.047	3.717	2.134	0.155	0.157	0.230	0.000	0.270
419U5	5	11.548	3.178	3.454	0.145	0.157	0.013	0.000	0.162
431AU2	10	12.429	3.438	3.150	0.076	0.247	0.000	0.000	0.000
431QMA	10	13.840	2.968	3.417	0.025	0.067	0.000	0.000	0.090
419U3	11.25	11.989	3.418	3.427	0.047	0.090	0.000	0.000	0.000
AMPH. LAYER & CPX.-AB. MYL.									
419u3a	12.5	3.482	2.298	1.838	1.709	0.000	0.000	0.089	0.252
419U2	14.75	0.088	1.999	2.558	1.828	0.000	0.000	0.015	0.234
419ACPX2	17.75	1.587	4.767	1.339	0.242	0.494	0.000	3.468	0.305
419L2A	20	2.997	2.868	0.877	1.637	0.067	0.000	0.997	0.503
419L2CPX	23	1.939	4.637	1.265	0.228	0.292	0.000	3.721	0.575
E3A-CPX	23	3.041	5.806	0.637	0.249	0.337	0.000	3.066	0.395
PINK GNEISS									
E3A-PG	25	19.349	2.348	2.891	0.014	0.112	0.000	0.015	0.036
419L5MY	28	18.556	3.268	2.097	0.061	0.135	0.000	0.015	0.036
419L7	34	19.085	2.568	2.558	0.069	0.045	0.000	0.000	0.036
419L9	41	17.146	2.218	3.251	0.076	0.112	0.000	0.000	0.108
419L10	44	15.383	2.518	3.380	0.087	0.022	0.026	0.000	0.054
419L14	57	14.413	3.188	2.891	0.054	0.202	0.066	0.000	0.108
419PG	61	16.440	3.168	2.568	0.000	0.090	0.178	0.000	0.036

S-1 TRANSECT

	distance	Q/mol	PL/mol	KSP/mol	AM/mol	MA/mol	BI/mol	SPH/mol	EP/mol	MU/mol
UG1	2	14.060	3.438	2.706	0.076	0.157	0.132	0.108	0.022	0.000
UG2	7	15.779	2.628	3.085	0.047	0.090	0.283	0.162	0.000	0.000
UG3	12	14.633	2.538	3.177	0.000	0.112	0.336	0.252	0.000	0.000
UG4	15.5	12.562	1.609	4.544	0.000	0.157	0.329	0.162	0.000	0.000
LG4	18	16.044	2.059	3.759	0.000	0.135	0.099	0.036	0.000	0.000
LG3	21.5	6.127	4.787	3.002	0.047	0.135	0.020	0.000	0.101	0.213
LG2	25.5	1.851	6.555	2.466	0.112	0.157	0.007	0.036	0.086	0.000
LG1	30	1.851	3.857	4.840	0.072	0.090	0.092	0.108	0.007	0.007

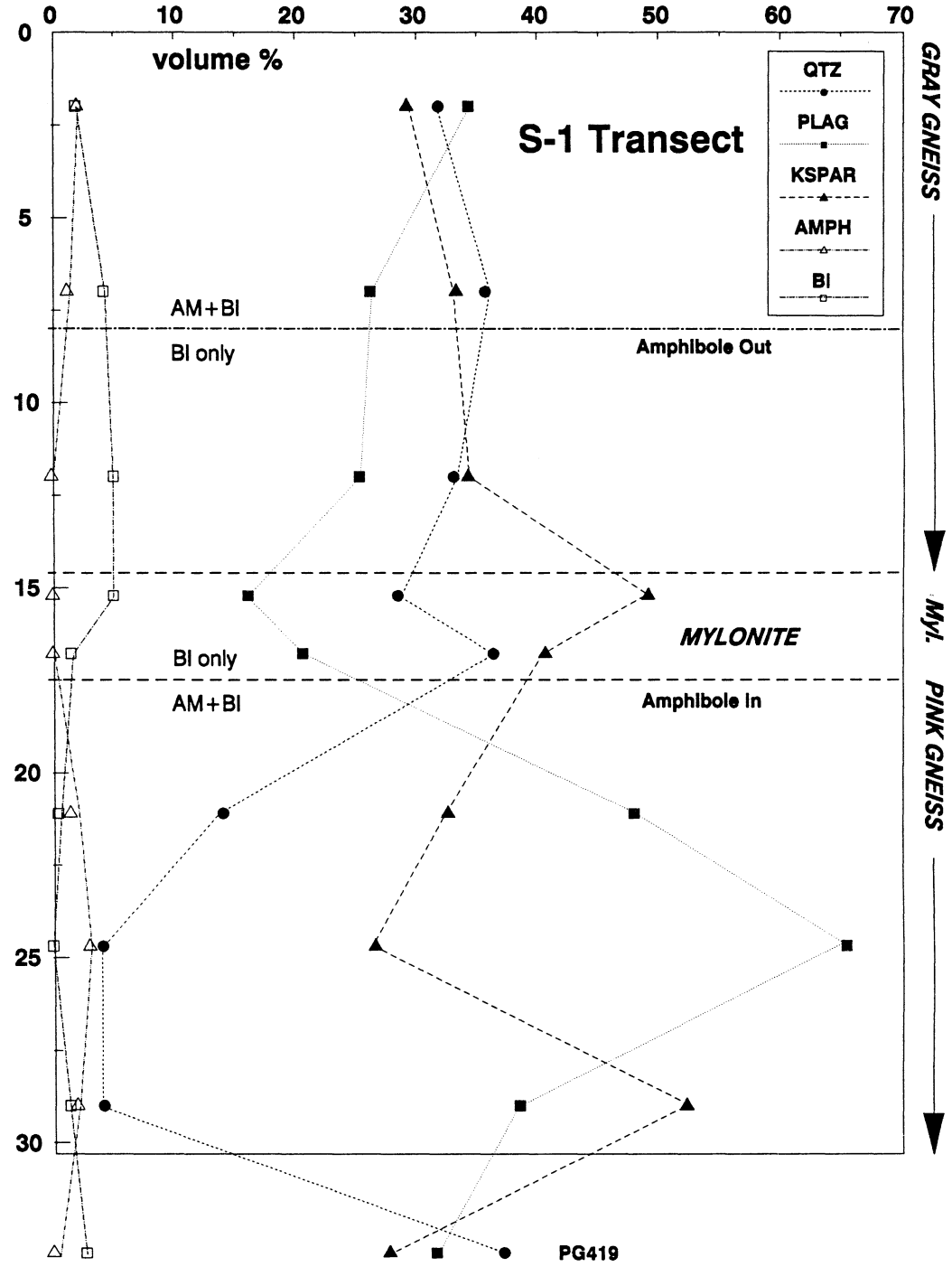


Figure 1.8. Modal analyses of thin sections from the S-1 transect as a function of distance.

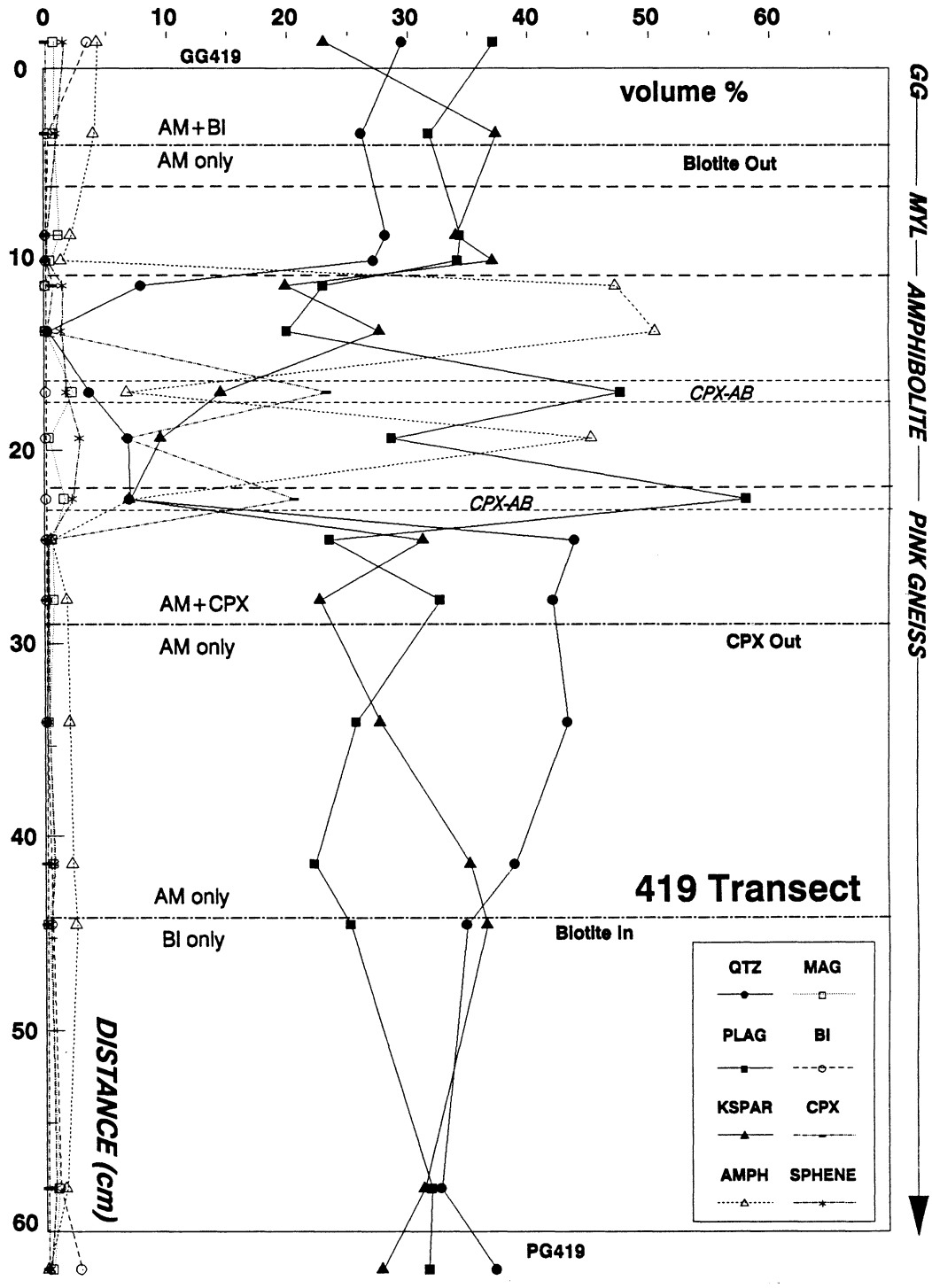


Figure 1.9. Modal analyses of thin sections from the 419 transect as a function of distance.

zone, and disappears entirely from the gneiss ≃4 cm above the mylonite, while biotite increases slightly in abundance and persists into the mylonite.

From the mylonite into the pink gneiss, the proportion of plagioclase increases, K-feldspar decreases and quartz decreases significantly to < 5%. Amphibole reappears in the pink gneiss immediately below the ductile deformation zone, and biotite is present in minute (< 1%) amounts. In comparison to a reference pink gneiss collected ≃ 70 cm below the ductile deformation zone (PG419), the S-1 pink gneisses are anomalously rich in plagioclase and poor in quartz. The plagioclase-rich, quartz-poor region of the S-1 pink gneiss also contains the highest proportion of retrograde epidote and muscovite.

Mineral modes across the 419 transect show similar, albeit less pronounced trends (Figure 1.9). The modal percentage of K-feldspar in the gray gneiss increases with increasing proximity to the gray gneiss-amphibolite contact and decreasing grain size, but no net enrichment of quartz in the mylonite is apparent. Plagioclase remains constant across the same sequence. Both biotite and amphibole decrease in abundance with increasing proximity to the gray gneiss-amphibolite contact, but only biotite disappears completely from the gneiss.

The gray gneiss-amphibolite contact is marked by a sharp increase in modal amphibole, slight decreases in plagioclase and K-feldspar, a sharp drop in the abundance of quartz, and the appearance of clinopyroxene. The modal proportions of amphibole and plagioclase in the remainder of the amphibolite remain relatively constant (except in the clinopyroxene-albite mylonites). By contrast, K- feldspar decreases in abundance, while the proportion of quartz increases, within the amphibolite from the gray gneiss-amphibolite contact to the pink gneiss-amphibolite contact. Clinopyroxene-albite mylonites are marked by sharp positive discontinuities in the contents of clinopyroxene, plagioclase and magnetite.

The pink gneiss-amphibolite contact is marked by a sharp increase in the modal abundance of quartz and K-feldspar, and a sharp decrease in plagioclase, amphibole and clinopyroxene. In the pink gneisses across the 419 transect, Qtz > Ksp > Pl, except in mylonitic domains where Qtz > Pl > Ksp. The persistently high modal proportion of quartz in the 419 pink gneiss is attributable to numerous quartz ribbons. As mentioned previously, clinopyroxene is present in the pink gneiss

from the pink gneiss-amphibolite contact to ≃8 cm below. Biotite is absent from this zone, but appears in a K-feldspar-rich porphyroclastic zone ≃23 cm below the pink gneiss-amphibolite contact (c.f. Figure 1.5).

Bulk Chemistry

Major element chemical data from both the S-1 and 419 transects are shown in Table 1.2, and Figures 1.10 and 1.11. In general, the S-1 transect and the portions of the 419 transect that represent gneiss-to-mylonite textural transitions are conspicuously different in terms of the enrichment and depletion patterns shown by the major elements. The 419 transect (Figure 1.10) shows relatively little change in bulk composition across the transition from the less-deformed gray gneiss to the mylonite, other than a systematic decrease in Ca, Mg, Fe and Ti, and a slight increase in Na and Si with increasing proximity to the gray gneiss-amphibolite contact. This is consistent with the relatively constant modal abundances of quartz and feldspars, and the steady decrease in ferromagnesian minerals with increasing proximity to the gray gneiss-amphibolite contact The contact itself represents a sharp chemical discontinuity (Figure 1.10). The amphibolite layer is characterized by high concentrations of Ca, Mg, Fe and Ti, and low concentrations of Na, K and Si in comparison to the adjacent mylonite, while Al remains approximately constant. The clinopyroxene-albite mylonitic zones within the amphibolite (ACPX) and at the pink gneiss-amphibolite contact (TZ) are depleted in Mg, Fe, Ca and Ti, and enriched in Na and Si relative to the amphibolite. The Na content of both clinopyroxene-albite mylonite zones is significantly higher than that of the amphibolite or either gneissic unit. This is strong evidence against a mixing origin for the clinopyroxene-albite mylonite. Beyond the pink gneiss-amphibolite contact, Na, Mg, Fe,

Table 1.2. Bulk chemical analyses and densities. (a) 419 transect, (b) S-1 transect.

419 Transect

	GRAY GNEISS			MYLONITE		AMPHIBOLITE				PINK GNEISS					
	GG462	419U6	419U5	419U4	419U3	419AA	419AC	419CPX	419AD	419TZ	419PGD	419PGC	419PGB	419PGA	419PG
SiO2	70.70	71.70	74.50	75.90	76.20	53.30	52.40	57.40	53.80	68.50	80.10	79.40	79.00	79.10	75.10
Al2O3	13.50	13.40	12.90	12.30	12.40	12.40	12.40	11.40	12.60	12.40	10.10	10.10	10.50	10.50	12.80
CaO	2.09	1.58	1.31	0.82	0.99	7.73	7.57	7.96	7.77	3.96	1.02	0.83	0.84	0.71	0.97
MgO	0.70	0.47	0.41	0.17	0.27	4.63	4.76	3.74	4.56	1.57	0.21	0.21	0.22	0.18	0.22
Na2O	4.08	4.08	3.80	4.02	4.24	4.04	3.61	5.01	4.40	5.78	3.35	3.17	3.38	3.69	3.82
K2O	3.66	4.99	5.04	4.51	4.32	3.01	3.12	1.75	1.75	2.04	3.37	3.90	3.88	3.71	4.88
Fe2O3	3.12	2.31	1.82	1.01	1.05	11.20	11.90	9.48	11.60	5.45	1.22	1.23	1.35	1.18	1.34
MnO	0.06	0.05	0.05	0.02	0.03	0.29	0.28	0.29	0.28	0.24	0.05	0.04	0.05	0.04	0.05
TiO2	0.48	0.34	0.28	0.10	0.13	1.70	1.70	1.35	1.78	0.59	0.17	0.16	0.17	0.13	0.19
P2O5	0.13	0.09	0.07	0.02	0.03	0.29	0.29	0.21	0.31	0.08	0.04	0.04	0.04	0.03	0.04
LOI	0.77	0.08	0.16	0.31	0.23	0.47	0.47	0.39	0.62	0.00	0.31	0.16	0.00	0.23	0.16
SUM	99.29	99.09	100.34	99.18	99.89	99.06	98.50	98.98	99.47	100.61	99.94	99.24	99.43	99.50	99.57
density	2.68		2.64	2.64	2.63	2.92		2.86	2.95		2.64			2.62	2.64

S-1 Transect

	GRAY GNEISS					P.M.	MYL.		PINK GNEISS						
	UGA	UGB	UGC	UGD	UGE	UGF	LGA	LGB	LGC	LGD	LGE	LGF	LGG	LGH	LGI
SiO2	71.52	73.01	72.71	72.57	73.40	75.47	79.79	78.71	77.74	70.83	63.34	62.69	63.93	64.42	64.58
Al2O3	13.30	12.99	13.33	13.93	13.15	12.29	9.28	10.60	12.41	15.25	19.85	19.87	19.51	19.63	19.31
CaO	1.55	1.56	1.59	1.44	1.26	0.75	0.52	0.53	0.87	1.79	2.88	2.97	2.01	2.03	1.77
MgO	0.90	1.11	1.07	1.13	1.13	1.01	1.29	1.06	1.17	1.23	0.91	1.49	1.27	1.54	1.23
Na2O	2.43	3.60	3.13	2.58	4.75	3.30	1.38	1.89	2.82	4.03	7.08	6.15	6.19	6.40	6.65
K2O	4.31	4.02	3.95	3.98	4.33	5.73	4.51	5.38	5.19	4.56	3.74	3.51	5.60	5.25	4.60
Fe2O3	2.75	2.76	2.99	2.50	2.47	1.89	1.22	1.20	1.26	1.81	2.86	2.52	2.02	2.15	1.87
MnO	0.09	0.09	0.09	0.08	0.08	0.07	0.06	0.06	0.06	0.08	0.10	0.09	0.08	0.09	0.09
TiO2	0.40	0.41	0.39	0.34	0.35	0.25	0.13	0.14	0.13	0.16	0.21	0.23	0.20	0.22	0.20
P2O5	0.08	0.09	0.08	0.07	0.07	0.05	0.01	0.01	0.01	0.02	0.05	0.05	0.04	0.04	0.04
LOI	0.50	0.39	0.69	0.53	0.33	0.26	0.58	0.30	0.31	0.31	0.33	0.25	0.21	0.19	0.31
SUM	97.83	100.03	100.02	99.15	101.32	101.07	98.77	99.88	101.97	100.07	101.35	99.82	101.06	101.96	100.65
density		2.64		2.67				2.62		2.62		2.65		2.62	

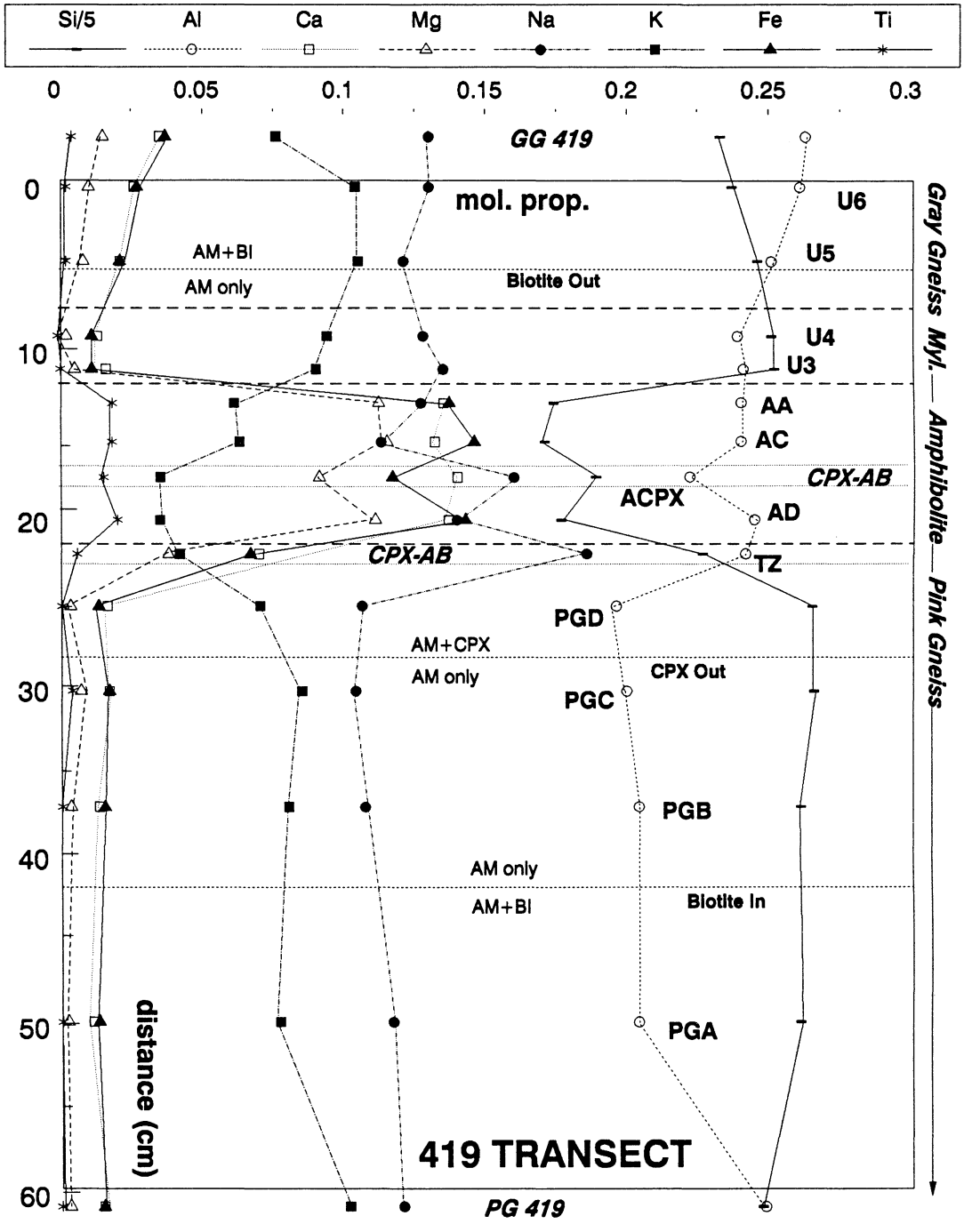


Figure 1.10. Bulk chemical analyses of slabs from the 419 transect: Labels correspond to samples listed in Table 2. Data plotted as molecular proportions.

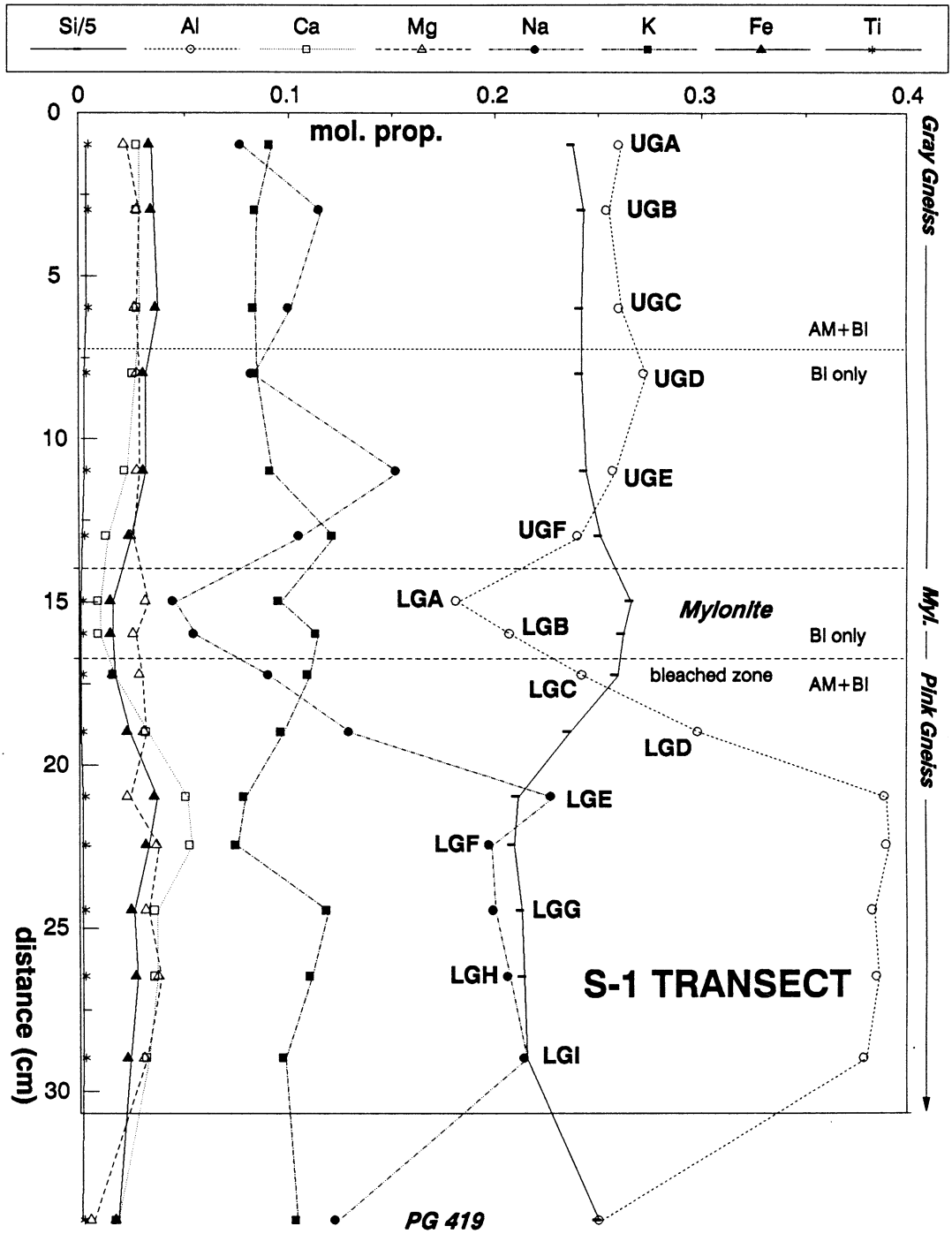


Figure 1.11. **Bulk chemical analyses of slabs from the S-1 transect:** Labels correspond to samples listed in Table 2. Data plotted as molecular proportions.

Ca, Ti and Al drop off sharply, and Si and K contents rise. The apparent bulk chemical uniformity of the pink gneiss at 419 may be an artifact of the increasing slab thicknesses.

Across the gray gneiss-to-mylonite transition of the S-1 transect (UGA through UGE), major element concentrations show relatively little change. In the protomylonitic gray gneiss slab adjacent to the ductile deformation zone (UGF), Na and Al are slightly depleted, while Si is enriched. The mylonite slabs (samples LGA and LGB) are markedly enriched in K and Si, and depleted in Na and Al. The transition from the mylonite into the pink gneiss is characterized by a sharp drop in K and Si, with a concomitant increase in Al and Na. The most Si-poor region of the pink gneiss (slabs LGE and LGF) is also characterized by relatively high levels of Ca, Mg and Fe, which reflect the local occurrence of secondary epidote and chlorite. The variations in Na, K, Si and Al are related to changes in the modal abundances of primary minerals, such as plagioclase, K-feldspar and quartz (Figure 1.11). A representative pink gneiss sample (PG 419) is also plotted on Figure 1.11, and is distinct from the S-1 pink gneiss in terms of its Si, Al, Na, K and Ca contents. These data, and bulk chemistry of several other pink gneiss samples from the outcrop, suggest that the high Al, Na, Fe, Mg and Ca contents, and the exceedingly low Si content of the S-1 gneisses is anomalous and may be related to the metamorphic processes which affected Si enrichment and alkali mobility elsewhere.

Systematic changes in major element chemistry across the transects are further illustrated through the use of isocon diagrams (Figures 1.12 and 1.13, see also Grant 1986). In these digrams, the composition-volume equations derived by Gresens (1967) are recast as a set of linear equations which relate the concentrations of elements in an altered rock (C^A) to those of the protolith (C^o). The isocon represents a line of equal concentration, and has a slope equal to the mass ratio (C^A / C^o) of a given element (or system component) between the protolith and the altered equivalent. In this fashion, changes in concentration of different components can also be stated with reference to model isocons based on several assumptions; constant volume, constant mass and constant concentration of a presumably immobile element. 'Best-fit isocons' (BFIs) arise when several element ratios form a quasi-linear array.

For each of the sample pairs shown here, density contrasts between the protolith and the altered equivalent do not exceed 5% (see also Table 1.2). This reflects the similar densities of the minerals, i.e. quartz, K-feldspar, and plagioclase (An_2 to An_{18}) which comprise 90 to 95 modal % of the gneisses and mylonites, and restricts the slope of the constant-volume isocon to within 5% of that of the constant-mass isocon which is fixed at 45° in C^O - C^A space. Not surprisingly, the greatest density contrast ($\simeq$5%) was found between the amphibolite and the clinopyroxene-albite mylonite.

A comparison between a less-deformed gray gneiss (GG419) and the mylonite slab farthest from the amphibolite layer (U4, Figure 1.12a) shows a slight negative ($\simeq$8%) departure of the constant Al isocon from the constant-mass, constant-volume isocon (a 45° line, in this case, because the densities of the two samples are essentially equivalent). The slight increase in Si ($\simeq$10%) and Na may reflect the higher Ab content of the plagioclase in the mylonite. Most importantly, a "best-fit" isocon (BFI) drawn through Fe, Ca, Ti and Mg indicates a net loss ($\simeq$60%) of these elements from the mylonite. The depletion of ferromagnesian elements in mylonite is related to the modal decrease in biotite, amphibole and titanite with decreasing grain size.

Pronounced and systematic bulk compositional contrasts are also apparent between the internal clinopyroxene-albite mylonite zone (419ACPX) and an adjacent amphibolite slab (419AC) (Figure 1.12b). The isocon diagram was plotted on the assumption that the clinopyroxene-albite mylonite represents a lithologic precursor to the amphibolite, given the textural and paragenetic relationships presented in the preceding and following sections. The clinopyroxene-albite mylonite has a 3% to 5% lower average density than the amphibolite (Table 1.2), thus the constant mass and constant volume assumptions are not colinear. The constant Al isocon has a slightly ($\simeq$10%) greater slope than the constant volume line, and Fe, Ti and Mg fall near it to form a best-fit isocon. By contrast Si, Ca and Mn fall on the constant volume line. Relative to either model, K shows an appreciable enrichment, and Na an appreciable loss, in the amphibolite.

Pink gneiss samples from the 419 transect are all very similar in terms of their bulk chemistry, and are plotted against the reference pink gneiss (PG 419) in Figure 1.12c. All major elements, except Ca and Na, plot along the constant Al isocon, which suggests that each of the pink gneiss

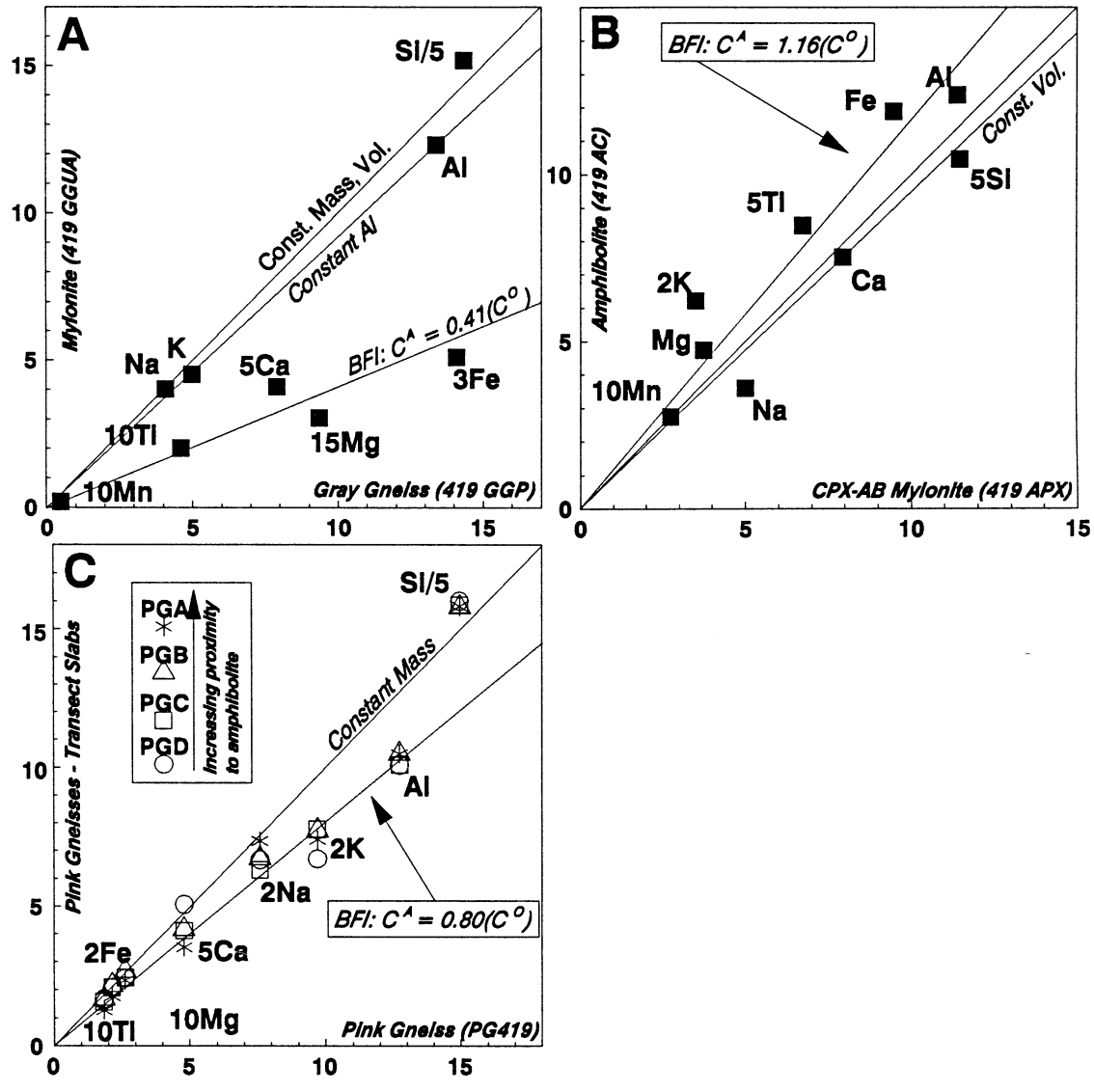


Figure 1.12. **Isocon diagrams of samples from the 419 transect:** (a) - gray gneiss GG 419 (see Figure 4 for reference) (C^O) and mylonite (C^A), (b) - clinopyroxene-albite mylonite (C^O) and amphibolite (C^A), and (c) - pink gneiss PG 419 (C^O) and pink gneiss slabs from the 419 transect (C^A). All data as wt. % oxides, scaling of various oxides shown on diagrams.

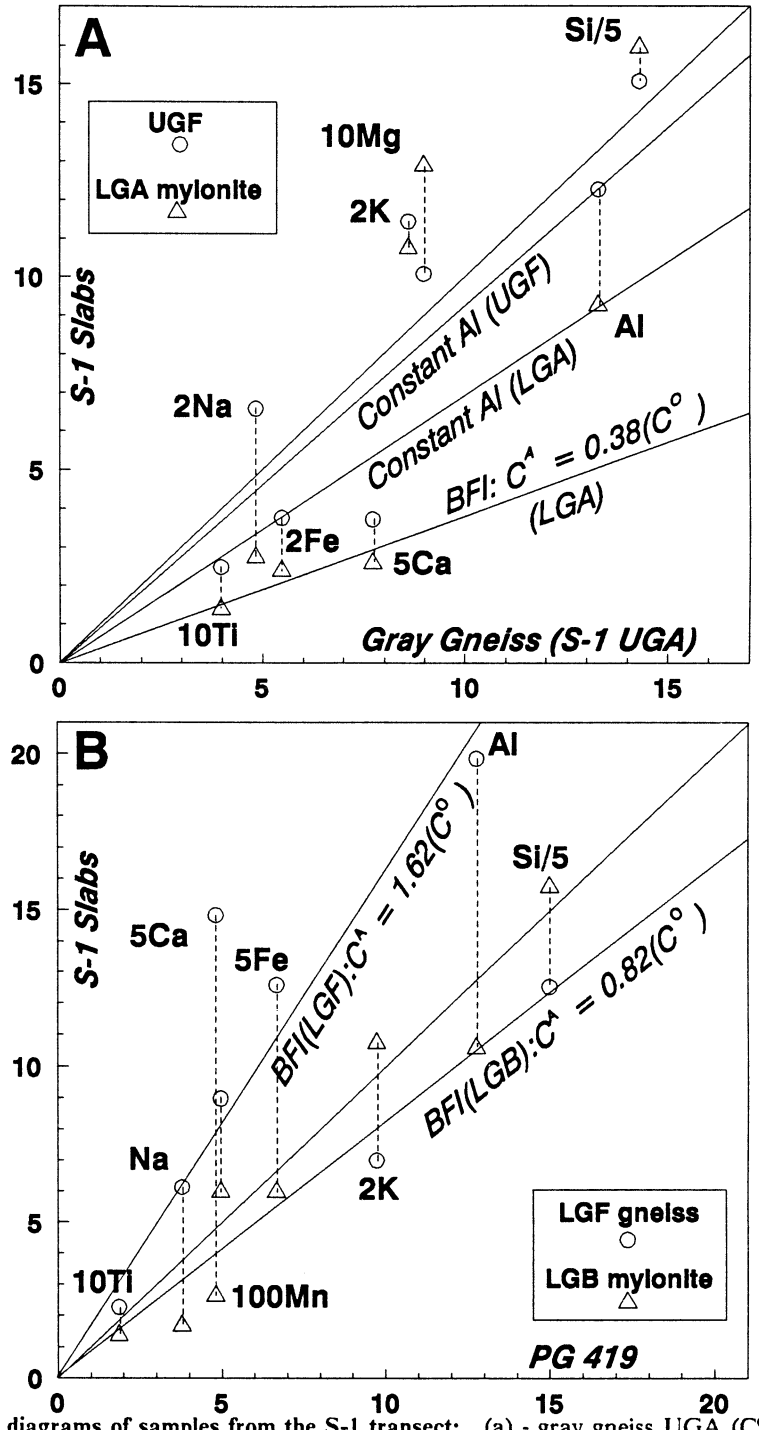


Figure 1.13. Isocon diagrams of samples from the S-1 transect: (a) - gray gneiss UGA (C^O) versus protomylonite adjacent to protomylonite UGF and mylonite LGA (C^A). (b) - Pink gneiss 419 (C^O) versus mylonite slab LGB and quartz-poor altered pink gneiss LGF (C^A) All data as wt. % oxides, scaling of various oxides shown on diagrams. See Figure 4 for reference.

samples experienced approximately the same degree (≃20%) of Si gain. The slabs are systematically enriched (by ≃ 20%) enriched in Na and depleted in Ca (also by ≃ 20%) with increasing proximity to the pink gneiss-amphibolite contact. Mineral chemical data show that plagioclase feldspars become more Ab-rich over the same transition.

Across the S-1 transect, a comparison between the bulk chemistry of the least-deformed gray gneiss (UGA), the protomylonitic gray gneiss (UGF) adjacent to the mylonite zone, and the mylonite itself (LGA) (Figure 1.13a) demonstrates that the bulk chemistry of the mylonite varies significantly from that of the adjacent, less-deformed protomylonitic gneiss, as the relative enrichment (and/or) depletion of Na, Al, Fe, Ti and Ca define distinct trends. For the protomylonite (UGF), the constant mass-volume and Al approximations are similar, although no BFIs obtain. For either model, Si, Mg, K and Na experience gains of 5% to 20%, and Ti, Fe and Ca show losses of 20% to 30%. In the mylonite sample (LGA), Na and Al are colinear and plot well below the constant mass-volume isocon, while K and Si are colinear and plot above it. Assuming a constant Al model, K and Si are enriched by ≃50% in the mylonite, and ≃40% depleted in Ca, Fe and Ti relative to the gray gneiss. These changes are a consequence of the overall decrease in the modal proportion of mafic silicates and plagioclase, and increase in K-feldspar, in the mylonite. The behavior of Mg across S-1 may correspond to compositional changes in biotite, or to the pervasive post-kinematic chloritization of biotite. Microprobe analyses of biotite presented in the next section indicate that the latter is the more likely explanation.

Figure 1.13b, shows the bulk chemical contrasts between a silica-rich mylonite slab (LGB) and a silica-poor, Na-rich pink gneiss slab (LGF), relative to a reference pink gneiss sample (PG419). For both samples, the constant Al isocon significantly departs from the constant mass-volume model and each defines a distinct trend, almost symmetrically disposed about a constant mass-volume line. The LGF pink gneiss data define a Al-Fe-Mn-Na-Ti BFI with a slope of ≃1.5. K and Si are depleted by ≃50% with reference to the BFI. By contrast, the mylonite data (LGB) defines an Al-Fe-Ti BFI which plots ≃ 20% below the constant mass-volume isocon, while Si and K plot considerably above it, and Na shows ≃25% loss relative to the BFI. For both samples, bulk chemical contrasts are mirrored by the modal mineralogy: the LGF gneiss slab is char-

acterized by extremely low quartz and K-feldspar contents, and extremely high plagioclase content. The high levels of Ca in the LGF slab reflect the local abundance of calcic amphibole, plagioclase and secondary epidote. In the mylonite, the relative enrichment of K and Si reflects the abundance of K-feldspar and quartz.

The chemical variability across both transects may be due to; 1) mechanical mixing, 2) transposition of primary igneous features, or 3) metasomatic changes associated with fluid-rock interaction during mylonitization. The data presented in Table 1.2 and Figures 1.10 and 1.11 show that the observed bulk chemical variations are not due to mixing of the various lithologies. By inspection of Table 1.2, it can be seen that the bulk compositions of the mylonites are not intermediate between those of the surrounding gneisses and amphibolites. The same can be said of the clinopyroxene-albite mylonite with reference to the surrounding amphibolite.

The possibility of local compositional variations stemming from purely igneous processes is more difficult to rule out. From the data in Table 1.2, it is apparent that the enrichment and depletion trends of Na and K in the mylonites relative to the protolith gneisses are dissimilar across the two transects. The mylonites at 419 and S-1 both experienced Si enrichment and depletion in Ca, Fe and Ti. At 419, the K and Na contents of the mylonite are similar to, or slightly higher than, those of the protolith while at S-1, K is enriched and Na is depleted. Although similar trends may arise via igneous processes which operate on a centimeter scale (e.g. Speer et al. 1989), the development of ductile deformation zones in the Ponaganset gneiss is not related to such phenomena. Instead, the concentration of strain-related features at both transects is more easily explained by rheologic contrasts, or the presence of a zone of weakness, across gneiss-gneiss or amphibolite-gneiss contacts. The bulk chemical trends in the ductile deformation zones also appear to be a function of the presence, or absence, of an intervening amphibolite layer. For example, isocon plots and mass balance relations (presented in a following section) show that the addition of Na to the mylonites and gneisses at 419 can be explained by the release of Na from the amphibolite layer during metamorphism. Furthermore, the symmetrical nature of the pattern of Na enrichment on either side of the amphibolite layer is suggestive of diffusive processes related to metamorphism rather than igneous fractionation. Textural evidence detailed in the previous section, and mineral

chemical data presented in the following section further support a metasomatic origin for the chemical variation observed across both transects.

The composition-volume relationships depicted in Figures 1.12 and 1.13 also provide a basis for the evaluation of the relative mobility of various elements in the gneisses, mylonites and amphibolite during (or after) deformation. The constant-mass and constant-volume assumptions are essentially equivalent due to the lack of density contrasts between the protolith gneisses and the mylonites. Because of their relatively low solubility in aqueous fluids (Helgeson et al. 1978), Al and/or Ti may also provide a suitable reference frame with which to evaluate the relative mobility of other elements. The choice of a constant Al or Ti reference frame necessitates that these elements were the least mobile during metamorphism, but does not require absolute immobility (see also Tracy et al. 1983). Immobile behavior for Al has been inferred for a wide range of metamorphic processes, and over a wide range of P-T conditions, in many rock types (Carmicheal 1969; Fisher 1970; Thompson 1975; Ferry et al. 1987; and others). While none of the data presented here is conclusive with regard to the absolute degree of Al or Ti mobility during metamorphism, the choice of a constant Al reference frame is appealing for several reasons. First, the constant volume approximation would require substantial Al mobility in several examples from the Ponaganset gneiss (see, for example, Figure 1.13b), and very little in others (Figure 1.12b). The choice of a constant Al isocon generally requires mass transfer of elements which typically show high degrees of mobility (e.g. Na, K, Si) to explain the observed chemical trends. This is often not the case for the constant-mass or constant-volume assumptions. However, Al and Ti do not always show coherent behavior across the gray gneiss-to-mylonite transition at either transect (e.g. Figure 1.12a). In these instances, Ti plots on a BFI with Ca, Fe and (at 419) Mg. Thus, the apparent decrease of the Ti/Al ratio may be related to the overall lack of ferromagnesian phases in the mylonite relative to the protolith gneiss.

Mineral Chemistry

Feldspars - 419 Transect

Plagioclase and alkali feldspars are ubiquitous in all lithologies of the Ponaganset gneiss. Unless otherwise specified, all microprobe analyses of feldspars were performed on recrystallized, metamorphic grains. Systematic compositional changes in plagioclase or alkali feldspar with respect to grain size, proximity of grains to partially recrystallized perthite augen, or location of grains in "tail" regions of augen were not observed. Recent work (Bell and Johnson, 1989) also suggests that the lack of compositional contrasts between new feldspar grains and the precursor feldspar grain is not unusual in granitic rocks deformed at amphibolite to granulite grade. However, the development of thin ($\simeq$ 10 - 20 μm) Ab-rich ($\simeq Ab_{95}$ to Ab_{98}) rims on plagioclase grains, and Ab-poor ($\simeq$ Ab_4 to Ab_2) rims on K-feldspar grains was observed throughout both transects, and was best developed in the pink gneiss. Such variations in Na content in feldspars are likely the result of late-stage exchange of alkalis with an intergranular fluid during cooling. In plagioclase of similar composition, Ab-rich rims may also be attributed to the separation and annealing of two exsolved phases on either side of the peristerite gap during recrystallization (e.g. Byerly and Vogel 1973). Backscattered electron images indicate that the Ab-rich rims are gradational rather than sharp, and tend to run parallel to grain boundaries, implying that they formed by late-stage chemical exchange with a fluid phase at the grain boundary. It is also apparent, from microprobe analyses, that these compositional effects are most pronounced at K-feldspar-plagioclase interfaces (c.f. Byerly and Vogel 1973).

Plagioclase compositions across both transects are plotted as a function of distance (Figures 1.14, 1.15). In general, the An content of plagioclase along the 419 transect decreases systematically in both gneiss units with increasing proximity to the contacts with the amphibolite. Plagioclase from the less-deformed gray augen gneiss farthest from the contact (GG419, Appendix B) has an

average composition of $Ab_{81.9}An_{16.5}Or_{1.6}$. With increasing proximity to the gray gneiss-amphibolite contact, the Ab content of plagioclase steadily increases to $Ab_{89.6}An_{9.5}Or_{1.0}$ (Figure 1.14), although the central regions of several large ($\simeq$500 μm) recrystallized grains from the protomylonite are more calcic (ca. An_{16}) The presence of a subtle gradient in plagioclase compositon within the ultramylonite, from $An_{11.5} \simeq$ 6.5 mm above the contact to $An_{9.5} <$ 2 mm above the gray gneiss-amphibolite contact, (Appendix B) suggests that the Na content of plagioclase is controlled, in part by proximity to the amphibolite, or to the contact itself.

Among feldspars in the amphibolite layer, plagioclase ($Ab_{90.4}An_{8.6}Or_{1.0}$) and alkali feldspar ($Or_{91.5}Ab_{7.8}An_{0.2}$) are both somewhat more sodic than feldspars from the adjacent ultramylonite. There is no systematic gradation in plagioclase composition in the amphibolite with respect to proximity to the ultramylonite. Alkali feldspar is often turbid, but the Ab contents of turbid and clear grains are similar, except in localized zones of visible alteration (e.g. late epidote and calcite filled fractures).

Feldspar compositions from the mylonitic CPX-rich layers within the amphibolite, and the CPX-rich "transition zone" at the amphibolite-pink gneiss contact, differ significantly from the rest of the amphibolite unit and from those of the surrounding gneisses. In these zones, fine-grained (50-150 μm) plagioclase is more albitic ($Ab_{95.5}An_{3.5}Or_{1.0}$), and fine-grained alkali feldspar is nearly pure ($Or_{96.8}Ab_{2.4}An_{0.3}$). Some plagioclase grains within the clinopyroxene-albite mylonite domains are reversely zoned (Appendix B), with Ab-rich cores and rims that approximate the composition of plagioclase from the rest of the amphibolite zone ($\simeq An_9$). In BSE images (not shown), the An-rich rims are irregularly distributed, asymmetric, and generally tend to run parallel to grain boundaries. In some grains, the An-rich regions are themselves rimmed by more albitic plagioclase. Approximately 5 cm below the CPX-rich transition zone at the pink gneiss-amphibolite contact, plagioclase returns to less albitic compositions ($Ab_{91.2}An_{7.9}Or_{0.9}$). In the same region, average K-feldspar compositions tend to be more Ab-rich (Appendix C), but show a significant amount of scatter that is probably due to late-stage alteration. Alkali feldspars are typically turbid, and plagioclase shows strong development of albitic rims. In the pink gneiss, no systematic relationships were obtained between the composition of feldspars from fine-grained (50-150 μm) mylonitic do-

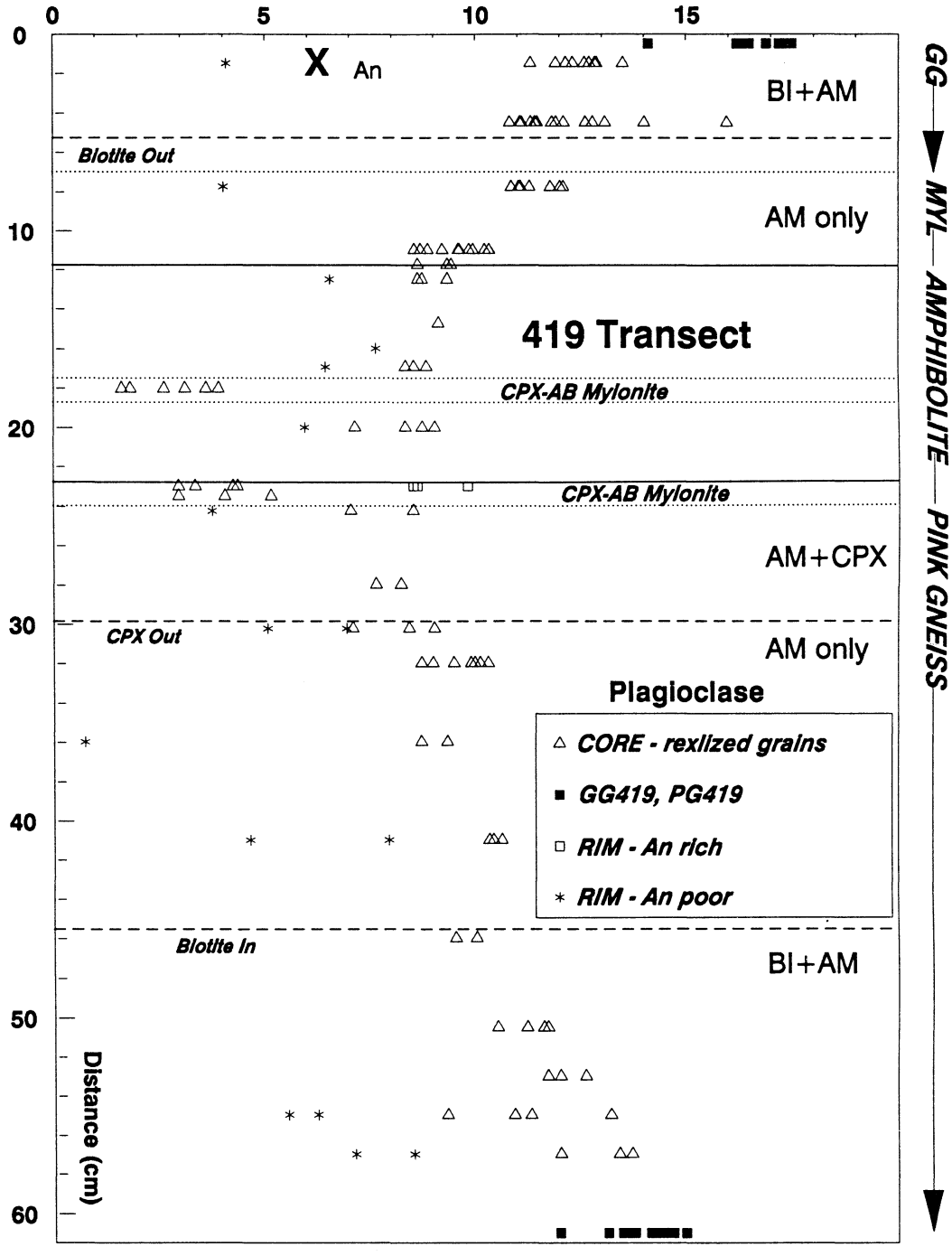


Figure 1.14. **Plagioclase composition as a function of distance across the 419 Transect:** Each data point represents a single microprobe analysis. Note the systematic changes in An content along 419 as a function of proximity to the amphibolite layer. * - denotes analyses of plagioclase rims contiguous to K-feldspar grains.

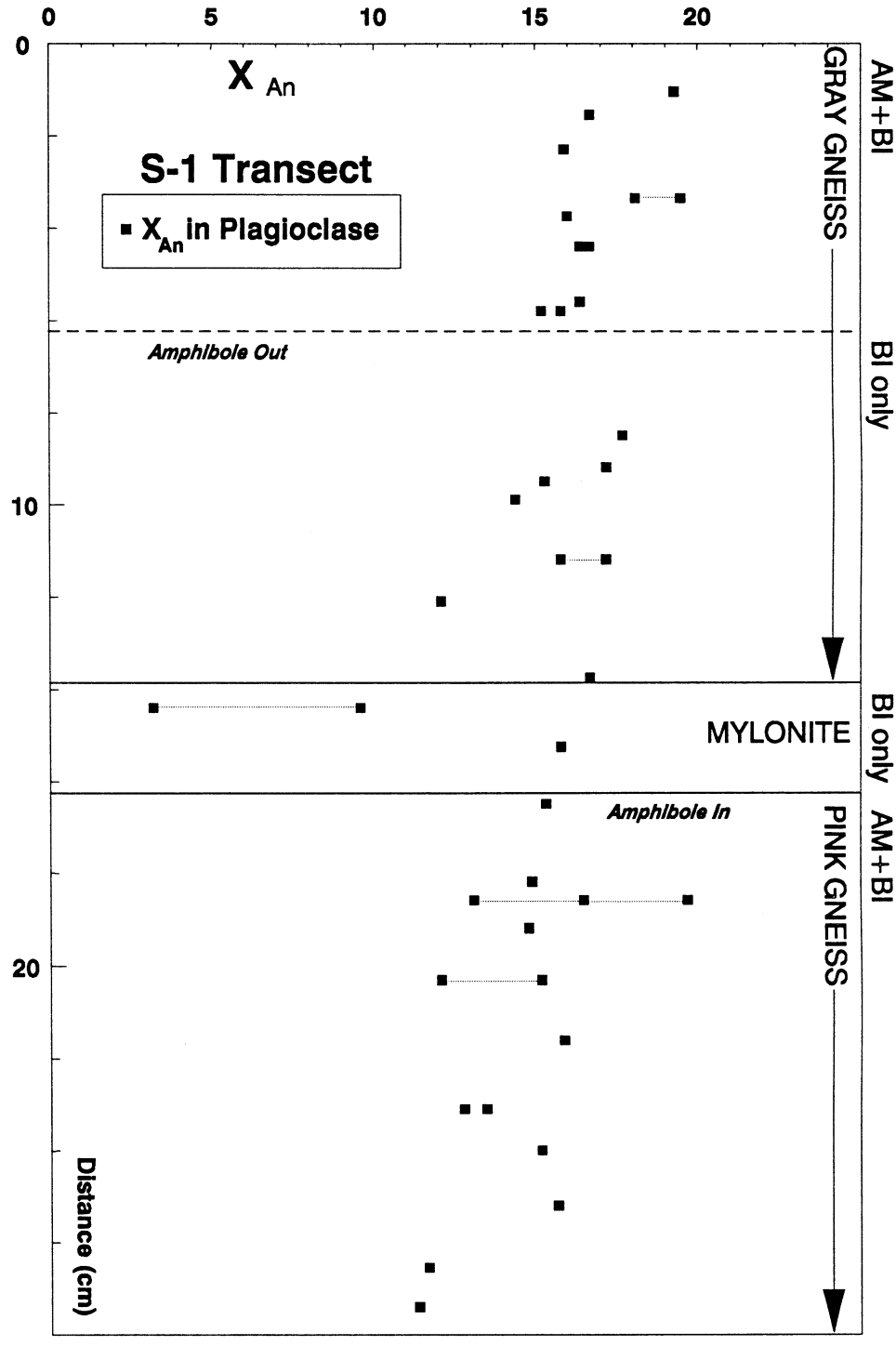


Figure 1.15. **Plagioclase composition as a function of distance across the S-1 Transect:** Each data point represents a single microprobe analysis. Note the and the lack of systematic compositional variation along S-1. See text for further discussion.

mains and coarser (500-1000 μm) "porphyroclastic" domains descibed earlier. Instead, the An content of plagioclase shows a smooth and systematic increase with increasing distance from the amphibolite-pink gneiss contact. The average plagioclase composition from the pink gneiss 75 cm below the contact is $Ab_{84.7}An_{14.0}Or_{1.3}$,. Over the same portion of the transect, K-feldspar compositions are variable, but show no systematic relationships to distance from the contact.

Plagioclase compositional trends across the S-1 transect (Figure 1.15) are less distinct than those observed across the 419 transect. Approximately 10 cm above the ductile deformation zone at the gray gneiss-pink gneiss contact, plagioclase compositions in the gray gneiss vary between $An_{19.5}$ to $An_{12.1}$, with a mean composition of $Ab_{81.1}An_{17.2}Or_{1.6}$. With increasing proximity to the contact (and increasing grain size reduction), plagioclase compositions become slightly more albitic. Within 10 mm of the mylonite, the mean plagioclase composition is $Ab_{82.9}An_{15.0}Or_{2.1}$. Fresh plagioclase from the ultramylonite shows considerable compositional spread ($An_{16.7}$ to $An_{1.2}$). In the pink gneiss 30 mm from the ductile deformation zone, plagioclase compositions range from $An_{19.7}$ to $An_{11.4}$, with a mean of $Ab_{82.6}An_{15.7}Or_{1.6}$., becoming somewhat more albitic with increasing distance from the contact. K-feldspars from both gneiss units and the ductile deformation zone show no systematic compositional variations.

Biotite

Figures 1.16 and 1.17 show biotite composition plotted as a function of fluorphlogopite activity (see Nordstrom and Munoz 1986, p.157);

$$a_{F-phl} = [X_{K+} X^3_{Mg2+} (X^3_{Si4+} X^{IV}_{Al3+}) X^2_{F-}] \times 9.481$$

plotted across both transects. This parameter is used to show only the relative departure of the observed biotite compositions from ideal fluorphlogopite, and assumes ideal mixing on all sites. Biotite was observed in both the pink and gray gneisses, but not in the mylonite or amphibolite

of the 419 transect. In all samples, biotite deviates from ideal fluorphlogopite primarily by the $Fe - Mg_{-1}$ and the $Al^{VI}Al^{IV}$ -$Mg_{-1}Si_{-1}$ substitutions and contains appreciable amounts of F, Ti and Mn (Appendix D). No attempt was made to calculate the Fe^{3+} content of biotite.

Biotite chemistry is apparently dependent on rock type (Figure 1.18). In the gray gneiss (419), average biotite contains 0.17 atoms per formula unit (apfu) Ti, 0.21 apfu Al^{VI}, 0.08 apfu Mn, and has Mg/(Mg+Fe) = 0.49. With increasing proximity to the gray gneiss-amphibolite contact (and increasing grain size reduction), biotite chemistries shift to slightly more Mg-rich compositions at constant Al^{VI} Approximately 6 cm above the contact, biotite disappears from the gray gneiss altogether. At 419, biotite reappears in the pink gneiss approximately 22.5 cm below the pink gneiss-amphibolite contact. At this point, the biotite is compositionally similar to the biotite from the gray gneiss (Figure 1.18). With increasing distance from the pink gneiss-amphibolite contact, biotites in the pink gneiss become systematically enriched in Fe and total Al, while losing Mg, Si and F (Appendix D). This trend is accentuated in biotites entrained within quartz ribbons.

In the S-1 transect, biotites in the gray gneiss and the mylonitic gneiss are compositionally similar to biotites from the gray gneiss at 419, (Figures 1.17, 1.18), and exhibit no systematic compositional changes with increasing proximity to the contact. Within the pink gneiss, biotite is extensively chloritized, and no satisfactory compositonal data were obtained.

Amphibole

Amphibole compositions from both transects are summarized in Figures 1.16 and 1.17, in terms of tremolite (Tr) activity, using an ionic model which assumes ideal mixing on all sites (Holland and Richardson 1979; Ghent 1988);

$$a_{Tr} = (X_{\square, A})(X^{2}_{Ca, M4}) (X^{5}_{Mg2+})(X^{4}_{Si, T1}),$$

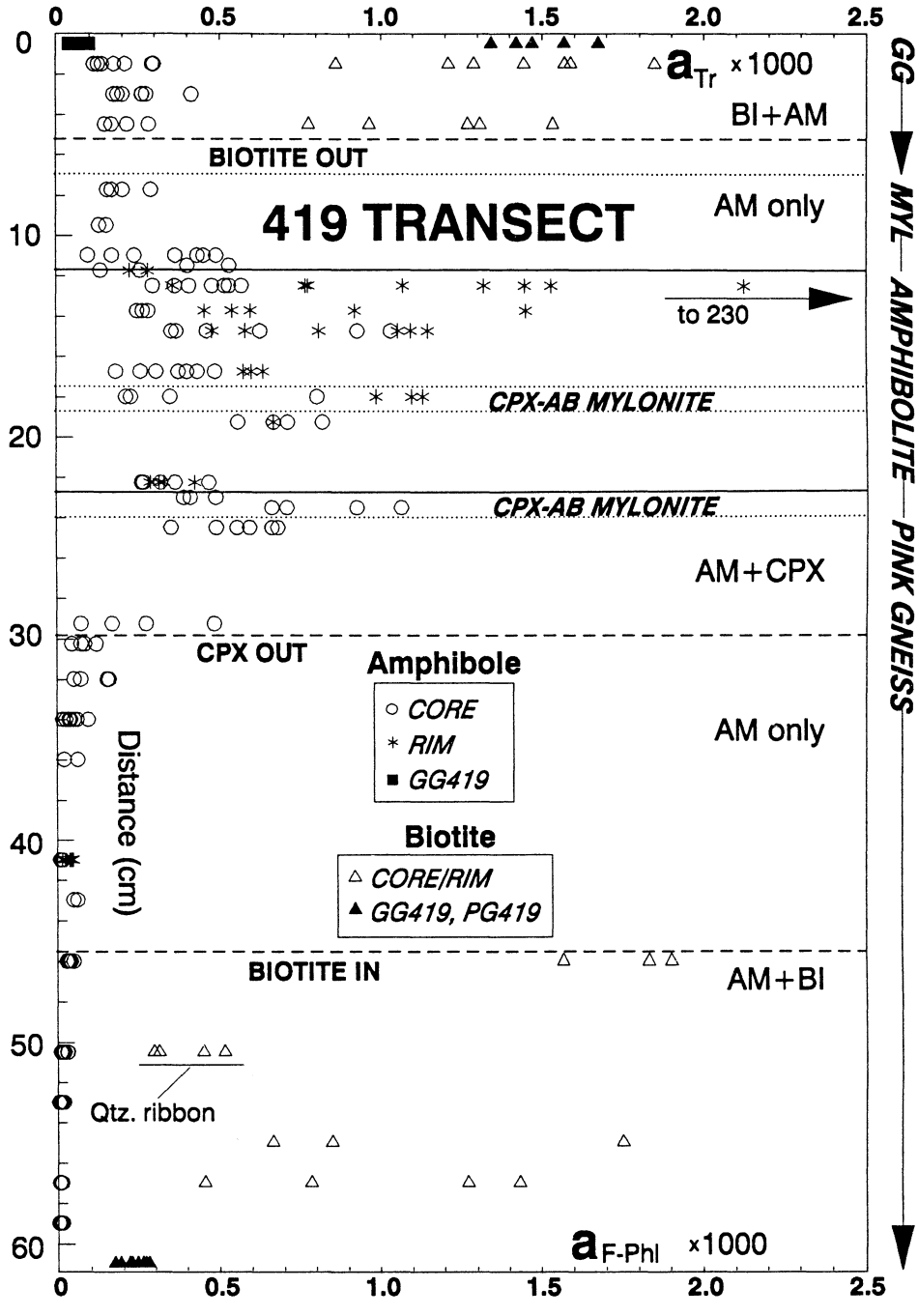


Figure 1.16. **Amphibole composition (as Tr activity) and biotite composition (as F-Phl activity) across the 419 Transect:** Each data point represents a single microprobe analysis. Analyses of Tr-rich amphibole rims from the amphibolite layer plot considerably above the vertical scale. Note also the spatial relationship between the data points for the Tr-rich rims, and the gray gneiss-amphibolite contact.

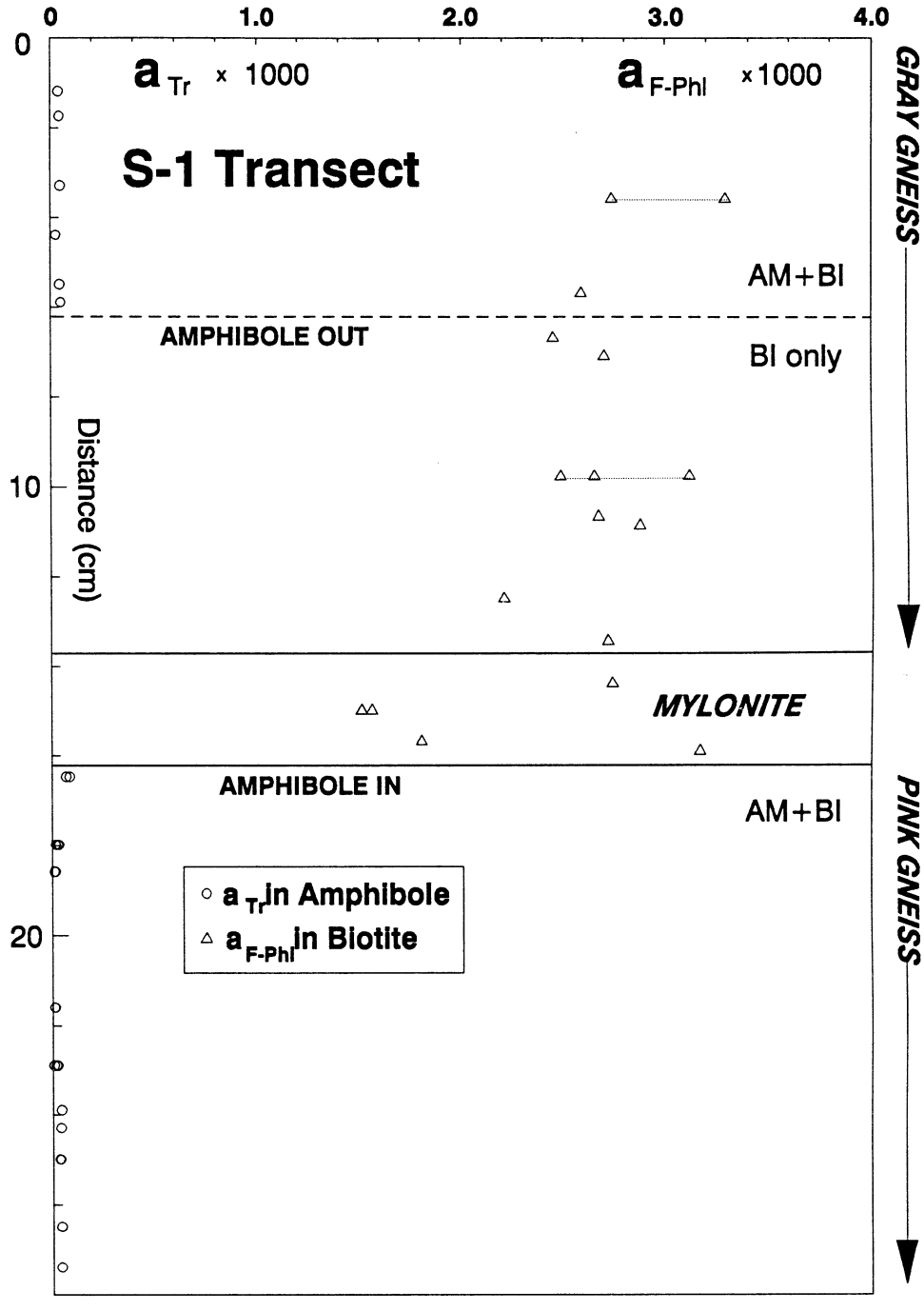


Figure 1.17. **Amphibole composition (as Tr activity) and biotite composition (as F-Phl activity) across the S-1 transect:** Each data point represents a single microprobe analysis. Note the lack of systematic compositional variation with increasing proximity to the mylonite zone.

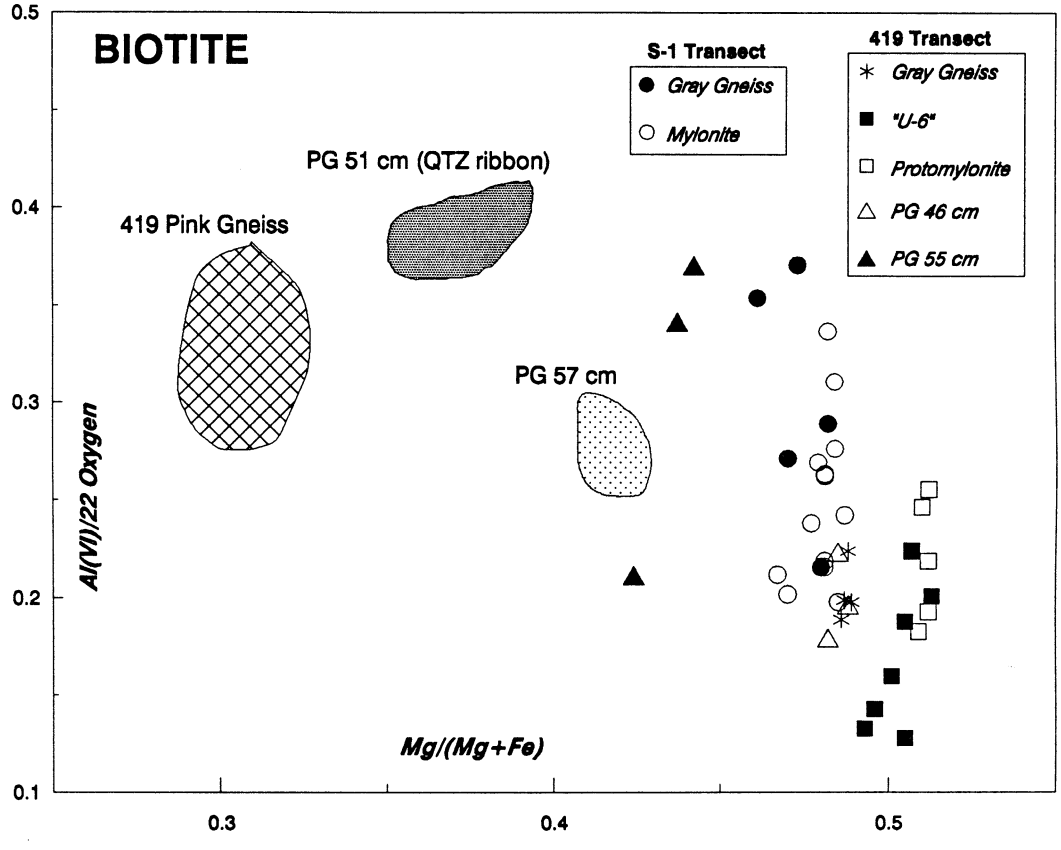


Figure 1.18. Variation of $Mg/(Mg+Fe^{+2})$ versus tetrahedral Al (per 22 O + F) in biotite from S-1 and 419

where $X_{\square, A}$ is the number of vacant A-sites. The use of the parameter a_{Tr} is intended purely as a basis by which the systematic variation of amphibole composition can be depicted, and not as an accurate model of the solution behavior of the various substituents. Dark green calcic amphibole is present across the entire 419 transect and shows pronounced systematic compositional variation from magnesian hastingsitic hornblende to edenite with respect to proximity to contacts and/or the degree of grain size reduction (Figures 1.19 and 1.20). While amphiboles from the less-deformed gneisses exhibit a relatively restricted range in composition relative to the variation seen across the entire transect, those from the amphibolite layer show large variations in Al, Si, Mg, Fe, Na and K contents. In all amphiboles from the Ponaganset gneiss (except actinolite), $Fe^{3+} > Al^{VI}$, A-sites are over 50% occupied and Ti never exceeds ~0.05 apfu. Vector representation (e.g. Thompson, et al. 1982) of the observed compositional changes in amphibole (Appendix E) indicate that the principal cation exchanges are $NaAlSi_{-1}$ (edenite = ed), $Al^{IV}Al^{VI}\ Mg_{-1}Si_{-1}$ (tschermakite = ts), $Fe\ Mg_{-1}$, KNa_{-1} and $F(OH)_{-1}$. Figure 1.21 shows the changes in the magnitude of the $FeMg_{-1}$ and ts vectors across the 419 transect. The trends depicted in the plot of the $FeMg_{-1}$ vector may reflect the compositional effects of the disappearance and appearance of biotite and clinopyroxene. For example, amphibole becomes progressively more Mg-rich from the top of the 419 transect to within . &app2 cm of the biotite-out boundary in the gray gneiss. At this point, amphibole compositions abruptly shift to more Fe-rich values, and then resume the Mg-enrichment trend with increasing proximity to the gray gneiss-amphibolite contact. Amphiboles also show a shift to more Mg-rich compositions following the loss of clinopyroxene in the pink gneiss.

In the gray gneiss farthest from the contact with the amphibolite, biotite coexists with amphibole, and amphibole compositions vary from magnesian hastingsite to magnesian hastingsitic hornblende (Appendix E, Figure 1.19a). No compositional zoning was observed in these grains. With increasing proximity to the gray gneiss-amphibolite contact, amphibole becomes systematically enriched in Mg and Si, and depleted in Fe^{2+}, total Al, total A-site cations and F. Ferric iron, Mn and Ti vary little. Amphiboles within the amphibolite layer are compositionally zoned, with rims that are often substantially more actinolitic than the cores (Appendix E, Figures 1.16, 1.20a, 1.21). This type of zoning occurs locally within the amphibolite layer, and is best developed in the

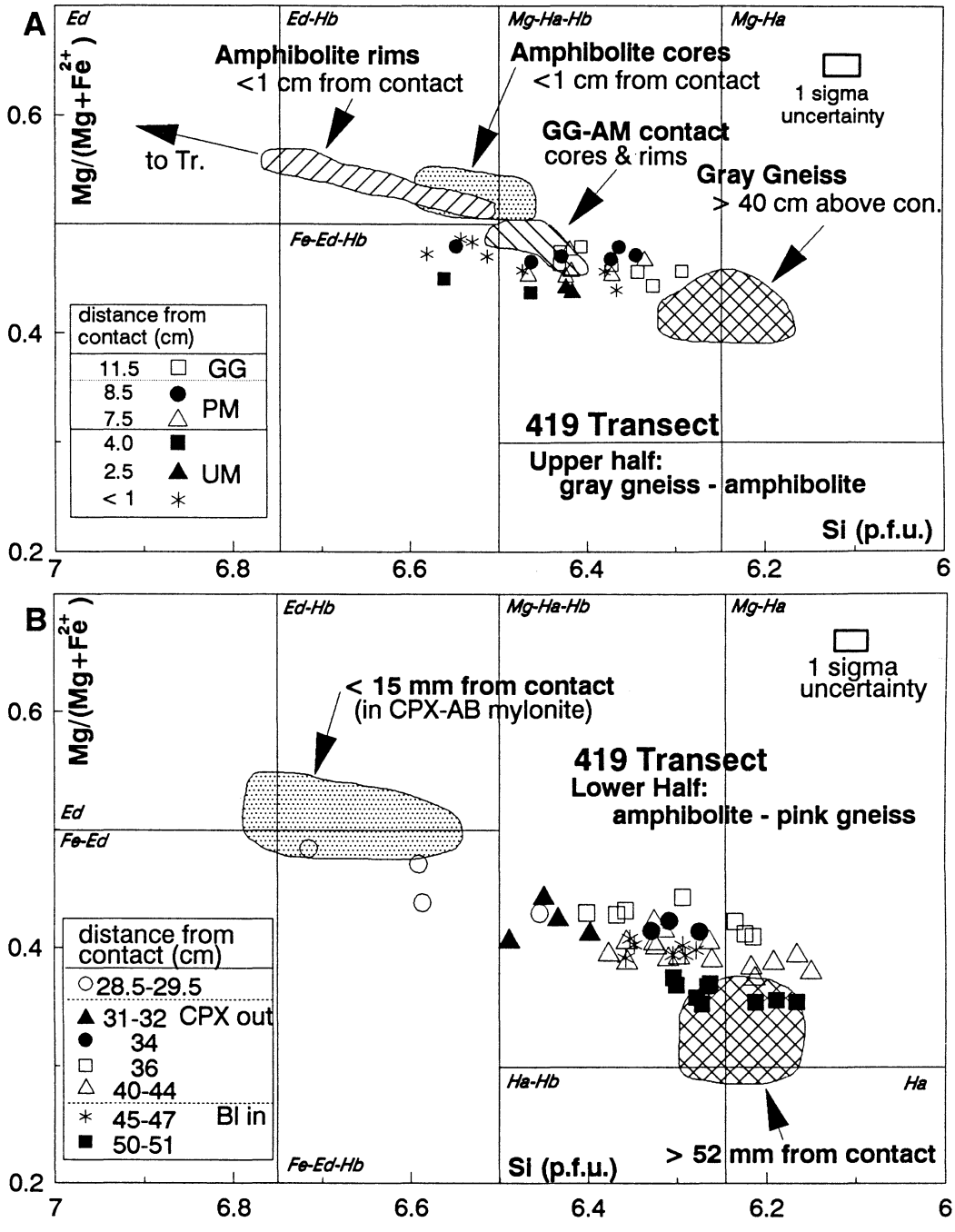


Figure 1.19. Variation of $Mg/(Mg+Fe^{+2})$ versus Si content (per 24 O + F) in amphibole: (a) - 419 transect gray gneiss and mylonite to gray gneiss-amphibolite contact (b) 419 transect pink gneiss-amphibolite contact to pink gneiss at the base of the transect. All amphiboles have: $Fe^{3+} > Al^{IV}$, $Na^{M4} > 0.5$ and $Ti < 0.5$. Fields labelled after the nomenclature of Leake (1978).

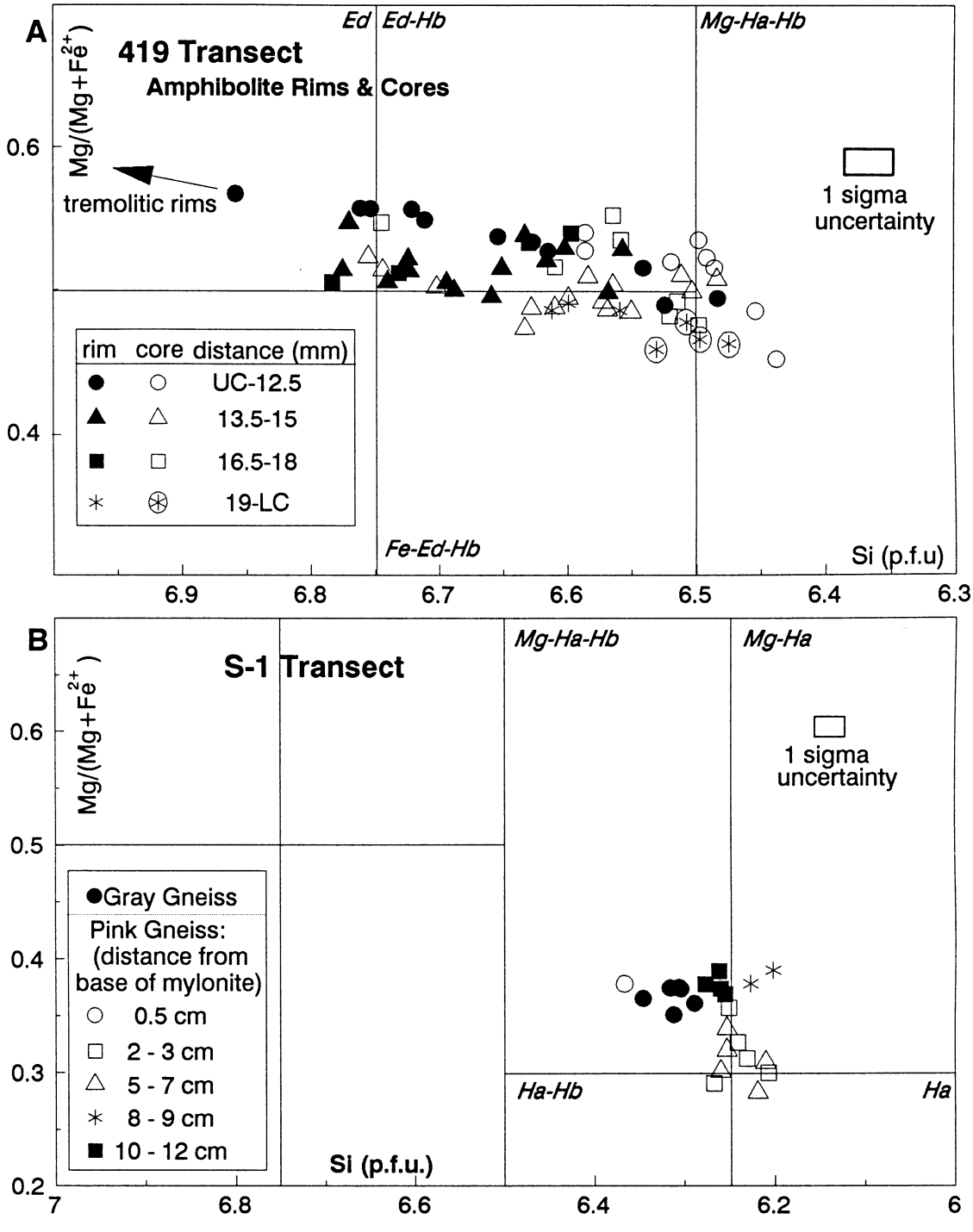


Figure 1.20. Variation of $Mg/(Mg+Fe^{+2})$ versus Si content (per 24 O + F) in amphibole: (a) - 419 transect amphibolite (cores and rims), the most Tr-rich analyses plot well outside the field depicted here. (b) - S-1 traverse, all lithologies. Fields labelled after the nomenclature of Leake (1978).

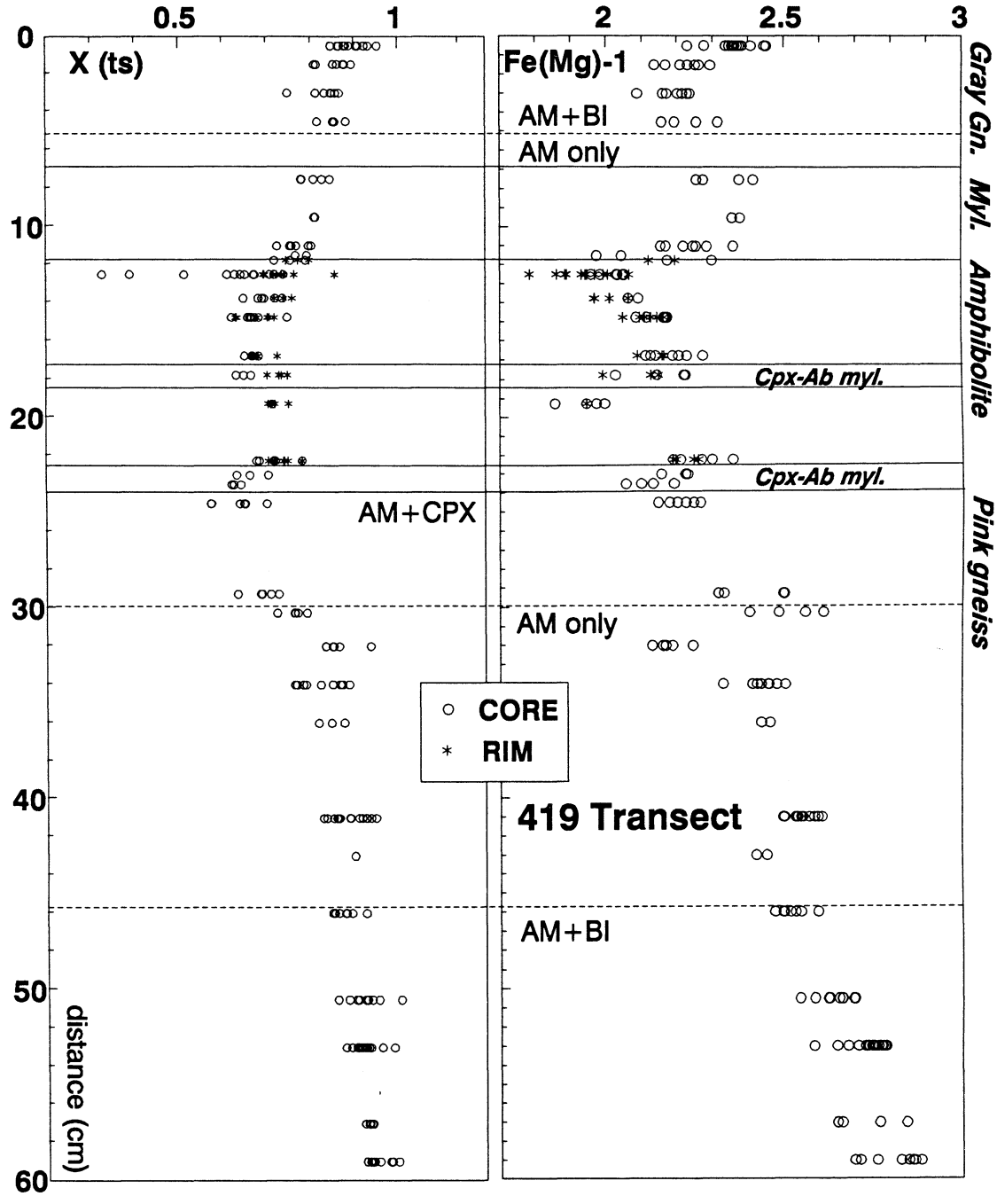


Figure 1.21. **$FeMg_{-1}$ and tschermakite (ts) vectors in amphiboles across the 419 transect:** Each data point represents a single microprobe analysis. The plot of $FeMg_{-1}$ shows discontinuities which have a spatial relationship to the biotite-out, biotite-in and clinopyroxene-out boundaries. The variation in the magnitude of the ts vector is relatively smooth across the biotite-in and biotite-out boundaries, but appears to increase in the vicinity of the clinopyroxene out boundary.

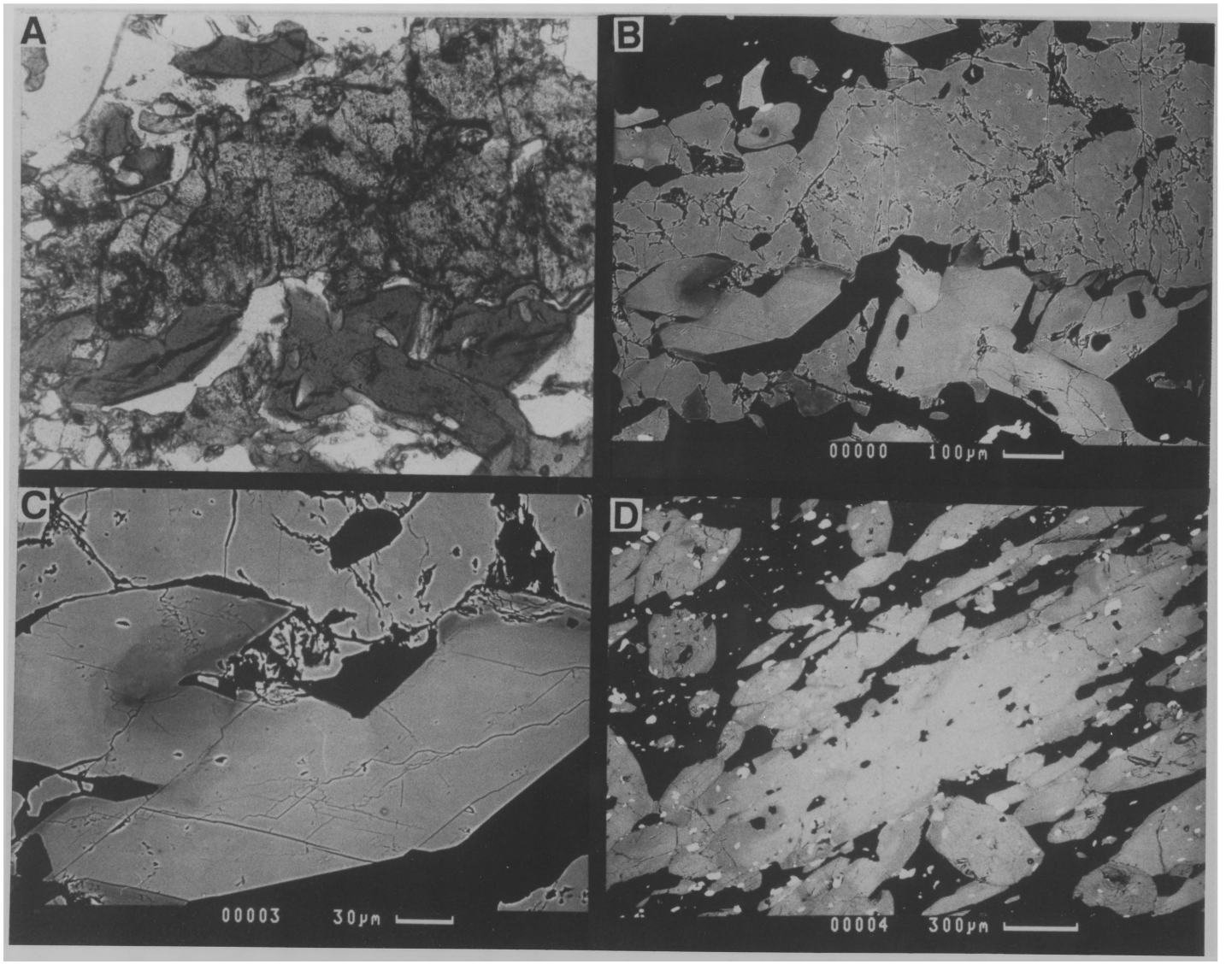
coarse-grained, poorly foliated bands at the margin of the amphibolite layer, which also contain quartz and clinopyroxene.

The physical nature of the zoning, as revealed by backscattered electron imaging (BSE), is irregular, patchy and discordant to the euhedral grain outlines (Figure 1.22 a-d). The intensity of the zoning also does not correlate to the presence of fractures or included phases. Instead, the most extreme compositional gradients recorded by amphiboles are associated with relatively large ($\simeq$ 1mm), anhedral, strained clinopyroxene grains (Figure1.22 a,b). With reference to the interior of the amphibole, the portions of the amphibole which penetrate the strained clinopyroxene porphyroclast are extremely depleted in Al and A-site cations. These regions also have $Mg/Mg + Fe^{2+}$ identical to that of the clinopyroxene, and much higher than that of the interior of the amphibole grain (Appendices E and F). The zoning pattern of these grains is strongly asymmetric, with the most actinolitic portions of the amphibole grains literally penetrating into the strained clinopyroxene microporphyroclast. Other portions of amphibole grains in contact with clinopyroxene are not as strongly zoned (Figure 1.22 b,c). The significance of the physical and chemical aspects is discussed further in a subsequent section.

At the pink gneiss-amphibolite contact, amphiboles are essentially unzoned, contain $\simeq$0.19 apfu Mn (as compared to $\simeq$0.08 for the amphibolite), and are richer in the ed and ts exchange components than amphiboles from the amphibolite layer. Within the pink gneiss, a positive gradient in Fe, A-site cations and total Al with increasing distance from the pink gneiss-amphibolite contact is established, and amphiboles farthest from the contact ($\simeq$32.5 cm) are magnesian hastingsitic hornblendes (Figure 1-19b). In the pink gneiss, chemically zoned amphiboles occur in the vicinity of quartz ribbons (Appendix E), and display the same general type of compositional changes (i.e rims depleted in Fe, Al and A-site cations) observed in the amphibolite, although they occupy a different region of composition space. These compositional trends are the opposite of those observed for biotite within the quartz ribbons (see preceding section).

In the S-1 transect, amphibole compositions from both gneiss units are similar to those observed in the gneisses at 419 and are tightly clustered (Figure 1.20b). Amphiboles from the some-

Figure 1.22. Zoned amphiboles from the 419 amphibolite layer: (a) - Transmitted light image of a clinopyroxene microporphyroclast surrounded by euhedral amphibole grains. This grain is located within 1 cm of the gray gneiss-amphibolite contact. (b) - BSE image of (a). Note the new euhedral amphibole surrounding and growing into the anhedral clinopyroxene microporphyroclast. Note also the progressive decrease in average Z-number (brightness) of the portions of the amphibole euhedra that are completely surrounded by clinopyroxene. Microprobe analyses of these grains (Table 6) confirm that the decrease in average Z-number corresponds to an increase in Tr content of the amphibole. The "dark" material at the amphibole-clinopyroxene interfaces is quartz. (c) - Close-up of an amphibole-clinopyroxene interface from (b). (d) - Typical irregular zoning seen in amphiboles not in direct contact with clinopyroxene microporphyroclasts. Note that the zoning pattern has no relation to the presence of inclusions (bright = titanite; dark = quartz and plagioclase) or fractures in the amphibole grain. Minute titanite subhedra define an internal foliation.


A
B
00000 100µm
C
00003 30µm
D
00004 300µm

what altered, quartz-depleted portion of the pink gneiss are richer in Fe (and Fe^{3+}) than those from the remainder of the S-1 transect.

Clinopyroxene

Clinopyroxene is common in the amphibolite layer at 419, where it occurs both as tiny (~50 μm) matrix grains and as larger (up to 2 mm), anhedral microporphyroclasts that are often partially recrystallized and/or mechanically twinned. Textural evidence (Figures 1.7c, 1.22 b,c) also suggests that the microporphyroclasts were not in chemical equilibrium and participated in amphibole-forming reactions. Compositionally, the clinopyroxene is a Di-Hd solid solution (Appendix F), with Al, Na and Ti contents below those observed in typical basaltic rocks. In the amphibolite layer, slight but significant, compositional differences distinguish the matrix clinopyroxene from the microporphyroclasts. The microporphyroclasts have consistently higher $Mg/(Mg+Fe^{2+})$, and lower Na and Al contents than the matrix grains (Figure 1.23). In BSE images, patchy irregular zoning is apparent in some clinopyroxene grains (Figure 1.22b), particularly the strained microporphyroclasts. BSE images of partially recrystallized clinopyroxene microporphyroclasts also reveal no systematic differences in average Z-number between new recrystallized clinopyroxene and strained precursor grains.

In the clinopyroxene-albite mylonite within the amphibolite, and at the pink gneiss-amphibolite contact, clinopyroxene tends also to be relatively enriched in Al, Na and Mn in comparison to clinopyroxene from the amphibolite layer (Appendix F). No systematic changes in the composition of clinopyroxene in the pink gneiss occur before it disappears ~5.0 cm below the amphibolite-pink gneiss contact. Compositional zoning is not apparent in clinopyroxene from the pink gneiss.

Titanite: Titanite, is an abundant accessory phase present in all units of the Ponaganset gneiss. Throughout the Ponaganset gneiss, titanite contains considerable amounts of Al and F, and

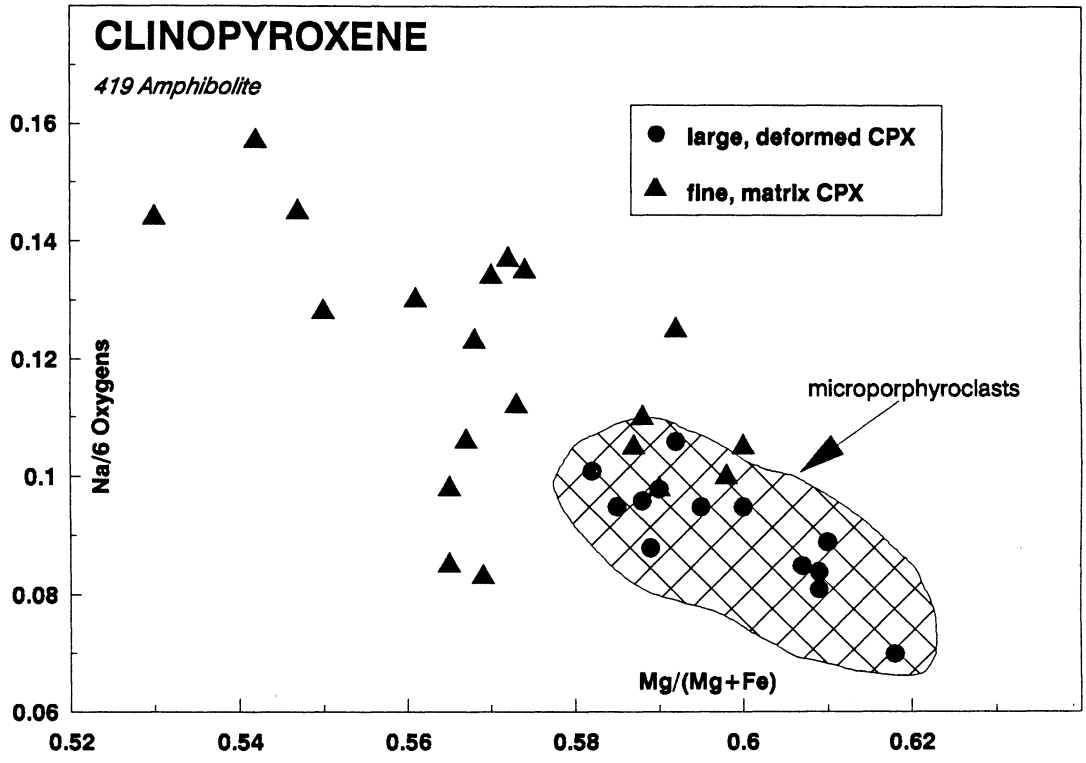


Figure 1.23. Variation of ($Mg/Mg+Fe^{+2}$) versus Na (per 6 O) in clinopyroxene from the 419 transect: Unstrained matrix grains tend to have higher Na (and total Al) contents, and lower Mg contents than relict microporphyroclasts.

subordinate amounts of Fe and Mn. Chaotic zoning is common in large (> 500 μm) titanite grains and aggregates from the gneisses, and suggests a complex growth history The observed chemical trends of titanite from each unit suggest that the dominant exchange mechanism is:

$$Ti^{4+} + O^{2-} \rightarrow Al^{3+} + F^{-}$$

Titanite is abundant in the amphibolite as tiny (< 50 μm) inclusions, mostly in amphibole grains, within which they define internal surfaces.

Other Minerals: Throughout the Ponaganset gneiss, magnetite is pure Fe_3O_4. Epidote is pistacite-rich (419:Ps_{18} to Ps_{33}, S-1: Ps_{25} to Ps_{30}) and occurs primarily as a late vein filling, as discrete grains within altered feldspars, and as thin, continuous rims on allanite grains. Chlorite and Fe-rich muscovite are present in minor amounts as alteration of feldspars, biotite and amphibole. Secondary calcite is essentially pure $CaCO_3$.

Geothermometry and Geobarometry

The Ponaganset gneiss recorded zircon U-Pb lower intercept ages of ca. 289 m.y. (Wayne et al., submitted) and Rb-Sr whole-rock ages of 266 to 293 m.y. were obtained from slabbed transects across both the gray gneiss-to-mylonite transition at S-1, and within the amphibolite layer at 419 (Wayne 1990). Regional constraints on the P-T conditions of the Alleghanian metamorphism recorded by the Rb-Sr, U-Pb and $^{39}Ar/^{40}Ar$ isotopic systematics and microstructural evolution of the Ponaganset gneiss (see also Wayne and Sinha 1988, 1989; Gromet 1989; Murray 1988; Simpson and Wintsch 1989; O'Hara and Gromet 1983; Dallmeyer et al. 1982, and others) suggest that the event reached amphibolite grade. This is also supported by $^{39}Ar/^{40}Ar$ age spectra of amphiboles from the Scituate granite (Dallmeyer et al. 1990) which consistently yield

Alleghanian ages (276 to 263 m.y.) regardless of the degree of deformation, or their proximity to the Hope Valley Shear Zone. The $^{39}Ar/^{40}Ar$ data suggest that the temperature of metamorphism in the region exceeded the closure temperature of hornblende (ca. 500°C). Peak metamorphic pressures in the southwestern portion of the Narragansett Basin are inferred to be 4 to 6 kb from the data of Grew and Day (1972) (see also Murray et al. 1981). However, pressure estimates for Alleghanian mineral assemblages farther to the north have not been obtained.

At the sample locality for this study, the estimation of P-T conditions during Alleghanian metamorphism and deformation is hampered by the general lack of temperature- and pressure-constraining mineral assemblages, as well as by the effects of mixing and partial re-equilibration between two chemically disparate lithologies. Oxygen isotope thermometry of quartz-magnetite pairs obtained from the pink gneiss, gray gneiss and two discrete mylonite zones (one from the 419 transect) at the outcrop consistently yields temperatures of $\simeq$600°C (Stakes, written communication 1990). Two ternary feldspar goethermometers were applied (Green and Usdansky 1986; Fuhrman and Lindsley 1988) to plagioclase - K-feldspar pairs from all lithologies. Temperatures recorded by coexisting feldspars using either model are consistently lower than the temperatures indicated by the partitioning of O isotopes between coexisting quartz and magnetite. In particular, convergent temperatures obtained using the Green-Usdansky model average $\simeq$ 480°C, while the Fuhrman-Lindsley model yields temperatures in the range 420 to 445°C. Feldspar pairs from the gray gneiss were in equilibrium (i.e. $T_{An} = T_{Ab} = T_{Ksp}$) according to the Fuhrman-Lindsley model, whereas feldspar pairs from the mylonitized gray gneiss, amphibolite and the pink gneiss were "close-to-equilibrium" (i.e.$T_{An} > T_{Ksp} \simeq T_{Ksp}$). This pattern suggests that feldspars in the mylonite, amphibolite and pink gneiss exchanged Ca and/or K after the exchange ceased in the gray gneiss

In the amphibolite, the compositions of coexisting amphibole and plagioclase are consistent with those observed in other amphibolite-grade mafic schists by Spear (1981), except that plagioclase compositions are distinctly An-poor (ca. An_9) in comparison to those expected to co-exist with highly edenitic amphiboles. The amphibolite layers within the Ponaganset gneiss also contain high amounts of K-feldspar (Table 1.1a), and the effects of two coexisting feldspars on the composition of a coexisting amphibole are not known.

Temperature estimates were also obtained across the entire 419 transect (Figure 1.24) using the semi-empirical amphibole-plagioclase thermometer of Blundy and Holland (1990). When applied to amphibole-plagioclase pairs within the quartzofeldspathic gneisses and mylonites, this technique yields temperatures (assuming 6 kb pressure) between 750°C and 775°C for the least-deformed gray gneiss, 695°C to 730°C in the mylonitized gray gneiss, 660°C to 715°C in the pink gneiss <5 cm below the pink gneiss-amphibolite contact, and 700°C to 765°C throughout the rest of the pink gneiss. Some of these temperatures exceed the experimentally determined stability limit for hastingsite (685 ± 5°C, 3 kb, FMQ buffer; Thomas 1982). As Thomas (1982) points out, substituents such as F, K, Mg and Mn may extend the stability field of hastingsite to considerably higher temperatures.

Within the amphibolite, temperatures derived from plagioclase-amphibole equilibria ranged from 500°C to 705°C, with the lowest temperatures obtained from the Mg-Si-rich, Na-Fe-Al-poor amphibole rims, and from the clinopyroxene-albite mylonite domains. Actinolitic amphibole from zoned grains adjacent to deformed clinopyroxene microporphyroclasts (Figure 1.22b, Appendix E) yielded temperatures in the range 500°C to 525°C.. In each case, the composition of coexisting plagioclase was assumed to be that of nearby (< 1 mm away), or contiguous matrix grains ($\simeq An_9$).

The effect of changing amphibole and plagioclase compositions with increasing proximity to a gneiss-amphibolite contact is reflected by a negative gradient in estimated temperatures (Figure 1.24). While the range of temperatures obtained from each point along the transect is within the stated 2σ uncertainty (± 75°C) stated in Blundy and Holland (1990), the total variation in temperatures obtained from the less-deformed gneisses to the gneiss-amphibolite contacts, and into the amphibolite itself, is greater than 75°C and is therefore not completely attributable to error in the calibration. The wide range of temperatures obtained from amphibole-plagioclase pairs in the gneisses, and their systematic decrease with proximity to the amphibolite layer can be explained by: 1) lack of complete equilibration between amphibole and plagioclase during metamorphism, 2) plagioclase unmixing across the peristerite gap and/or 3) bulk compositional variations. It is beyond the scope of this study to fully evaluate the effects of bulk compositional variations on the tem-

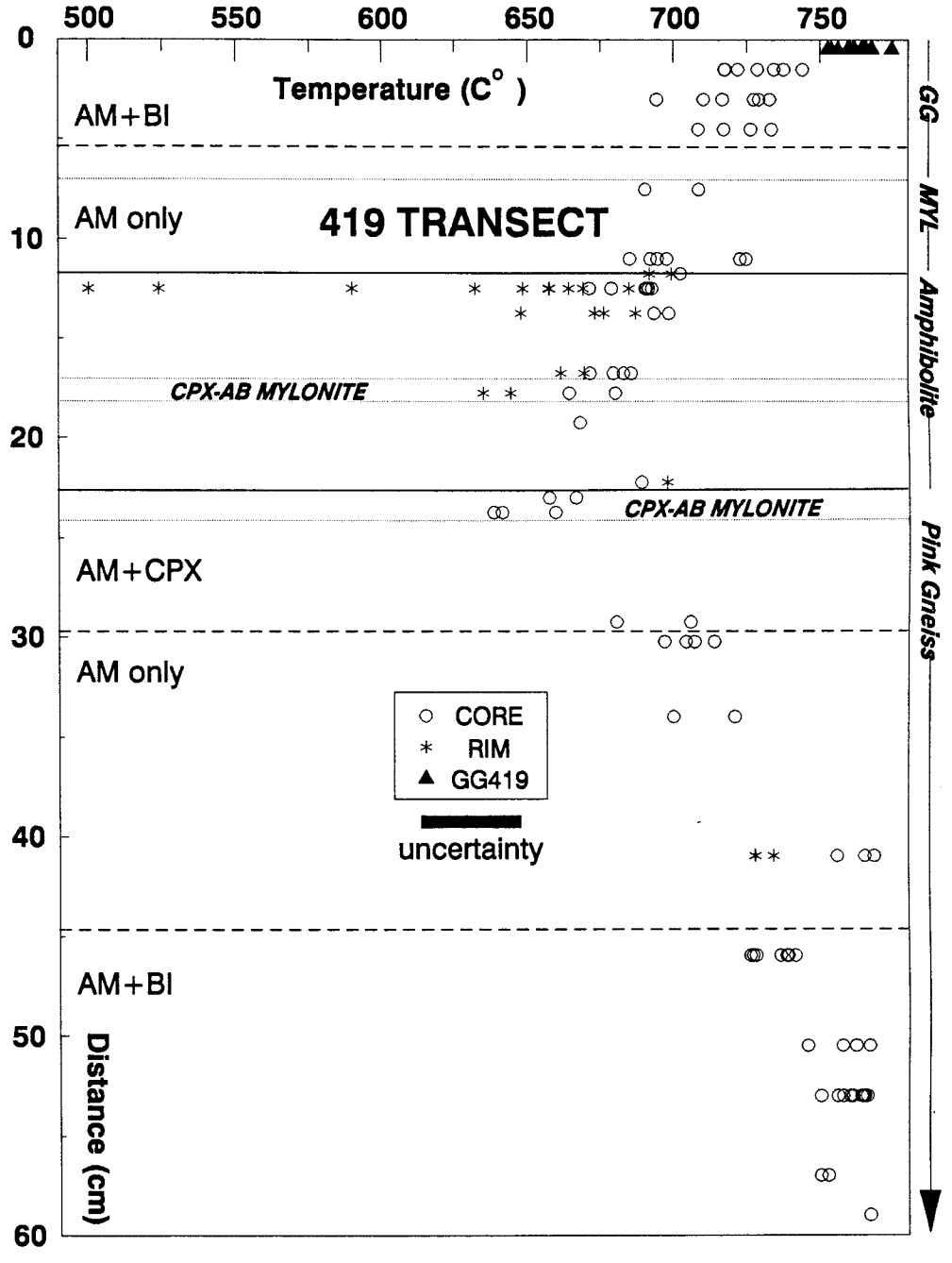


Figure 1.24. Temperature estimates from plagioclase - amphibole pairs (using the method of Blundy and Holland 1990): Temperature estimates from both gneiss lithologies systematically decrease as a function of both the increasing Ab content of plagioclase, and the increasing Si content of amphibole. These compositional variations are, in turn, related to the proximity of each plagioclase - amphibole pair to an amphibolite-gneiss contact. See text for further discussion.

peratures obtained from amphibole-plagioclase equilibria. The calibration of Blundy and Holland (1990) encompasses amphibole data from a wide range of bulk compositions, and their application of the geothermometer yields consistent results over a wide range of bulk compositions. Therefore, as a first approximation, bulk compositional insensitivity will be assumed. Either factor (1) or (2) could also result in spuriously high temperatures (Blundy and Holland 1990), although it is also possible that the temperatures recorded by the plagioclase-amphibole pairs represent real differences in their growth and re-equilibration across the transect through time.

In the amphibolite, amphibole compositon varies smoothly across single zoned grains and it is difficult to infer which amphibole composition (i.e. core vs. rim) represents equilibrium with the matrix plagioclase. Assuming a highly albitic plagioclase (An_3) is in equilibrium with amphibole reduces the estimated temperature only slightly ($\simeq$10°C). Conversely, a change in pressure from 6kb to 5kb increases the temperatures by 10°C to 20°C. Thus, small changes in metamorphic pressure and changes in plagioclase composition within the range observed in the amphibolite produce only slight changes in the estimated temperature.

The combined geothermometric data set implies a peak metamorphic temperature of $\simeq$600°C. Evidence for disequilibrium (i.e. development of Mg, Si-rich rims) is extensive in the amphibolite, although temperatures obtained from the amphibole rim-plagioclase pairs (635°C to 675°C) approximate, within the estimated 2σ uncertainty of the geothermometer ($\pm$ 75°C, Blundy and Holland 1990), the temperature obtained from O-isotope partitioning between quartz-magnetite pairs (Stakes, written communication 1990). The differences in plagioclase and amphibole composition reflect the reequlibration of these phases along a cooling path which was marked by the continued breakdown of clinopyroxene in the amphibolite. These reactions proceeded to $\simeq$ 500°C. Lower temperatures ($\simeq$425°C) obtained from the ternary feldspar mixing model may indicate a protracted period of cooling below the closure temperatures of the other geothermometers, the effects of exsolution processes related to the peristerite gap, or the exchange of K, Na or Ca with intergranular fluids during alteration.

Mass transfer calculations

Mass balance and reaction progress calculations (Tracy et al. 1983; Ferry 1983, 1984, 1985; Ferry et al. 1987) were performed to evaluate both the scale and extent of mineral-fluid reactions relevant to the modal and mineral chemical changes observed in the gneisses, mylonites and amphibolite. The calculations are based on modal data (Table 1.1b) and average mineral chemistry (Appendices B-F), and allow the formulation of model mineral-fluid reactions between a set of genetically related samples (or assemblages) through the application of the generalized mass balance equation (Ferry 1984):

$$[\sum \alpha_{i,j}\, n_j\,]_A = [\sum \alpha_{i,j}\, n_j\,]_B$$

$\alpha_{i,j}$ represents the number of atoms of element i per formula unit of mineral j, and n_j is the number of moles of mineral j in the rock (A,B). The mass balance relationships were based on a constant Al reference frame for each sample suite. The molar Al content of all gray gneiss and gray gneiss-derived mylonite samples across the 419 transect was normalized to that of the gray gneiss sample farthest from the amphibolite layer (GG419). Following the same rationale, the Al content of gray gneiss and mylonite samples across the S-1 transect was normalized to UGA, all pink gneiss samples were normalized to PG419, and the amphibolite samples were normalized to the Al content of the least hornblende-rich sample of clinopyroxene-albite mylonite (L2CPX). Thus, Al conservation is built into the mass balance relations and the model metamorphic reactions derived from them. All elements besides Al can be exchanged between samples, presumably as complexed ionic species in a fluid phase (Ferry et al. 1987).

The results of the mass balance calculations are shown in Table 1.3. Each column represents the difference, in moles of each element, between selected samples across each transect. Uncertainties, also shown in Table 1.3, were calculated by propagating 2σ errors obtained from repeated analyses of microprobe standards through the mass balance equations. These results were then

averaged for each rock type. Generally, the same phases are present on both sides of the model reaction, and they are not tabulated for the sake of brevity. Only the appearance and disappearance of key phases is noted on Table 1.3. The reaction coefficients of the phases involved in each reaction are simply the number of moles of each mineral in each sample, and these are shown in Table 1.3. Thus the data in Table 1.3 corresponds to the number of moles of each element gained by, or lost from, each sample as a consequence of the model reaction which could not be accounted for by the observed modal or mineral chemical changes. Note also that positive reaction coefficients denote those components consumed by the reaction (net gains) and negative reaction coefficients denote those components liberated as a consequence of the model reaction (net losses). The smaller the coefficients for a given reaction, the more similar the two samples under consideration.

Across the 419 transect, the transition from gray gneiss to mylonite requires a decrease in modal biotite and amphibole and an increase in the Ab component of plagioclase and modal K-feldspar. Model reactions based on mass balance calculations predict the liberation of Ca, Mg and Fe, and variable behavior of Na, K and Si. From the less deformed gray gneiss to the protomylonite (U5), significant Si loss occurs while K is consumed. The ultramylonite (U3) shows slight gains in Na and Si relative to U5, and continued depletion of Ca, Fe and Mg.

In the amphibolite, the reactions that resulted in the formation of amphibolite from the clinopyroxene-albite mylonite are of particular interest. Reaction relationships between several amphibolite-clinopyroxene-albite mylonite pairs were studied (ACP-- > U2, ACP-- > L2A, and L2CP-- > L2A), and all predict significant consumption of Mg, Fe, H and F, and liberation of Na and Mn. Si is also lost from the clinopyroxene-albite, but the reaction coefficients are highly variable. The behavior of K and Ca is inconsistent. For example, the formation of amphibole L2A from clinopyroxene-albite mylonite ACP requires addition of K and Ca loss, while the other samples suggest slight Ca gain and K loss. The non-systematic behavior of K and Ca may reflect original, small-scale bulk chemical inhomogeneity, or a change in the nature of the metamorphic reaction. as a function of proximity to the gray gneiss-amphibolite contact Amphibolite samples U2 and U3 are located within 3 cm of the gray gneiss-amphibolite contact, and thus may have experienced higher fluid-rock ratios, and/or a greater degree of interaction with fluids that equilibrated

Table 1.3. Results of mass balance calculations for successive slab pairs (in moles/liter); 419 and S-1 transects.

	419 TRANSECT			419 TRANSECT				
	Gray Gneiss--Mylonite Trans (bi out) ->GG-AM contact			CPX-AB Mylonite--Amphibolite Trans.				
	GG419>U5	U5>U3	avg.err.	U2>U3	ACP>U2	ACP>L2A	L2CP>L2A	avg.err.
SI	-1.384	0.539	0.070	3.583	-5.449	-0.217	-1.470	0.108
AL	-	-	0.077	-	-	-	-	0.111
TI	-0.109	-0.133	0.001	0.021	-0.010	0.240	-0.000	0.019
FE2	-0.367	-0.284	0.003	-0.009	0.791	1.184	1.231	0.161
MG	-0.268	-0.194	0.003	0.251	0.997	1.867	1.682	0.079
MN	-0.012	-0.011	0.000	0.021	-0.111	-0.040	-0.061	0.009
CA	-0.409	-0.366	0.035	0.240	-0.676	0.729	0.146	0.070
NA	-0.399	0.282	0.118	0.396	-2.349	-1.359	-1.404	0.157
K	0.865	-0.059	0.055	-0.474	1.121	-0.099	-0.063	0.033
FE3	-0.395	-0.179	0.006	0.080	2.320	2.475	2.487	0.059
H	-0.027	-0.116	0.005	-0.009	0.318	0.552	0.730	0.098
F	-0.097	-0.041	0.001	0.001	0.337	0.348	0.325	0.024

	419 Transect Pink Gneiss (cpx out) ------> incr. distance from pink gneiss-amphib. contact						
	E3Ag<L5	L5<L7	L7<L9	L9<L10	L10<L14	L14<PG419	err.
SI	1.706	-0.253	2.108	3.616	3.076	-1.754	0.059
AL	-	-	-	-	-	-	0.066
TI	0.001	-0.004	-0.060	0.047	-0.037	0.038	0.002
FE2	-0.000	-0.055	-0.094	0.057	-0.151	0.030	0.005
MG	0.018	-0.111	-0.001	-0.041	0.042	-0.000	0.004
MN	0.002	-0.015	-0.001	-0.001	0.002	0.002	0.000
CA	-0.058	-0.110	-0.048	0.015	-0.119	0.157	0.029
NA	-0.795	0.707	0.411	-0.051	-0.314	0.037	0.096
K	0.893	-0.523	-0.634	0.135	0.794	-0.015	0.046
FE3	-0.014	0.054	-0.083	0.105	-0.148	0.151	0.006
H	0.017	-0.125	-0.002	-0.051	-0.001	-0.119	0.009
F	0.003	-0.023	-0.025	0.003	-0.007	0.010	0.002

	S-1 Transect (am.out) (am. in)							
	GRAY GNEISS----------> MYLONITE ----------> PINK GNEISS							
	UG1>UG2	UG2>UG3	UG3>UG4	UG4>LG4	LG4*>LG3	LG3>LG2	LG2>LG1	avg.err.
SI	3.470	-1.213	-2.310	5.769	-14.906	-3.243	0.839	0.086
AL	-	-	-	-	-	-	-	0.096
TI	0.058	0.074	-0.058	-0.123	-0.034	0.017	0.047	0.006
FE2	0.103	-0.039	0.021	-0.303	0.028	0.070	-0.117	0.017
MG	0.171	-0.009	-0.035	-0.262	-0.037	0.006	-0.002	0.008
MN	0.007	-0.003	0.000	-0.015	0.003	0.004	-0.007	0.001
CA	-0.098	-0.029	-0.287	-0.158	0.479	0.033	-0.310	0.045
NA	-0.396	-0.125	-0.830	0.766	0.785	0.618	-1.151	0.144
K	0.656	0.177	1.170	-0.596	-1.710	-0.599	1.659	0.061
FE3	-0.075	0.001	0.037	-0.012	-0.031	-0.049	-0.075	0.013
H	0.235	0.005	-0.023	-0.361	0.274	-0.321	0.011	0.031
F	0.069	0.023	-0.038	-0.108	-0.015	0.009	-0.003	0.008

* - Al content normalized to PG 419

with the K-rich, Ca-poor quartzofeldspathic mylonite. The transition from U2 amphibolite ($\simeq$2.0 cm below the gray gneiss-amphibolite contact) to U3 amphibolite (0 to 1.5 cm below the contact) sugests that U3 has gained considerable amounts of Si (and minor amounts of Mg and Na), and contains less K relative to U2.

The pink gneiss samples show a consistent increase in Si with increasing proximity to the amphibolite. Other elements show no consistent trends, although portions of the pink gneiss dominated by porphyroclastic K-feldspar (E3Ag, L9, L10) typically show an increase in K and loss of Na relative to the surrounding rock, while mylonitic domains (L5) are characterized by Na gain and K loss. These differences reflect the changes in the modal proportions of plagioclase and K-feldspar.

Across the S-1 transect, model reactions in the gray gneiss predict progressive loss of Ca and Na, and K-gain from the gray gneiss farthest from the ductile deformation zone (UG1) to the gneiss adjacent to the ductile deformation zone (UG4). Si shows variable behavior across the same transition: after an initial gain from UG1 to UG2, Si is lost from UG3 and UG4. Fe, Mg and Ti may display similar trends, but generally undergo very minor changes. The reaction relationship between the gray gneiss and the mylonite (LG4) requires consumption of Si and Na, while all other elements (Fe, Mg, Ca and K) are liberated. By contrast, the transition from the mylonite (LG4) to the pink gneiss is characterized by extreme Si depletion ($>$ 50%), K loss, and concomitant gains in Ca and Na. The succeeding pink gneiss sample (LG2) shows continued loss of Si and K, and Na gain, while the pink gneiss farthest from the ductile deformation zone (LG1) experienced relative gains in Si and K and loss of Fe, Ca and Na.

For both sample suites, mass balance equations based on modes and mineral chemistry generally mimic the bulk chemical trends shown by whole rock analyses. Differences between the two datasets arise largely as the result of sampling scale: i.e. single thin sections versus 0.5 to 5 kg of rock. While the scale of observation may introduce some bias into the mass balance calculations, the whole rock analyses have the effect of averaging over volumes of rock that may exceed the volume of rock that has achieved equilibrium. In summary, the mass balance calculations suggest: 1) Fe and Mg were consumed, and Na and Si were released by the amphibolite-producing reaction.

Systematic changes in mass balance relation between contiguous amphibolite samples occur as a function of increasing proximity to the gray gneiss-amphibolite contact, 2) significant gradients in alkali, Si and Ca content occur over the gneiss-to-mylonite transition at S-1, but no such gradients occur across the same textural transition at 419, and 3) the gain and loss of K, Na, and to a lesser extent Ca and Si, in the pink gneiss samples across the 419 transect may be related to proximity to the pink gneiss-amphibolite contact, and to grain size reduction.

The chemical data from both transects suggests that substantial movement of Si, Na, Ca and K occurred during metamorphism and that ductile deformation zones acted as loci for Si deposition, especially at S-1. At S-1 (Figure 1.25), the mass balance calculations and the bulk chemical systematics infer that, while SiO_2 and K_2O were lost from the pink gneiss, portions of the adjacent ductile deformation zone experienced gains of these elements. The evolution of these different chemical domains, while probably not the result of closed system processes, was certainly limited to small scale volumes of rock. The mylonite zone contains foliation-parallel quartz ribbons, which may represent either pre-deformational quartz veins that were transposed into the foliation, or syn-deformational quartz segregations and/or veins formed as a consequence of fluid-rock interaction during mylonitization. Textural and chemical evidence favors the latter, as the increasing abundance of foliation-parallel quartz segregations corresponds to decreasing grain size and inceasing proximity to lithologic discontinuities. Quartz segregations in the ductile deformation zones are often enveloped by monominerallic (or nearly so) polycrystalline K-feldspar$\pm$ plagioclase aggregates. These aggregates do not occur adjacent to every quartz ribbon, but are a prominent feature in several mylonite samples and are indicative of new feldspar growth and/or alkali exchange between pre-existing feldspars and the fluid phase involved in quartz precipitation. The migration of quartz and K-feldspar into the mylonite may have occurred as a consequence of dilatancy sometime during deformation. Such a process would be favored by the relatively high molar volumes of quartz and K-feldspar, in comparison to plagioclase.

The availability of K, Fe, Mg, Ti, and H_2O during deformation may also explain why the gray gneiss-derived mylonite zones at the 419 and S-1 transects are so different in terms of their bulk chemistry and mineral assemblages. The gray gneiss-derived mylonite at 419 shows no increase in

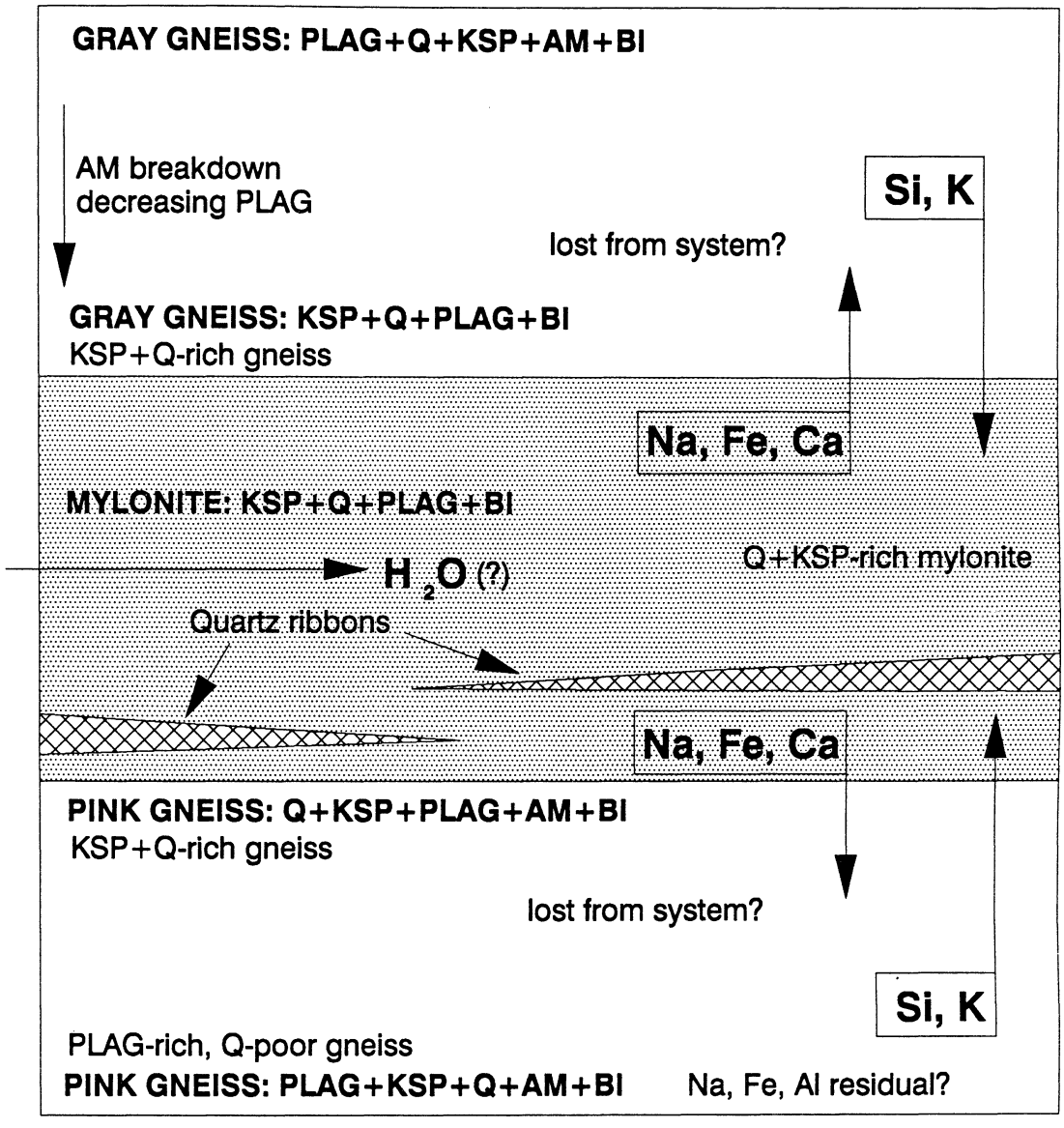


Figure 1.25. **Schematic diagram of mass transfer (constant Al reference frame) across the S-1 transect:** Mylonites and the immediately adjacent gneisses are highly enriched in Si and K, and depleted in Na, Ca and Fe, in relation to the protolith gray(?) gneiss. Quartz ribbons within the mylonite are associated with segregations of K-feldspar, and occur mainly near the contact with the pink gneiss. There is no evidence of Ca and Fe enrichment in the gray gneiss, but a constant Al approximation supports the non-mobility of Fe and Na in, and the addition of Ca to, the quartz-poor region of the pink gneiss. The enrichment of quartz and K-feldspar in the mylonite may be a response to dilatancy during deformation. The primary bulk chemical trends across the S-1 transect do not support or refute the existence of an externally-sourced aqueous fluid.

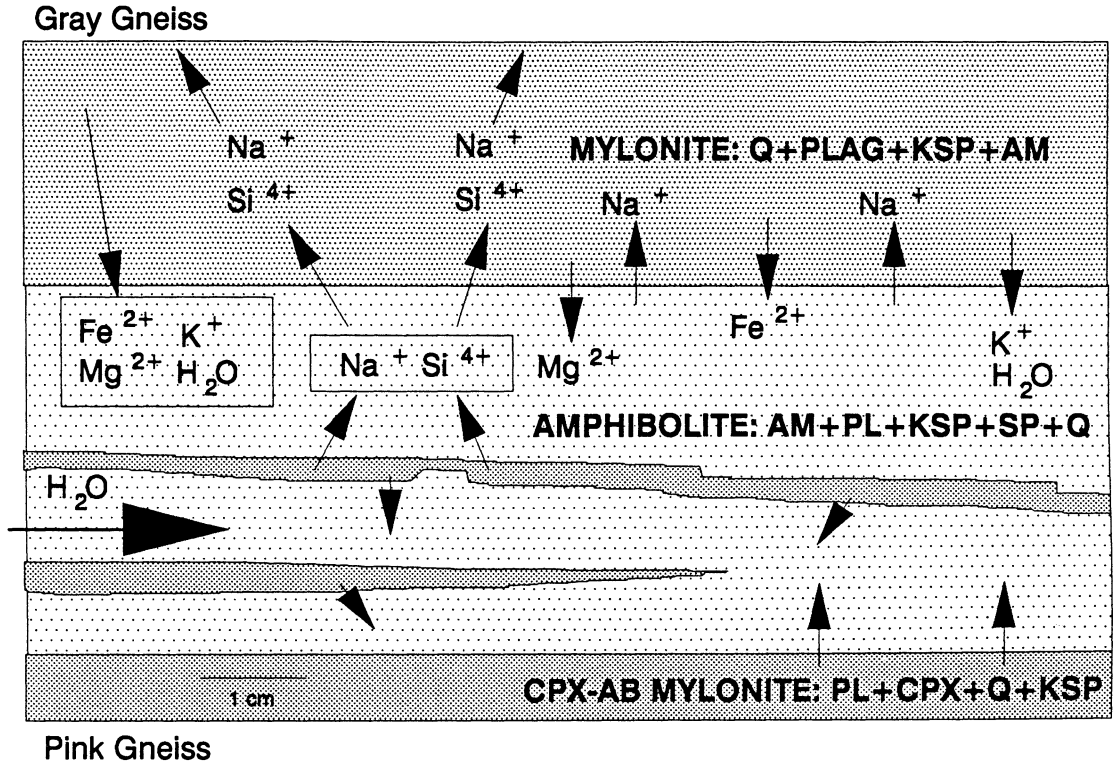


Figure 1.26. **Schematic diagram of chemical mobility (constant Al reference frame) between mylonite and amphibolite:** Hydration and reaction of the clinopyroxene-albite mylonite results in the release of Na and Si into the surrounding quartzofeldspathic mylonites. Mg, Fe and K are added to the reacting mafic layer and may be derived from the mylonite, which experienced a net loss of these elements (relative to the protolith gneiss).

K, and only a slight increase in Na and Si. The differential geochemical behavior of the mylonite adjacent to the amphibolite layer may be explained, in part, by the reaction of a clinopyroxene-albite-rich assemblage to form amphibolite. The bulk chemical and mass balance data also support the mobility of Mg and Fe and between the amphibolite and the contiguous mylonitic gneisses (Figure 1.26). Mylonitized gneiss proximal to the amphibolite is depleted in Fe, Mg, Ca and Ti with reference to the protolith gray gneiss, while the amphibolite experienced a gain of Fe, Mg, Ti, K and H_2O. The gray gneiss-derived mylonites at 419 contain no biotite, and are not as K- and Si-rich as the mylonite at S-1. Possibly, more fluid was available to the mylonite at S-1 because of the absence of a mafic layer which acted as a H_2O sink during the hydration of the clinopyroxene-rich assemblage. This may also explain the lack of a strong K gradient in the mylonite at 419, and the presence of a gradient in K content within the amphbiolite.

Metamorphic reactions in the amphibolite

Reaction progress modelling

To further assess the fluids and ion exchange reactions in the amphibolite layer, the reaction progress approach (Brimhall 1979; Ferry 1983, 1984, 1986) was utilized. In order to constrain the system to a thermodynamically valid number of linearly independent reactions, a set of system components (c_s) and a set of phase components (c_p) were chosen following the methods of Thompson et al. (1982). The composition space occupied by the amphibolite layer can be described by the following 11 oxide components: SiO_2, Al_2O_3, TiO_2, Fe_2O_3, FeO, MnO, MgO, CaO, Na_2O, K_2O and H_2O. The fluid phase is assumed to be pure H_2O, but was allowed to exchange

alkalies with the solid assemblage via an exchange vector in order to mimic the metasomatic effects observed in the amphibolite layer.

A system of phase components (c_p) were chosen to fully describe the amphibolite layer (Table 1.4), in which the minerals are represented as a combination of a single additive component (typically an idealized end-member composition) and a set of geochemically relevant exchange vectors which accurately describe the deviation of the observed mineral chemistry from the end-member. For the amphibolite assemblage, the total number of c_p is 28 (Table 1.4). The total number of linearly independent reactions in the amphibolite system can be determined by the equation (Thompson et al. 1982):

$$n_r = c_p - c_s = 28 - 11 = 17.$$

Of these 17 reactions, 11 are taken as pure exchange reactions (e.g. $FeMg_{-1}$ [AMPH] = $FeMg_{-1}$ [BIO]. Because the progress of exchange reactions does not effect changes in the modal quantities of the additive components, they are not considered. The remaining net transfer reactions (n_{nt}) are those that involve the destruction, or formation, of one (or more) of the additive components. For the system under consideration here, n_{nt} = 6 (Table 1.4).

Gauss-Jordan row reduction techniques (Thompson et al. 1982) were used to find the 6 net transfer reactions relevant to the system. As noted by Gilotti (1989) and Ferry (1984), the choice of reactions is arbitrary provided that they are linearly independent. To ensure linear independence, and to facilitate computational ease, the net transfer reactions were chosen such that each one was responsible for the formation (or destruction) of a single, unique additive component (Ferry 1984). These are listed in Table 1.4. The system of equations for the amphibolite was further modified by using the observed average Mg/(Mg + Fe) ratios for amphibole and clinopyroxene, rather than pure end member components. Note that these reactions, taken individually, do not describe the actual metamorphic processes. The net transfer reactions can be linearly combined, according to the observed modal variations, to yield a total metamorphic reaction that does approximate the transformation of one assemblage into another. Because of the importance of ion exchange reactions in the

Table 1.4. Additive components, exchange components and net transfer reactions for the 419 amphibolite.

AMPHIBOLITE	
SiO_2	
$KAlSi_3O_8$	KNa_{-1}
$NaAlSi_3O_8$	KNa_{-1} , pl
$Ca_2(Mg,Fe)_5Si_8O_{22}(OH)_2$	KNa_{-1}, $FeMg_{-1}$, $FeAl_{-1}$, $CaMg_{-1}$, $MnMg_{-1}$ pl, ed, ts
$CaMgSi_2O_6$	$FeMg_{-1}$, $CaMg_{-1}$, $MnMg_{-1}$, ed, ts
$CaTiSiO_5$	$FeAl_{-1}$, ta
Fe_3O_4	
H_2O	NaH_{-1}
$c_s = 11$ $n_{ex} = 11$	
$c_p = 28$ $n_{nt} = 6$	

1) KSP + NaK_{-1} = 4 QTZ + ed

2) AB = 4 QTZ + ed

3) Tl = 0.5 $CaMg_{-1}$ + ta + 0.5 ed + 0.5 pl + 0.5 ts + 2.5 QTZ

4) MAG + $CaMg_{-1}$ = ed + $FeMg_{-1}$ + pl + $FeAl_{-1}$ + 2QTZ

5) CPX + ts = 0.39 $FeMg_{-1}$ + pl + 3 QTZ

6a) HBD + 2 Na^+ + $CaMg_{-1}$ + 4 ts = 5 ed + 2.5 $FeMg_{-1}$ + 3 pl + 12 QTZ + 2 H^+

6b) HBD + 1.44 $CaMg_{-1}$ + 3.33 ts = 3.33 ed + 2.56 $FeMg_{-1}$ + 3.33 pl + 11.11 QTZ + H_2O

ed = edenite $(Na\hat{A}\ Al^{IV})\ Si_{-1}$

ts = tschermakite $(Al^{VI}\ Al^{IV})\ (MgSi)_{-1}$

pl = plagioclase $(CaAl)\ (NaSi)_{-1}$

ta = Ti-Al substitution (2 Al) $(MgTi)_{-1}$

development of metamorphic assemblages in the amphibolite (see the preceding section), a model assuming pure NaH_{-1} substitution in the fluid phase was chosen as a first pass. The H_2O-bearing system was solved separately to estimate minimum fluid-rock ratios.

Reaction progress can be evaluated by monitoring changes in modal abundance, phase ratio and mineral composition across a suite of genetically related samples. For this study, reaction progress in the amphibolite was evaluated by using the measured changes in the modal abundance. Thus, the reaction progress variables reduce to (Ferry 1984):

$$\xi_i = (n_{j,i})_{products} - (n_{j,i})_{reactants},$$

where the $n_{j,i}$ represent the number of moles of the additive component (j) in each net transfer reaction (i). Mineral-fluid reactions can be written by summing the products of the ξ_i values and the stoichiometric coefficients over the total number of net transfer reactions in the system (Ferry 1984; Gilotti 1989).

The results for both the pure H_2O model, and the NaH_{-1} ion exchange model are shown in Table 1.5. The total reaction between any two samples can be determined by summing over all intervening samples. Because only 6 net transfer reactions were permitted by the thermodynamic constraints on the system, a model reaction progress variable, ξ^* was obtained for quartz. The level of agreement between the measured ξ value for quartz and the model ξ^* is never exact, but in most cases the sign of the model variable is consistent with the observed ξ value. The magnitude (and sign) of the model variable is also a function of the model chosen for the fluid phase. The pure H_2O model overestimates the amount of quartz produced for most of the samples. The NaH_{-1} exchange model obtains reasonable model progress variables for the samples closest to the gray gneiss-amphibolite contact, but underestimates the amount of quartz produced by the hydration reaction in the center of the amphibolite layer. Note, however, that the hydration reactions closer to the periphery of the amphibolite (reaction ACP > U2, Table 1.5) consume quartz and produce K-feldspar, while the reactions in the center of the layer (reactions ACP > L2A and L2C > L2A, Table 1.5) layer produce quartz and consume K-feldspar. Thus, the availability of K^+ ions in the

mafic layer closest to the contact had a strong effect on the amphibolite-producing reactions. In this case, the NaH_{-1} exchange model may be a more accurate description of the overall metamorphic reaction close to the gray gneiss-amphibolite contact The reaction in the interior of the amphibolite can be successfully modelled with, or without, a provision for ion-exchange with the fluid.

The choice of an ion exchange or pure H_2O model also had an effect on the amount of ed and pl exchange vector produced, or consumed, during the reaction. One disconcerting aspect of the net reactions is that they require An-rich plagioclase as a reactant. In reality, a more An-rich plagioclase was produced during the reaction. Given the large magnitude of the $CaMg_{-1}$ vector produced by each reaction, it is possible that a further modification of the model to allow influx of Mg^{2+} ions could remedy this inconsistency.

Minimum fluid-rock ratios for the hydration of the amphibolite layer were calculated by converting the number of moles of H_2O per liter of rock consumed by the hydration reactions to a volumetric fluid-rock ratio using the molar volume data of Burnham et al. (1969) for pure H_2O at 6 kb, 600°C (see Gilotti 1989). Results of these calculations are also reported in Table 1.5, and all values are below 0.05 moles H_2O per liter of rock. The fluid-rock ratio calculated in this manner is a direct consequence of the efficiency of the clinopyroxene-consuming reactions. As pointed out by McCaig (1984), the efficiency of hydration reactions in ductile deformation zones (as well as in other environments) is critically dependent on fluid-rock ratios. If the clinopyroxene-albite mylonites represent the last remnants of the amphibolite protolith, the varying degrees of preservation of the anhydrous assemblage may indicate that the degree of fluid-rock interaction within the mafic layer at 419 varied on a millimeter to centimeter scale.

Amphibole zoning

Amphiboles in the amphibolite layer may be compositionally zoned, with thin (5-20 μm), irregularly developed, optically continuous Mg-Si-rich rims on Fe-tk-ed rich cores. The most in-

Patron,

Page 86 is repeated in enumeration.

Table 1.5. Results of reaction progress calculations in the amphibolite, in moles/liter of rock.

Amphibolite--H2O Model

CPX-AB mylonite---->Amphibolite

	U2>U3	ACP>U2	ACP>L2A	L2C>L2A	L2C>E3A
Q/mol	3.394	-1.499	1.410	1.058	-1.102
PL/mol	0.300	-2.768	-1.899	-1.769	-1.169
KSP/mol	-0.720	1.219	-0.462	-0.388	0.628
AM/mol	-0.119	1.586	1.395	1.409	-0.022
MA/mol	0.000	-0.494	-0.427	-0.225	-0.045
CPX/mol	0.074	-3.453	-2.471	-2.724	0.655
SPH/mol	0.018	-0.072	0.198	-0.072	0.180
QUARTZ	2.739	0.103	1.721	1.774	0.081
ed	0.809	-3.202	-1.955	-2.275	0.568
NaK-	-0.720	1.219	-0.462	-0.388	0.628
CaMg-	-0.181	1.826	1.483	1.840	-0.166
Ti(MgAl)-	-0.018	0.072	-0.198	0.072	-0.180
plag	0.314	-1.298	-1.845	-1.707	-0.628
FeAl-	0.000	0.494	0.427	0.225	0.045
FeMg-	0.269	-2.124	-2.096	-2.235	-0.156
tscher	-0.332	1.864	2.074	2.004	0.493
H2O	-0.119	1.586	1.395	1.409	-0.022
F/R*	0.031	0.034	0.030	0.030	-

* - minimum volumetric F/R ratio (liters H2O/ liter of rock)

Amphibolite--Na-H Exchange Model

CPX-AB mylonite---->Amphibolite

	U2>U3	ACP>U2	ACP>L2A	L2C>L2A	L2C>E3A
Q/mol	3.394	-1.499	1.410	1.058	-1.102
PL/mol	0.300	-2.768	-1.899	-1.769	-1.169
KSP/mol	-0.720	1.219	-0.462	-0.388	0.628
AM/mol	-0.119	1.586	1.395	1.409	-0.022
MA/mol	0.000	-0.494	-0.427	-0.225	-0.045
CPX/mol	0.074	-3.453	-2.471	-2.724	0.655
SPH/mol	0.018	-0.072	0.198	-0.072	0.180
QUARTZ	2.845	-1.308	0.480	0.520	0.100
ed	1.008	-5.851	-4.284	-4.628	0.605
NaK-	-0.720	1.219	-0.462	-0.388	0.628
CaMg-	-0.128	1.128	0.869	1.220	-0.156
Ti(MgAl)-	-0.018	0.072	-0.198	0.072	-0.180
plag	0.274	-0.774	-1.385	-1.242	-0.635
FeAl-	0.000	0.494	0.427	0.225	0.045
FeMg-	0.269	-2.124	-2.096	-2.235	-0.156
tscher	-0.411	2.926	3.008	2.948	0.478
Na+	-0.238	3.172	2.789	2.818	-0.043
H+	0.238	-3.172	-2.789	-2.818	0.043

Patron,

Page 87 is omitted from enumeration.

teresting feature of the zoning is its irregular distribution in the amphibolite, and the relationship between rim composition and proximity to strained clinopyroxene microporphyroclasts. Fine grained ($\simeq$100 μm), well foliated and strongly lineated amphibolite domains typically contain no clinopyroxene and compositionally homogenous amphibole. Rim growth is most pronounced near the gray gneiss-amphibolite contact, in relatively coarse-grained, weakly foliated amphibolite domains which contain relatively high modal abundances of clinopyroxene, quartz and feldspars. Clinopyroxene in these domains occurs as fine (50-100 μm) annealed matrix grains, and as coarse microporphyroclasts which preserve considerable evidence of strain accumulation. Several lines of evidence suggest that the driving forces of grain boundary migration are related to gradients in both strain energy and chemical potential.

Actinolitic rims are not developed on amphibole grains in the vicinity of strain-free matrix clinopyroxene grains. The spatial relationship between actinolite-rimmed amphibole and clinopyroxene microporphyroclasts which appear to have retained strain energy accumulated during deformation suggests that the breakdown of clinopyroxene was kinetically favored during post-kinematic recrystallization. The catalytic effects of stored strain energy on dissolution reactions (Wintsch and Dunning 1984; Helgeson et al. 1978) are well known, but poorly characterized for most minerals. Strain energies in minerals with extremely high dislocation densities ($> 10^{10}$ cm^{-2}) are of a sufficient magnitude to affect reaction rates (Helgeson et al. 1978). Although no direct evidence of high dislocation densities in the clinopyroxene microporphyroclasts (e.g. TEM images) are presented here, the dislocation densities in these grains are certainly higher than in the annealed matrix grains. The microporphyroclasts preserve a number of features associated with high amounts of stored strain energy: mechanical twinning, undulose extinction, subgrain formation, and core and mantle structures. Thus, actinolite-producing, clinopyroxene-consuming reactions may have been overstepped for unstrained clinopyroxene grains, but not for grains with high accumulated strain energies.

Chemical evidence suggests that the progress of actinolite-forming reactions was dominantly a function of proximity to clinopyroxene grains. The most Mg-Si- rich portions of the rimmed grains penetrate the clinopyroxene microporphyroclasts, and have $Mg/(Mg+Fe^{2+})$ equal to that

of the adjacent clinopyroxene. Hydration of clinopyroxene to form actinolite requires a net influx of H_2O, into the local system, and may indicate late-stage differences in f_{H2O} along the gray gneiss-amphibolite contact relative to the rest of the amphibolite. Amphibole growth may have occurred by the reaction:

1) $H_2O + 3.5\ CPX + QTZ = HBD + 1.5\ CaMg_{-1}$,

although other reactions cannot be ruled out. The H_2O and Si requirements of reaction 1 may explain, in part, the localization of clinopyroxene hydration in the amphibolite near the gray gneiss-amphibolite contact, which may have experienced a somewhat higher fluid input during deformation. Mass balance criteria also support a net loss of Ca, and a net gain of Mg from the amphibolite (relative to the clinopyroxene-albite mylonite) nearest the gray gneiss-amphibolite contact (see Table 1.5), which agrees with the sign of the exchange vector in reaction 1. Presumably, both the exchange and transport of these components were facilitated by the presence of an intergranular fluid film. An interesting feature of all of the actinolite-clinopyroxene intergrowths is the ubiquitous presence of a boundary layer of quartz between adjacent grains. If the hydration of clinopyroxene occurred via reaction 1, the presence of a quartz boundary layer is consistent with the operation of a process which consumes clinopyroxene at a faster rate than quartz (Fisher 1976, p. 391). Finally, the euhedral nature of the new actinolitic regions (cf. Figure 1.22 b,c) may also be diagnostic of diffusion-controlled growth in the presence of a fluid film (Cumbest et al. 1989; Drury and van Roermund 1988 and others).

Metamorphic reactions in the mylonites and gneisses

Biotite, amphibole and clinopyroxene stability

The disappearance of biotite from the mylonitized gray gneiss at 419 is enigmatic in that no substantial chemical changes, other than a slight increase in $Mg/Mg+Fe^{2+}$ and a slight decrease in F occur as biotite becomes less abundant and disappears from the rock altogether $\simeq$5.5 cm above the gray gneiss-amphibolite contact. The same can be said of the occurrence of biotite in the pink gneiss, where it is absent from a 23 cm thick band below the pink gneiss-amphibolite contact (see Figure 1.5). Across the gray gneiss-to-mylonite transition the disappearance of biotite is preceded by a marked decrease in grain size, suggesting that the destabilization of biotite was favored as a function of decreasing grain size, and increasing surface area. The increase in surface area would serve to promote surface exchange, and the resulting local enrichment of the fluid phase in K^+ would serve to further enhance the destabilization of the phyllosilicate with increasing grain size reduction (Wintsch 1975). The increase in surface area provided more sites for surface exchange reactions in a K^+ -Na^+- rich fluid concentrated at the margins of the gneiss blocks, but may have had a negligable effect on fluid composition due to the low modal abundance of biotite in the gneiss. In Wintsch's (1975) model, the K^+ released by the hydrogenation of muscovite surfaces during grain size reduction is sufficient to locally stabilize feldspars in favor of muscovite by the reactions:

$$MU + 6\,QTZ + 2\,K^+ = 3\,KSP + 2\,H^+$$

$$MU + 6\,QTZ + 3\,Na^+ = 3\,AB + 2\,H^+ + K^+$$

The analogous biotite-consuming ion exchange reactions are necessarily more complex because they involve the transfer of Al^{3+}, Fe^{2+}, and Mg^{2+} cations. Hypothetically, reactions such as:

2) H_2O + 32 QTZ + 3.33 BI + 4 pl + 4.67 Na^+ = 6.67 KSP + 0.67 AB + 2 HBD + 4.67 K^+.

3) H_2O + 14 QTZ + 0.67 PHL + 2 ts + 3.33 Na^+ = 1.33 KSP + 3.33 AB + 3.33 H^+.

could explain the loss of biotite during interaction and exchange with a Na^+ -rich fluid. Similar reactions would obtain if K^+ was substituted for Na^+. Note that reactions 2 and 3 are consistent with decreasing An content of plagioclase, and decreasing ts content in amphibole which are both characteristic of the mineral chemical changes observed adjacent to the amphibolite. Both reactions consume large amounts of quartz which is abundant in the gneiss and was probably also present as a dissolved aqueous species. The small quantity of biotite present in the gneiss suggests that the volumetric importance of these reactions, if they did occur, was rather small.

Biotite-out reactions in the pink gneiss also go to completion as the pink gneiss-amphibolite contact is approached, although there is no apparent relationship between the presence of biotite and grain size. The occurrence of biotite in the pink gneiss does appear to be related to deformation in that it appears first in relatively coarse-grained, K-feldspar-rich aggregates and not in the mylonitic domains.

Clinopyroxene and amphibole in the pink gneiss may have been stabilized by their high Mn content. The amphibolite layer contains $\simeq$0.3 to 0.4 wt.% MnO, but the adjacent pink gneiss contains less than 0.1 wt.% MnO. Microprobe analyses reveal a strong discontinuity in the Mn content of clinopyroxene and amphibole approximately 0.5 cm above the pink gneiss-amphibolite contact, within the clinopyroxene-albite (Appendices E and F). Anomalously high Mn contents (ca. 1.5 wt.%) persist in both clinopyroxene and amphibole until they diappear 5.5 cm and 23 cm, respectively, below the pink gneiss-amphibolite contact. The $Mg/Mg+Fe^{2+}$, of both minerals decreases with decreasing distance from the contact, but upon the disappearance of clinopyroxene, the

Mn content of amphibole rises slightly, while $Mg/Mg+Fe^{2+}$ continues to drop off (Appendix B). The same trends were observed in biotite upon the disappearance of amphibole. No other Mn-bearing phases are present in the pink gneiss.

By contrast with the 419 transect, the mylonitized gray gneiss at S-1 contains biotite, but no amphibole. Application of SVD calculations (Fisher 1989) predict that the mylonites at S-1 and 419 do not overlap in n-dimensional composition space. Therefore, the distribution of amphibole and biotite in the ductile deformation zone is due, in part, to changes in rock composition. It is important to note that these bulk chemical contrasts need not be primary igneous features. A more interesting possibility is that the presence of the mafic layer had a strong local influence on mylonite chemistry. Specifically, infiltrating fluids would preferentially react with the anhydrous clinopyroxene-albite mylonites to produce amphibolite, and the adjacent quartzofeldspathic mylonites would develop in an environment that was relatively "dry". As a consequence, fluids had less opportunity to interact with feldspars in the mylonite adjacent to the amphibolite. In a case where the clinopyroxene-albite-rich precursor was not present, or where hydration reactions in the amphibolite had gone to completion, the adjacent quartzofeldspathic mylonite would then be more extensively metasomatized. For example, the mylonite at S-1 shows extensive local enrichment in K and Si, which represent an episode of K-metasomatism and SiO_2 influx. Thus, the disappearance of amphibole within the ductile deformation zone at S-1 may also be related to hydration and/or ionic equilibria. The following reactions may be written:

4) $HBD + 3\ H_2O + tk + 4\ K^+ =$

$QTZ + 2\ BIO + 2\ mc + 4\ H^+$

5) $0.39\ KSP + 0.17\ HBD + 0.42\ H_2O + 0.33\ ed + 0.39\ K^+ =$

$0.33\ AB + 0.39\ PH + 0.33\ mc + 0.39\ H^+$

6) $1.75\ HBD + 5.37\ H_2O + 2\ tk + 7.42\ K^+ =$

$0.58\ KSP + 3.42\ BIO + 3.5\ mc + 7.42\ H^+$

While none of these reactions, as those that describe biotite breakdown, are necessarily those that actually occurred in the rock, they do give a schematic representation of processes that could have produced the mineral assemblages present in the mylonite at S-1. Note that reactions 4 - 6 yield biotite, plus albite, quartz and K-feldspar at the expense of ed-tk-rich amphibole, H_2O and K ions, and necessitate Ca loss from the system (as the mc exchange vector). None of these reactions require a change in biotite composition, and only slight changes in the modal proportions of biotite and feldspars.

Instability of muscovite and epidote

Muscovite and epidote are absent from the peak metamorphic assemblage, but do appear as late-stage retrograde products of the hydration of feldspars. The lack of primary epidote and muscovite in the gneisses, mylonites and amphibolite is probably not a direct result of the P-T conditions of metamorphism (Liou 1973; Helgeson et al. 1978; Wintsch 1975), and both muscovite and epidote appear as constituents of peak mineral assemblages from other samples from the same outcrop. Liou (1973) showed experimentally that oxygen fugacity is a critical factor in determining the stability of epidote. According to his data, epidote is stable at 600°C, 4 to 6 kb in the presence of magnetite. Both magnetite and titanite are abundant in the Ponaganset gneiss, therefore oxygen fugacity was high enough to support the stable existence of epidote. Judging from the ubiquity of the mineral association magnetite + titanite, and from the high and consistent Fe^{3+}/Fe_{total} of amphibole throughout both transects, it is also unlikely that oxygen fugacity varied significantly in either the gneiss or the amphibolite during metamorphism. Thus, the absence of epidote from the transects is most likely due to bulk compositional effects. For example, the high K and Na content of the amphibolite layers may have stabilized K-feldspar and plagioclase in favor of epidote.

The inferred metamorphic conditions are also suitable for the stabilizaton of the assemblage muscovite + quartz, assuming $P_{fluid} = P_{total}$ (Helgeson et al. 1978). Given the evidence for the ex-

tensive mobility of a reactive Na^+ - K^+ - Si^{4+}-bearing fluid phase during metamorphism, it is likely that the local absence of muscovite is due to the relatively high K^+, Na^+ , and/or Si^{4+} contents of the metamorphic fluid, which stabilized K-feldspar in favor of muscovite + quartz (e.g. Wintsch 1973, 1975; Wintsch and Dunning 1984).

The scale of element transport in the Ponaganset gneiss

The mineralogic and chemical evidence presented in the preceding sections indicates that the presence of an amphibolite layer within the ductile deformation zone at 419 has clearly influenced mineral compositions within the surrounding gneisses. In the gneisses and gneiss-derived mylonites, these changes are manifested over several cm perpendicular to the contacts as rather smooth negative gradients in the An content of plagioclase, ed and K content of amphibole and the tk, F and Fe^{2+} contents of both biotite and amphibole (Figures 1.14, 1.16, 1.21). Superimposed on these gently sloping chemical gradients are sharp variations in plagioclase composition within the clinopyroxene-albite mylonites, which represent the last remnants of a pre-existing mineral assemblage. By contrast, actinolitic amphibole rims at the gray gneiss-amphibolite contact represent late metamorphic growth of amphibole at the expense of deformed clinopyroxene microporphyroclasts.

Variations in mineral chemistry are slight across a ductile deformation zone which does not contain an intervening amphibolite layer, as in the case of the S-1 transect. This is not surprising in the light of the geochemical similarity of the two gneissic units, and suggests that the lack of significant gradients in mineral chemistry across the S-1 transect are due to the initial lack of sufficient chemical potential gradients to drive the diffusive exchange of mobile components.

Some of the data presented here also supports syn-to-post-deformational mass transfer of Na, K and Si via an infiltrative mechanism. Significant discontinuities in bulk chemistry and modal

mineralogy occur at amphibolite-gneiss and gneiss-gneiss contacts. These features are associated with textural evidence for fluid-rock interaction along contacts such as the presence of foliation parallel quartz ribbons walled by monomineralic layers of plagioclase or K-feldspar. The results of mass balance and reaction progress calculations are also consistent with greater degrees of Fe, Na, K and Si exchange (and hydration of the clinopyroxene-albite rich precursor) at the contacts. Thus, mass transfer in the Ponaganset gneiss may have been accomplished by two temporally and spatially distinct mechanisms: a diffusive mechanism which enabled transport perpendicular to foliation on a centimeter scale, and an infiltrative mechanism which operated parallel to foliation during deformation, and resulted in significant variations in whole rock chemistry within spatially restricted domains. Fluid infiltration into the mafic layer during deformation also hydrated clinopyroxene (forming amphibole and biotite in the process), and released Na to the adjacent mylonites.

Closer inspection of the mineral chemical gradients depicted in Figures 1.14, 1.16, and 1.21 reveals that the gradients in plagioclase and amphibole compositions are strongly asymmetrical on either side of the amphibolite layer. This suggests that, through time, the transport of ions across each of the amphibolite-gneiss boundaries was not uniform. For example the albite content of plagioclase decreases smoothly outwards from both gneiss-amphibolite contacts (Figure 1.14). The gradient was caused presumably by the diffusive movement of Na^+ ions out of the amphibolite during the hydration reactoins described earlier. In the gray gneiss, the concentration profile is relatively steep. In the pink gneiss, plagioclase composition remains at the level observed in the amphibolite layer (An_9) over a 6 cm distance outward from the pink gneiss-amphibolite contact, until it rises to $\simeq An_{11.5}$ at the approximate locality of the clinopyroxene out boundary (Figure 1.14). The "s-shaped" composition profile could be interpreted as the result of combined advective and static diffusive transport of Na^+ ions away from the pink gneiss-amphibolite contact (Fletcher and Hoffman 1974), or as a local Ca anomaly produced by the destabilization of clinopyroxene.

Chemical profiles of amphibole compositions across the transect show similar trends. The plot of the magnitude of the tschermakite and $FeMg_{-1}$ exchange vectors versus distance (Figure 1.21) show a relatively steep slope from the gray gneiss to the gray gneiss-amphibolite contact, and a shallow gradient from the pink gneiss to the pink gneiss-amphibolite contact. The shape of both

profiles is consistent with the influx of Fe^{2+} ions into the amphibolite, as predicted by the mass balance calculations deduced from whole rock chemical analyses. The $FeMg_{-1}$ profile within the amphibolite, however, is a strong function of the kinetics of clinopyroxene breakdown as suggested by the spatial relationship of actinolitic amphibole rims to clinopyroxene microporphyroclasts and by the similarity of the $Mg/(Fe^{2+} + Mg)$ of the actinolite rims to the clinopyroxene.

The asymmetry of mineral chemical gradients across the 419 transect could be the result of several factors. Such patterns could arise as an effect of the different mechanical behavior of the gneisses during deformation, which is readily apparent from the degree of grain size reduction in each unit as a function of proximity to the contact. Diffusive and transport rates are dependent on both grain size and path tortuosity, and both of these parameters would be altered as the result of deformation. Grain size, in particular, is not a smooth function of proximity to the gneiss-amphibole contact in the pink gneiss, but is much more so in the gray gneiss. The relative steepness of the chemical potential gradients between the amphibolite and each gneissic unit must also be taken into consideration.

Conclusions

1) Deformation and grain size reduction in the Ponaganset gneiss was accompanied by considerable exchange of Na, K, Si, Fe, and Mg between adjacent lithologies. Mass transfer was facilitated by the presence of an aqueous fluid phase present, perhaps, as a grain-boundary film. Deformation was accompanied by the hydration of clinopyroxene-albite rich mafic bands located between the gneissic units. These reactions released Na into the surrounding gneisses, and consumed Fe, Mg, H_2O. Trends in K and Ca abundance are variable, and are related to distance from the gray gneiss-amphibolite contact and pink gneiss-amphibolite contact. Interestingly, Fe and Mg

are depleted from the mylonites adjacent to the mafic layer. Evidence for external buffering of components (other than H_2O) is tenuous, but open system behavior cannot be ruled out entirely.

2) Mineral chemistry, particularly amphibole and plagioclase composition, varies systematically as a function of proximity to the mafic layer. The mineral chemical gradients on either side of the amphibolite are approximately bell-shaped, but are asymmetrical. The effect of grain size reduction on mineral composition is minimal, as evidenced by the lack of systematic gradients across the S-1 transect. However, grain size reduction may have played a role in the disappearance of biotite from the mylonites and gneisses adjacent to the mafic layer. Asymmetry of mineral chemical variations across the gray gneiss-amphibolite contact and the pink gneiss-amphibolite contact may be also due to contrasts in the mechanical behavior of the distinct gneissic units.

3) Geothermometry, using O-isotope fractionation (D. Stakes, pers. comm.) and amphibole-plagioclase equilibria (Blundy and Holland 1990), indicates that peak metamorphic temperatures were in the 600°C to 650°C range. Ternary plagioclase thermometry (Green and Usdansky 1986; Fuhrman and Lindsley 1988) records significantly lower temperatures (420-470°C), which may reflect re-equilibration during cooling, late-stage alkali exchange, or peristerite exsolution.

Across the 419 transect, amphibole-plagioclase geothermometry yields results which vary systematically from the less-deformed gneisses to the amphibolite layer. The lowest temperatures (500-650°C) were obtained from the amphibolite layer, and the highest (775-750°C) were obtained from the gneiss samples farthest from the gneiss-amphibolite contact. If these temperatures are not the result of bulk compositional contrasts, plagioclase exsolution across the peristerite gap, or disequilibrium between pairs of adjacent mineral grains, the negative temperature trend indicates that plagioclase-amphibole pairs within restricted portions of the amphibolite continued to re-equilibrate along a cooling path to temperatures as low as 500°C. The lowest temperature estimates are given by actinolitic amphibole rims within the amphibolite $<$ 1 cm from the gray gneiss-amphibolite contact.

4) Reaction progress calculations predict relatively low minimum volumetric fluid/rock ratios ($\simeq$0.03 l/liter of rock) were necessary for the hydration of the clinopyroxene-albite-rich assemblage

to form a hornblende-albite-rich amphibolite. Partial preservation of clinopyroxene-rich rocks suggests that the hydration reactions did not proceed to completion, possibly due to millimeter-to-centimeter-scale variations in fluid-rock ratio. Total calculated metamorphic reactions suggest that significant exchange of K and Na occurred between the outermost 2 cm of the amphibolite and the adjacent, gray gneiss-derived mylonite. The presence of a significant gradient in the K content in the amphibolite may be explained by alkali exchange between the rock and the metamorphic fluid.

References

Albee, A.L. and Ray, L. (1970) Correction factors for electron-probe microanalysis of silicates, oxides, carbonates, phosphates and sulphates. Analytical Chem., 42, 1408-1414.

Allison, I. and LaTour, T.E. (1977) Brittle deformation of hornblende in a mylonite: a direct geometrical analogue of ductile deformation by translation gliding., Can. J. Earth Sci., 14, 1953-1958.

Beach, A. (1973) The mineralogy of high temperature shear zones at Scourie, N.W. Scotland., J. Petrol., 14, 231-248.

Bell, T.H. and Johnson, S.E. (1989) The role of deformation partitioning in the deformation and recrystallization of plagioclase and K-feldspar in the Woodroffe Thrust mylonite zone, central Australia. J. Metamorphic Geol., v. 7, p. 151-168.

Bence, A.E. and A.L. Albee, (1968) Empirical correction factors for the electron microanalysis of silicates and oxides. J. Geol., 76, 382-403, 1968.

Bickle, M.J. and Baker, J. (1990) Advective-diffusive transport of isotopic fronts: an example from Naxos, Greece., Earth Planet. Sci. Lett., 97, 78-93.

Blundy, J.D. and T.J.B. Holland (1990) Calcic amphibole equilibria and a new amphibole-plagioclase geothermometer. Contrib. Mineral. Petrol., 104, 208-224.

Boullier, A.M. and Bouchez, J-L. (1978) Le quartz en rubans dans les mylonites., Bull. Soc. Geol. France, 7, 253-262.

Brodie, K.H. (1981) Variation in amphibole and plagioclase composition with deformation. Tectonophys., v. 78, p. 389-402.

Brodie, K.H. and Rutter, E.H. (1985) On the relationship between deformation and metamorphism, with special reference to the behavior of basic rocks. *In* Thompson, A.B. and Rubie, D.C. (eds.), Metamorphic Reactions: Kinetics, Textures and Deformation, Springer-Verlag Press, p. 138-179.

Burnham, C.W., J.R. Holloway and N.F. Davis (1969) Thermodynamic properties of water to 1,000°C and 10,000 bars. Geol. Soc. Am. Special Paper 132., 96 p.

Byerly, G.R. and T.A. Vogel (1973) Grain boundary processes and development of metamorphic plagioclase. Lithos., 6, 183-202.

Carmichael, D.M. (1969) On the mechanism of prograde metamorphic reactions in quartz-bearing pelitic rocks. Contrib. Mineral. Petrol., 20, 244-267.

Cumbest, R.J., M.R. Drury, H.L.M. van Roermund and C. Simpson (1989) Dynamic recrystallization and chemical evolution of clinoamphibole from Senja, Norway. Contrib. Mineral. Petrol., 101, 339-349.

Dallmeyer, R.D. (1982) $^{39}Ar/^{40}Ar$ ages from the Narragansett Basin and southern Rhode Island basement terrane: Their bearing on the extent and timing of Alleghanian tectonothermal events in New England. Geol. Soc. Am. Bull., 93, 1118-1130.

Dallmeyer, R.D., Hermes, O.D. and Gil-Ibarguchi, J.I. (1990) $^{39}Ar/^{40}Ar$ mineral ages from the Scituate Granite, Rhode Island: implications for late Paleozoic tectonothermal activity in New England. Jour. Metamorphic Geol., 8, 145-157.

Drury, M.R. and H.L.M. van Roermund (1989) Fluid assisted recrystallization in upper mantle peridotite xenoliths from kimberlites., J. Petrol. 30, 133-152.

Etheridge, M.A. and Cooper, J.A. (1981) Rb-Sr isotopic and geochemical evolution of a recrystallized (mylonite) zone at Broken Hill. Contrib. Min. Pet., v. 78, p. 74-84.

Etheridge, M.A., Wall, V.J. and Cox, S.F. (1984) High fluid pressures during regional metamorphism and deformation: implications for mass transport and deformation mechanisms. Jour. Geophys. Res., 89, 4344-4358.

Etheridge, M.A., Wall, V.J. and Vernon, R.H. (1983) The role of fluid phase during regional metamorphism and deformation. Jour. Meta. Geol., v. 1, p. 205-226.

Ferry, J.M. (1983) Applications of the reaction progress variable to metamorphic petrology. J. Petrol. 24, p. 343-376.

Ferry, J.M. (1984) A biotite isograd in south-central Maine, U.S.A.: mineral reactions, fluid transfer and heat transfer. J. Petrol., 25, 871-893.

Ferry, J.M. (1986) Reaction progress: a monitor of fluid-rock interaction during metamorphic and hydrothermal events. *In* Walther, J.V. and Wood, B.J. (eds.) Fluid-rock interactions during metamorphism, Springer-Verlag Publishers, New York, p. 60-88.

Ferry, J.M., L.J. Mutti and G.J. Zuccala (1987) Contact metamorphism/hydrothermal alteration of Tertiary basalts from the Isle of Skye, northwest Scotland., Contrib. Mineral. Petrol., 95, 166-181.

Fisher, G.W. (1970) The application of ionic equilibria to metamorphic differentiation: An example., Contrib. Mineral. Petrol., 29, 91-103.

Fisher, G.W. (1977) Nonequilibrium thermodynamics in metamorphism *In* Fraser, D.G. (ed.) Thermodynamics in geology, Proceedings of the NATO Advanced Study Institute, Oxford. D. Reidel Publishers, Boston, p. 381-402.

Fisher, G.W. (1989) Matrix analysis of metamorphic mineral assemblages and reactions., Contrib. Mineral. Petrol., 102, 69-77.

Fletcher, R.C. and A.W. Hoffman (1974) Simple models of diffusion and combined diffusion-infiltration metasomatism. *In* Hoffman, A.W., B.J. Giletti, H.S. Yoder, Jr. and R.A. Yund, (eds.) Geochemical transport and kinetics, Carnegie Institute of Washington, Publication 634, Washington, D.C., p. 243-259.

Fuhrman, M.L. and Lindsley, D.H.(1988) Ternary-feldspar modeling and thermometry. Am. Min., v. 73, p. 201-215.

Getty, S.R. and Gromet, L.P. (1988) Alleghanian polyphase deformation of the Hope Valley Shear Zone, southeastern New England. Tectonics, 7, 1325-1338.

Getty, S.R. and Gromet, L.P. (1989) Late Paleozoic extension and doming of the basement-cover contact at the Willimantic Dome, eastern Connecticut. *In* Geol. Soc. Am. Abst. with Prog., v. 21, p. A69.

Ghent, E.D. (1988) Tremolite and H_2O activity attending metamorphism of hornblende-plagioclase-garnet assemblages. Contrib. Mineral. Petrol., 98, 163-168.

Gilotti, J. A. (1989) Reaction progress during mylonitization of basaltic dikes along the Sarv thrust, Swedish Caledonides., Contrib. Mineral. Petrol., 101, 30-45.

Grant, J.A. (1986) The isocon diagram--a simple solution to Grensens' Equation for metasomatic alteration. Econ. Geol., v. 81, p. 1976-1982.

Green, N.L., Usdansky, S.I. (1986) Ternary feldspar relations and thermo-barometry. Am. Min., v. 71, p. 1100-1108.

Grew, E.S. and H. W. Day (1972) Staurolite, kyanite and sillimanite from the Narragansett Basin of Rhode Island. U.S. Geological Society Professional Paper 800-D., 151-157.

Gromet, L.P. (1989) Avalonian terranes and late Paleozoic tectonism in southeastern New England; Constraints and problems. Geol. Soc. Am., Special Paper 230, 193-211.

Gromet, L.P. and Getty, S.R. (1989) Direct dating of deformational fabrics in high-grade rocks using a microstructural-geochronological approach. Geol. Soc. Am. Abst. with Prog., v. 21, p. A227.

Gromet, L.P. and O'Hara, K.D. (1985) The Hope Valley Shear Zone -- a major late Paleozoic ductile shear zone in southeastern New England. *In* Guidebook for fieldtrips in Connecticut and adjacent areas of New York and Rhode Island, NEIGC 77th Annual Meeting, State Geol. Nat. Hist. Survey of Conn. Guidebook 6, p. 277-295.

Helgeson, H.C., J.M. Delany, H.W. Nesbitt and D.K. Bird (1978) Summary and critique of the thermodynamic properties of rock-forming minerals. Am. J. Sci., 278-A, 229 p.

Hermes, O.D. and Zartman, R.E. (1985) Late Proterozoic and Devonian plutonic terrane within the Avalon zone of Rhode Island. Geol. Soc. Am. Bull., 96, 272-282.

Holland, T.J.B. and S.W. Richardson (1979) Amphibole zonation in metabasites as a guide to the evolution of metamorphic conditions. Contrib. Mineral. Petrol., 70, 143-148.

Jan, M.Q. (1988) Geochemistry of amphibolites from the southern part of the Kohistan arc, N. Pakistan., Min.Mag., 52, 147-159.

Kerrich, R. (1986) Fluid infiltration into fault zones: Chemical, isotopic and mechanical effects. Pure Appl. Geoph., 124, 225-268.

Kerrich, R., Fyfe, W.S., Gorman, B.E. and Allison, I. (1977) Local modification of rock chemistry by deformation, Contrib. Min. Pet., v. 65, p. 183-190.

Kerrich, R., T.E. LaTour and L. Willmore (1984) Fluid participation in deep fault zones: evidence from geological, geochemical and $^{18}O/^{16}O$ relations, J. Geophys. Res., 89-B6, 4331-4343.

Kneller, B.C. and A.G. Leslie (1984) Amphibolite facies metamorphism in shear zones in the Buchan area of NE Scotland. J. Meta. Geol., 2, p. 83-94.

Knipe, R.J. and Wintsch, R.P. (1985) Heterogenous deformation, foliation development and metamorphic processes in a polyphase mylonite. *In* Thompson, A.B. and Rubie, D.C. (eds.), Metamorphic Reactions: Kinetics, Textures and Deformation, Springer-Verlag Press, p. 180-210.

LaTour, T.E. and R. Kerrich (1982) Microstructures, mineral chemistry and oxygen isotopes of two adjacent mylonite zones: a comparative study. *In* Goodman, R.E. and F.E. Heuze (eds.), Issues in rock mechanics. Proceedings, Twenty-third symposium on rock mechanics, University of California, Berkeley, California. Society of Mining Engineers of the A.I.M.E., Inc., New York., p. 389-396

Laird, J. (1980) Phase equilibria in mafic schist from Vermont. J. Petrol., v. 21, p. 1-37.

LaTour, T.E. (1981) Metamorphism and geothermometry near Coniston, Ontario: a clue to the tectonic evolution of the Grenville Front. Can. J. Earth Sci., 18, 884-898.

Leake, B.E. (1978) Nomenclature of amphiboles. Am. Mineral., 63, 1025-1052.

Liou, J.G. (1973) Synthesis and stability relations of epidote., J. Petrol., v. 14, p. 381-413.

McCaig, A.M. (1984) Fluid-rock interaction in some shear zones from the Pyrenees. Jour. Meta. Geol., v. 2, p. 129-141.

McCaig, A.M. and R.J. Knipe (1990) Mass-transfer mechanisms in deforming rocks: recognition using microstructural and microchemical criteria. Geology, in press.

Murray, D.P. (1988) Post-Acadian metamorphism in the Appalachians *In* Harris, A.L and Fettes, D.J. (eds.), The Caledonian-Appalachian Orogen, Geological Society Special Publication No. 38., Blackwell Scientific Publications, Oxford, U.K., p. 597-609.

Murray, D.P., J.D. Raben, P.C. Lyons, and H.B. Chase, Jr. (1981) The geologic setting of coal and carbonaceous material, Narragansett Basin, southeastern New England. *In* Boothroyd, J.C. and O.D. Hermes (eds.), Guidebook for Field Trips in Rhode Island and Adjacent Areas, New England Intercollegiate Geological Conference, 73rd Annual Meeting, University of Rhode Island, Kingston, R.I., p. 175-195.

Nordstrom, D.K. and J.L. Munoz (1986) Geochemical thermodynamics., Blackwll Scientific Publications, Palo Alto., 477 p.

Norrish, K. and Chappell, B.W. (1977) X-ray fluorescence spectroscopy. *In* Zussman, J. (ed.), Physical Methods in Determinative Mineralogy., John Wiley and Sons, New York., p. 201-207.

O'Hara, K. and Gromet, L.P. (1983) Textural and Rb-Sr isotopic evidence for late Paleozoic mylonitization within the Honey Hill fault zone, southeastern Connecticut. Amer. Jour. Sci., 283, 762-779.

O'Hara, K. and Gromet, L.P. (1985) Two distinct late Precambrian (Avalonian) terranes in southeastern New England and their Paleozoic juxtaposition. Amer. Jour. Sci., v. 285, p. 673-709.

Philippot, P. and J.-R. Kienast (1989) Chemical-microstructural changes in eclogite-facies shear zones (Monviso, Western Alps, north Italy) as indicators of strain history and the mechanism and scale of mass transfer. Lithos, 23, 179-200.

Robie, R.S., B.S. Hemingway and J.R. Fisher (1978) Thermodynamic properties of minerals and related substances at 298.15 K and 1 bar (10^5 pascals) pressure and higher temperatures. U.S. Geol. Survey Bull. 1452, 456 p.

Rucklidge, J.C. (1971) Specifications of the Fortran program SUPERRECAL. Department of Geology, University of Toronto.

Simpson, C. and Wintsch, R.P. (1989) Evidence for deformation-induced K-feldspar replacement by myrmekite, J. Meta. Geol., v. 7, p. 261-275.

Sinha, A.K., Hewitt, D.A., Rimstidt, J.D. (1988) Metamorphic petrology and strontium isotope geochemistry associated with the development of mylonites: an example from the Brevard fault zone. Amer. Jour. Sci., v. 288A, p. 115-147.

Solberg, T.N. and J.A. Speer (1982) QALL, a 16-element analytical scheme for efficient petrologic work on an automated ARL-SEMQ: application to mica reference samples. *In* K.F.J. Heinrich (ed.), Microbeam Analysis - 1982., San Francisco Press, San Francisco., 422-426.

Spear, F.S. (1980) NaSi → CaAl exchange equilibrium between plagioclase and amphibole. Contrib. Min. Pet., v. 72, p. 33-41.

Spear, F.S. (1981) An experimental study of amphibole stability and compositional variation in amphibolite. Amer. J. Sci., v. 281, p. 697-734.

Spear, F.S. and C. Kimball (1984) RECAMP - a Fortran IV program for estimating Fe^{3+} contents in amphiboles. Comp. Geosci., 10, 317-325.

Speer, J.A., A. Naeem and A.A. Almohandis (1989) Small-scale variations and subtle zoning in granitoid plutons; the Liberty Hill pluton, South Carolina, U.S.A., Chem. Geol., 75, 153-181.

Thomas, W.M. (1982) Stability relations of the amphibole hastingsite. Am. Jour. Sci., 282, 136-164.

Thompson, A.B. (1975) Calc-silicate diffusion zones between marble and pelitic schist. J. Petrol. 16, 314-346.

Thompson, J.B., J. Laird, and A.B. Thompson (1982) Reactions in amphibolite, greenschist and blueschist., J. Petrol. 23, 1-27.

Tracy, R.J., D.M. Rye, D.A. Hewitt and C.M. Schiffries (1983) Petrologic and stable-isotopic studies of fluid-rock interactions, south-central Connecticut: I. The role of infiltration in producing reaction assemblages in impure marbles., Am. J. Sci., 283-A, 589-616.

Walther, J.V. and Wood, B.J. (1984) Rate and mechanism in prograde metamorphism. Contrib. Min. Pet., v. 88, p. 246-259.

Watts, M.J., Williams, G.D. (1983) Strain geometry, microstructure and mineral chemistry in metagabbro shear zones: a study of softening mechanisms during progressive mylonitization. J. Struct. Geol, v. 5; p. 507-517.

Wayne, D.M. and A.K. Sinha (1988b) Mosaic equilibrium in ultramylonites: constraints on isotopic dating of shear zones. In: Abstracts with Programs, Geological Society of America 1988 Annual Meeting, Denver, CO., A331.

Wayne, D.M. and A.K. Sinha (1989a) Isotopic and mineralogic data from the Hope Valley Shear Zone (HVSZ) in south-central Massachusetts. In: Abstracts with Programs, Geological Society of America 1989 Annual Meeting, Northeast Section, New Brunswick, NJ.,74.

Wayne, D.M. and A.K. Sinha (1989b) Differential response of the zircon U-Pb system across a lithologic boundary: an example from southern New England. In: Abstracts with Programs, Geological Society of America 1989 Annual Meeting, St.Louis, MO.,A226.

Weaver, B.L, J. Tarney, B.F. Windley and B.E. Leake (1982) Geochemistry and petrogenesis of Archaean metavolcanic amphibolites from Fiskenaesset, S.W. Greenland., Geochim. Cosmochim. Acta., 46, 2203-2215.

Wintsch, R.P. (1973) Solid-fluid equilibria in the system $KAlSi_3O_8$- $NaAlSi_3O_8$- Al_2SiO_5-SiO_2-H_2O-HCL. J. Petrol. 16, p. 57-79.

Wintsch, R.P. (1975) Feldspathization as a result of deformation. Geol. Soc. Am. Bull., 86, 35-38.

Wintsch, R.P. and J. Dunning (1985) The effect of dislocation density on the aqueous solubility of quartz and some geologic implications: A theoretical approach. J. Geophys. Res., 90, 3649-3657.

Chapter 2: Physical and chemical response of zircons to deformation.

Abstract

An investigation of U-Pb isotopic systematics in zircons from mylonitized Henderson Gneiss (Sinha and Glover 1978) revealed that selected zircon fractions from the mylonite zone suffered total loss of radiogenic Pb at ~460 m.y. To further investigate the relationship between Pb loss, U gain, and grain size reduction associated with increasing strain in the shear zone, we have characterized the chemistry and morphology of zircons in the mylonitic rocks, using both electron microprobe analysis and scanning electron microscopy.

SEM photographs of the zircons indicate that strain-correlated fracturing and size reduction of the zircons accompanied Pb loss throughout the mylonite zone. Stresses imposed by the expansion of initially U-rich, α-damaged portions of the crystal resulted in microfracturing of the more brittle crystalline material proximal to the U-rich zones. During mylonitization, fractures propagated preferentially along these zones allowing metamorphic fluids to penetrate the easily-leached,

α-damaged portions of the zircons. Removal of ~75% of the radiogenic Pb from zircons in the least-deformed zone of the mylonites may have occurred via this mechanism.

Irregular, porous zircon overgrowths are also evident from the SEM photographs. Overgrowths are strongly enriched in U, Y and P with respect to the relict, Henderson Gneiss-derived cores, and tend to increase in volume from the protomylonite to the blastomylonite. Thus, the development of overgrowths on the zircons accounts for the U gain observed by Sinha and Glover (1978), and indicates that the transport of high field strength cations (e.g. Zr^{4+}, Hf^{4+}, U^{4+}, etc.) occurred during prograde mylonitization at 460 m.y.

A retrograde shearing event at ~273 m.y. caused no further disturbance in the U-Pb isotopic systematics of the zircons. Pb retention by zircons during the later episode may have been the result of 1) the participation of H_2O-rich, relatively noncorrosive fluids and/or 2) the lack of further fracturing and size reduction in a strain gradient of lower magnitude than the prograde event.

Introduction

Discordant U-Pb ages arise when zircons (or other U-Th bearing phases) lose or gain U, Th, Pb, or intermediate daughter products by processes other than radioactive decay. Several models have been developed in order to explain isotopic discordance in light of the attendant geologic phenomena. These models include: loss of radiogenic Pb during a relatively short episode of open system behavior of the U-Pb system after crystallization (Wetherill 1956a, b), continuous (Tilton 1960) or time-dependent (Wasserburg 1963) diffusion of radiogenic Pb out of zircons into the surrounding media, combined diffusional and episodic loss (Wetherill 1963), multiepisodic loss (Allegre et al. 1974), and intracrystalline mixing of multiple U-Pb signatures as the result of primary heterogeneities in the distribution of U and Th (Steiger and Wasserburg 1966).

Geochronological studies of metamorphic rocks of a variety of bulk compositions and reigonal settings show that the magnitude of Pb loss (or U gain), attributable to a given metamorphic episode of known intensity, is extremely variable. Isotopic discordance has been observed in zircons from high temperature contact aureoles (Hart et al. 1968), high-grade regional metamorphic rocks (Grauert 1974; Schenk 1980; Gebauer et al. 1981; Gulson and Krogh 1975), migmatites (Peucat et al. 1985) and regionally metamorphosed chlorite-to-almandine grade metasediments (Gebauer and Grunenfelder 1976). Discordance in contact aureoles and high-grade metamorphic rocks is often accompanied by the growth of a new population of zircon crystals at the time of metamorphism. The "new" zircons occur either as discrete grains with characteristically complex morphologies or as overgrowths on pre-existing zircon grains. The growth of zircon necessitates considerable movement of zirconium and other high field strength cations during metamorphism. By contrast, Gebauer and Grunenfelder (1976) attributed the nearly total (90%) U-Pb discordance of zircons from low to medium grade metasediments to the annealing of completely metamict zircons in a relatively low temperature (~400°C), fluid rich, regional metamorphic setting. Unlike contact zones and areas of regional metamorphism, few studies have focused directly on U-Pb systematics in shear zones and associated mylonites.

Geologic Setting

The Brevard fault zone in North Carolina records a complex polytectonic polymetamorphic history (Hadley and Nelson 1971; Roper and Dunn 1973; Hatcher 1971; Bryant and Reed 1970; Sinha and Glover 1978). The first prograde metamorphic and mylonitic event reached the almandine-amphibolite facies and reset U-Pb ages of zircons to 460 m.y. (Sinha and Glover 1978). The second event consisted of a period of greenschist-grade mylonitization accompanied by the formation of a retrograde mineral assemblage, and has been dated by whole rock Rb-Sr method at 273 m.y. (Sinha et al. 1987).

The zircon samples discussed in this paper were obtained from variably mylonitized Henderson Augen Gneiss at Rosman, NC (see Sinha and Glover 1978 and Sinha et al. 1986 for details of areal geology).

U-Pb Systematics of Zircons in Shear Zones

Isotopic discordance directly attributable to the physicochemical effects of mylonitization was documented by Sinha and Glover (1978), who analyzed zircons from the unsheared Henderson Gneiss and from adjacent Brevard Zone mylonites. Zircons from the Henderson Gneiss yielded an upper intercept age of ~590 m.y. for the crystallization of the granitic protolith. The initial almandine-amphibolite grade metamorphic event, M_{1a} of Roper and Dunn (1973), produced

mylonite zones and a prograde assemblage which contained almandine garnets and, locally, staurolite and either sillimanite or kyanite (Roper and Dunn 1973). During this event the U-Pb system of zircons in the mylonite was severely affected, resulting in total Pb loss from zircons in the high-strain zones. $^{207}Pb/^{206}Pb$ ages of zircons in the blastomylonite and ultramylonite show little variation (452-462 m.y.). Chemical and morphological data from the Brevard mylonite zircons suggest that strain-correlated size reduction, Pb loss and U-gain occurred during this episode of deformation. A later retrograde shearing event (~273 m.y.) had no observable effect on the U-Pb age, $^{207}Pb/^{206}Pb$ age, or chemistry of zircons in the sheared rocks.

Lancelot et al. (1983) conducted an isotopic study of zircons from a shear zone at the margin of the Iforas granulite (Mali). By contrast to the initial Brevard zone deformation, the late Pan-African shearing event occurred at greenschist facies (~300-400°C, Boullier 1980). Zircons from the mylonite were fractured, corroded and reduced in size, but remained a closed system with regard to U-Pb isotopic signature. The substantially younger apparent upper intercept age of the zircons from the mylonite was attributed, by Lancelot et al. (1983), to the mixing of two isotopically distinct populations of zircons: one from the granulite itself, which retained a 3.1 to 3.3 b.y. old inherited Pb component and another from pegmatoid leucosomes within the granulite which were presumed to have formed during the metamorphic event.

Bickford et al. (1981) and Chase et al. (1983) were able to constrain the timing of a major shearing event in a mylonite within the Bitterroot Dome, Northeastern Idaho Batholith, using U-Pb systematics of concordant zircons. The data collected from sheared quartz monzonites, granodiorites and pegmatites indicated that the mylonitization had no effect on zircon U-Pb or $^{207}Pb/^{206}Pb$ ages. Although no data were collected on the unsheared equivalents of these rocks, petrographic relationships and U-Pb data from monazite from the mylonite support the apparent lack of isotopic discordance in zircons from the sheared rocks.

The studies of Lancelot et al. (1983) and Chase et al. (1983) should not, however, be taken as evidence that U-Pb discordance cannot be generated during mylonitization. Unlike the shear zones investigated by those authors, the development of the Brevard shear zone is characterized by the formation of a prograde mineral assemblage, followed by later greenschist-grade deformation

which had no observable effect on the U-Pb systematics of zircons. Furthermore, Sinha and Glover (1978) observed a three-fold increase in the uranium content of zircons from the Brevard mylonites compared to zircons from the unsheared Henderson Gneiss. Therefore, the response of zircons in the Brevard zone, both isotopically and chemically, must be related to variations in strain (grain size reduction), pressure, temperature and the presence of metamorphic fluids.

Other instances of new zircon growth (or resetting) associated with mylonitization and grain size reduction are not unknown. Peterman et al. (1980) report that U/Pb ages of zircons from a "highly cataclasized" Archean tonalitic gneiss, located at Watersmeet in the western portion of the northern peninsula of Michigan, are nearly concordant at 1755 m.y. and agree with the metamorphic Rb-Sr whole rock and single-mineral isochrons from the same locality.

In this paper, we present data to provide a better understanding of the relationship between U-Pb discordance and the U-gain, fracturing and size reduction of zircons during amphibolite-grade mylonitization in a fluid rich environment. The zircons selected for this study are splits of the samples analyzed by Sinha and Glover (1978). For convenience, the sample numbers used by Sinha and Glover (1978) have been retained in this study. Hgn denotes relatively undeformed Henderson Gneiss, B8A denotes protomylonite, B8B denotes blastomylonite and B8C denotes ultramylonite. The + and - symbols preceding each sample number refer to zircons greater than 200 mesh size (+) and zircons less than 200 mesh size (-).

Analytical Procedures

Individual zircons from each mylonite fabric type were analyzed using an automated ARL-SEMQ 9-channel microprobe at the Department of Geological Sciences, VPI&SU. Operating conditions during all analyses were: 15 kV accelerating voltage, 50 nA sample current (measured in synthetic $ZrSiO_4$) and a 1 micron beam diameter (point mode). The cathodoluminescence of

zircon facilitated beam focusing. X-ray lines of the analyzed elements, peak and background standards, counting times and detection limits for each element are listed in Table 2.1. Besides Zr, Si and Hf, the only elements detected at, or above, their detection limits were trace amounts of Y, U, P, Ca and Fe. Th was not included in the analytical scheme.

The large number of elements in the analytical scheme (16) and the desire for high precision analyses of trace elements in a single phase made it convenient for us to use "on peak" background measurements on chemically pure synthetic standards. All raw data were corrected using the empirical method of Bence and Albee (1969).

The synthetic zircon standard was analyzed repeatedly during the five-day data gathering period, primarily to monitor instrumental drift (which was computer corrected), and as a check on the accuracy and reproducability of the results yielded by our analytical techniques. Levels of all minor and trace elements in the zircon standard (measured before and after a group of traverses across mylonite zircons) are at or below the detection limits compiled in Table 2.1. The total variation of the zircon standard analyses over a three-day period is approximately 0.04 wt. % for HfO_2 and between 0.008 and 0.013 wt. % for the remaining minor and trace element oxides (Wayne et al. 1987). Calculated errors (2σ) due to counting statistics for the minor and trace elements in selected mylonite zircons range from ~0.04 wt % (HfO_2) to ~0.01 wt. % (Y_2O_3, UO_2, P_2O_5).

Single crystal (rim-core-rim) traverses consist of 5 to 17 analysis points (depending on grain size) directed parallel or perpendicular to [001] or [100] (depending on grain orientation). In a few cases (B8A + 200), traverses were broken into parallel segments due to intense fracturing of the zircon crystal. Great care was taken to avoid inclusions. All reported analyses are representative of stoichiometric (Zr, Hf) SiO_4; thus there is little evidence for the existence of intergrown or exsolved phases at the micron scale. Further details on the analytical procedures used in this study can be found in Wayne et al. (1987).

Table 2.1. X-ray lines, standards, counting times and detection limits for zircon microprobe analyses.

Element	X-ray Line	Peak Std.	Back. Std.	Counting Time (sec.)	Detection Limit (wt % oxide)
Zr	L_α	$ZrSiO_4$	YAG	200	—
Si*	Kα	$ZrSiO_4$	YAG	1000	—
Ce	L_α	CeO_2	$ZrSiO_4$	200	0.024
La	L_α	$LaVO_4$	$ZrSiO_4$	200	0.024
Mn	Kα	MnO_2	$ZrSiO_4$	200	0.008
Yb	L_α	$YbVO_4$	$ZrSiO_4$	200	0.064
Hf	M_α	$HfSiO_4$	$ZrSiO_4$	200	0.046
P	K	Durango Apatite	$ZrSiO_4$	200	0.022
Ca*	K_α	Durango Apatite	$ZrSiO_4$	1000	0.006
F	K_α	Durango Apatite	$ZrSiO_4$	1000	0.022
Y	L_α	YAG	$ZrSiO_4$	200	0.024
Al*	K_α	YAG	$ZrSiO_4$	1000	0.010
U	M_α	UO_2	$ZrSiO_4$	400	0.016
Fe*	K_α	Kakanui Hornblende	$ZrSiO_4$	1000	0.008
K*	K_α	Kakanui Hornblende	$ZrSiO_4$	1000	0.006
Mg*	K_α	Kakanui Hornblende	$ZrSiO_4$	1000	0.014

Physical Characterization

The strong correlation of U-Pb and Pb-Pb ages with increasing strain throughout the mylonitized Henderson Gneiss (Sinha and Glover 1978) may be due to several different physicochemical processes that occur in a fluid rich, high strain environment. Scanning electron microscopy (SEM) was used to qualitatively evaluate the degree of fracturing, overgrowth formation and recrystallization incurred by zircons during mylonitization. The use of the SEM permits the observation of surface features due to dissolution-precipitation phenomena, fracturing and size reduction. We have also examined the relationship between radiation damage and relative Pb loss by using the hydrofluoric acid leaching technique described by Krogh and Davis (1975). Prior to examination by SEM, polished sections of zircons were exposed to the vapor over 48% HF for 40 seconds. The difference in the extent of HF attack is attributable to differences in the intensity of radiation damage incurred by various portions of a structurally zoned zircon crystal. Leached zones correspond to areas of concentrated radiation damage and isotopic discordance within the zircon. Regions of the zircon that are resistant to HF attack are characterized by low levels of radiation damage and, most importantly, a relatively unperturbed U-Pb isotopic system (Krogh and Davis 1975).

Fracturing

Sinha and Glover (1978) optically examined zircons separated from the mylonitized Henderson Gneiss and observed a progressive decrease in both grain size and length-width ratio of the zircons with increasing strain. Zircons from the Henderson Gneiss are prismatic (L:W$\sim$3), euhedral and relatively free of inclusions. With increasing strain, length-width ratio decreases steadily, reaching a minimum of $\sim$1.85 in the ultramylonite. The average grainsize of + 200 and -200 zircons measured by Sinha and Glover (1978) decreases steadily, with increasing strain, from

the relatively unstrained Henderson Gneiss into the blastomylonite, but increases somewhat in the ultramylonite. Thus, fracturing and disaggregation of zircons were the dominant proceses in the protomylonite and blastomylonite zones. The size increase observed in ultramylonite may be due to the accelerated growth of a new zircon population in a fluid-rich environment. Boullier (1980) also observed strain-correlated size reduction of zircons in a shear zone, without a concomitant reduction of length-width ratio or any apparent growth of new zircon.

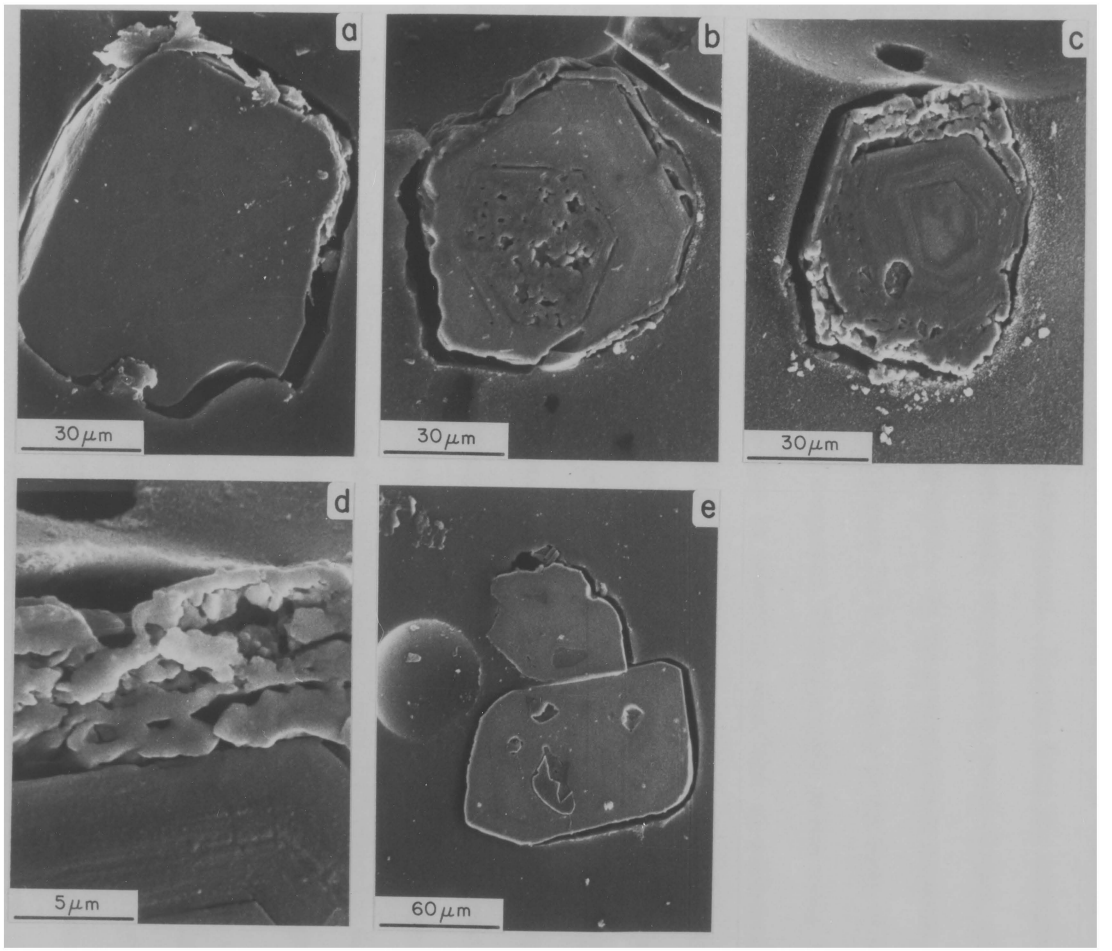
Prismatic zircons from the relatively unsheared Henderson Gneiss are rarely fractured, as shown by scanning electron micrographs of individual grains (Figures 2.1a, 2.2a). Fracturing is more common in zircons from protomylonite (B8A) and blastomylonite (B8B) (Figure 2.1, b and c) These cracks, like those observed by Boullier (1980), are not crystallographically controlled and propagate along planes oblique to (001) (Figure 2.1b). HF-etched cross sections of fractured zircons reveal that the cracks are through-going, and tend to run parallel to internal structural zonations (Figure 2.1c). If the preferentially leached areas of the zircon in Figure 2.1c have incurred a relatively high α-dosage, as suggested by Krogh and Davis (1975), the lattice expansion associated with radiation damage (e.g. Holland and Gottfried 1955; Chakoumakos et al. 1987) of restricted portions of the crystal may have led to the accumulation of internal stresses proximal to the metamict areas. Subsequent fracturing of the zircons would then be concentrated in the stressed areas. Fractures that propagated along the relatively crystalline portions of individual zircons could have served as conduits for fluids present during mylonitization. Conceivably, the rate of Pb-loss would be enhanced where fluids were allowed access to the metamict portions of the zircon via through-going cracks.

By contrast, zircons from the ultramylonite (B8C) tend to have fewer throughgoing cracks (Figure 2.1f). Fractures incurred by these zircons early in their deformation history either resulted in disaggregation and size reduction (e.g. Boullier 1980) prior to annealing, or were partially healed. Healing of fractures may have taken place during the development of overgrowths, as "new" zircon coated fracture surfaces and grain perimeters.

Figure 2.1. **Scanning electron micrographs of zircons from the Henderson gneiss and mylonites (B8A, B8B, B8C):** (a) - Rounded, euhedral zircons from relatively undeformed Henderson gneiss (HGN + 200). (b) - Zircons from the protomylonite (B8A-200) with solution pits and transverse fractures inclined approximately 45° to [001]. (c) - Polished, HF-etched cross section of a protomylonite zircon (B8A-200). Note the parallelism of fractures within the leached, radiation-damaged central portion of the crystal. (d) - Zircon from protomylonite (B8A + 200) with rough, pitted surface texture. (e) - Completely overgrown zircon from the blastomylonite (B8B-200). (f) - Relatively euhedral, low fracture-density zircons from ultramylonite (B8C-200).

a
60 μm
b
60 μm
c
30 μm
d
60 μm
e
30 μm
f
60 μm

Figure 2.2. Scanning electron micrographs of polished, HF-etched zircon cross-sections: (a) - Unfractured zircon from the relatively undeformed Henderson Gneiss (HGN + 200). (b) - Zircon from the blastomylonite (B8B-200). Note the thin continuous overgrowth (<5 μm) and the radiation-damaged inner zone. (c) - Zircon from the blastomylonite (B8B-200) showing a thick (~10 μm maximum) preferentially etched, continuous overgrowth and a relict, zoned core. The overgrowth appears to be considerably thicker on the pyramid faces. (d) - Close up of 2c, showing the sharp core-overgrowth interface. (e) - Zircon from the ultramylonite (B8C-200) with preferentially etched inclusions.


a
30 μm
b
30 μm
c
30 μm
d
5 μm
e
60 μm

Surface features

The relatively small sample populations (50-125 crystals) preclude a rigorous, statistically-based morphological characterization of zircons from each mylonite zone. SEM images permit rough estimates of percentages of zircons from a given population that bear, or lack, particular surface features with reference to the strain enviroment. Zircons from the unmylonitized gneiss (Figure 2.1a) are smooth, euhedral and have easily recognizable morphologies, although a few (~10 to 15%) grains show some surface irregularities. In the protomylonite separate, ~75% of the zircons bear significant surface irregularities (Figure 2.1 b, d), usually in the form of irregular, unevenly distributed pits due, possibly, to fluid corrosion. Pitting is most severe along fracture traces and on fracture surfaces. Inclusions may also be selectively dissolved, as evidenced by negative crystal forms in the surface of several individual grains. However, surface pitting is never so severe that the crystal morphology is completely destroyed. A large percentage (~90%) of the zircons from the blastomylonite bear surface alterations, and a significant proportion of these (~35 - 40%) are so altered that only a vague suggestion of the original morphology is discernable. Such grains are characterized by an irregular, rough or spongy surface texture (Figure 2.1e). The remainder of the altered zircons from the blastomylonite bear pits similar to those observed on zircons from the protomylonite. The surface features on ultramylonite zircons (Figure 2.1f) resemble those observed in the blastomylonite separate, except that there are fewer (~10 - 20%) individual grains with the distinct porous, irregular surface texture.

HF leaching of polished cross sections revealed zones of relatively high radiation damage within zircons from the parent gneiss and within gneiss-derived cores of overgrown zircons from the protomylonite (B8A) and blastomylonite (B8B) (Figure 2.2 b, c). Metamorphic overgrowths are visible in the polished, HF-etched sections as relatively thin, irregular rims that are severely pitted by the action of HF vapor (Figure 2.2 b, c, d). Metamorphic overgrowths apparently correspond to the irregular or spongy surface textures observed in the SEM images of whole grains. Polished, etched cross sections revealed that the metamorphic overgrowths tend to increase in thickness at the terminations of individual crystals (Figure 2.2 c). Furthermore, the thickness of the zircon over-

growths consistently increased in samples from zones of successively higher strain. Metamorphic overgrowths on zircons from the -200 fraction of the protomylonite tend to be thin (<5 μm) and discontinuous, while overgrowths on zircons from the blastomylonite are thicker (up to 20 μm) and often envelop entire grains. Typically, the core-rim interface is sharp and flat (Figure 2.2 d), and the overgrowths are partially detached from the cores by the curing shrinkage of the epoxy mounting medium. HF leaching of zircons from the ultramylonite (B8C) (Figure 2.2e) revealed no radiation-damage related features attributable to zoning or overgrowth formation. A few individual grains showed little resistance to HF attack and were completely destroyed after 40 seconds of exposure. A greater percentage of the ultramylonite zircons contain numerous, relatively large (up to 15 μm) inclusions of sphene, apatite and biotite (identified using EDAX) which are preferentially dissolved by HF (Figure 2.2e).

We interpret the observed decrease in fracture density and the lack of relict features (e.g. zoning) in the ultramylonite zircons to be the result of structural annealing in a fluid-rich amphibolite facies environment. Experimental studies by Pidgeon et al. (1966, 1973) demonstrated that annealing of metamict Sri Lankan zircon fragments takes place in the presence of aqueous fluids at temperatures as low as 500°C. The rate and extent of annealing may be dependent on the pH and composition of the fluid (Pidgeon et al. 1973). Geochemical studies of the Henderson Gneiss mylonites (Sinha et al. 1986, 1987) show that conditions during the peak of the 460 m.y. mylonitization event were characterized by temperatures of 450-500°C and the presence of abundant fluids. If fluid flow was focused through the ultramylonite, as suggested by Sinha et al. (1986), extensive annealing of the partially radiation-damaged zircons therein may have occurred.

Microprobe Analyses

In order to develop a better understanding of the relationship between zircon chemistry and the observed U-Pb isotopic data, selected zircon crystals were analyzed for both major (Zr, Si) and trace (Hf, Y, U, P, Ca and Fe) elements. Although zircons are often chemically inhomogenous (e.g. Steiger and Wasserburg 1966; Sommerauer 1974, 1976)), the trace element abundance trends in single zircons from the mylonitized portion of the Henderson Gneiss appear to be correlated to increasing strain and subsequent radiogenic Pb loss. Microprobe traverses (rim-core-rim) of individual zircons from the protomylonite and blastomylonite revealed sharp chemical discontinuities which correspond to the interface of a Henderson Gneiss-derived core and a metamorphic overgrowth, presumably developed during the ~460 m.y. prograde mylonitization event. The statistical significance of the microprobe data for the minor and trace elements is consistently at, or below, ~0.04 wt.% oxide. Therefore, variations in trace element contents on the order of 0.1 wt. % are significant.

Crystal chemistry of zircon

In natural zircons, 8-coordinated Zr^{4+} may be replaced, by coupled substitution, by other large, high valence cations such as U^{4+}, Th^{4+}, Hf^{4+}, Y^{3+} and $HREE^{3+}$ (Mumpton and Roy 1961; Ramakrishnan et al. 1969; Watson 1979). Tetravalent cations may replace Zr^{4+} via isomorphous substitution [e.g. $(Hf, U, Th)^{4+} = Zr^{4+}$)]. Chemical data from natural zircons (Romans et al. 1974) indicate that trivalent substituents for Zr^{4+} may be charge-compensated to some extent by a coupled substitution involving P^{5+} and Si^{4+} in tetrahedrally coordinated sites. The coupled substitution $(Y, HREE)^{3+} + (P)^{5+} = Zr^{4+} + Si^{4+}$ predicts a parallelism in the trends of Y, HREE and P abundances in zircons. Although no rigorous experimental verification for the cou-

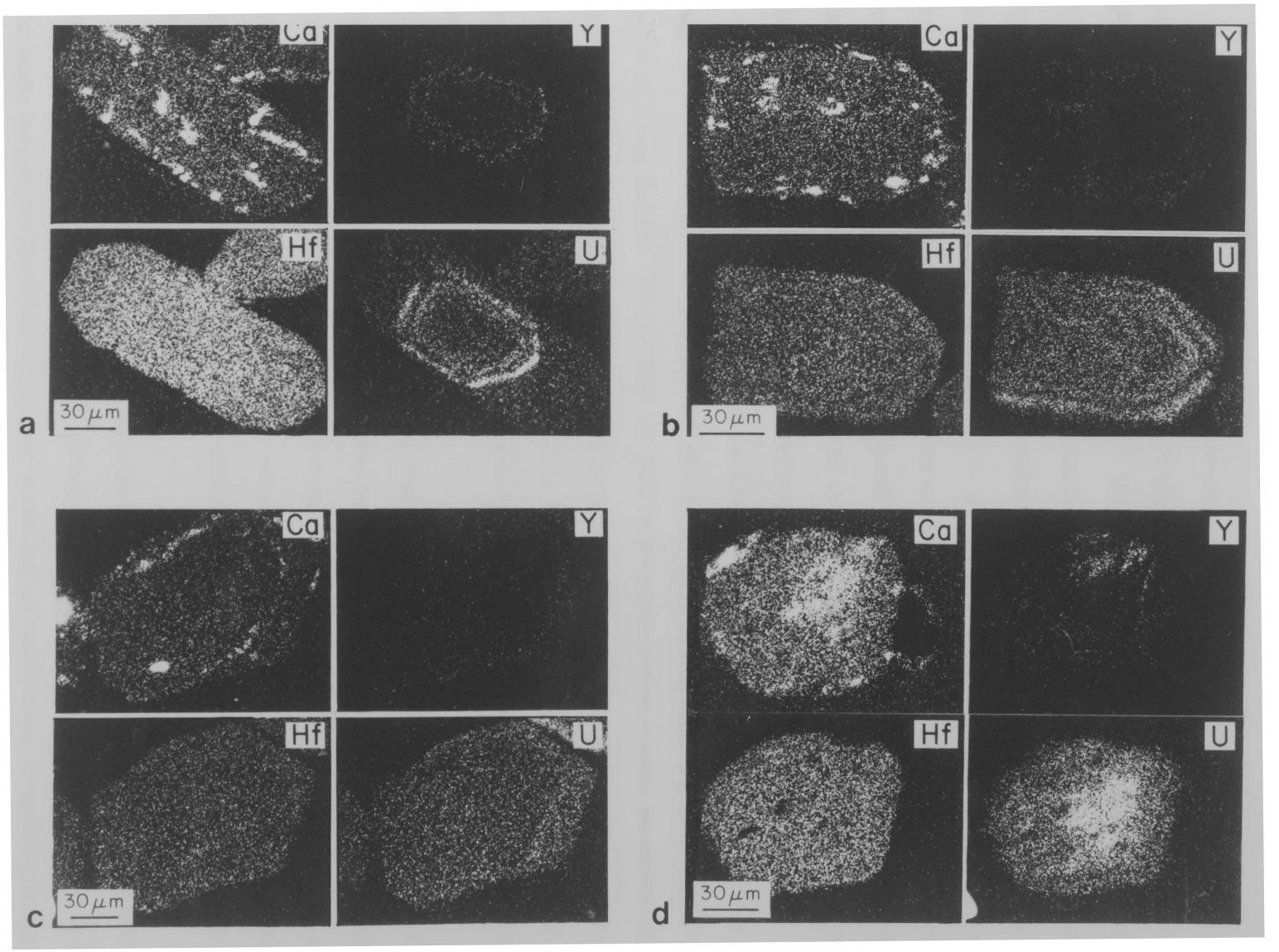
pled substitution exists, our data show that Y^{3+} and P^{5+} abundance trends correlate well in the zircons from the Henderson Gneiss.

Other reported substituents (Ca, Fe, Al, Ti, Sc, Nb, (OH), etc.) appear to be more significant in metamict pegmatitic zircons and, to a lesser degree, in the radiation-damaged portions of zircons from all rock types (e.g. Sommerauer 1974, 1976; Aines and Rossman 1986). The presence of these structurally incompatible elements in minor or trace amounts appears to be related to the large number of defect sites available within a radiation-damaged structure. Consequently, their role in zircon crystal chemistry *sensu stricto* is poorly defined.

Behavior of Ca and Fe

In most cases, the content of Ca, Fe and other elements in the zircons is at, or below, the detection limits of the electron microprobe. Enrichment in Ca or Fe corresponds to inclusions of apatite and sphene, as shown by x-ray emission maps (Figure 2.3). These inclusions are localized at grain boundaries and fracture surfaces in zircons from the relatively undeformed Henderson Gneiss (Figure 2.3a). Further nucleation and growth of apatite and sphene at the surface of zircon grains may have occurred during mylonitization, as many overgrown zircons contain concentrations of Ca-rich phases at the core-overgrowth interface (Figure 2.3 b, c). The x-ray emission map (Figure 2.3d) of Ca from a "cloudy" ultramylonite zircon, however, suggests that portions of the zircon itself may be enriched in crystallochemically "incompatible" elements. The Ca-enriched zones are highly irregular and sporadically distributed throughout the crystal. This pattern of enrichment suggests that the presence of Ca and Fe in the ultramylonite zircons is a secondary phenomenon related, perhaps, to high α-dosages.

Figure 2.3. **X-ray emission maps showing the distribution of selected minor elements (Hf, Ca, U, Y) within zircons:** (a) - Henderson Gneiss (HGN-200), (b) - protomylonite (B8A-200), (c) - blastomylonite (B8B-200), - (d) ultramylonite (B8C-200)


Ca
Y
Hf
U
30 μm
a
Ca
Y
Hf
U
30 μm
b
Ca
Y
Hf
U
30 μm
c
Ca
Y
Hf
U
30 μm
d

Behavior of U, Y and P

Observed trace element abundances of zircons from both size fractions (Hgn +200, -200) of the relatively undeformed Henderson Gneiss are typically at, or below, 0.2 wt % Y_2O_3 and close to the detection limits for U and P (Table 2.2). Extreme local variations in the abundance of U, P, and Y, shown by composition profiles (Figure 2.4 a), correspond to oscillatory zoning features and radionuclide-rich "hot spots". X-ray emission photographs of a zoned zircon (Figure 2.3a) show that enrichment of U and Y is restricted to two narrow, roughly parallel, zones within the crystal. The trace element-enriched zones do not coincide precisely, suggesting that U and Y may be enriched in different portions of the same crystal. The composition of zircon cores throughout the mylonite zone is broadly similar to that of the zircons from the parent gneiss, although net trace element abundances in zircon cores appear to increase with increasing strain.

Chemically distinct overgrowths were not identified from the +200 protomylonite fraction using the electron microprobe. Internal zones of high U, Y and P abundance (Figure 2.4 b) correspond to zoning features. Zircons from the B8A +200 protomylonite fraction are extensively fractured, and the traverses depicted in Figure 2.4 b do not represent straight lines. Instead, the traverses consist of several parallel segments, 50 to 100 μm in length, separated by fractures. Similarly, each zircon domain, bounded by fractures, represents a potential, chemically heterogenous nucleus for overgrowth formation.

Zircons from different mylonitic fabrics may or may not bear metamorphic overgrowths. SEM, electron microprobe and optical data show that the percentage of zircons with metamorphic overgrowths increases from protomylonite (~10%, -200 fraction only) to the blastomylonite (35-40%, both fractions). Typically, zircons without overgrowths are characterized by low trace element abundances and relatively flat trace element distribution profiles (Figure 2.5 a, line C; Figure 2.5 b, line C; Figure 2.6a, line B).

Microprobe traverses across zircons from the B8A -200 protomylonite, B8B +200 and -200 blastomylonite, and B8C +200 and -200 ultramylonite fractions suggest that the chemical discontinuity between the Henderson Gneiss-derived core and the metamorphic overgrowth is sharp,

Table 2.2. Microprobe analyses of zircons. Numbers in parentheses denote 1σ standard deviation.

	Hgn+200(A) Avg. of 9	Hgn+200(B) Avg. of 12	Hgn+200(C) Avg. of 7	Hgn+200(C) Avg. of 4	B8A+200A&B Avg. of 17	B8A+200A&B Avg. of 12	B8A-200C&D Avg. of 6 Rim	B8A-200C&D Avg. of 13 Core
ZrO_2	65.79(91)	65.18(65)	65.42(184)	64.33(56)	65.48(122)	64.55(139)	64.18(104)	64.25(89)
SiO_2	31.66(32)	31.93(30)	32.36(13)	31.62(15)	31.83(57)	31.45(15)	31.09(131)	32.40(59)
HfO_2	1.31(06)	1.22(09)	1.49(06)	1.74(05)	1.59(09)	1.27(08)	1.48(25)	1.76(20)
Y_2O_3	0.13(06)	0.15(04)	0.16(04)	0.62(12)	0.10(03)	0.75(35)	0.41(10)	0.05(02)
P_2O_5	0.06(02)	0.08(02)	0.07(02)	0.28(15)	0.04(01)	0.15(05)	0.13(04)	n.d.
UO_2	tr.	tr.	0.08(03)	0.41(13)	0.06(01)	0.23(08)	0.21(10)	0.08(03)
CaO	n.d.	n.d.	tr.	tr.	n.d	n.d.	n.d.	n.d.
FeO	tr.	tr.	tr.	tr.	tr.	tr.	tr.	tr.
Total	99.95(135)	98.56(110)	99.58(212)	99.00(16)	99.10(193)	98.40(210)	97.50(284)	98.55(173)
Zr/Hf	43.96(226)	46.68(342)	38.37(91)	32.34(60)	36.04(194)	44.44(286)	38.86(669)	32.22(418)

	B8B+200A&B Avg. of 5 Rim	B8B+200A&B Avg. of 12 Core	B8B+200C Avg. of 3 Rim	B8B+200C Avg. of 9 Core	B8B-200A Avg. of 5 Rim	B8B-200A 1 Analysis Core	B8B-200C Avg. of 8	B8B-200D Avg. of 6 Rim
ZrO_2	64.88(166)	65.53(159)	62.97(68)	65.52(126)	64.90(91)	63.83	67.61(40)	65.06(118)
SiO_2	31.52(43)	31.79(46)	31.59(10)	31.49(59)	30.91(13)	31.20	31.30(32)	31.88(22)
HfO_2	1.63(14)	1.42(17)	1.73(08)	1.31(03)	1.58(11)	1.41	1.49(02)	1.55(07)
Y_2O_3	0.28(08)	0.13(05)	0.21(05)	0.14(05)	0.45(09)	0.23	0.11(01)	0.19(04)
P_2O_5	0.11(05)	0.06(02)	0.06(02)	0.06(01)	0.18(12)	0.08	tr.	0.11(02)
UO_2	0.18(06)	0.06(02)	0.12(04)	0.04(00)	0.22(04)	0.06	n.d.	0.08(02)
CaO	tr.	tr.	n.d.	n.d.	n.d.	n.d.	n.d.	n.d.
FeO	0.04(00)	tr.	n.d.	n.d.	tr.	0.08	tr.	0.04(01)
Total	98.64(242)	98.99(231)	96.68(97)	98.56(194)	98.24(14)	96.89	100.51(75)	98.91(156)
Zr/Hf	34.98(377)	40.91(542)	31.80(160)	43.57(77)	36.05(270)	39.41	39.70(47)	36.80(172)

	B8B-200D Avg. of 4 Core	B8C+200B Avg. of 10 Clear	B8C+200D Avg. of 6 Cloudy	B8C-200A Avg. of 4 Cloudy	B8C-200AB Avg. of 7 Clear	B8C-200B Avg. of 4 Rim	B8C-200B Avg. of 4 Core	B8C-200C Avg. of 5 Rim
ZrO_2	64.60(126)	68.49(63)	66.50(91)	62.20(108)	65.55(72)	63.92(66)	66.02(62)	64.74(125)
SiO_2	31.29(33)	31.03(21)	30.99(37)	30.63(21)	30.75(36)	30.47(34)	30.90(06)	29.93(24)
HfO_2	1.24(04)	1.32(06)	1.49(08)	4.80(26)	1.41(04)	1.69(04)	1.33(07)	1.39(09)
Y_2O_3	1.14(53)	0.12(04)	0.40(08)	0.48(08)	0.13(07)	0.43(23)	0.13(03)	0.43(14)
P_2O_5	0.37(12)	0.06(02)	0.16(02)	0.24(03)	0.11(08)	0.20(10)	0.08(01)	0.19(09)
UO_2	0.34(11)	n.d.	0.2(06)	0.71(05)	tr.	0.15(07)	tr.	0.13(04)
CaO	n.d.	n.d.	n.d.	tr.	n.d.	n.d.	n.d.	n.d.
FeO	0.05(01)	n.d.	tr.	0.10(04)	n.d.	tr.	n.d.	tr.
Total	99.03(24)	101.02(96)	99.75(152)	99.16(175)	97.95(127)	98.86(144)	98.46(79)	96.81(185)
Zr/Hf	45.48(209)	45.41(249)	39.09(210)	11.35(79)	40.55(102)	33.06(106)	43.38(238)	40.72(324)

Table 2.2. Microprobe analyses of zircons, continued.

	B8C-200C Avg. of 5 Core	B8C-200D&E Avg. of 11 Cloudy
ZrO_2	66.67(59)	63.42(157)
SiO_2	30.31(08)	31.80(173
HfO_2	1.03(19)	1.67(15)
Y_2O_3	0.17(09)	0.52(28)
P_2O_5	0.06(03)	0.25(20)
UO_2	0.03(01)	0.60(40)
CaO	n.d.	0.07(07)
FeO	n.d.	0.30(25)
Total	98.27(99)	98.63(465)
Zr/Hf	57.59(905)	33.36(312)

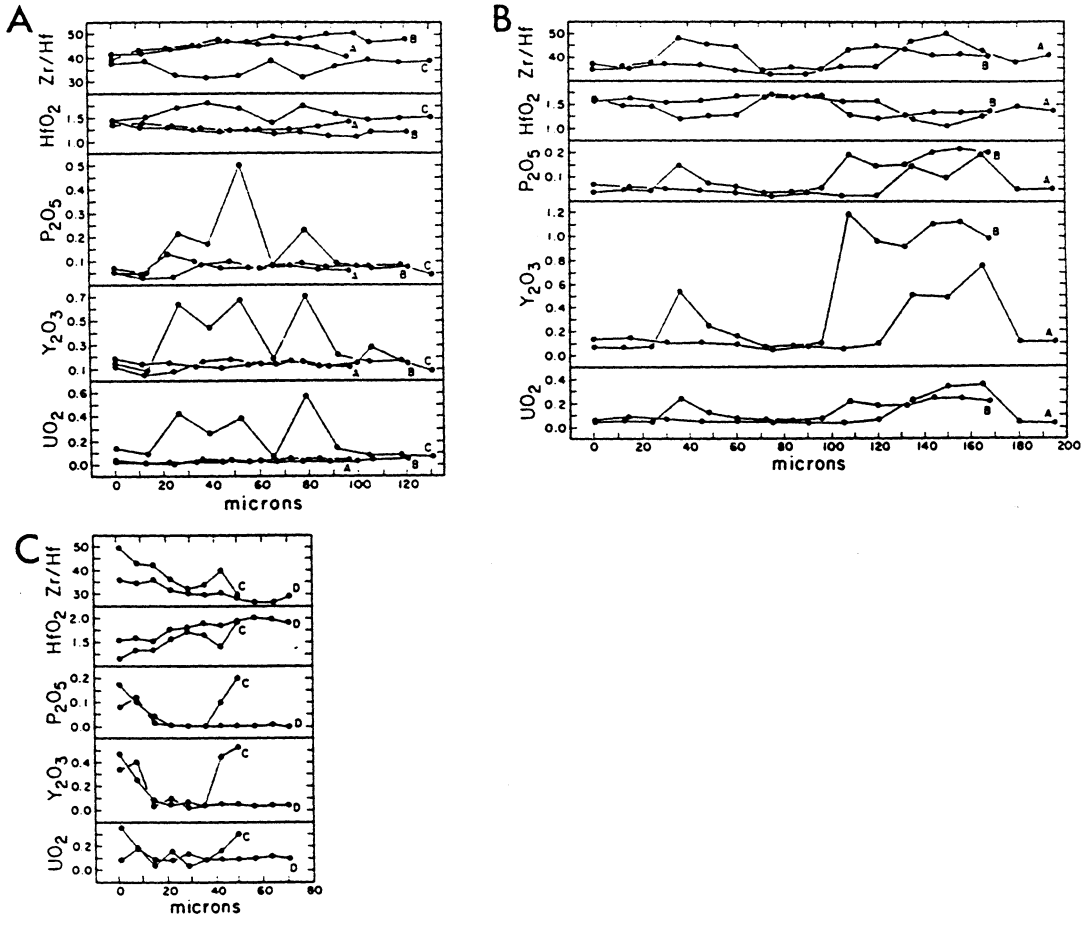


Figure 2.4. Zr/Hf ratios and distributions of selected trace elements in zircons from electron microprobe analyses: (a) - Henderson Gneiss (HGN + 200, lines A & B; HGN-200, line C), (b) - protomylonite (B8A + 200), (c) - protomylonite (B8A-200). Concentrations are in wt. % oxide. Traverse distances (rim-core-rim) are in microns. Breaks in traverses across B8A + 200 zircons denoted by vertical black bars (see text).

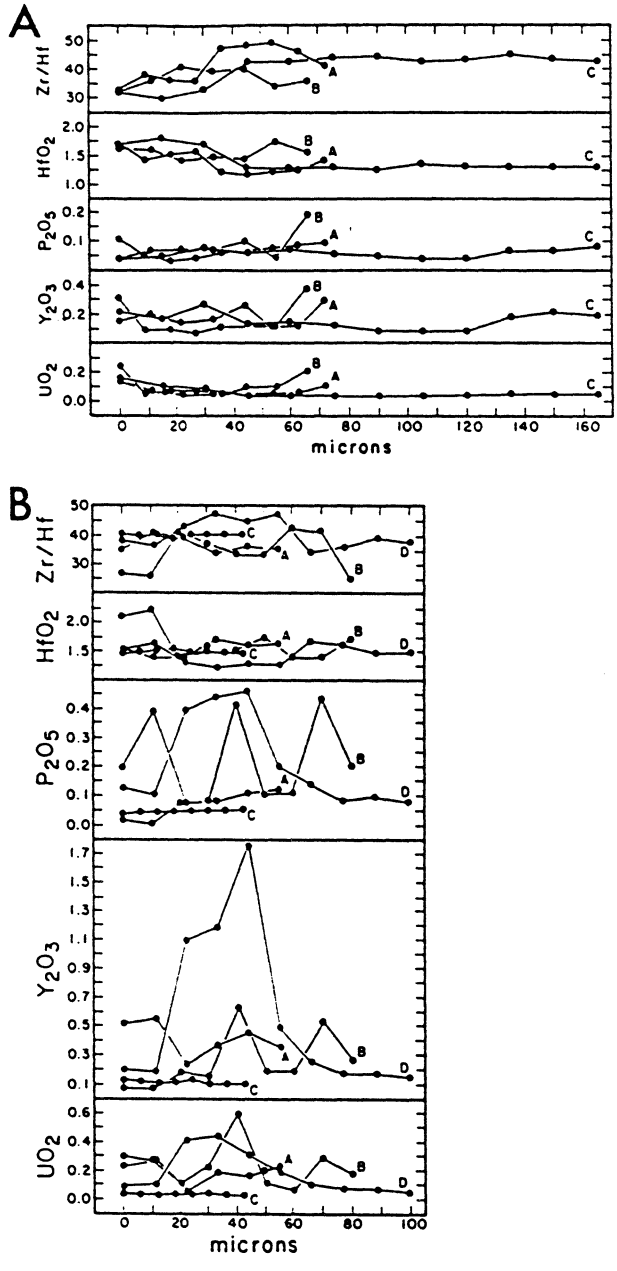


Figure 2.5. Zr/Hf ratios and distributions of selected trace elements in zircons from electron microprobe analyses: (a) - blastomylonite (B8B + 200), (b) - blastomylonite (B8B-200). Concentrations are in wt. % oxide. Traverse distances (rim-core-rim) are in microns.

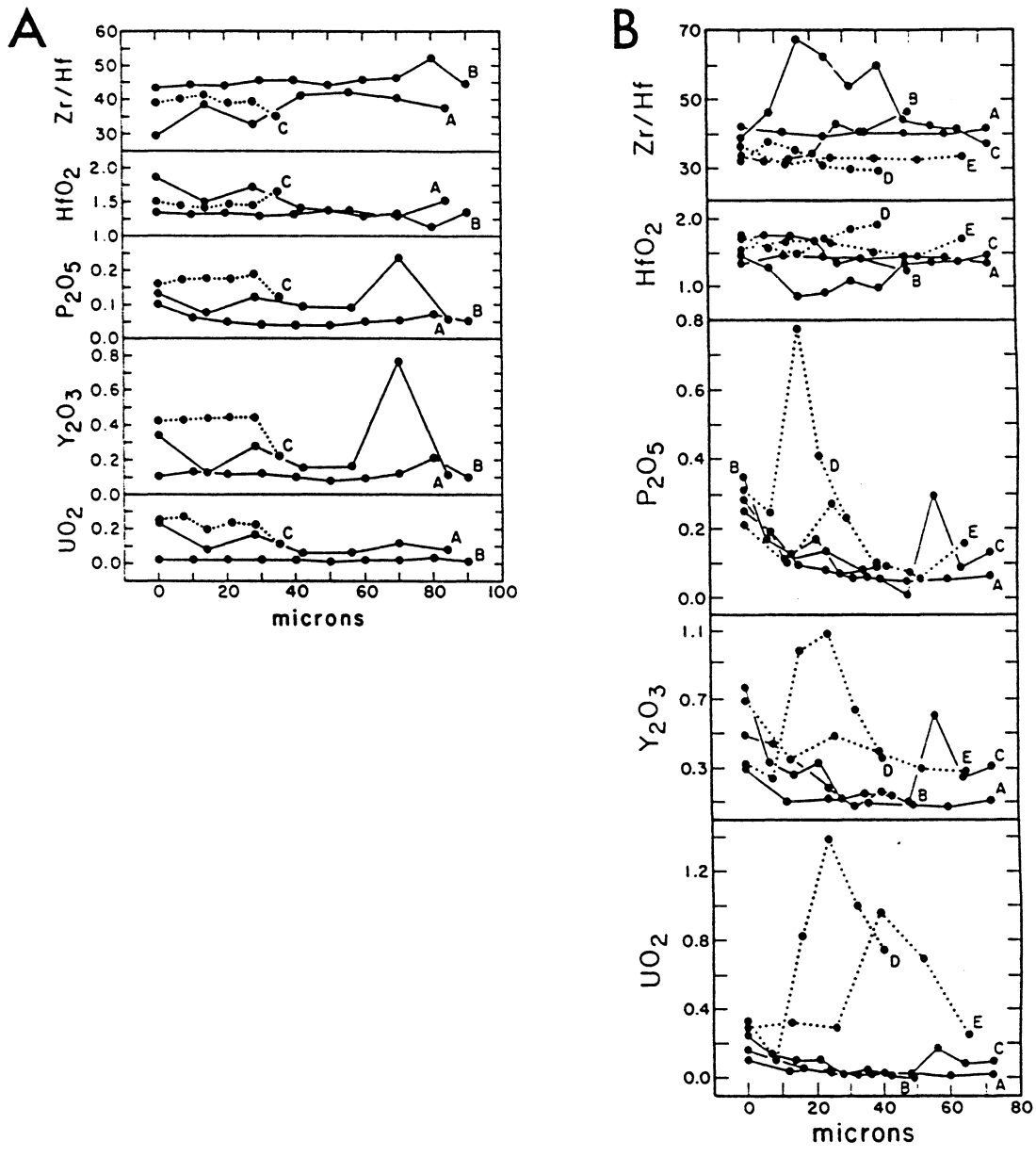


Figure 2.6. Zr/Hf ratios and distributions of selected trace elements in zircons from electron microprobe analyses: Dotted lines refer to traverses of "cloudy" zircons (see text). (a) - ultramylonite (B8C+200), (b) - ultramylonite (B8C-200). Concentrations are in wt. % oxide. Traverse distances (rim-core-rim) are in microns.

distinct, and corresponds to the rim-core boundary observed optically and with SEM. Comparisons of the average chemical compositions of zircon cores and overgrowths obtained from microprobe traverses across selected zircons from each mylonitic fabric (Table 2.2) demonstrate that U, Y and P are consistently enriched in the overgrowths by a factor of 2 to 5 times their abundance in the core. Trace element distribution profiles of overgrowth-bearing mylonite zircons (Figures 2.4c, 2.5a) are characterized by high U, Y and P contents in the outer 5 to 25 μm of the grain. In some cases, however, a trace element enriched portion of a relict zircon apparently provided the nucleus for overgrowth formation. This phenomenon produces a reverse trend of relative trace element enrichment (e.g. Figure 2.5b, line D). The trace element content of the overgrowths on these individuals appears to be unrelated to that of the relict core.

Zircons from the ultramylonite can be classified into two populations: 1) clear, recrystallized zircons and 2) cloudy zircons with or without cores. The recrystallized zircons constitute the largest population (~70 - 80%) and characteristically contain low amounts of all trace elements. They also appear to be free of relict zoning, hot spots and metamorphic overgrowths but contain numerous inclusions (Figure 2.2e). The second group generally exhibits the same physical and chemical trends observed in the relatively less strained portions of the shear zone except that the volume of overgrowth may be significantly greater than that of the core. In some traverses (e.g. Figure 2.6, lines D and E) no core is evident, presumably because of sample preparation. Metamorphic overgrowths on zircons from the ultramylonite tend to contain greater concentrations of trace elements than do the metamorphic overgrowths from the blastomylonite or protomylonite (Table 2.2), and may be chemically zoned with U, P, Y, Ca and Fe contents increasing toward the relict core (Figure 2.3d). The presence, in localized areas, of detectable amounts of Ca and Fe may be due to both the large number of inclusions in these zircons and to the large number of defect sites available due to radiation damage.

Behavior of Hf

Variation in Hf contents between relict cores and metamorphic overgrowths, like that of U, P and Y, is on the order of tenths of weight percent. Hf is irregularly distributed in zircons from relatively undeformed Henderson Gneiss. Zones enriched in other trace constituents may be enriched or depleted in Hf with respect to other parts of the crystal. Metamorphic rims on zircons from the protomylonite are, on average, slightly depleted in Hf with respect to the core (e.g. Table 2.2). This trend is reversed throughout the rest of the mylonite. Overgrowths formed on zircons in the blastomylonite and ultramylonite characteristically show slight, but consistent, enrichment in Hf with respect to the cores. Relict cores from the protomylonite to the ultramylonite show a slight net decrease in average Hf content, corresponding to the degree of strain. Two of the cloudy zircons from the ultramylonites (out of the 10-15 grains studied) show a marked enrichment in HfO_2 in excess of 5.0 wt % HfO_2) (e.g. B8C - 200F).

The Hf abundance trends observed over most of the mylonite zone may be due to the lack of an effective source or sink for Hf besides zircon itself. The Hf liberated during the prograde mylonitization episode most likely came from relatively radiation-damaged portions of zircons, which are more susceptible to leaching and dissolution by fluids than completely crystalline zircons (Ewing et al. 1982). Similarly, all Hf in solution was probably partitioned into metamorphic overgrowths as they developed on zircons in the mylonite. Slight, but consistent, Hf depletion observed in relict cores from the blastomylonite and ultramylonite may be indicative of the through-going nature of zircon fracturing and dissolution during mylonitization. The extremely localized enrichment of Hf in metamorphic overgrowths on zircons from the ultramylonite hints at fluid phase fractionation of Hf and Zr. Hf contents of recrystallized zircons from the ultramylonite are low and generally within the range observed for zircons from the parent gneiss.

Discussion and Conclusions

Previous studies of U-Pb systematics in shear zones (e.g. Lancelot et al. 1983; Chase et al. 1983) and impact structures (Aberg and Bollmark 1985) indicate that isotopic discordance is not necessarily a consequence of fracturing or size reduction of zircons, even when they are in contact with H_2O-rich fluids at T~300°C. By contrast, Pb loss was apparently accelerated in zircons that were fractured during amphibolite grade (T~500°C) mylonitization in the Brevard shear zone. Fractured +200 mesh zircons from the protomylonite (B8A) yield $^{207}Pb/^{206}Pb$ ages that are approximately 75% discordant (Sinha and Glover 1978). Much of this Pb loss took place prior to the formation of metamorphic overgrowths on zircons throughout the mylonite zone. Pb loss was accomplished by the penetration of radiation-damaged portions within the zircon via through-going cracks. The metamict or semi-metamict portions of the zircon crystal were then preferentially leached of radiogenic Pb by metamorphic fluids. This process is shown schematically in Figure 2.7.

Fracturing induced by external strain (e.g., mylonitization) may have been facilitated by the prior presence of stresses, or fractures, due to the differential swelling of U-Th rich portions of chemically zoned zircons. Radionuclide-rich zones, or portions, of a crystal (i.e., "hot spots") will accumulate α-damage faster than radionuclide-poor zones. The swelling induced by α-damage will then establish stresses within the crystal, eventually leading to brittle failure. Chakoumakos et al. (1987) attribute the fracturing observed in zoned, partially metamict Sri Lankan zircons to differential α-damage induced swelling, and the radial fractures observed in chemically zoned zircons from numerous other localities (e.g., Peterman et al. 1986) may also be due to this process.

Fracturing and disaggregation also increases the effective surface area of the zircons, which may also enhance the rates of Pb-loss and U-gain in a fluid rich environment. The increase in surface area versus the number of through-going fractures, shown graphically in Figure 2.8, is plotted for three different cases: 1) a spherical grain with planar cracks passing through its center; 2) a cylindrical grain with evenly spaced planar cracks parallel to its base; and 3) a cylindrical grain with evenly spaced planar cracks inclined 45° to its base. In all cases, the total surface area of the

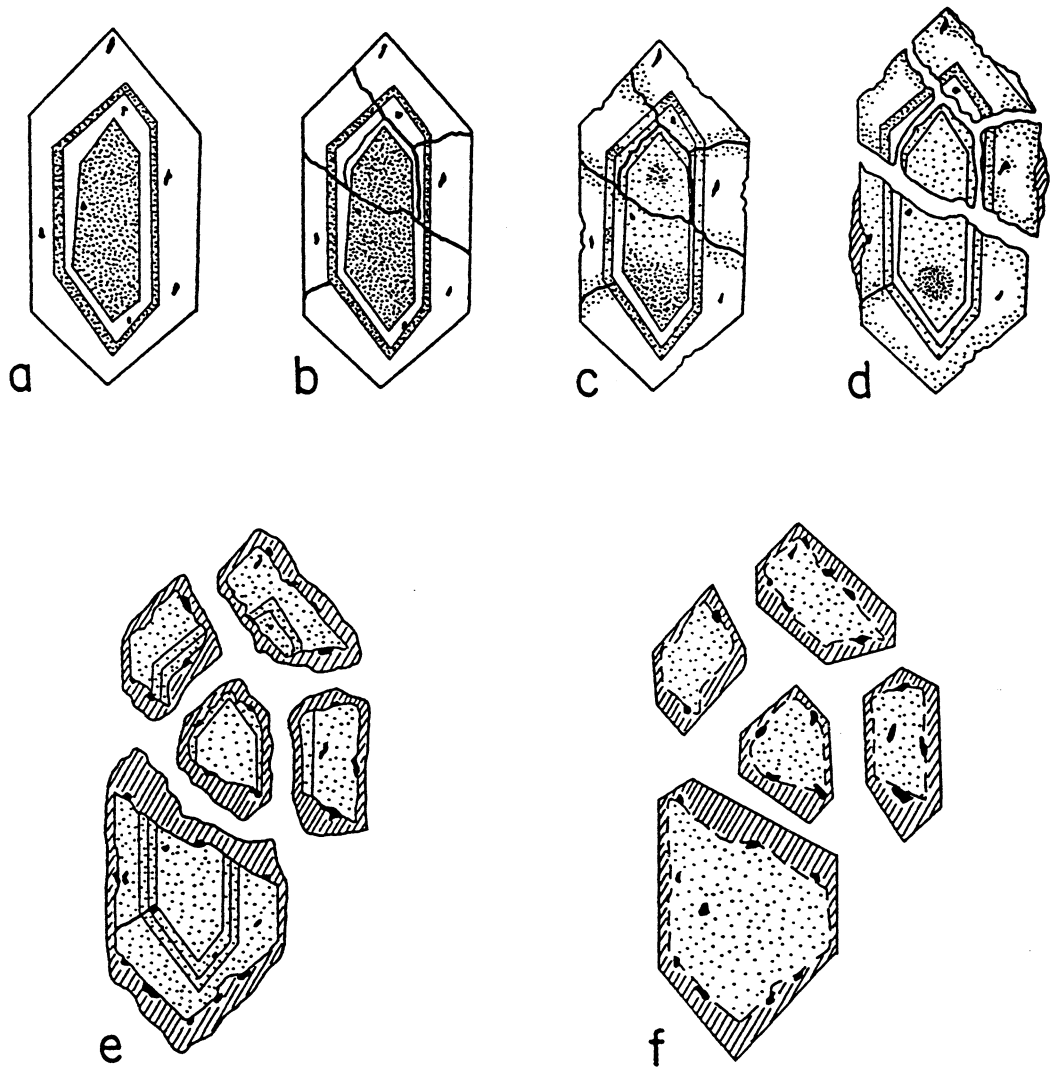


Figure 2.7. Schematic diagram depicting the mechanisms pertinent to Pb-loss and U-gain of zircons in the Brevard Shear Zone: (a) - Zircon with primary, igneous zoning. Densely stippled areas denote U, Th and trace-element rich zones. Black areas denote inclusions. (b) - Fracturing of zircons across and parallel to radiation-damaged, trace-element rich zones during mylonitization. (c) - Fluids penetrate fractured zircons, preferentially leaching radiogenic Pb out of the crystal (sparse stipple). Minor etching also occurs. (d) - Zircon may also disaggregate as ε (strain rate) increases during mylonitization. Leaching of Pb continues. (e) - Zircon crystals and crystal fragments develop overgrowths (hatched pattern). Inclusions of sphene, apatite and biotite may nucleate and grow at the overgrowth-core interface. Primary, trace element-rich portions may also be overgrown, small fragments may dissolve. (f) - Partial refaceting and annealing of zircons occurs, removing igneous zoning. Relict zircon cores have lost the U-Pb isotopic signature of the igneous protolith due to prior leaching.

grain is doubled by 2 to 4 fractures, depending on its morphology and, for the cylindrical cases, on the obliquity of the fractures. The cylinder with oblique fractures is the closest approximation to the observed fracture patterns in zircons from the Brevard mylonites. Based on the observed fracture densities of these zircons, we estimate conservatively that their effective surface area was doubled due to fracturing. Fracturing thus could have enhanced the release of radiogenic Pb into metamorphic solutions, and possibly provided additional nucleation sites for zircon precipitated from solution during mylonitization.

Calculated ages based on Pb diffusion (e.g. Tilton 1960) may also be affected by fracturing and size reduction of zircons during metamorphism. In principle, fractures represent new grain boundaries, and continuous diffusion may only take place within the volume of zircon between the fractures. Thus, the effective diffusion radius, a, is reduced as a result of fracturing. The reduction of a corresponds to an increase in the magnitude of the parameter D/a^2 (where D is the diffusion coefficient for radiogenic Pb in zircon). The increase in D/a^2, in turn, corresponds to a greater loss of Pb via diffusion over a given time period.

The formation of overgrowths on protolith-derived zircons is a process normally associated with extremely high-grade metamorphic rocks and migmatites. Isotopic discordance due to refaceting, or the formation of overgrowths, has been reported from migmatites (Peucat et al. 1985), eclogites (e.g. Gebauer et al. 1981), granulites (e.g. Grauert 1974) and contact aureoles immediately proximal to a cooling igneous intrusion (Hart et al. 1968). Pressure estimates from these lithologies vary, but peak metamorphic temperatures generally lie within the range 600-900°C.

The occurrence of overgrowths on zircons from the Brevard zone mylonites suggests that new growth is also possible during amphibolite-facies metamorphic conditions, provided great amounts of fluids are present. The physical nature of the zircon overgrowths from the Brevard mylonite is unlike that observed in high-grade metamorphic rocks. Instead of appearing refaceted, the surfaces of overgrown zircons from the mylonite appear lumpy, irregular or somewhat porous, and very similar in appearance to the "metamorphic" zircon observed in a mylonitized tonalitic gneiss (M-48) by Peterman et al. (1980). New growth of zircon in the Brevard zone also suggests that Zr, Hf, U, Y and P were mobilized at some point during the earlier prograde deformation event. Mobility

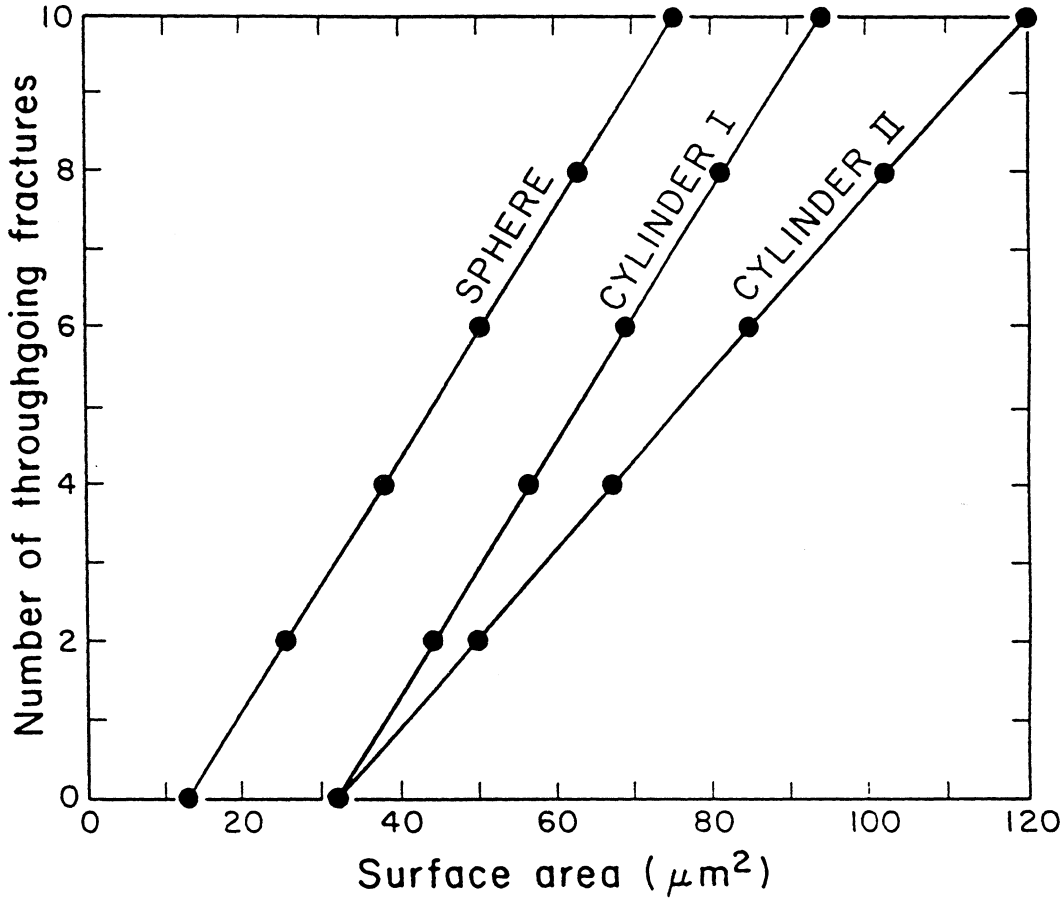


Figure 2.8. Plot of surface area (in μm^2) versus the number of throughgoing fractures: (a) - a sphere of 1 unit radius, (b) - a cylinder of 1 unit radius and 4 units height with basal fractures (Cylinder I), (c) - a cylinder of 1 unit radius and 4 units height with oblique fractures at a 45° angle to the base (Cylinder II).

of Zr, Y, P and REE is not unknown in mylonitized quartzofeldspathic rocks. Vocke et al. (1987) observed Y, Zr and HREE enrichment and xenotime (YPO_4) overgrowths on zircons from a phengite-rich mylonite in a deformed granite porphyry that had undergone high pressure-low temperature metamorphism (~200 - 400°C, 5-7 kbar).

The growth of U-rich rims on zircons during mylonitization undoubtedly contributed to isotopic resetting. Sinha and Glover (1978) found that the total U content of the blastomylonite (B8B) zircon separate was approximately three times that of the Henderson Gneiss zircons. The microprobe data generated during this study concurs with the findings of Sinha and Glover (1978) and further suggests that the addition of U, Y and P to the mylonite zircons is due to the new growth of zircon during the initial (~460 m.y.) amphibolite-grade mylonitization event. Thus, the trace element contents of the mylonite zircons increase with their overgrowth-to-core volume ratios. Sinha and Glover (1978) observed a slight decrease in the total U content of ultramylonite zircons. U loss in the ultramylonite may have been caused by pervasive structural annealing and recrystallization in the most highly strained and fluid-rich portions of the shear zone. However, the interpretation of U-Pb data as a mixing model involving Henderson Gneiss-derived cores and ~460 Ma old overgrowths is inappropriate due to the loss of Pb prior to the appearance of overgrowths.

Extensive recrystallization of the zircons in the Brevard zone mylonite probably only occurred in the ultramylonite. Recrystallized zircons from the ultramylonite are characteristically clear, faceted, relatively unfractured and free of relict zoning. It should be noted that the majority of zircons from the protolith are almost totally crystalline, as shown by powder diffraction data (Table 2.3). Severe radiation damage, if present, is restricted to narrow, concentric zones within the central portion of the grain.

Chemical and isotopic data from this study and Sinha and Glover (1978) indicate that complete resetting of U-Pb ages in the mylonite occurred in zircons from the protomylonite and blastomylonite prior to recrystallization. Experimental data (Pidgeon et al. 1966, 1973) suggest that annealing and Pb loss from totally metamict (i.e. x-ray amorphous, optically isotropic) zircon fragments may be induced at low temperatures (ca. 350°C) in the presence of fluids. The extent

Table 2.3. Cell dimensions of zircons from the Henderson Gneiss (HGN) and the Brevard Zone mylonites.

Fraction	a_0 (Å)	c_0(Å)	Volume (Å^3)
HGN+200	6.609(1)	5.987(1)	261.50
HGN-200	6.610(1)	5.988(1)	261.65
B8A+200	6.612(1)	5.991(1)	261.91
B8A-200	6.614(1)	5.993(1)	262.17
B8B+200	6.611(1)	5.993(1)	261.95
B8B-200	6.611(1)	5.994(2)	261.96
B8C+200	6.612(2)	5.994(5)	262.36

of Pb loss and annealing appears to be most dependent on temperature and fluid composition. Similarly, isotopic discordance (ca. 90% Pb loss) of zircons from greenschist-grade, regionally metamorphosed pelitic sediments has been attributed to low temperature annealing of detrital metamict zircons (Gebauer and Grunenfelder 1976) in the presence of large volumes of metamorphic fluids. The experiments of Pidgeon et al. (1966, 1973) have been taken as evidence of a causal relationship between structural annealing and Pb loss from severely radiation-damaged zircons. While this may be true for zircons which have suffered α-dosages in excess of 10^{16} alphas/mg, weakly radiation-damaged zircons from the Henderson Gneiss lost a significant amount of their radiogenic Pb (up to 100%) prior to structural annealing. Annealing probably occurred only in the most deformed regions of the shear zone, where fluid content was maximal.

Whole rock Rb/Sr isotopic data (Sinha et al. 1987) provide evidence for the generation of the observed mylonitic textures and phase assemblages in the Brevard fault zone during at least two discrete events. The first event, dated at ~460 m.y. by reset zircons within the mylonite and ~445 m.y. by whole rock Rb/Sr within unretrogressed portions of the mylonite, produced a prograde (garnet + biotite) assemblage, a strong pervasive foliation and, locally, zones of mylonite within the Henderson Gneiss. The second event, dated by Rb/Sr at ~273 m.y. using only retrograde mineral assemblages within the mylonite, represents a greenschist-grade reactivation of the 460 m.y. shear zone along the original fault plane. The foliation developed during the Taconic event acted as a conduit for aqueous fluids during the later event.

Zircons within the mylonite lost Pb and gained U during the 460 m.y. event, but remained closed during the reactivation of the shear zone at 273 m.y. (Sinha and Glover 1978). The retention of the 460 m.y. Pb signature by the zircons in the retrograded portions of the mylonite may be attributed to a number of factors. First, the lack of further Pb loss may be due, in part, to the composition of fluids present during the later greenschist-grade shearing event. Experimental studies of metamict zircons in hydrothermal solutions (Pidgeon et al. 1966, 1973) indicate that the rate and extent of Pb loss, U loss and annealing is dependent on time, temperature and the ionic strength and pH of the experimental fluid. Solutions consisting of pure H_2O had little effect on the U-Pb systematics and crystallinity of zircons. By contrast, dilute (2 molar) solutions of NaCl and

HCl caused significant annealing and loss of α-activity over short periods of time. Increased temperatures accelerated Pb-loss and annealing further. By analogy, if fluids present during the ~273 m.y. retrograde event in the Brevard Zone were of low ionic strength and near-neutral pH, they may have had little effect on the U-Pb systematics of the zircons in the mylonite. Although temperatures may have had an effect on the susceptibility of zircons to Pb-loss and/or annealing, it is difficult to ascertain whether or not the lower metamorphic grade of the later shearing event was of critical importance. In order to gain a better understanding of isotopic discordance in fluid-rich environments, we are currently conducting hydrothermal experiments to investigate the rate and extent of U-Pb (loss or gain) in weakly metamict natural zircons and non-metamict synthetic zircons for a variety of solution compositions.

We also speculate that stresses attained during the ~273 m .y. shearing episode were not sufficient to cause additional fracturing and size reduction of a significant population of zircons. Boullier (1980) suggests that brittle minerals, such as zircon, reach a stress-dependent equilibrium grain size beyond which no further fracturing may occur. Following a similar line of reasoning, we suggest that without new fractures to allow the penetration of metamorphic fluids into the radiation-damaged portions of the zircons, no further Pb-loss or U-gain could occur. Furthermore, metamorphic reactions during the retrograde event resulted in the growth of abundant muscovite and biotite (Sinha et al. 1987). As a result, the overall tendency of the rock to accommodate stress in a ductile fashion (e.g. via dislocation glide), rather than by brittle failure, may have increased. A net increase in the proportion of ductile matrix, accomplished by the growth of muscovite at the expense of alkali feldspar, may also have increased the equilibrium grain size of brittle minerals for a given strain rate (e.g. Mitra 1978). Thus, due to their relatively small grain size (~250 μm), zircons may have escaped further fracturing, and subsequent leaching by metamorphic fluids during the 273 m.y. retrograde event.

References

Aberg G, Bollmark B (1985) Retention of U and Pb in zircons from shocked granite in the Siljan impact structure, Sweden. Earth Planet Sci Lett 74:347-349.

Aines RD and Rossman GR (1986) Relationships between radiation damage and trace water in zircon, quartz and topaz. Am Min 71:1186-1193.

Allegre CJ, Albarede F, Grunenfelder M, Koppel V (1974) $^{238}U/^{206}Pb$ - $^{235}U/^{207}Pb$ - $^{232}Th/^{208}Pb$ zircon geochronology in Alpine and non-Alpine environments. Contrib Mineral Petrol 43:163-194.

Bence AE, Albee AL (1968) Empirical correction factors for the electron microanalysis of silicates and oxides. J Geol 76:382-403.

Bickford ME, Chase RB, Nelson BK, Shuster RD, Arruda EC (1981) U-Pb studies of zircon cores and overgrowths and monazite: implications for age and petrogenesis of the northeastern Idaho Batholith. J Geol 89:433-457.

Boullier AM (1980) A preliminary study on the behavior of brittle minerals in a ductile matrix: example of zircons and feldspars. J Struct Geol 2:211-217.

Bryant B, Reed JC (1970) Geology of the Grandfather Mountain window and vicinity, North Carolina and Tennessee. US Geol Surv Prof Pap 615, 190 p.

Chakoumakos BC, Murakami T, Lumpkin GR and Ewing, RC (1987) Alpha-decay-induced fracturing in zircon: the transition from the crystalline to the metamict state. Sci 236:1556-1559.

Chase RB, Bickford ME, Arruda EC (1983) Tectonic implications of Tertiary intrusion and shearing within the Bitterroot Dome, northeastern Idaho Batholith. J Geol 91:462-470.

Ewing RC, Haaker RF, Lutze W (1982) Leachability of zircon as a function of alpha dose. In *Scientific basis for radioactive waste management - V.* Mat Res Soc Symp Proc 11. Lutze W (ed), New York, Elsevier, 389-394.

Gebauer D, Bernard-Griffiths J, Gr&udi.nenfelder M. (1981) U-Pb zircon and monazite dating of a mafic-ultramafic complex and its country rocks. Contrib Mineral Petrol 76:292-300.

Gebauer D, Grunenfelder M (1976) U-Pb zircon and Rb-Sr whole rock dating of low-grade metasediments, example: Montagne Noire (Southern France). Contrib Mineral Petrol 59:13-32.

Grauert B (1974) U-Pb systematics in heterogeneous zircon populations from the Precambrian basement of the Maryland Piedmont. Earth Planet Sci Lett:238-248.

Gulson BL, Krogh TE (1975) Evidence of multiple intrusion, possible resetting of U-Pb ages and new crystallization of zircons in the post-tectonic intrusions ("Rapakivi granites") and gneisses from South Greenland. Geochim Cosmochim Acta 39:65-82.

Hadley JB, Nelson AE (1971) Geologic map of the Knoxville quadrangle, North Carolina, Tennessee and South Carolina. US Geol Surv Misc Geol Investigations Map I-654, scale 1:250,000.

Hart SR, Davis GL, Steiger RH, Tilton GR (1968) A comparison of the isotopic mineral age variations and petrologic changes induced by contact metamorphism, in *Radiometric dating for geologists* New York, John Wiley and Sons, 73-110.

Hatcher RD (1971) Stratigraphic, petrologic and structural evidence favoring a thrust solution to the Brevard problem. Am J Sci 270:177-202.

Holland HD and Gottfried D (1955) The effect of nuclear radiation on the structure of zircon. Acta Cryst 8:291-300.

Krogh TE, Davis GL (1975) Alteration in zircons and differential dissolution of altered and metamict zircon. Carn Inst Wash Yearbook 1974-1975, 619-625.

Lancelot JR, Boullier AM, Maluski H, Ducrot J (1983) Deformation and related radiogeochronology in a Late Pan-African mylonitic shear zone, Ardrar des Ifuras (Mali). Contrib Mineral Petrol 82:312-326.

Mitra G (1978) Ductile deformation zones and mylonites: the mechanical processes involved in the deformation of crystalline basement rocks. Am J Sci 278:1057-1084.

Mumpton FA, Roy R (1961) Hydrothermal stability studies of the zircon-thorite group. Geochim Cosmochim Acta 21:217-238.

Peterman ZE, Zartman RE and Sims PK (1980) Tonalitic gneiss of early Archean age from northern Michigan. Geol Soc Am Special Pap 182:125-134.

Peterman ZE, Zartman RE and Sims PK (1986) A protracted Archean history in the Watersmeet Gneiss dome, northern Michigan. In *Shorter Contributions to Isotope Research*, USGS Bull 1622:51-64.

Peucat JJ, Tisserant D, Caby R, Clauer N (1985) Resistance of zircons to U-Pb resetting in a prograde metamorphic sequence of Caledonian age in East Greeland. Can J Earth Sci 22:330-338.

Pidgeon RT, O'Neil JR, Silver LT (1966) Uranium and lead isotopic stability in a metamict zircon under experimental hydrothermal conditions. Sci 154:1538-1540.

Pidgeon RT, O'Neil RJ, Silver LT (1973) Observations on the crystallinity and the U-Pb system of a metamict Ceylon zircon under experimental hydrothermal conditions. Fortschr Mineral 50:118.

Ramakrishnan SS, Gokhale KVGK, Subbarao FC (1969) Solid solubility in the system zircon-hafnon. Mat Res Bull 4:323-328.

Romans PA, Brown LL, White JC (1975) An electron microprobe study of yttrium, rare earth and phosphorus distribution in zoned and ordinary zircon. Am Mineral 60:475-480.

Roper PJ, Dunn DE (1973) Superposed deformation and polymetamorphism, Brevard Zone, South Carolina. Geol Soc Am Bull 84:3373-3386.

Schenk, V (1980) U-Pb and Rb-Sr radiometric dates and their correlation with metamorphic events in the granulite-facies basement of the Serre, Southern Calabria (Italy). Contrib Mineral Petrol 73:23-38.

Sinha AK, Glover III L (1978) U/Pb systematics during dynamic metamorphism, a study from the Brevard fault zone. Contrib Mineral Petrol 66:305-310.

Sinha AK, Hewitt DA, Rimstidt JD (1986) Fluid interaction and element mobility in the development of ultramylonites. Geol 14:883-886.

Sinha AK, Hewitt DA, Rimstidt JD (1987) Metamorphic petrology and strontium isotope geochemistry associated with the development of mylonites: an example from the Brevard fault zone, North Carolina. Submitted to Am J Sci, Wones Memorial Volume.

Sommerauer J (1974) Trace element distribution patterns and the mineralogical stability of zircon -- an application for combined electron microprobe techniques. Electron Micros Soc of Southern Africa Proc 4:71-72.

Sommerauer J (1976) Die chemisch-physikalische stabilit&adi.t nat&udi.rlicher zirkone und ihr U-(Th)-Pb system. Unpub Ph.D. diss 5755, Swiss Fed Inst Tech, Zurich.

Steiger RH, Wasserburg GJ (1966) Systematics in the Pb^{208} - Th^{232} , Pb^{207} - U^{235}, and Pb^{206} - U^{238} systems. J Geophys Res 71:6065-6090.

Tilton GR (1960) Volume diffusion as a mechanism for discordant lead ages. J Geophys Res 65:2933-2945.

Vocke RD, Hanson GN, Grunenfelder M (1987) Rare earth element mobility in the Roffna Gneiss, Switzerland. Contrib Mineral Petrol 95:145-154.

Wasserburg GJ (1963) Diffusion processes in lead-uranium systems. J Geophys Res 68:4823-4846.

Watson EB (1980) Some experimentally determined zircon/liquid partition coefficients for the rare earth elements. Geochim Cosmochim Acta 44:895-897.

Wayne DM, Solberg TN, Sinha AK (1987) Microprobe analysis of isotopically reset zircons from a Brevard Zone mylonite. Submitted to Microbeam Analysis - 1987, ed. R. Geiss. San Francisco Press, CA.

Wetherill GS (1956a) An interpretation of the Rhodesia and Witwatersrand age patterns. Geochim Cosmochim Acta 9:290-292.

Wetherill GS (1956b) Discordant uranium-lead ages, I. Trans Amer Geophys Union 37:320-326.

Wetherill GS (1963) Discordant uranium-lead ages, II: discordant ages resulting from diffusion of lead and uranium. J Geophys Res 68:2957-2965.

Chapter 3: The effects of fluids on zircon U-Pb systematics in ductile deformation zones.

Abstract

The ability of the zircon U-Pb system to yield useful geochronologic information on the timing of deformational events is a complex function of the degree of metamictization of the zircons, the chemistry and mineralogy of the enclosing rock, the P-T conditions of metamorphism and the presence and composition of metamorphic fluids. The possible effects of dynamic metamorphism on the isotopic ages obtained from zircons range from no apparent Pb loss to complete resetting of the isotopic "clock". The two examples presented here represent the two extremes: the mid-Paleozoic, greenschist-grade Rockfish Valley Fault Zone, and the Pennsylvanian-Permian amphibolite-grade Hope Valley Shear Zone. In the mylonites of the Rockfish Valley Fault Zone, zircons underwent brittle failure and were comminuted in the ductilely deforming matrix. Comparative U-Pb isotopic studies of zircons from the mylonites and from the Grenville-aged charnockitic protolith demonstrate that no appreciable Pb loss occurred as the result of intense

mylonitization, despite the presence of aqueous fluids during deformation which affected the hydration of the mylonitic mineral assemblages.

A detailed U-Pb isotopic study of a single outcrop of the late Precambrian Ponaganset gneiss was also undertaken. Amphibolite-grade mylonitization associated with movement along the Hope Valley Shear Zone caused some grain size reduction ofthe zircons in the mylonite zones. However, the primary cause of isotopic disturbance in these zircons is the extensive growth of U-rich metamorphic zircon during, or shortly after, metamorphism. Corrosion of pre-existing zircon also occurred during metamorphism/deformation, but it is difficult to quantify its effects on U-Pb systematics. The lower intercept ages of 289± 24 m.y. and 265± 62 m.y. from the pink gneiss and gray gneiss, respectively, both fall within the range of other published age estimates (e.g. Zartman et al. 1988) for Alleghanian deformation and metamorphism in southeastern New England.

Introduction

Numerous studies of the petrogenesis, geochemistry and structural evolution of mylonite zones have clarified and constrained both the deformational history, and the extensive and intensive parameters of the associated metamorphic processes (e.g. Gilotti 1989; Sinha et al. 1988; Brodie and Rutter 1985; Knipe and Wintsch 1985; and others). On the other hand, geochronologic studies of mylonitic rocks have met with varying degrees of success in determining the timing of deformation (Sinha et al. 1988; Lindh and Schoberg 1988, and others). The combined effects of intense metamorphism, mineral deformation and, potentially, of open system behavior tend to introduce scatter into isotopic data, resulting in trends that are equivocal and often difficult to interpret. Thus, estimates of the age of mylonitization are often inferred using a combination of geochronologic data and regional geologic constraints. While such estimates are often quite sufficient, critical field data may not always be available in terrain where exposures are poor and/or widely scattered. Furthermore, precise ages acquired from isotopic studies can provide greater resolution and, when constrained by P-T estimates from systematic geothermometry and geobarometry, can also permit more detailed tectonic interpretations in polymetamorphosed and polydeformed regions.

The application of standard whole-rock isotopic techniques (typically Rb-Sr) to mylonitized rocks is problematic in that the re-equilibration of parent-daughter systems may not be complete, or that the scale of re-equilibration may not be apparent from routine petrographic studies. For example, the development of metamorphic mineral assemblages within shear zones may not be resolvable, even on a thin section scale, due to intense grain-size reduction, local equilibrium phenomena produced by varying degrees of reaction progress during fluid infiltration, the production of fine-scale lamellar textures, or the physical transposition of discrete isotopic domains against each other. In some cases, Rb/Sr and Nd/Sm isotopic data obtained from mineral separates can be used to date episodes of recrystallization and/or mineral growth in mylonites that developed at temperatures in excess of the closure temperature of the most refractory phase considered. Mineral ages

are particularly well-suited for tectonites in which relationships between metamorphic paragenesis and fabric development are clearly established (e.g. Getty and Gromet 1989).

Direct dating of deformation using U-Pb methods is also highly effective, particularly when several minerals (e.g. zircon, titanite and monazite) from the same sample are considered collectively. However, relatively few attempts at utilizing the U-Pb isotopic systematics of refractory accessories as a dating technique for mylonitization have been documented in the literature (e.g. Sinha and Glover, 1978; Scharer 1978; Peterman et al. 1980; Chase, et al. 1983; Stern, et al. 1989; Gehrels, et al. 1987; Gehrels and Saleeby 1987; Lancelot, et al. 1983; Phair, et al. 1971; Lindh and Schoberg 1988; and Van Breemen, et al. 1986). The body of work on this topic indicates that the degree of perturbation of the zircon U-Pb system in rocks that have undergone severe grain size reduction and dynamic recrystallization is extremely variable. The observed effects range from no loss of radiogenic Pb at the time of deformation (Chase et al. 1983, and this study) to partial disturbance (Lindh and Schoberg 1988; this study), to complete resetting of the U-Pb system during mylonitization (e.g. Sinha and Glover 1978). Furthermore, it is difficult, and perhaps inappropriate, to attribute the observed variability in the response of the zircon U-Pb isotopic system to any single factor, such as the P-T conditions of metamorphism.

The aim of this study is to provide additional insight into the physicochemical mechanisms that produce U-Pb discordance in zircons from mylonitized quartzofeldspathic rocks. To this end, we present new U-Pb data from an amphibolite-grade mylonite (a portion of the Hope Valley Shear Zone in south-central Massachusetts), and a greenschist-grade mylonite (the Rockfish Valley Fault Zone in central Virginia). This data set provides an interesting and instructive contrast with similar U-Pb data collected from other shear zones.

U-Pb systematics of zircon in mylonites

Previous studies of U-Pb isotopic systematics in mylonites suggest that the ability of zircon to date dynamic metamorphism is dependent on both its mechanical and chemical response to the process of mylonitization (Lancelot et al. 1983; van Breemen et al. 1986; Lindh and Schoberg 1988; Sinha and Glover 1978). Isotopic discordance in zircon and other U-Th-bearing phases occurs when radiogenic Pb is lost, or U-Th is gained, at some time after primary crystallization and closure of the isotopic system. Lead loss is prevalent over other discordance-producing mechanisms because α-decay events, of which radiogenic Pb is a product, render portions of the zircon lattice disordered and distorted and thus less able to retain the daughter product during episodes of heating and/or fluid-rock interaction.

The likelihood of Pb loss is enhanced when zircons are fractured during mylonitization, particularly when metamorphic fluids are present to provide a medium for the dissolution and transport of Pb ions (Wayne and Sinha 1988). Fracturing, by itself, is not responsible for Pb-loss (Aberg and Bollmark 1985, and this study), however it does serve to increase the surface area available for reaction with metamorphic fluids and provides additional high-diffusivity paths to enhance the mobility of radiogenic Pb. Specifically, fracturing of zircon on any scale provides a pathway for direct fluid access to the most radiation-damaged portions of a zircon crystal. Microfracturing is common in chemically zoned zircons (Chakoumakos, et al 1988, and others) where inhomogenous initial distribution of U and Th in single grains results in sharp gradients in α-dosage. As α-decay proceeds at different rates in the radionuclide-poor and radionuclide-rich portions of the crystal, differential swelling occurs. The differential swelling, in turn, sets up an internal stress field which may result in microfracturing. Brittle failure of zircons in an external stress field has also been documented (Boullier 1980; Wayne and Sinha 1988, and this study) and could conceivably be initiated preferentially in grains which have undergone stress buildup or incurred microfractures due to differential swelling associated with α-damage. Thus, chemically zoned zircons may be

predisposed to extensive grain size reduction via fracturing and physical disaggregation when subjected to simple shear, while unzoned or U-Th poor zircons may tend to resist breakage.

On the other hand, uranium gain is most often accomplished via growth of new zircon during a metamorphic or hydrothermal episode (van Breemen et al. 1986; Wayne and Sinha 1988, and others). Although the processes by which zircon growth takes place during metamorphism or hydrothermal alteration are not well understood, the growth of metamorphic or hydrothermal zircon has been documented from contact aureoles (Hart et al. 1968; Davis et al. 1968), regional metamorphic terrains (O'Nions and Baadsgaard 1971; Krogh and Davis 1972), migmatites (Gulson and Krogh 1975), hydrothermally altered rocks (Rubin et al. 1989), and amphibolite to granulite grade shear zones (van Breemen et al, 1986; Wayne and Sinha 1988).

Geologic setting of study areas

The Hope Valley Shear Zone

The Hope Valley Shear Zone (Figure 3.1), in southeastern New England, is a major amphibolite-grade ductile shear zone of Alleghanian age (O'Hara and Gromet 1983,1985; Gromet and O'Hara 1985; Wayne and Sinha 1988,1989). At the sample locality, it dips shallowly (10° to 30°) to the west, strikes N-S and cuts a 10 to 15 km wide swath through late Proterozoic and Paleozoic rocks, predominantly of quartzofeldspathic composition (O'Hara and Gromet 1985). The northern segment of the Hope Valley Shear Zone, which extends from south-central Massachusetts to extreme southeastern Connecticut, constitutes the contact between the late Precambrian Ponaganset gneiss to the east and the Hope Valley alaskite gneiss to the west. To the southeast, the Hope Valley Shear Zone represents the contact between the Devonian Scituate granite and the Hope Valley and Potter Hill gneisses (O'Hara and Gromet 1985). O'Hara and Gromet (1985) and Gromet (1989) interpret the Hope Valley Shear Zone as the boundary between two tectonically and petrologically distinct fault-bounded Avalonian fragments: the Hope Valley terrane and the Putnam-Nashoba terrane to the west, and the Esmond-Dedham terrane to the west.

Kinematic indicators, such as quartz c-axis fabrics, and the deflection of regional structural lineations into the shear zone suggest that movement along the Hope Valley Shear Zone is principally right lateral strike-slip, although a component of south-directed thrusting is apparent along the southeast trending, northeast-dipping portion in Rhode Island (O'Hara and Gromet 1985; Getty and Gromet 1988). Thus, the Hope Valley Shear Zone may record either a single episode of oblique thrusting, or polyphase movement. O'Hara and Gromet (1985) point out that the maximum age of this movement is constrained regionally by the deformation of the Devonian (370 m.a., Zartman and Naylor 1984) Scituate granite, and by the apparent intrusive relationship of the early Permian (273 m.a., Zartman and Hermes 1987) Narragansett Pier granite. A middle Pennsylvanian

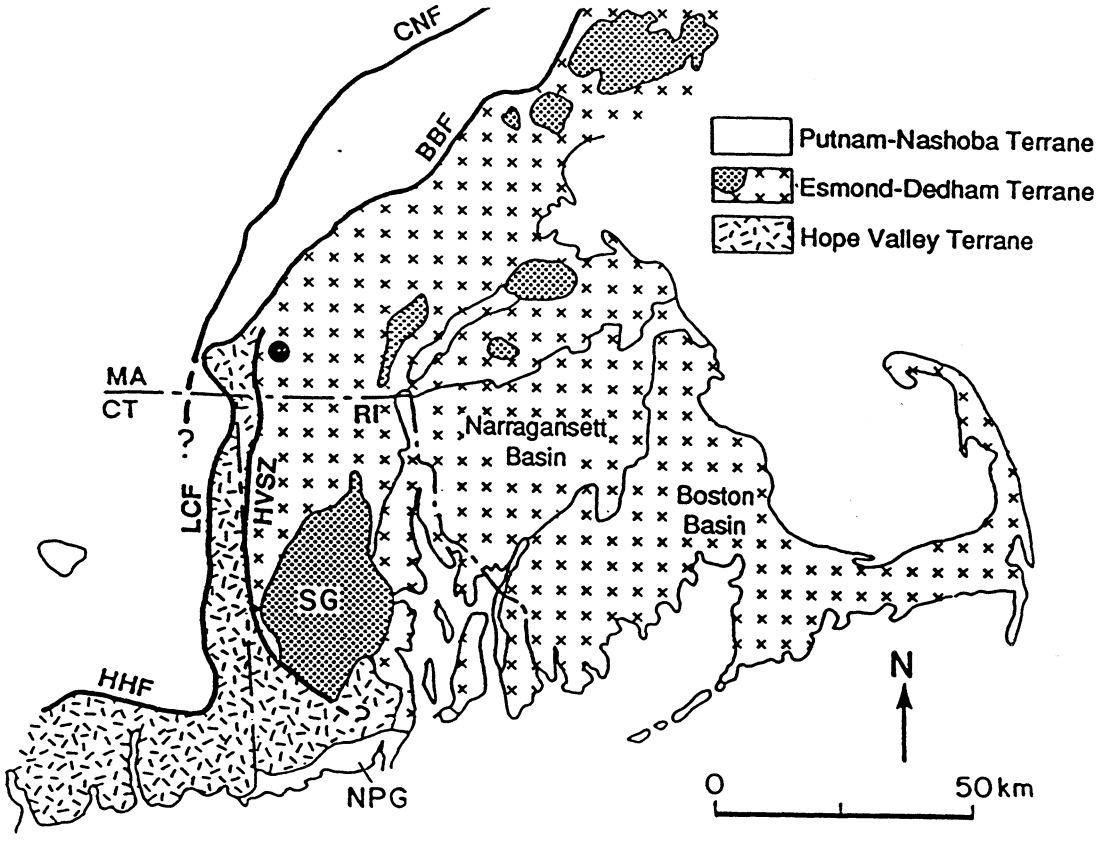


Figure 3.1. Generalized geologic map of southeastern New England, adapted from O'Hara and Gromet (1985): Major fault zones and proposed terrane boundaries are denoted - LCF = Lake Char Fault, HHF = Honey Hill Fault, BBF = Bloody Bluff Fault, HVSZ = Hope Valley Shear Zone.

to lower Permian age for metamorphism in the area is also suggested by the regional prevalence of Permian U-Pb zircon and titanite lower intercept ages (e.g. Wintsch and Aleinikoff 1987; Zartman et al. 1988, and others) and lower intercept ages of zircons from the Ponaganset gneiss itself (Wayne and Sinha 1989; this study). Permian ages have also been obtained from ductilely deformed rocks from the vicinity of the Willimantic Dome (Gromet and Getty 1989) using U-Pb data from titanite and Rb-Sr and Nd-Sm mineral isochrons, and from gneisses of the Hope Valley terrane (Dallmeyer 1982) and the Scituate Granite (Dallmeyer et al. 1990) using $^{39}Ar/^{40}Ar$ data from coexisting biotite and hornblende.

A late Precambrian to earliest Cambrian primary age for the Ponaganset gneiss was obtained from whole rock Rb-Sr data (Wayne and Sinha 1988, 1989). These ages are in agreement with U-Pb and Rb-Sr isotopic data from other Avalonian intrusive and metavolcanic rocks in southeastern New England (Zartman and Naylor 1984; Kovach et al. 1977), and with the U-Pb data presented in this study.

Sample Location

All samples used in our study of the Hope Valley Shear Zone were taken from a single roadcut (Figure 3.2) along MA route 146, near the town of Auburn (stop 9 in Gromet and O'Hara, 1984). The outcrop is situated approximately 1.5 km east of the Hope Valley Shear Zone proper, as mapped by O'Hara and Gromet (1985). At the sample locality (also described in Gromet and O'Hara 1984), the Ponaganset gneiss consists of two mineralogically and texturally distinct units: a fine grained, porphyroclastic gray augen gneiss, and a fine-to-medium grained pink granitic gneiss. The two units occur as discrete alternating tabular units, tens of meters thick, which are often bounded by thin (5-15 cm), attenuated amphibolite layers (Figure 3.2). Macroscopic and microscopic structural evidence indicates that the gneissic units were dynamically juxtaposed during metamorphism. Contacts between the gneisses are characterized by the development of mylonitic

ductile deformation zones. Grain size reduction and the obliteration of porphyroclasts, particularly in the gray augen gneiss, is well-developed within 20 cm of the contact. Within 10 cm of contact, intense grain size reduction results in the formation of narrow, fine-grained, equigranular mylonite zones. By contrast, the pink granitic gneiss is characterized by alternating bands of relatively fine-grained (100-300 μm) mylonitic material and distinctly coarser-grained material (500-1000 μm) oriented subparallel to the foliation. This texture occurs throughout the pink gneiss at the study area, regardless of the proximity to contacts with the gray gneiss or amphibolite layers. Fine-grained domains generally broaden and coalesce in the vicinity of the contacts, but laterally extensive (e.g. meter scale) mylonitic zones are rare in the pink gneiss. Typically, the attitudes of the contacts, amphibolite layers, and mylonite zones are similar and parallel the plane of foliation (see also Gromet and O'Hara 1984). The foliation plane strikes nearly perpendicular to the regional strike of the Hope Valley Shear Zone, and asymmetric tails of feldspar augen indicate a southward thrusting direction (Gromet and O'Hara 1984; O'Hara and Gromet 1985). Small-scale features, such as the mylonites developed within the pink granitic gneiss, tend to lie at low angles ($\simeq$10°) to the foliation.

Although mineral assemblages in both gneiss units are dominated by alkali feldspar, plagioclase and quartz, the mafic assemblages in each unit are distinct: the gray gneiss contains hornblende with subequal quantities of biotite, and the pink gneiss contains biotite and very little hornblende. Evidence for retrogression of the original mylonitic/metamorphic assemblages in these rocks is generally lacking, except locally along fissures (which often contain muscovite and/or chlorite) and along late, crosscutting quartz veins (often surrounded by haloes of stained, altered feldspar). Also present at the outcrop are meter-sized, deformed pegmatite pods which are mineralogically identical to the surrounding gray gneiss. For this study, 50 to 100 kg samples of both gneisses, an amphibolite layer ($\simeq$20 cm. wide), a single ($\simeq$10 cm. wide) mylonite zone developed at the contact between the gray gneiss and an amphibolite layer (UM 419), and a single ($\simeq$5 to 7 cm. wide) garnetiferous mylonite layer developed within the pink gneiss (UM 872) were taken along the length of the outcrop (approximately down dip).

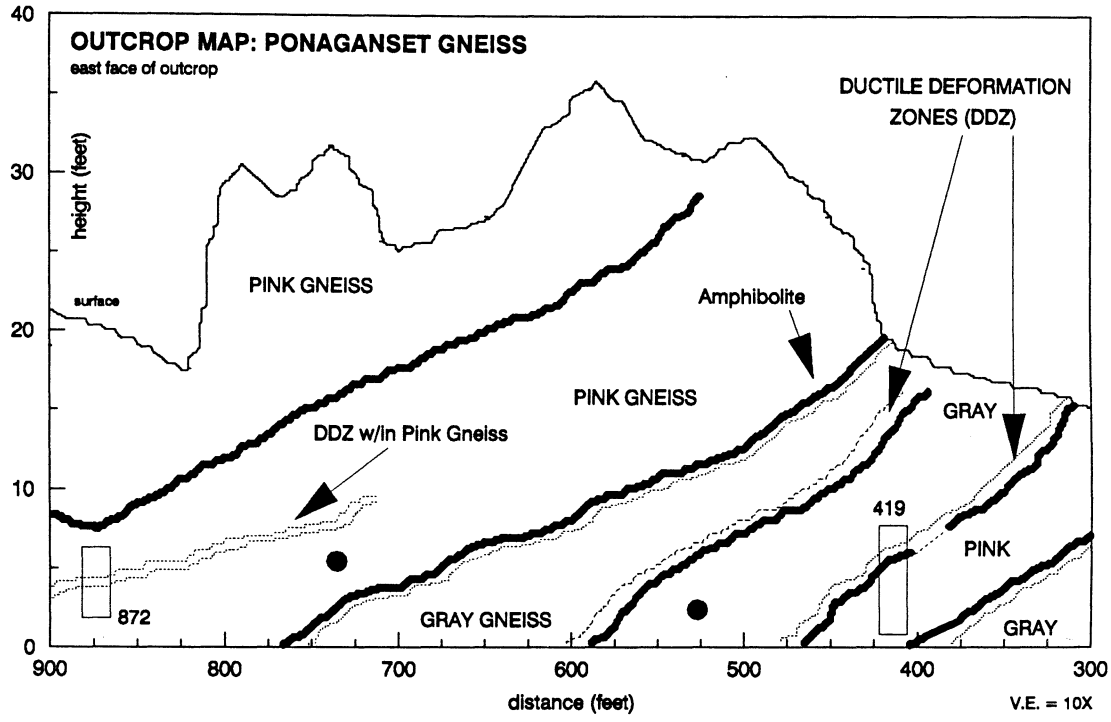


Figure 3.2. **Schematic scale map of the sample locality for the Ponaganset gneiss:** This map shows the distribution of the major lithologic units (gray gneiss, pink gneiss, amphibolite), ductile deformation zones (DDZ) and the locations of the samples taken for zircon separates. Mylonites at 872 and 419 are denoted by rectangles, bulk samples of pink and gray gneiss are denoted by solid black circles. The widths of the amphibolite layers and ductile deformation zones are somewhat exaggerated. Pegmatite pods and quartz veins are not shown.

Petrography of the Ponaganset gneiss

Gray Augen Gneiss

The gray gneiss is typified by the dominant assemblage KSP + PLAG + QTZ + HBD ± BIO, plus accessory titanite, magnetite, zircon and apatite. Porphyroclastic relict perthite augen are partially recrystallized, and often exhibit myrmekitic rims (Simpson and Wintsch 1989) and/or core and mantle structures. Porphyroclastic plagioclase is rare and occurs as thoroughly recrystallized aggregates of coarse subhedral grains. Hornblende is often coarse (up to 1 cm), resorbed and poikiloblastic, with numerous inclusions of titanite, quartz, plagioclase, and, rarely, epidote. The foliation is defined by the alignment of elongated hornblende prisms and biotite plates. The matrix consists of a polygonal mosaic (~ 300-100 μm) of recrystallized plagioclase, alkali feldspar, quartz and aligned, grain boundary-pinning biotite plates. Accessory titanite, magnetite, and rare allanite euhedra, are associated with biotite and hornblende in trains that parallel foliation. Zircon is a relatively common accessory in the gray gneiss, and is typically associated with (and included within) amphibole and biotite, along with other accessory phases. Alteration is sparse and consists of static local chloritization of biotite along cleavage planes and sericitization of plagioclase cores. Alkali feldspar augen are often turbid, but rarely contain late muscovite or epidote grains.

Within $\simeq$ 50 cm of the contact with the amphibolite, matrix grain size decreases to ~50-150 μm and polycrystalline quartz eyes with sutured internal grain boundaries become prominent. The cores of perthitic augen often show slip along cleavage planes.The undeformed regions of the augen are bounded by stringers of finely recrystallized microcline and quartz, and there is often considerable lattice offset between the slipped and unslipped domains. Some of the perthitic augen are extensively recrystallized, and are partially rimmed with coarse (~ 1 mm) quartz, microcline and subhedral twinned plagioclase rather than myrmekite. Within $\simeq$ 10 cm of the contact with the amphibolite, quartz eyes increase in abundance and become increasingly stretched (some have aspect ratios >10:1). Hornblende grains originally at high angles to the fabric appear to have under-

gone slip along cleavage planes (see Allison and LaTour 1977) to rotate into foliation and become highly attenuated.

Mylonite derived from the Gray Augen Gneiss (UM 419)

The mylonite derived from the gray gneiss (UM 419) is a thoroughly recrystallized, mosaic-textured aggregate of polygonal 50 to 150 μm plagioclase and quartz grains, with variable amounts of microcline, sparse accessory hornblende and/or biotite and less abundant titanite and magnetite. In general, the mineral assemblages observed in the mylonites are identical to those observed in the central regions of the less-deformed protolith gray gneiss blocks. However, the mineralogy of the mylonites derived from the gray gneiss varies laterally over 10's to 100's of cm, particularly with reference to the presence or absence of biotite, amphibole and clinopyroxene.

Intense syn-to-post kinematic recrystallization has destroyed nearly all evidence of the specific mechanisms that originally effected the grain size reduction. Well-recovered quartz ribbons (type 3 of Boullier and Bouchez 1978), often with deformation bands normal to the plane of foliation, are locally abundant. Intensely recrystallized, stretched and flattened K-feldspar augen are rare. Accessory hornblende occurs as relatively small (<400 μm long) prismatic to acicular euhedra with strong grain shape preferred orientation, and as somewhat larger subequant fractured and resorbed poikiloblasts. Biotite, if present, pins grain boundaries and tends to occur in trains. Magnetite grains are comminuted and strung out along foliation. Relatively coarse (>200μm), anhedral titanite is common and appears, in some instances, to overgrow the foliation. The mylonite-amphibolite contacts are sharp and are characterized by persistent quartz ribbons and an abrupt modal increase in hornblende.

The thorough recrystallization of plagioclase, amphibole and alkali feldspar, and the similarity of the mineral assemblages of the protolith to those observed in the mylonites suggests that the metamorphism and mylonitization of the Ponaganset gneiss took place at middle amphibolite grade (~600°C) conditions. Typical retrograde and/or hydrated phases such as muscovite, epidote,

chlorite and calcite, if present, occur exclusively as fracture fillings, or locally overgrow the mylonitic foliation.

Pink granitic gneiss

The pink gneiss is a strongly recrystallized, foliated KSP + PLAG + QTZ gneiss with minor (< 5 % modal) biotite, plus accessory titanite, magnetite, zircon, fluorite and allanite. Garnet and hornblende also occur in the pink granitic gneiss. The foliation of this unit is defined by the parallelism of quartz rods and the alignment of biotite plates. Textures are dominated by alternating bands and lenses of fine-grained ($\simeq$100 to 300 μm) mylonitic material, polycrystalline quartz ribbons (Type 3 of Boullier and Bouchez 1978) of varying thickness (1 mm to 1 cm), and bands and lenses of relatively coarse-grained ($\simeq$500 to 1000 μm) material dominated by partially recrystallized, turbid alkali feldspar clasts and rare, completely recrystallized plagioclase porphyroclasts. Transitions between these three textural domains may be gradational, or abrupt and bounded by concentrations of titanite and magnetite. The mylonitic regions coarsen conspicuously away from the contacts (with either the amphibolite or the gray augen gneiss), and consist of a mosaic of equant plagioclase, microcline, quartz, and trails of sphene and magnetite grains, with or without aligned, grain boundary-pinning biotite and/or hornblende. Quartz ribbons are strongly recovered, with deformation bands and fluid inclusion trails oriented normal to foliation. The feldspar-rich domains also contain equant quartz, randomly oriented mafic minerals (usually biotite), and a variably developed array of static retrograde phases: muscovite, epidote, calcite and chlorite. The intensity of this alteration varies dramatically on a centimeter scale, but the modal amount of the retrograde minerals never exceeds ~5% of the total rock. Zircon is less abundant in the pink gneiss than in the gray gneiss, and occurs primarily in association with biotite and other accessories.

Mylonite within the Pink Granitic Gneiss (UM 872)

A mylonite from within a pink gneiss unit was also sampled (UM 872). Texturally, this mylonite is similar to the mylonites developed elsewhere on the outcrop: equigranular, mosaic-textured, thoroughly recrystallized with abundant 120° triple junctions. The boundary between the mylonite and the adjacent pink granitic gneiss is sharp, and lacks the gradual decrease in grain size and matrix-to-porphyroclast ratio that typifies the gneiss-mylonite transitions observed elsewhere on the outcrop. In terms of mineral assemblage, UM 872 is very similar to the host pink gneiss, with some minor exceptions. The pink gneiss ~25 cm away from the mylonite zone consists of KSP + PLAG + QTZ + BIO with accessory titanite, magnetite, fluorite, apatite, garnet and zircon. With increasing proximity to the mylonite zone, there is a systematic decrease in the modal amount of biotite, from ≃ 5% to <1 %. The mylonite consists of QTZ + KSP + PLAG with minor biotite and magnetite, and accessory titanite, fluorite, garnet and zircon. Within the mylonite (UM 872), there occurs a narrow (~1 cm wide), discontinuous, planar zone oriented parallel to foliation, which contains the assemblage PLAG + FL + GT + MAG ± BIO ± AMP with accessory epidote, titanite and quartz. Garnet occurs as tiny pale pink euhedra, often surrounded by anhedral fluorite, which are intimately associated with, and may replace, dark green, resorbed hastingsite. Structurally, the "garnet zone" is attenuated and locally forms boudins within the quartzofeldspathic mylonite.

Amphibolite

The amphibolite layers are thin (up to 10 cm) planar, concordant units with strong foliation parallel to the contact surfaces with the gneissic units. A strong lineation is also locally developed (see O'Hara and Gromet, 1985). The mineralogy of these units is dominated by HBD + KSP + PLAG, with abundant (up to 4%) accessory titanite, variable amounts of CPX, BI and QTZ, and

trace amounts of secondary epidote and calcite. The bright green hornblende euhedra, up to 1 cm long, are set in a fine-grained (100-200 μm) matrix of anhedral, recrystallized plagioclase, K-feldspar and, locally, clinopyroxene. Hornblende grain size varies dramatically across foliation, but has no correlation with the relative proximity to the contacts with the gneisses. The amphibolite also contains narrow (<1 cm wide) conformable bands of pale green, fine-grained (100-200 μm), mylonitic, clinopyroxene-rich material. Coarse-grained (up to 2mm) clinopyroxene, quartz and feldspars may occur in the central portions of these layers. Clinopyroxene-rich layers are also developed at the pink gneiss-amphibolite contact. From the relative modal proportions of HBD, BI, and CPX it is possible to infer local variations in bulk composition, fluid pressure and/or fluid composition to explain the apparent stabilization of the wide range of metamorphic assemblages in the amphibolite. Other factors, such as the degree of mixing with the gneissic assemblages, may also be used to explain the mineralogical variability observed in the amphibolite. Extensive sampling of the amphibolite ($\simeq$ 90 kg) yielded less than 1 mg of zircon, which precluded a conventional U-Pb isotopic study.

The Rockfish Valley Fault Zone

Regional geology, geologic setting and sample locality

Located in the Blue Ridge of central Virginia, the Rockfish Valley Fault Zone (Figure 3.3) is a NE-SW trending, regionally extensive, greenschist-grade ductile deformation zone. Two distinct composite granulite-grade, $\simeq$ 1.0 b.y. old blocks, the Pedlar massif to the northwest and the Lovingston massif to the southeast, lie on either side of the Rockfish Valley Fault Zone (Bartholomew et al. 1981; Sinha and Bartholomew 1984). The age of the mylonitization has not

been directly measured, but is inferred to be middle Paleozoic (≃450 m.y.), on the basis of field relationships (Bartholomew et al. 1981). Dallmeyer (1975) also obtained mid-Paleozoic ages for a retrograde event in the southern Blue Ridge basement using $^{39}Ar/^{40}Ar$ data from biotite and hornblende. A whole rock study (Pettingill, et al 1984) of the charnockite and mylonitized charnockite samples of the Pedlar massif (also used to obtain zircon for this study) showed that the disturbance of the Rb-Sr system by mylonitization was only partial, yielding a mixing line, while Nd-Sm data from the same sample suite show no discernable effects attributable to mylonitization.

Field investigations (e.g Mitra 1978; Bartholomew et al. 1981) show that the Rockfish Valley Fault Zone is characterized by a series of ductile deformation zones, rather than a single fault zone. Mildly deformed felsic gneisses are often cut by narrow zones (1 to 4 mm) of much finer grained mylonitic material. Across these zones, an abrupt reduction in grain size is accompanied by an increase in the modal proportions of phyllosilicates, calcite, epidote-group minerals and actinolite at the expense of feldspars, orthopyroxene and red-brown biotite. Individual ductile deformation zones vary in width from <1 cm to approximately 100 m and are partially to completely replaced by retrograde mineral assemblages.

The undeformed charnockite (of the Pedlar Massif) consists of quartz, alkali feldspar, plagioclase, biotite and orthopyroxene with abundant accessory magnetite/ilmenite, zircon and apatite. Myrmekite is also present, as thin selvages on the edges of plagoclase grains, and as large anhedral altered aggregates. Texturally, the rock is coarse grained, granoblastic, unfoliated and strongly fractured. Alkali feldspar and pleochroic, red-brown biotite are relatively fresh. Plagioclase is partially altered to sericite and chlorite, particularly along grain boundaries and fracture surfaces. Orthopyroxene is severely altered, approximately 90% has been replaced by a dark brown-green aggregate of chlorite and opaques. Fractures are occaisonally filled with calcite. Although the fracture sets are conjugate (Pettingill, et al 1984), the rock is unfoliated and the abundant deformation bands in quartz grains (within single thin sections) appear to have random orientations. Sharp, euhedral, strongly zoned zircons typically occur in association with apatite and clusters of subhedral opaques which are, themselves, intimately associated with orthopyroxene and biotite. Less often, zircon occurs as inclusions within quartz and feldspars.

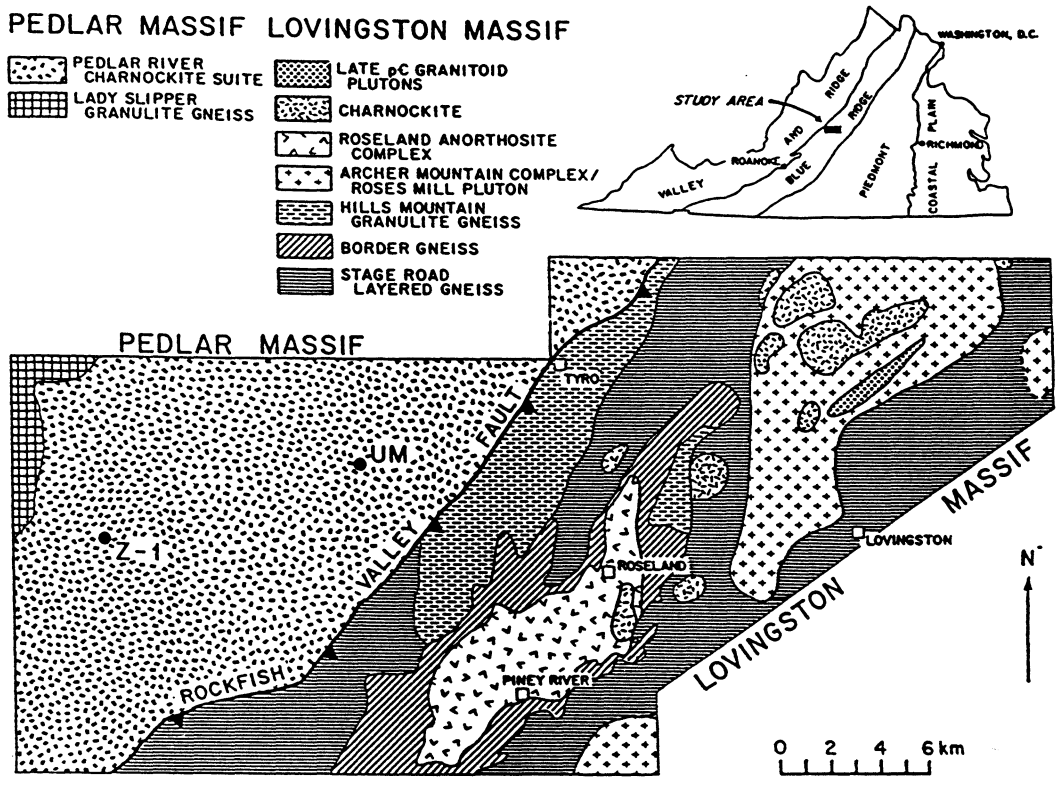


Figure 3.3. Geologic map of the central Virginia Blue Ridge (adapted from Pettingill et al. 1984): This map shows the location of the charnockite unit, and the mylonite zone sampled for this study.

The ultramylonite derived from the charnockite consists of isolated anhedral grains of weakly deformed relict quartz, feldspar and orthopyroxene, with pleochroic amphibole, opaques and zircon suspended in a strongly foliated, extremely fine-grained matrix of phyllosilicates (dominantly chlorite, green biotite and muscovite), quartz and minor calcite. In a few samples, there is evidence for late-to-post tectonic growth of chlorite. Tectonic microstructures produced in the deformation zones are primarily the result of ductile processes, although relict quartz, feldspar and orthopyroxene porphyroclasts, and accessory grains of zircon, show evidence of brittle failure (see also: Mitra 1978). Anastomosing zones of intense deformation are extremely fine grained and enriched in residual opaque particulate matter (mostly Fe-oxides). Preferred orientation of relict quartz grain shapes is moderately to poorly developed, and deformation bands in quartz grains are randomly oriented with respect to the foliation (on a thin section scale). Recrystallization textures in quartz are weak to nonexistant, consisting of core-mantle structures in some grains. Relict feldspar grains are fractured, anhedral, undulose and are often partially altered to muscovite. Zircon is not uncommon, and usually have a rounded, equant morphology or are extensively fractured. The hydrated, phyllosilicate-rich mineral assemblages pervasively developed throughout the ultramylonites of the Rockfish Valley Fault Zone indicate that deformation and metamorphism of the charnockite took place at greenschist-grade conditions, in the presence of a H_2O rich fluid phase.

Analytical techniques

Electron Microprobe, SEM

Microchemical analyses of zircons were performed on an automated Cameca SX-50 4-channel electron microprobe located in the Department of Geological Sciences, VPI&SU. The microprobe was operated at an accelerating potential of 15 kv, with a sample current of 50 na (point mode). Analytical standards are as follows: Zr, Si - synthetic $ZrSiO_4$; Hf - synthetic $HfSiO_4$; Y, Al - YAG; Er - synthetic $Er_2Si_2O_7$; Yb - synthetic $YbVO_4$; Th - synthetic $ThSiO_4$; U - synthetic UO_2; Ca - synthetic $CaSiO_3$; Fe - synthetic Fe_2O_3; P - apatite, Wilberforce, Ontario. On-peak counting times were 24 sec. for Hf, Y, Th, U, Er, Yb and P, and 10 sec. for Fe, Ca, Si and Zr. Off-peak background counting times were 12 sec. and 5 sec. respectively, for the same groups of elements. Counting statistics yield detection limits in the range of 0.005 to 0.01 wt.% oxide for each of the trace and minor elements analyzed in this study, with the exception of Yb and Er which have detection limits of 0.01 to 0.015 wt.% oxide. To accurately monitor instrumental drift and the reproducability of the analyses, the synthetic $ZrSiO_4$standard and a set of synthetic trace element-doped Al, Mg, Ca silicate glasses (V, W and X) were analyzed repeatedly during the data collection period. The synthetic glasses contain 0.79 wt.% HfO_2, ThO_2 and Y_2O_3, 0.76 wt.% UO_2 and 0.71 wt% FeO. Averaged results of the repeated analyses (n = 12) show a consistent negative bias (0.03 to 0.1 wt%) in the measured concentrations of each of the above oxides, except FeO. The average measured concentrations each oxide (except HfO_2) are within 1 standard deviation of the stated concentrations, and the total variance from the mean ranges from 0.011 (UO_2) to 0.001 (Y_2O_3). These disparities may not be entirely due to the analytical limitations of the instrument, as a previous study on a different microprobe (Wayne, unpub. data) yielded similar results. Some of the observed variation may also be due to real inhomogeneities in the compositions of the synthetic

glasses. All raw microprobe data were corrected using the method of Bence and Albee (1968) and Albee and Ray (1970).

SEM work included both secondary electron images for information on surface features and backscattered electron (BSE) images for information on variations in mean atomic number within single zircon grains. Details on the application of these techniques are presented in Lloyd (1981) and Paterson, et al (1989). Some of the secondary electron images were collected on a JEOL JSM-35C in the Virginia-Maryland Regional School of Veterinary Medicine. The remaining secondary electron images and all BSE data were collected at 20 kv on a Camscan Series 2 SEM in the Department of Geological Sciences at VPI&SU.

Whole rock Zr concentrations were obtained by X-ray fluorescence methods, which were carried out by Nuclear Activation Services, Inc., Ann Arbor, Michigan. The estimated reproducibility of the trace element data is $\simeq$ 5 to 10% (2σ) at the concentration levels typical of the samples used in this study.

Mass Spectrometry

Zircon fractions were separated from fresh 45-90 kg rock samples via standard mineral separation techniques. Final zircon separates were seived and handpicked for purity ($>99\%$). Zircons from the pink gneiss unit of the Ponaganset gneiss were further separated into clear and overgrowth-bearing fractions by further handpicking. Air abrasion techniques were not utilized because of our desire to study the nature of zircon discordance as a function of core-to-overgrowth ratios, corrosion and grain size reduction. Samples were washed in warm, Teflon-distilled 8N HNO_3, rinsed in Teflon-distilled H_2O and teflon-distilled acetone. Acid-washed zircon fractions (4 to 20 mg) were dry-aliquotted and dissolved in a 10 to 1 mixture of doubly-distilled Teflon HF and Teflon-distilled HNO_3 in Teflon capsules for 3 to 5 days at 225 °C. The remaining steps in the processing and purification of Pb and U from zircon follow the method of Krogh (1972).

Alkali feldspar separates from the Ponaganset gneiss were obtained from large (> 1 cm) single porphyroclasts from each gneissic unit, and from mineral separates from an amphibolite layer (AM367), and two mylonite zones (UM 419 and UM 872). The porphyroclasts were crushed under acetone in an agate mortar, seived to less than 100 mesh and handpicked to 99% purity. The separates were purified to a similar level using heavy liquids, magnetic separation and handpicking. Some dilution of the alkali feldspar by plagioclase occurred in the amphibolite separate because the two feldspars have identical densities, thereby rendering heavy liquid separation techniques ineffective. All alkali feldspar separates (68 to 226 mg) were acid-washed following the same procedures used for zircon, dry-aliquotted and dissolved in a 5-to-1 mixture of doubly distilled Teflon HF and Teflon-distilled HNO_3 in Savillex capsules for 3 to 5 days at $\simeq$150°C. The residues were dried, converted to chlorides, redissolved in a 5-to-1 mixture of 1N Teflon HBr and 6N Teflon HCl, and allowed to equilibrate overnight. Lead was separated using a two step elution procedure: first with HBr and HCl in 3 ml quartz columns, followed by a "clean-up" elution identical to the Pb elution for zircon. The U elution also required two steps: first with HNO_3, HCl and dilute HF in 3 ml quartz columns, followed by a "clean-up" elution identical to the U elution for zircon. Over the period of this study, total blanks (for $\simeq$10 mg zircon samples) varied from 195 to 530 pg of Pb (n = 8, avg.= 311 pg) and 12 to 15 pg of U (n = 3, avg.= 14 pg). Total Pb blanks for the processing of alkali feldspar were slightly higher (~410 pg) due to the larger volumes of acid required by the elution procedures.

The measurement of U and Pb isotopic ratios was performed on a modified, semi-automated AVCO 35 cm radius 90° sector solid source thermal ionization mass spectrometer, using single Re filaments and standard P_2O_5 - silica gel techniques for Pb, and P_2O_5 - Ta_2O_5 techniques for U. Measurements of the NBS-SRM 983 standard (n = 11) and the NBS U500 standard (n = 6) were used to correct for instrumental mass fractionation, which averaged 0.12 ± 0.04% per a.m.u for Pb and 0.08 ± 0.03 per a.m.u. for U. All decay constants used in the data reduction conform to the values recommended by Steiger and Jaeger (1977). Isotopic ratios were corrected for blanks and fractionation, plus all Pb and U concentrations and ratios were calculated using the PBDAT software package (Ludwig 1988). Alkali feldspar data were also corrected for in situ U decay. Errors

(2 σ) in measured Pb isotopic ratios range from 0.015 to 0.07 percent for $^{207}Pb/^{206}Pb$, 0.013 to 0.1 percent for $^{206}Pb/^{208}Pb$ and from 0.9 to 5.5 percent for $^{206}Pb/^{204}Pb$. Errors in Pb/U ratios range from approximately 0.5 to 1.2 percent, with the exception of one zircon (PG+ 100 C) in which the errors in Pb/U ratios reach 2.0 percent. For all samples, errors in Pb and U concentrations vary from 0.5 to 1.0 percent.

For zircons from the Ponaganset gneiss, the composition of initial common Pb in zircon was assumed to be identical to the composition of common Pb in the appropriate alkali feldspar separates. As a comparison, initial Pb compositions obtained from the two-stage Pb evolution model of Stacey and Kramers (1975) were also applied. The effect of the two common Pb correction techniques is negligable in terms of both the isotopic ages, and the upper and lower intercept ages of the zircon suites. However, the alkali feldspar-corrected data is preferred because: 1) they yield consistently lower errors in Pb/U and Pb/Pb ages, 2) they provide additional information on the Pb isotopic systematics of the gneisses and mylonites. For all gray gneiss samples, the +200 fraction from UM 419, and the overgrowth-free zircons from the pink gneiss, the initial common Pb was assumed to be that observed in the presumably relict alkali feldspar porphyroclasts. The data from the -200 UM 419 fraction was common corrected using the isotopic composition of Pb from alkali feldspar in UM 419. The initial common Pb of the overgrowth-bearing zircons from the pink Ponaganset gneiss and UM 872 was assumed to be that of the alkali feldspar separated from UM 872. In fact, heterogenous zircons which consist of a Precambrian igneous core and a Pennsylvanian/Permian metamorphic overgrowth might realistically be corrected for an initial common Pb that is a weighted average of the two age components. Besides the uncertainty associated with estimates of core-to-rim volume ratio, it is also likely that the proportion of common Pb associated with the zircon cores may be somewhat less than anticipated from core-to-rim volume ratios because of the variable degrees of zircon leaching associated with metamorphism in the pink gneiss. Due to the relatively high $^{206}Pb/^{204}Pb$ ratios of most samples, however, such estimates would most likely produce negligable changes in the age data. All zircon data from the Rockfish Valley Fault Zone were corrected for a 1030 m.y. old common Pb component calculated using the model of Stacey and Kramers (1975).

Regression errors were calculated using Model 2 of Ludwig (1982), with corrected Pb/U ratios, rho values and the associated errors obtained from PBDAT (Ludwig 1988). Uncertainties on upper and lower intercept ages are stated at the 2σ level.

Zircon Morphology

Ponaganset gneiss

In the Ponaganset gneiss, zircons separated from the gray augen gneiss and the pink granitic gneiss are distinct with regard to their morphology and apparent response to metamorphism and deformation. Zircons from the gray augen gneiss are clear, honey-colored, relatively inclusion-free, euhedral and posess relatively simple morphologies: typically {100} prisms, modified by {110} secondary prisms, often with simple pyramidal {101} terminations (Figures 3.4 a and 3.5 a). Zircons from the mylonites derived from the gray augen gneisses (UM 419) are clear, honey-colored, euhedral and very similar in their overall appearance to the zircons from the protolith gray augen gneiss (Figures 3.4b and 3.5b). Measurements of length-width ratios (Table 3.1) suggest that, for a given size fraction, the average length of the UM 419 zircons is about 38% less than that of zircons from the less deformed gray augen gneiss, but that the average length-width ratio for both the UM 419 and gray augen gneiss fractions are similar. The percentage of broken or fragmented grains in both the gray augen gneiss and the mylonite is small ($\simeq$ 10%). Zircons from the gray augen gneiss and UM 419 bear no evidence of surface pitting or corrosion (Figure 3.5 a,b), although a small proportion of the UM 419 -200 fraction ($\simeq$ 10%) consists of cloudy, nearly equant, grains with a porous or "spongy" appearance, despite an otherwise euhedral morphology (Figure 3.5c).

Table 3.1. Morphologic characteristics of zircons from the Ponaganset gneiss and the Rockfish Valley Fault Zone.

SAMPLE	n	avg. l (mm)	avg l:w ratio
Ponaganset Gneiss			
Gray +200	54	0.214 +/-56	2.97 +/-76
419UM +200	42	0.133 +/-32	3.11 +/-87
Pink C+200	40	0.178 +/-35	2.63 +/-62
Pink OG+200	40	0.144 +/-21	2.02 +/-41
880UM +200	26	0.143 +/-35	1.38+/- 21
Rockfish Valley Fault Zone			
Charnockite +200	22	0.266 +/-63	2.11 +/-43
RVFZ+200 not fractured	20	0.218 +/-35	2.21 +/-58
RVFZ+200 fractured	30	0.179 +/-25	1.48 +/-26

Figure 3.4. Photomicrographs of zircon separates: (a) Ponaganset gray gneiss +200. (b) UM419 (+200) (c) Ponaganset pink gneiss (+200). Both clear ("C fraction") and opaque ("O fraction") are present in the field of view. (d) UM872 (prior to handpicking). Clear grains are apatite. (e) Charnockite from the Pedlar Massif (+200). (f) Ultramylonite derived from charnockite, Rockfish Valley Fault Zone (+200). Note the paler color of the zircons from the ultramylonite in comparison to the zircons from the charnockite protolith. Long dimension of each photograph is $\simeq$ 1 mm.

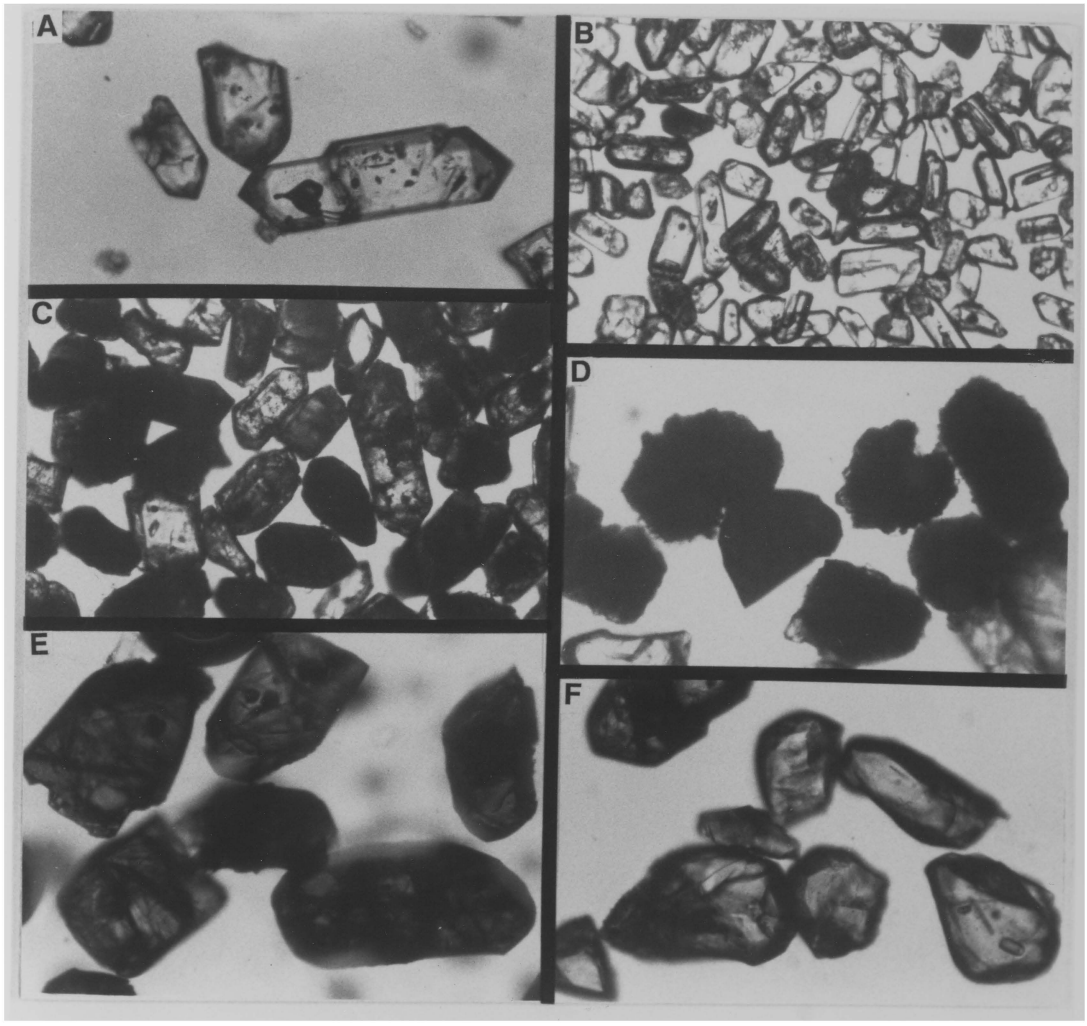
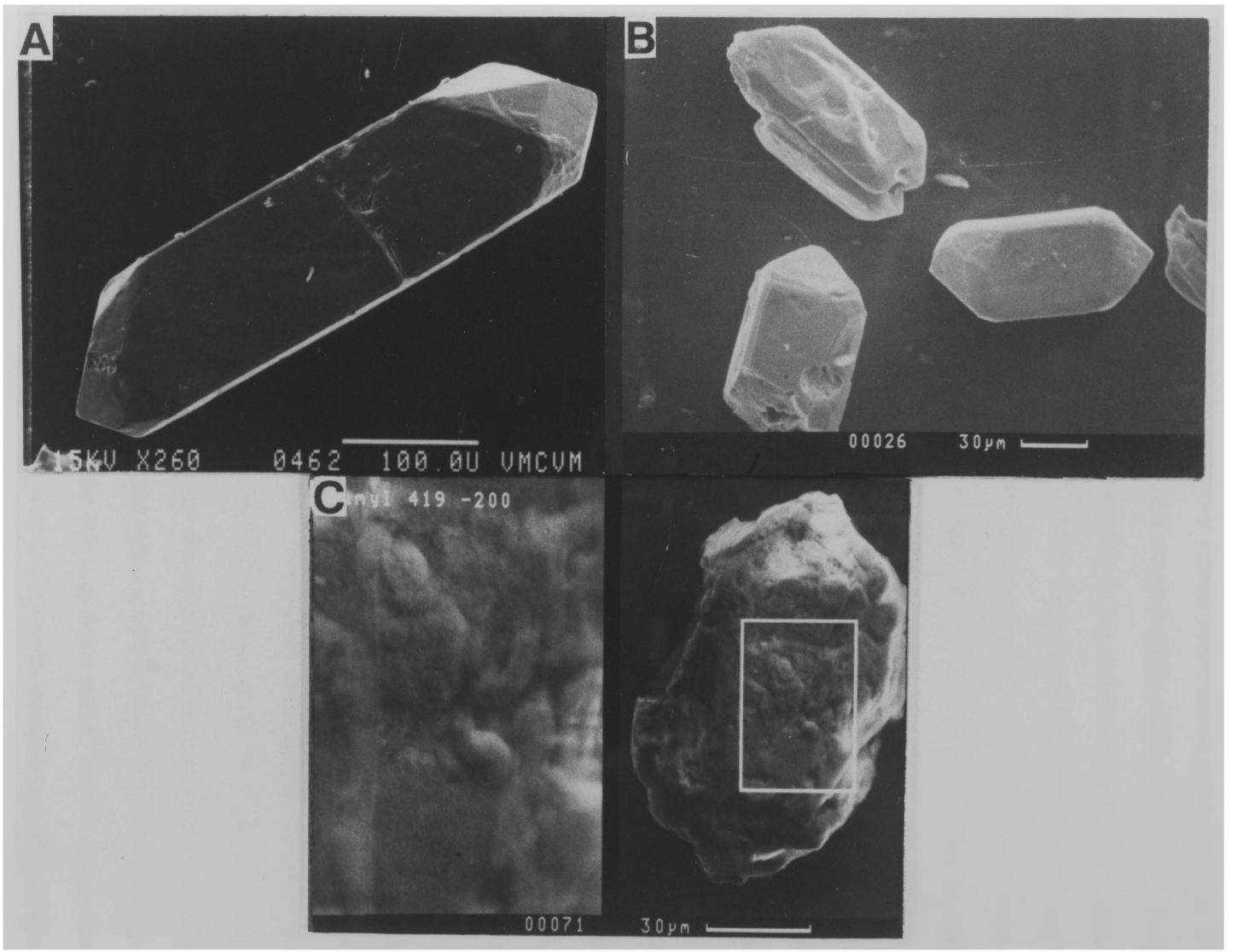

A
B
C
D
E
F

Figure 3.5. **Secondary electron images of zircons from the gray gneiss:** (a) - typical euhedral zircon (+200) from the gray gneiss. (b) +200 zircons from the mylonite (UM419) derived from the gray gneiss (c) - a "spongy"-textured zircon from the -200 fraction of UM419.

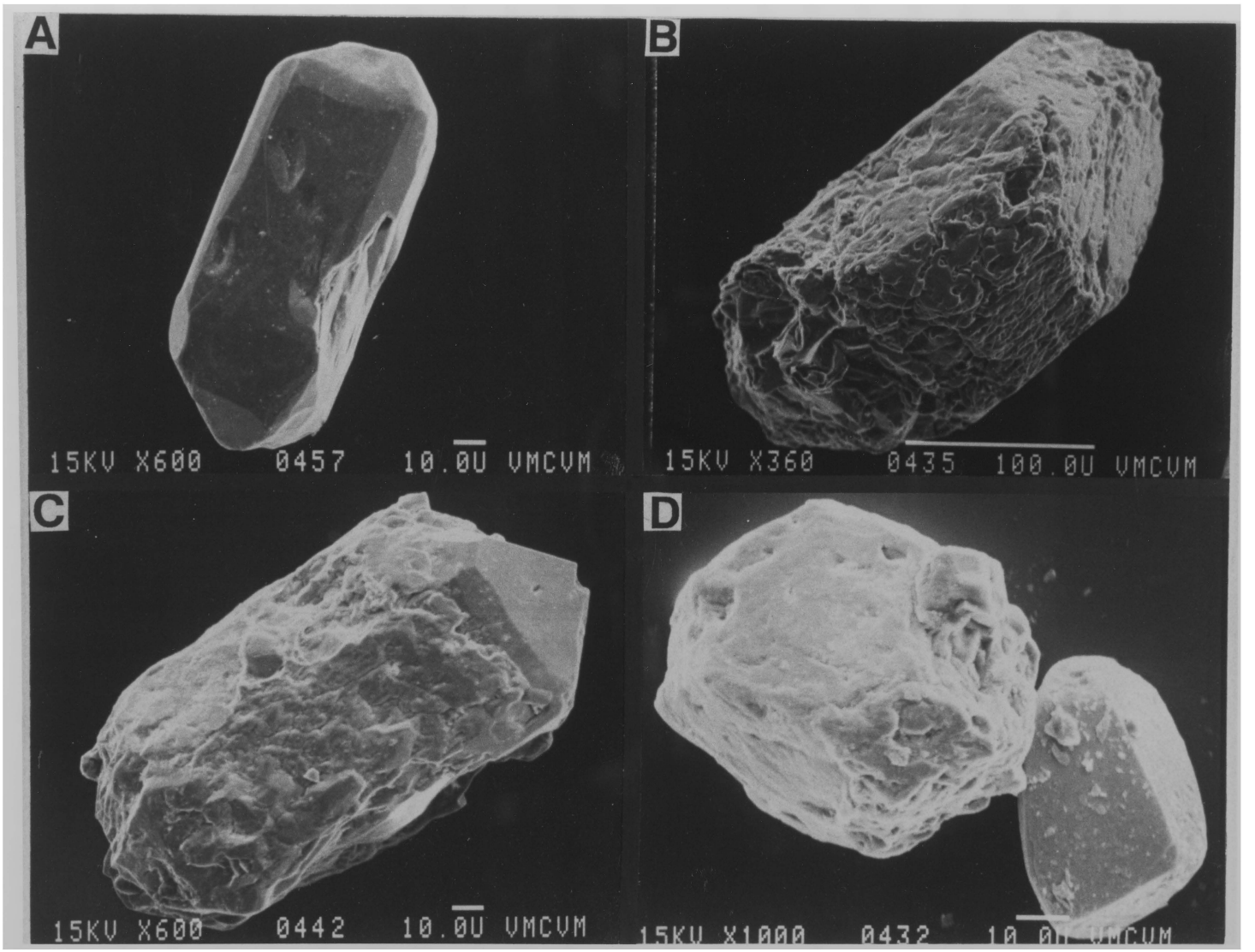

A
15KV X260 0462 100.0U VMCVM
B
00026 30µm
C
mv1 419 -200
00071 30µm

The pink granitic gneiss unit contains two distinct zircon populations (Figure 3.4c): relatively clear (but often inclusion-rich) pale yellow euhedra with well-developed internal zoning (hereafter referred to as the C fraction) and cloudy to completely opaque yellow-brown grains (hereafter referred to as the OG fraction). The C fraction zircons are morphologically similar to the zircons from the gray gneiss: {100} prisms, modified by {110} secondary prisms, terminated by {101} pyramids (although an additional higher order pyramid is evident in Figure 3.6a). The crystal morphology of the OG fraction is difficult to ascertain due to the lumpy, irregular nature of the overgrowths. Both fractions contain grains with rough or pitted surface textures indicative of corrosion, as well as sharp, euhedral individuals (Figure 3.6 a, b). The OG fraction (Figure 3.6c) is more abundant (70 to 80%) in all size fractions, and generally similar in length and average length-width ratio to zircons from the C fraction (Table 3.1). Zircons separated from a mylonite zone within the pink gneiss (Figure 3.4d, 3.6d) are brown, opaque and otherwise strongly resemble the OG fraction from the pink gneiss, except that they are nearly equant (Table 3.1).

Secondary electron images of the OG fraction reveal surface features that are best interpreted as irregular overgrowths (Figure 3.6c). In these composite grains, a slightly corroded euhedral zircon core is enveloped in an irregular mass of material, which was subsequently identified as zircon using the electron microprobe. This type of structure is also typical of zircons from the mylonite zone within the pink gneiss, and was observed in ~200 zircons from UM 419.

The reduction in size at a constant length-width ratio within the ultramylonites derived from the gray gneiss (UM 419) is indicative of a process involving stresses related to dislocation pileups within zircon grains (White et al. 1980; Boullier 1980). The relative rarity of large zircons in the ultramylonite (where the + 100 fraction was nearly nonexistent) in comparison to the less intensely deformed gray augen gneiss also suggests that the grain size reduction mechanism operative during deformation was dependent on particle size, consistent with a model involving dislocation buildup. In the pink gneiss and the associated mylonites, the effects of zircon growth tend to obscure the effects of grain size reduction, and make speculation as to the specific mechanism(s) of grain size reduction difficult.

Figure 3.6. Secondary electron images of zircon from the pink gneiss: (a) - An uncorroded zircon from the +200 C fraction. (b) - A severely corroded zircon from the +200 C fraction. (c) - A zircon from the +200 OG fraction. The euhedral core is plainly visible, and is enveloped in an irregular mass of metamorphic zircon. Note the incipient corrosion at the core-overgrowth boundary. (d) - Euhedral, porous zircon from UM872.


A
15KV X600 0457 10.0U VMCVM
B
15KV X360 0435 100.0U VMCVM
C
15KV X600 0442 10.0U VMCVM
D
15KV X1000 0432

Charnockite from the Pedlar massif and related ultramylonites

Zircons from the charnockite within the Pedlar massif are subhedral and rounded, with complex terminations (Figure 3.4e, 3.7a) which are typical of zircons from granulite-grade rocks (e.g. Duchesne et al. 1987). Outgrowths are not uncommon, and a moderate proportion ($\simeq$ 25%) of the zircons are fractured or fragmented. Unfractured zircons in the charnockite are extremely variable in terms of their length-width ratio (Table 3.1), with an average value of $\simeq$2. The zircons from the charnockite are also typified by a wide range in color: from dark brown and nearly opaque to pale lilac and transparent. Concentric internal zoning and radial fractures are readily apparent in grains immersed in oil and in thin section. No corrosion or surface pitting is evident from secondary electron images.

Zircons from the retrograde ultramylonites of the Rockfish Valley Fault Zone (Figure 3.4f, 3.7b) are less diverse in terms of color, morphology and zoning than the zircons from the protolith. Zircons from the ultramylonite are typically pale lilac in color (some are stained yellow-brown by Fe oxides) and the majority ($\simeq$ 60%) bear one or more fracture surfaces (Figure 3.7b). Unbroken crystals display the same complex terminations and rounded appearance as the zircons from the protolith. In terms of length-width ratio, complete crystals from the ultramylonite are similar to the zircons from the undeformed charnockite. in average size (Table 3.1). The fractured grains, however, have a slightly lower average length-width ratio, although there is some overlap at the 1-σ level with the measurements from unfractured grains (Table 3.1). Thin section studies (Figure 3.6 c) reveal features that are consistent with brittle failure of zircons in a strain gradient. Broken grains are typically fractured at the center along planes nearly perpendicular to the foliation, and the widest fracture spacing occurs at the center. Such fracture patterns are broadly similar to those produced by brittle failure via a fiber loading mechanism (e.g. White et al. 1980). The distribution of fractures also indicates that the zircon in Figure 3.6 c was subjected to a maximum tensional stress oriented approximately parallel to its c-axis. However, the zircon fragments tend to follow a somewhat curvilinear path, which suggests that a rotational component was also involved.

Figure 3.7. **Secondary electron images of zircons:** (a) - charnockite unit of the Pedlar Massif (+200), (b) - greenschist-grade mylonite of the Rockfish Valley Fault Zone (+200). (c) - BSE image of a zircon in a thin section of mylonite, showing fracture patterns indicative of fiber loading. Mylonitic foliation is parallel to long axis of photograph.

A
00022 100µm
B
+100
00071 100µm

Backscattered electron imaging

Backscattered electron (BSE) images of polished sections of zircons from the Ponaganset gneiss indicate that the two gneissic units contain zircons with distinct zoning patterns and trace element distributions. Zircons from the gray augen gneiss (Figure 3.8a, b) are characterized by extremely fine scale (< 1 μm) oscillatory zoning, although some grains display no contrasts in average Z-number (or atomic number) at all. Rare grains from the gray augen gneiss also have high-U, metamict central regions (Figure 3.8b) surrounded by radial cracks. Zircons from UM 419 generally resemble those from the protolith gray augen gneisses, although a significant population ($\simeq$10%) of zoned (Figure 3.8c) and overgrowth-bearing (Figure 3.8d) grains (which are not present in the gray gneiss) is present.

Zircons from the C fraction of the pink gneiss are also zoned, but the individual zones are much wider (Figure 3.9a) and display very high apparent Z-number contrasts relative to the gray gneiss zircons. pink gneiss zircons are often radially fractured and, unlike those from the gray augen gneiss, are subject to differential leaching by HF vapor. The OG fraction (Figure 3.9 b,c,d) is characteristically heterogenous, and reflects two apparent stages of growth. OG zircons consist of a fractured, euhedral, concentrically-zoned igneous core and an irregular, porous overgrowth, which is subject to severe attack by HF vapor. The overgrowth-core boundary is typically sharp and well-defined, and fractures in the core do not propagate across it (Figure 3.9 b,c,d). This feature suggests that some Pb loss could have occurred during the development of the overgrowths. The BSE images show that the porous overgrowths consistently have a higher average Z number than any region within the primary core. Microprobe data (presented in the next section of this paper) suggests that the high Z-number contrast between the overgrowth and the core is largely due to the

Figure 3.8. BSE images of zircons from the Ponaganset gray gneiss. and UM419: (a) and (b) - Gray gneiss. Note the extremely fine-scale (ca. 1 μm) oscillatory zoning. (c) and (d) - UM419. Note the zoning in both (c) and (d), and the porous overgrowth in (d).

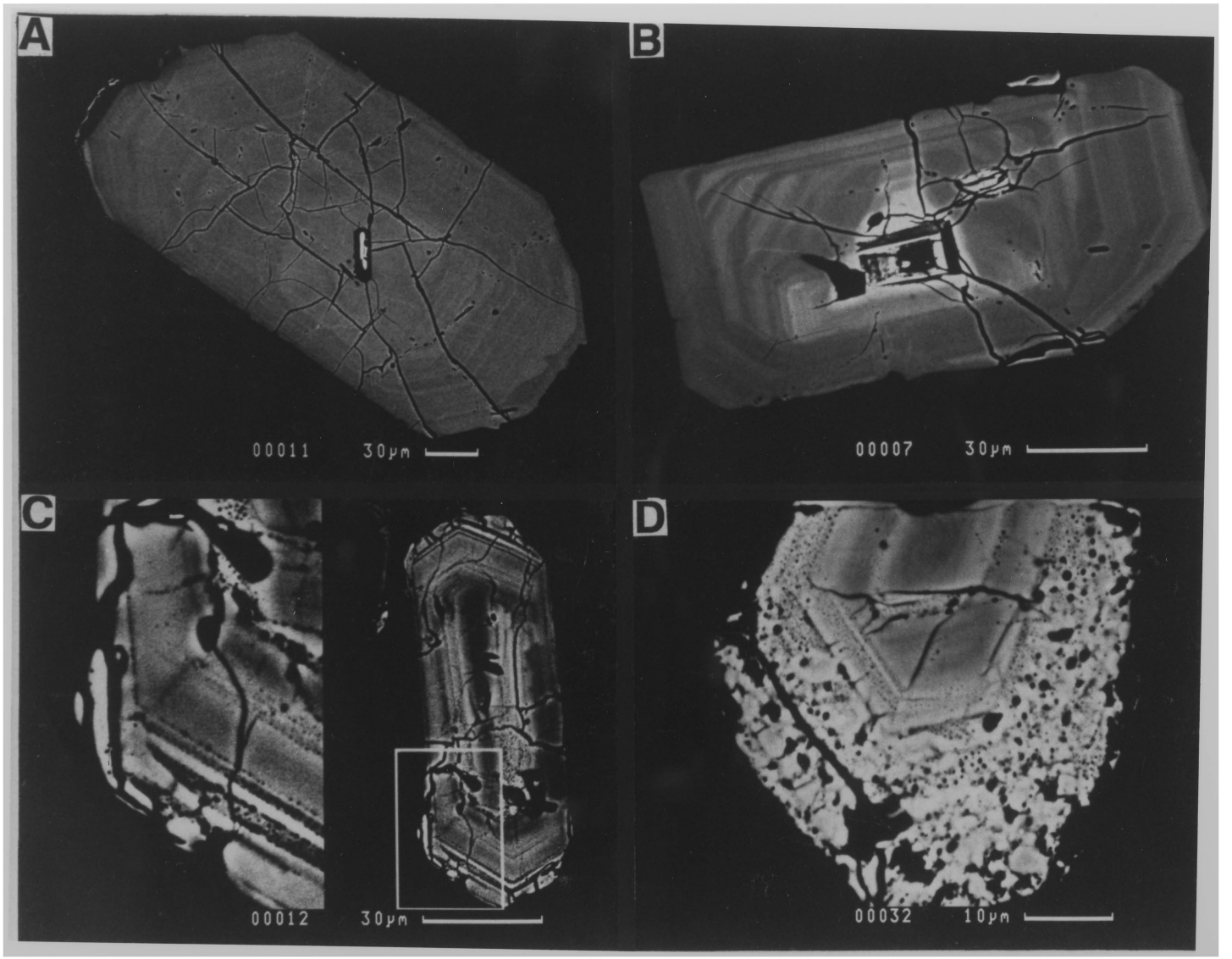
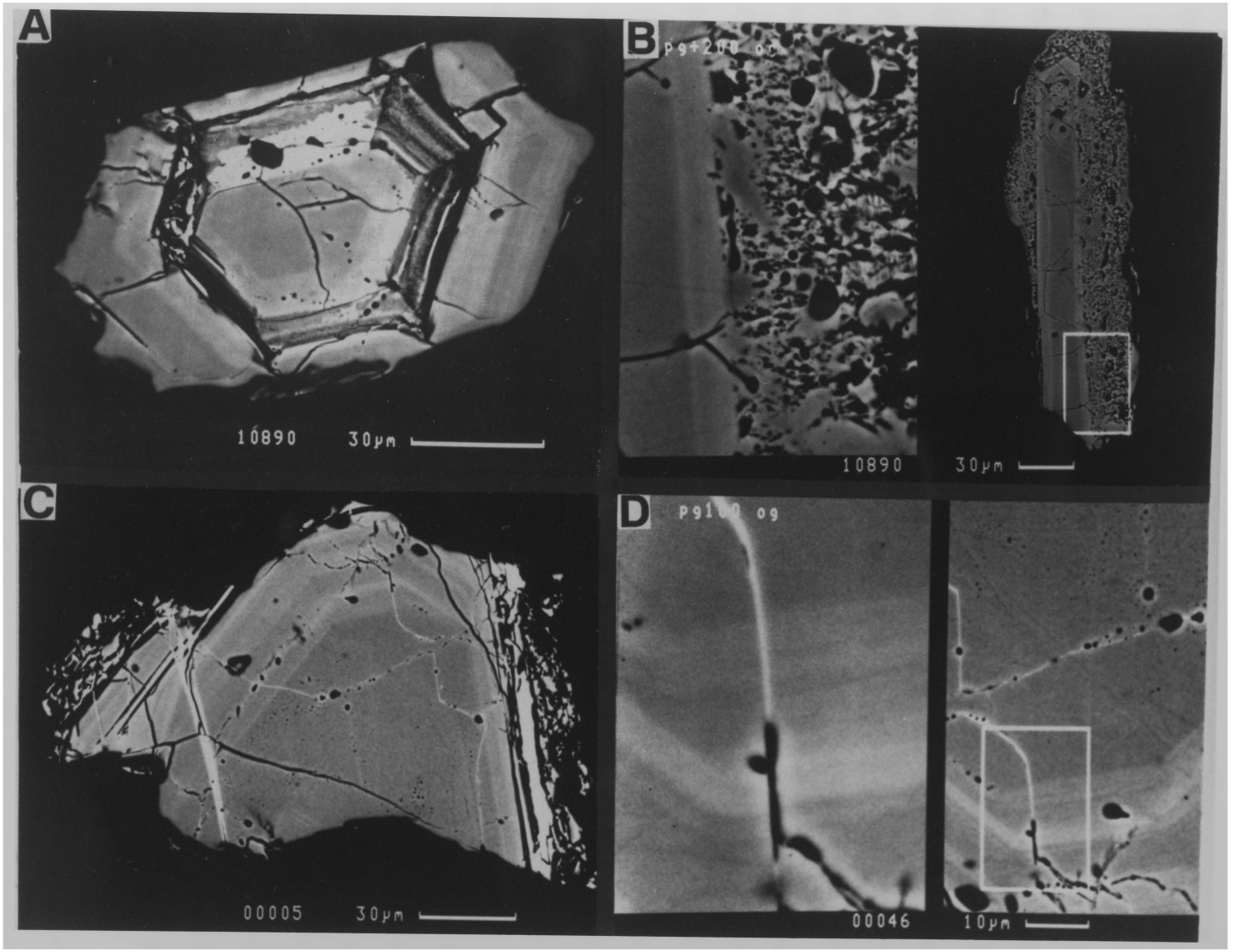

A
00011
30µm
B
00007
30µm
C
00012
30µm
D
00032
10µm

Figure 3.9. BSE images of zircons from the pink granitic gneiss.: Primary, magmatic concentric zoning is apparent in all images, and some grains (a) have internal zones that are preferentially etched by HF vapor. OG zircons (b) consist of a euhedral, concentrically zoned core, and a porous (not etched in HF) outer region. Fractures in the core stop at the core-overgrowth interface. Large zircon fragments (c and d) from the + 100 mesh fraction show evidence of fractures within the core which were later healed by zircon of higher average Z-number (see section on microprobe analysis).


A
10890 30µm
B
10890 30µm
C
00005 30µm
D
00046 10µm

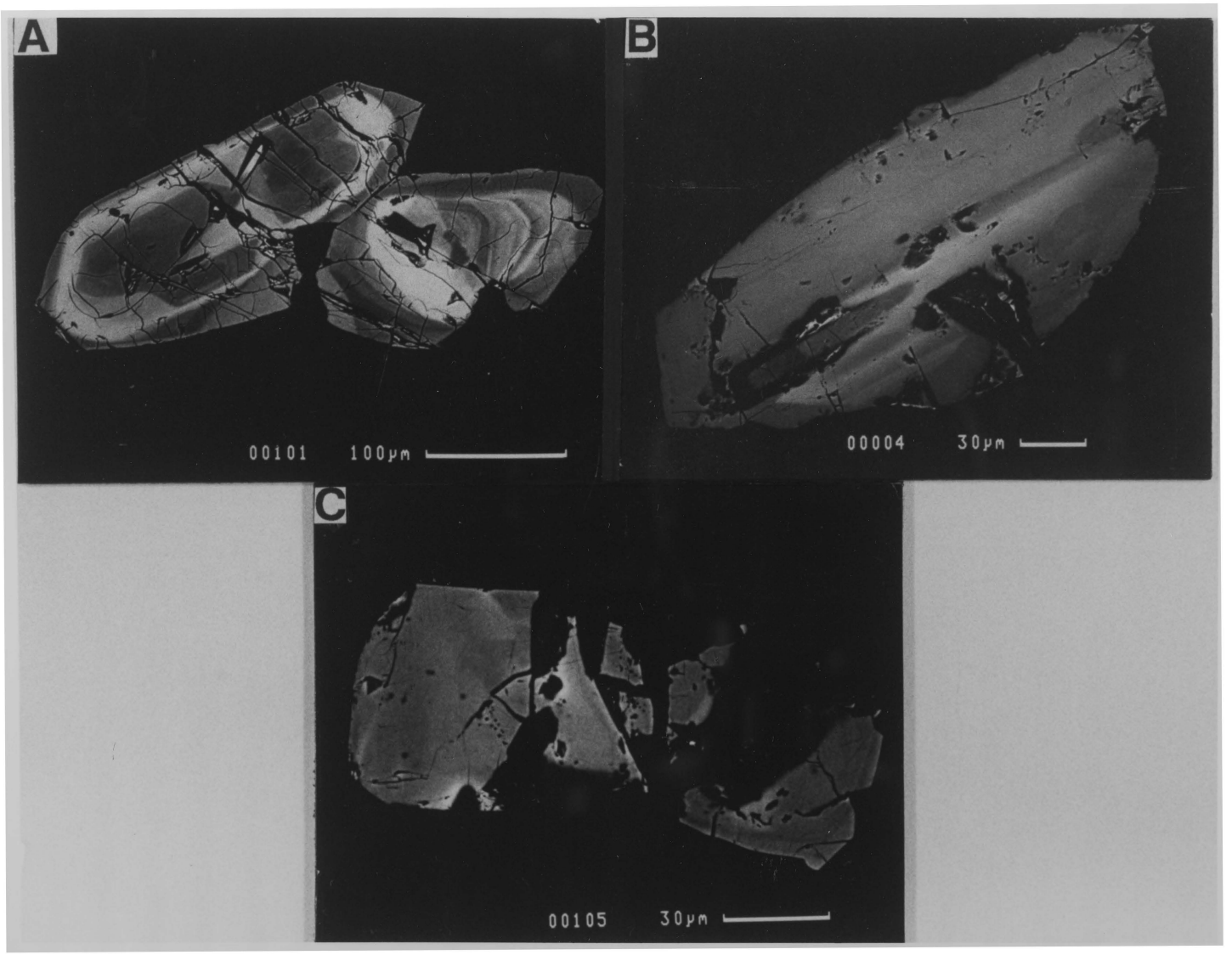
very high HfO_2 content of the overgrowth. Thus, in many respects, the OG zircons from the pink gneiss unit are strikingly similar to those from the Brevard Zone mylonites (Sinha and Glover 1978; Wayne and Sinha 1988).

The presence of zircon overgrowths on pre-existing magmatic zircon in the Ponaganset gneiss requires that zirconium was mobile during some phase of its metamorphic history, particularly in the pink granitic gneiss unit. Zirconium mobility is further supported by the presence of zircons with pitted and corroded surfaces in both the C and OG fractions of the pink granitic gneiss. Additional evidence of Zr mobility is the occurrence of cracks healed with zircon within large zircon grains (+ 100 fraction) in the pink gneiss. Figure 3.9c shows a large, concentrically-zoned, fractured magmatic zircon core with a thin ($\simeq$20 μ) metamorphic rim. The fractures cross-cut the zones within the core, but not the metamorphic rim, and are filled with zircon that has a higher average Z than the core. Higher magnification (Figure 3.9d) reveals areas where individual, continuous fractures pass from unfilled to filled. Healed cracks within zircons have also been noted by Grauert (1974), and may be an extremely important factor in Pb loss/U gain processes. Given the lack of Zr-bearing phases other than zircon, and the strong etching and corrosion observed in the pink gneiss zircons, it is likely that the primary source for Zr mobilized during the metamorphism and mylonitization of the Ponaganset gneiss was pre-existing magmatic zircon.

Zircons from the charnockite unit of the Pedlar Massif are typified by complex, concentric zoning (Figure 3.10a). When viewed under a polarizing microscope, the average Z number contrast apparent in the BSE corresponds to birefringence contrasts. In the thin section (which is of standard thickness: 30 μm), zones which have relatively low birefringence (1° yellow to red) correspond to zones of brightness in the BSE, and highly birefringent zones (2° green) correspond to dark zones in the BSE. This suggests that the contrasts in average Z are correlable to changes in the total α-dosage of the different zones by virtue of their relatively high contents of high Z-number substituents (e.g. U, Th).

Besides the zoning features, at least three distinct fracture sets are apparent in these zircons (Figure 3.10a): 1) crosscutting, unstable cracks, some of which extend into adjacent mineral grains (not seen in BSE), 2) radial microfractures which tend to die out in zones of relatively high average

Figure 3.10. BSE images of zircons from the charnockite and the Rockfish Valley Fault Zone: (a) - Zircons from the charnockite are euhedral, zoned and contain both crosscutting, tectonically-induced unstable cracks, and internal microfractures. One population of microfractures is radially oriented, while the other set follows a curvilinear path roughly parallel to the zoning. (b) - Zoning in the zircon from the mylonite is not readily apparent, but remnants of a zone having a relatively low Z-number are visible around the perimeter of the grain. The long axis of the zircon in (b) is roughly parallel to the mylonitic foliation.


A
00101 100µm
B
00004 30µm
C
00105 30µm

Z number, 3) curved internal microfractures which follow trajectories that roughly parallel the concentric zoning. Type 1 cracks are probably related to late-stage fracturing of the charnockite itself in the vicinity of the Rockfish Valley Fault Zone Type 2 radial fractures are due to internal stresses exerted by differential swelling as the result of the accumulation of point defects related to α-recoil damage (e.g. Chakoumakos et al. 1988). The termination of the radial microcracks in zircon of relatively high Z-number (and relatively high α-dosage) may be due to crack-tip blunting brought on by the inability of the crack to propagate through the dense tangle of dislocations and point defects present in the damaged zircon (Clinard and Hobbs 1986). Type 3 cracks may arise by a similar process whereby the crack, unable to propagate through the zones of high α-dosage, seeks a low-energy path roughly parallel to the discontinuity. The degree to which the latter two processes are accentuated or assisted by external stresses is not known, although similar fracture patterns have been observed in zoned zircons from the Brevard Shear Zone (Wayne and Sinha 1988).

Backscattered electron images of the zircons from the Rockfish Valley Fault Zone (Figures 3.7c and 3.10b) reveal a lack of the compositional zoning that characterized the zircons of the charnockite protolith. The effects of greenschist-grade mylonitization is typified by the zircon shown in Figure 3.10b, where zoning is diffuse or completely absent in most of the grain, but remnants of a zone having relatively low average Z are still visible on its outer perimeter. Three explanations for this phenomenon seem plausible: 1) the zircons were partially annealed during greenschist-grade mylonitization in a H_2O-rich environment, 2) less strongly zoned (hence less metamict), pale lilac zircons were more resistant to fracturing than the large zoned grains, and 3) the rounded, rather homogenous zircons of the ultramylonites represent portions of the zoned grains from the charnockite. Model 1 would require partial (if not total) resetting of the U-Pb isotopic system during the late Paleozoic event. Models 2 and 3 require the operation of purely mechanical processes during mylonitization. In model 3, the outer portions of the zircons, already riddled with microcracks, would be more susceptible to removal and comminution during grain size reduction in a stress field dominated by a simple shear component.

Electron microprobe analyses

A detailed electron microprobe study of the zircons from the Ponaganset gneiss, the Pedlar charnockite and the associated mylonites was undertaken to chemically characterize different zircon populations within each unit, as well as to characterize distinct chemical domains within single grains. Many workers (e.g. Black et al. 1986) have pointed out that the presence of discrete chemical domains (i.e. optically distinct cores and/or rims) within single zircon crystals does not necessitate a polygenetic history of zircon growth. Conversely the opposite may also be true: the absence of such zones does not necessitate a single stage of zircon growth. However, when a correlation between chemistry, morphological features and the ages of zircon populations can be established, a great deal more can be said about the processes involved in the growth history of the zircons and their subsequent isotopic evolution.

Microscopic evidence presented thus far suggests that, in the pink granitic unit of the Ponaganset gneiss, extensive new growth of zircon occurred, presumably during an amphibolite-grade deformational/metamorphic event. During the same event, such growth did not occur in the gray augen gneiss unit and progressed only to a very limited extent in the ultramylonites derived from the gray gneiss. By contrast, zircons from the retrograde mylonites of the Rockfish Valley Fault Zone show no signs of metamorphic overgrowths, but do lack the pronounced internal zoning that characterized the zircons from the charnockite protolith. Thus, the vastly different physical processes involved in the observed morphological changes should also have a distinct chemical signature, which can be systematically studied using microanalytical techniques.

For the most part, the measured concentrations of trace and minor elements (e.g. REE, U, Th, etc.) in zircons from the gray gneiss are at (or below) the stated detection limits of the electron microprobe, although Y and Hf are comparatively abundant (Table 3.2, analysis a). Regions of zircon with comparatively high (i.e. bright) BSE response contain significantly higher amounts of U, Hf, Yb and Y than the surrounding material (Table 3.2, analysis b) However, discrete trace element-enriched zones are uncommon in zircons from the gray gneiss, and the typical pattern of

variation in trace element concentrations is exemplified by the subtle, fine-scale oscillatory zoning apparent in Figure 3.8a. Zircons from the mylonite UM419 show a wider range in zoning patterns (as revealed in Figure 3.8 c and d) and trace element chemistry (Table 3.2, analysis c) than do the zircons from the gray augen gneiss protolith, but are, in most aspects, chemically similar to zircons from the protolith gray augen gneiss. Unlike the zircons from the gray augen gneiss, or the +200 fraction from UM419, a small proportion of zircons in the -200 fraction of UM419 bear porous metamorphic overgrowths (Figure 3.8 d). Microanalysis of the overgrowth shown in Figure 3.8 d (Table 3.2 d) reveals a sharp positive discontinuity in the concentrations of all trace and minor constituents, with respect to their abundance in the core.

Similar chemical trends are evident among the zircons from the pink granitic gneiss and the associated mylonites (UM872), which are dominated by overgrowth-bearing grains. These grains typically consist of a zoned, euhedral core (Table 3.2, analyses e, g, h, i, k) and an irregular, porous overgrowth (Table 3.2, analyses f, l). Chemical zonation within the cores is typified by systematic variations in the concentrations of Hf, Y, and to a lesser extent, U and HREE. Duplicate spot analyses within sharply bounded internal zones of varying brightness (Figure 3.9 c; and Table 3.2, analyses g, h, i) show systematic variations between the brightness of the BSE response and the abundances of elements with high Z-numbers (e.g. Hf, U, etc.). As expected, the brightest zones in the core have the highest concentrations of high Z-number elements. Within the same zircon grain, a narrow region of maximum BSE intensity (Table 3.2, analysis j) which abruptly crosscuts the concentric zoning pattern (presumably a healed fracture) contains 2.9 wt.% HfO_2 and almost 0.06 wt.% UO_2, which well exceed the concentrations of these elements in the remainder of the core. This implies that early fractures incurred by large zircon grains during dynamic metamorphism were subsequently healed by a later generation of trace-element-enriched zircon.

Porous zircon rims are typically enriched in Hf, U and Yb with reference to the cores. The low totals of these analyses are attributable to both surface irregularities, and adsorption of H_2O as the result of the relatively high degree of radiation damage that stems from the high U concentrations. Interestingly, the rims themselves are distinctly inhomogenous in terms of their trace and minor element concentration levels. Within-rim chemical variation is high, as evidenced by the high

Table 3.2. Microprobe analyses of zircons. See Figures 8, 9, 10 for BSE images of all analyzed grains (except k,l,m).

	a: 8B	b: 8B	c: 8D		d: 8D		e: 9B		f: 9B	
	GG+200(L)	GG+200(H)	UM419 -200 CORE		UM419 -200 RIM		PG+200 CORE		PG+200 RIM	
	(2)	(2)	(4)	*STD*	(4)	*STD*	(10)	*STD*	(10)	*STD*
P2O5	0.056	0.280	0.121	*0.026*	0.163	*0.118*	0.069	*0.023*	0.030	*0.027*
SiO2	33.047	32.138	32.611	*0.323*	31.938	*0.480*	32.437	*0.167*	31.769	*0.250*
ZrO2	64.808	64.647	65.176	*0.437*	62.275	*0.886*	65.800	*0.368*	63.668	*0.794*
HfO2	1.367	1.809	1.324	*0.042*	1.926	*0.182*	1.630	*0.040*	1.824	*0.241*
ThO2	0.027	0.021	0.062	*0.044*	0.350	*0.102*	0.026	*0.029*	0.026	*0.020*
UO2	0.000	0.126	0.033	*0.040*	0.911	*0.155*	0.050	*0.042*	0.072	*0.034*
Y2O3	0.094	0.266	0.275	*0.056*	0.436	*0.216*	0.181	*0.090*	0.111	*0.039*
Er2O3	0.008	0.034	0.073	*0.032*	0.128	*0.047*	0.050	*0.057*	0.099	*0.046*
Yb2O3	0.036	0.105	0.129	*0.047*	0.252	*0.041*	0.094	*0.057*	0.204	*0.077*
CaO	0.002	0.003	0.023	*0.034*	0.144	*0.083*	0.011	*0.009*	0.051	*0.031*
FeO	0.008	0.074	0.416	*0.568*	0.049	*0.021*	0.020	*0.022*	0.059	*0.035*
total	99.452	99.504	100.243	*0.288*	98.572	*1.301*	100.368	*0.572*	97.912	*1.013*

	g: 9C	h: 9C	i: 9C	j: 9C	k		l		m	
	CORE(L)	CORE(I)	CORE(H)	FRACTURE	PG+200 CORE		PG+200 RIM		UM 872 *	
	(2)	(2)	(2)	(2)	(3)	*STD*	(4)	*STD*	(4)	*STD*
P2O5	0.072	0.072	0.072	0.047	0.062	*0.008*	0.453	*0.627*	0.16	*0.13*
SiO2	32.676	32.891	32.903	32.687	32.579	*0.196*	29.710	*1.945*	30.36	*0.19*
ZrO2	66.043	65.848	65.715	64.823	65.622	*0.472*	63.190	*2.093*	59.59	*0.59*
HfO2	1.033	1.373	1.720	2.902	1.617	*0.013*	1.977	*0.189*	4.83	*0.30*
ThO2	0.005	0.000	0.008	0.029	0.041	*0.033*	0.049	*0.026*	0.13	*0.03*
UO2	0.000	0.000	0.022	0.057	0.020	*0.021*	0.178	*0.074*	0.38	*0.13*
Y2O3	0.053	0.093	0.080	0.050	0.169	*0.022*	0.190	*0.021*	0.32	*0.07*
Er2O3	0.032	0.117	0.028	0.076	0.057	*0.046*	0.051	*0.058*	N.A.	-
Yb2O3	0.000	0.057	0.036	0.056	0.067	*0.039*	0.268	*0.083*	0.36	*0.08*
CaO	0.003	0.011	0.006	0.011	0.001	*0.001*	0.295	*0.196*	0.09	*0.05*
FeO	0.010	0.000	0.000	0.009	0.020	*0.014*	0.384	*0.298*	0.23	*0.20*
total	99.926	100.462	100.590	100.748	100.256	*0.697*	96.746	*2.869*	96.45	*1.89*

* = analysis performed on the ARL-SEMQ probe (see Chapter 2).

Table 3.2. Electron microprobe analyses of zircons, continued.

	n: 10A PC LOW BSE		o: 10A PC HIGH BSE		p: 10B RVFZ RIM		q: 10B RVFZ CORE	
	(3)	*STD*	(4)	*STD*	(6)	*STD*	(3)	*STD*
P2O5	0.061	*0.008*	0.028	*0.014*	0.014	*0.012*	0.050	*0.021*
SiO2	32.956	*0.124*	32.558	*0.128*	33.060	*0.174*	32.797	*0.060*
ZrO2	65.805	*0.277*	64.682	*0.429*	66.592	*0.083*	66.032	*0.221*
HfO2	1.230	*0.020*	1.854	*0.034*	1.341	*0.061*	1.127	*0.011*
ThO2	0.018	*0.026*	0.019	*0.018*	0.007	*0.009*	0.014	*0.016*
UO2	0.000	*0.000*	0.277	*0.022*	0.003	*0.007*	0.023	*0.032*
Y2O3	0.059	*0.015*	0.086	*0.019*	0.011	*0.016*	0.186	*0.002*
Er2O3	0.063	*0.045*	0.112	*0.045*	0.050	*0.051*	0.074	*0.059*
Yb2O3	0.057	*0.081*	0.099	*0.061*	0.011	*0.016*	0.073	*0.049*
CaO	0.012	*0.004*	0.018	*0.006*	0.015	*0.012*	0.006	*0.009*
FeO	0.021	*0.024*	0.026	*0.026*	0.206	*0.054*	0.113	*0.013*
total	100.284	*0.302*	99.758	*0.528*	101.310	*0.183*	100.494	*0.257*

standard deviations of the averaged analyses. The abundance of trace and minor constituents in the rims also varies dramatically from grain to grain, which suggests that the availability or the partitioning behavior such as U, Hf and Y was locally controlled during zircon growth. Several rim analyses (not shown) further indicate that the rims, in some cases, consist of a mixture of trace-element-rich zircon and a Y-phosphate mineral, probably xenotime. Concentration levels of Hf, Y, U and other trace constituents in zircons from UM872 (Table 3.2, analysis m) exceed those observed anywhere else in the Ponaganset gneisses and mylonites.

Microprobe analyses of zircon from the charnockite unit of the Pedlar Massif a demonstrate a strong correlation between BSE intensity and the relative concentration levels of trace and minor elements (Figure 3.10 a; Table 3.2, analyses n and o). The bright zones contain greater amounts of U, Hf and REE than do the dull zones. The high U content of the bright zones is also consistent with their lower birefringence, caused by the accumulation of lattice defects due to α-decay. Zircons from the Rockfish Valley Fault Zone typically lack both the well-defined concentric zones of bright BSE response and regions with high U content (Figure 3.10 b; Table 3.2 p and q). Compositionally, zircons from the Rockfish Valley Fault Zone are similar to the regions of zircons from the protolith charnockite which have low BSE response.

Results of the microprobe study of the zircons from the Ponaganset gneiss suggest that: 1) a compositionally distinct population of trace-and-minor-element- enriched zircon grew in UM872, the pink granitic gneiss, and to a lesser extent in UM419, while none grew in the gray augen gneiss unit, 2) the chemistry of the zircon formed during the amphibolite-grade metamorphism of the Ponaganset gneiss is similar to the high U, Y, Hf, P zircon which grew during metamorphism/mylonitization of the late Precambrian Henderson gneiss (Sinha and Glover 1978; Wayne and Sinha 1988), 3) differential BSE response in the zircons analyzed using the electron microprobe corresponds to quantifiable differences in minor and trace element chemistry, namely variation in concentrations of HfO_2 and UO_2, and 4) zircons from the Rockfish Valley Fault Zone lack the well-defined, U-rich zones that characterize zircons from the charnockite protolith.

Isotopic Analyses

Ponaganset Gneisses and Mylonites: Zircon data

Lead isotopic compositions, and Pb and U concentrations, were determined for four size fractions (+100, +200, +325, -325) of zircons from the Ponaganset gray gneiss, two size fractions (+200, -200) from the mylonite derived from the gray gneiss (UM 419), three size fractions (+100, +200, +325) of clear (fraction C) zircons from the pink gneiss, and three size fractions (+100, +200, +325) of opaque (fraction OG) zircons from the pink gneiss. In addition, Pb and U isotopic data was collected on an unsorted fraction from the pink gneiss (-325) and on an unsized fraction of opaque zircons from a mylonite zone from within the pink gneiss (UM 872). The data from each gneiss unit and the associated mylonite zone (Table 3.3) were pooled and plotted on separate concordia diagrams (Figures 3.11, 3.12). In each case, linear mixing arrays resulted which indicate a latest Precambrian magmatic crystallization age and Pennsylvanian to Permian metamorphism/ deformation.

In the Ponaganset gneiss, zircons from the gray augen gneiss unit have $^{207}Pb/^{206}Pb$ ages which range from 598 m.y. (+325 fraction) to 574 m.y. (+200 fraction). The $^{207}Pb/^{206}Pb$ ages do not vary systematically with grain size, nor do the Pb/U ages, Pb concentrations or U concentrations (Table 3.3, Figure 3.13a). The $^{206}Pb/^{238}U$, $^{207}Pb/^{235}U$ and $^{207}Pb/^{206}Pb$ ages of the zircons from the mylonite derived from the gray gneiss (UM 419) are slightly, but consistently, younger than those obtained from the gray gneiss. Thus, the zircon U/Pb isotopic system did not remain closed during amphibolite-grade mylonitization of the gray augen gneiss. The +200 UM 419 fraction contains comparable, but significantly lower concentrations of U and Pb than any of the gray gneiss fractions. The observed differences in U and Pb concentration are above the analytical uncertainties utilized in this study, and reflect either primary variability in the U and Pb content of the different zircon populations, or a slight loss of Pb and U from the +200 UM 419

Table 3.3. U-Pb isotopic data from the Ponaganset gneiss and the Rockfish Valley Fault Zone, corrected for mass fractionation, blank, common Pb.

sample	U (ppm)	Pb (ppm)	$^{206}Pb/^{204}Pb$ #	$^{207}Pb/^{206}Pb$ #	$^{206}Pb/^{208}Pb$ #	$^{207}Pb/^{235}U$ *	$^{206}Pb/^{238}U$ *	$^{207}Pb/^{206}Pb$ *	$^{207}Pb/^{206}Pb$ Age(m.y.)
Ponaganset Gneiss									
Gray augen gneiss and UM 419									
GG+100	252	25	1,487	0.06899	4.7525	0.7306	0.08948	0.05922	575 +/-16
GG+200	264	25	1,796	0.06728	5.2420	0.7206	0.08830	0.05919	574 +/-18
GG+325	276	28	3,669	0.06380	4.9462	0.7561	0.09162	0.05985	598 +/- 2
GG-325	233	24	9,000	0.06130	4.4684	0.7478	0.09085	0.05970	593 +/- 4
UM+200	212	21	1,127	0.07210	4.9841	0.7106	0.08705	0.05920	574 +/- 6
UM-200	592	51	4,909	0.06178	5.5137	0.6450	0.07954	0.05882	560 +/- 5
Pink granitic gneiss and UM 872									
PG+100 C@	183	17	605	0.08276	4.6788	0.6636	0.08254	0.05832	542 +/-33
PG+200 C	416	36	4,456	0.06224	5.9720	0.6669	0.08207	0.05893	565 +/- 8
PG+325 C	374	34	1,143	0.07200	5.3128	0.6774	0.08315	0.05908	570 +/- 5
PG+100OG	1,196	84	467	0.08696	5.1135	0.4682	0.06108	0.05560	436 +/- 9
PG+200OG	1,277	82	3,138	0.06056	7.6340	0.4779	0.06200	0.05590	448 +/- 5
PG+325OG	1,370	86	2,897	0.06119	7.4916	0.4709	0.06083	0.05615	458 +/- 5
PG-325	1,314	85	4,930	0.05919	7.5107	0.4881	0.06296	0.05623	462 +/- 3
UM 872	1,183	66	4,708	0.05836	11.8310	0.4283	0.05621	0.05526	423 +/- 4
Rockfish Valley Fault Zone									
ultramylonite									
RV+100	190	36	9,666	0.07521	7.0756	1.8281	0.17980	0.07374	1034 +/- 2
RV+200	185	31	2,979	0.07820	6.2130	1.5735	0.15544	0.07342	1026 +/-12
RV+325	181	30	2,736	0.07848	6.0409	1.5774	0.15614	0.07327	1022 +/-14
charnockite **									
PC+200	273	43	9,237	0.07526	10.0200	1.5948	0.15690	0.07372	1034 +/- 4
PC+325	286	45	10,108	0.07499	9.8943	1.5826	0.15601	0.07358	1030 +/- 2

All fractions nonmagnetic 1.75 amps. on Frantz seperator

= data corrected for mass fractionation, blank, common Pb

** = see also Sinha and Bartholomew

@ = sample not used in regression due to large errors

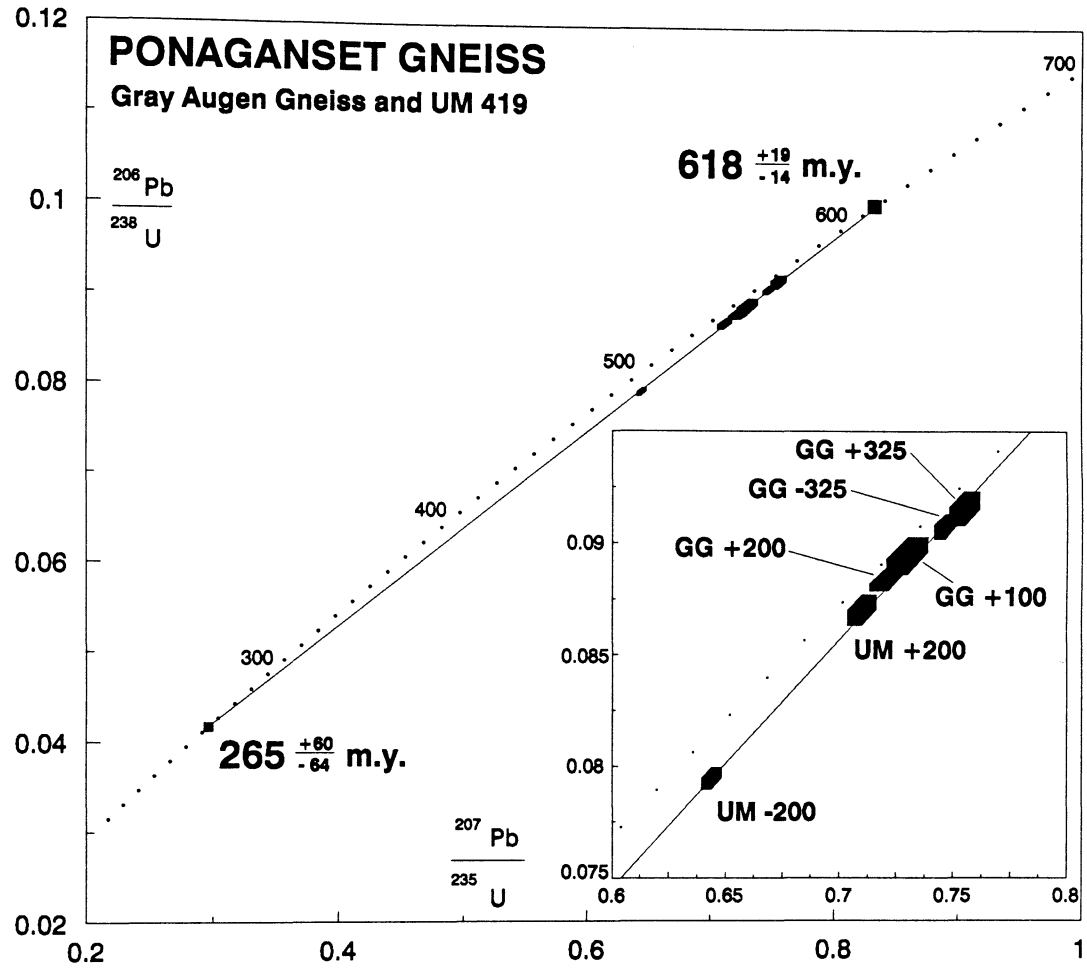


Figure 3.11. Zircon U-Pb data from the Ponaganset gray gneiss: All errors represent 2σ uncertainties.

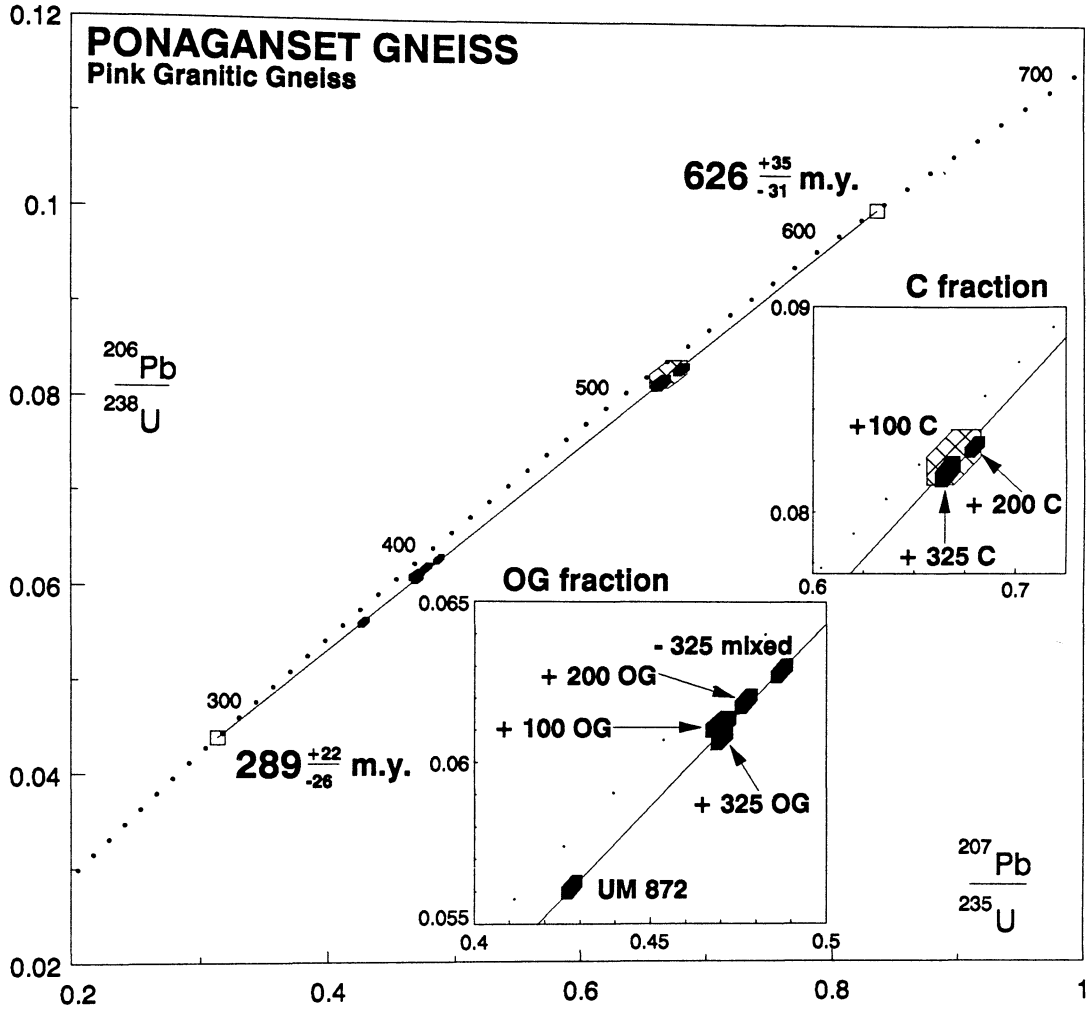


Figure 3.12. Zircon U-Pb data from the Ponaganset pink gneiss: All errors represent 2σ uncertainties.

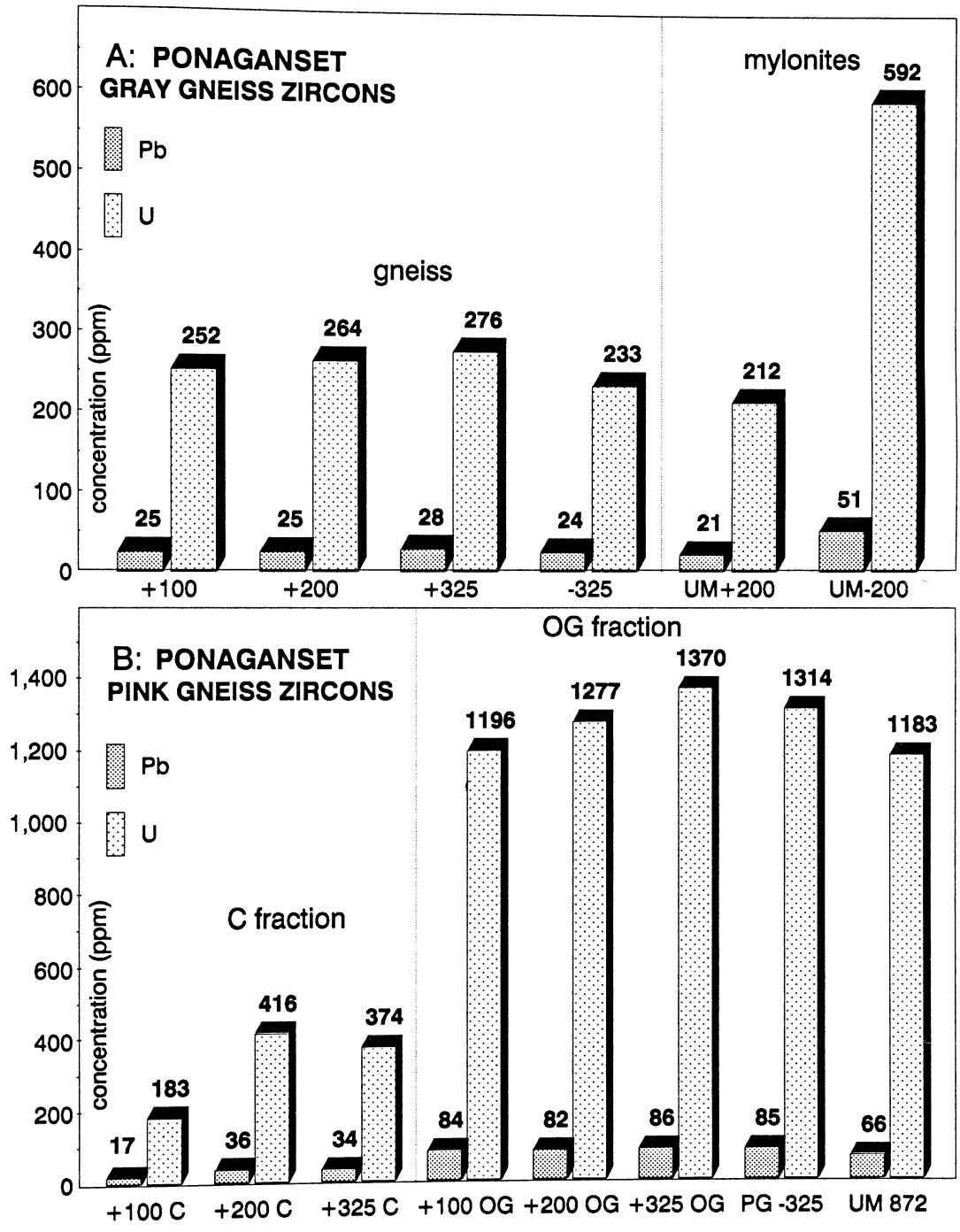


Figure 3.13. **U and Pb concentrations of zircon separates from the Ponaganset gneiss:** (a) - gray gneiss, (b) - pink gneiss. Note the strong correlation between high U concentration with the presence of metamorphic overgrowths in the samples from the pink gneiss.

fraction. By contrast, both U and Pb concentrations are greater in the -200 UM 419 fraction than in the +200 UM 419 zircons, or in any fraction from the gray gneiss, by a factor of two. The sharp rise in the U and Pb concentrations and the marked discordance of the -200 UM 419 fraction is best attributed to the presence of a small amount of cloudy-to-opaque, U rich metamorphic zircon (e.g. Figure 3.8d). These data suggest that the slight discordance of the +200 UM 419 fraction is due to Pb loss, while the discordance of the -200 UM 419 zircons is caused primarily by U gain.

Combined, the four gray gneiss fractions and the two UM 419 fractions describe a chord with an upper intercept of 617 (+21/-15) m.y., and a lower intercept of 256 (+65/-69) m.y. Although the lower intercept age approximates the age of deformation, the large error on this age is due to the clustering of five (out of six) data points to within $\simeq$15 % of the upper intercept (Figure 3.11).

The U-Pb isotopic systematics and chemistry of the pink gneiss zircons are highly correlated to the presence of apparent metamorphic overgrowths. The $^{207}Pb/^{206}Pb$ ages of three size fractions of clear, yellow (C fraction) zircons range from 578 m.y. to 558 m.y., and increase with decreasing grain size. The U and Pb concentrations (Table 3.3, Figure 3.13 b) of the +100 C fraction are markedly lower than those observed for the +200 and +325 C fractions. This may be due to 1) inability to obtain a 100% pure separate of overgrowth-free zircon from the smaller size fractions by hand picking, 2) Pb and U loss facilitated by preferential corrosion of the +100 fraction by metamorphic fluids, and/or 3) primary variability of U and Pb contents among the different zircon populations.

Data from three fractions of pale brown, turbid zircons (OG fraction), a mixed (C and OG fractions not separated) population of -325 mesh zircon and a fraction from the mylonite derived from the pink gneiss (UM 872) yield considerably younger $^{207}Pb/^{206}Pb$ and U/Pb ages, and substantially higher Pb and U concentrations (66 to 86 ppm Pb; 1186 to 1373 ppm U). Among the OG fractions from the pink gneiss, the $^{207}Pb/^{206}Pb$ ages are inversely correlated to size, with the finest fraction (+325) giving the oldest age. The youngest $^{207}Pb/^{206}Pb$ age was obtained from the UM 872 sample, indicating that these zircons have the highest overgrowth-to-core ratio. However, it is important to note that isotopic ages obtained from the heterogenous OG fractions are perhaps

not entirely a function of overgrowth to core ratio, particularly where loss of radiogenic Pb may have resulted from corrosion and leaching.

On a concordia diagram, pooled data from all C fractions, all OG fractions, the -325 fraction and the UM 872 fraction (eight data points) describe a chord with equally well-constrained upper and lower intercept ages of 626 (+31/-27) m.y. and 287 (+23/-26) m.y., respectively. These ages agree, within 2 σ errors, with those obtained from the gray augen gneiss zircons. Note also the strong grouping of data from the C fraction and the OG fraction

Ponaganset Gneisses and Mylonites: Feldspar data

Lead isotopic ratios obtained from alkali feldspars (Table 3.4) provide information on the isotopic composition of Pb possibly incorporated into zircon during magmatic crystallization, and during the formation of metamorphic overgrowths. The feldspar data also shed some light on the processes involved in the redistribution of Pb during mylonitization. The isotopic composition of Pb in alkali feldspar porphyroclasts taken from both the pink granitic gneiss and the gray augen gneiss is substantially more radiogenic than the isotopic composition of common Pb (at 620 m.y.) estimated using the two-stage model of Stacey and Kramers (1975). Measured μ values ($^{238}Pb/^{204}Pb$) of the alkali feldspar porphyroclasts from each unit differ substantially and systematically according to rock type (Table 3.4). The differences in the Pb isotopic compositions and μ values in porphyroclasts from the pink granitic gneiss and the gray augen gneiss suggests that the respective units are reservoirs of isotopically distinct Pb. This conclusion is reinforced by the results of whole-rock Rb-Sr studies (Wayne 1990) and stable isotope studies (Stakes, personal communication 1990), which show that the two units also differ in terms of their Sr initial ratios, and oxygen isotopic signatures.

Lead isotopic compositions from alkali feldspar separated from a mylonite at a gray gneiss-amphibolite contact (UM 419), and from a mylonite within a pink gneiss body (UM 872) are dis-

Table 3.4. Pb data for alkali feldspar porphyroclasts and recrystallized alkali feldspar from the Ponaganset gneiss.

sample	Pb	U	$^{206}Pb^{*}/^{204}Pb$	$^{207}Pb^{*}/^{204}Pb$	$^{208}Pb/^{204}Pb$	model age# (m.y.)	mu#
Gray Augen Gneiss							
porphyroclast	21	0.099	18.777 +/- 16	15.670 +/- 20	38.677 +/- 64	33	9.90
UM419	22	0.750	19.219 +/- 17	15.716 +/- 20	39.108 +/- 65	-198	10.02
Amphibolite	12	0.278	18.938 +/- 19	15.687 +/- 21	38.756 +/- 67	- 51	9.94
Pink Granitic Gneiss							
porphyroclast	28	0.884	19.585 +/- 18	15.953 +/- 21	39.765 +/- 67	33	10.95
UM872	29	0.704	19.562 +/- 17	15.751 +/- 20	39.349 +/- 65	-376	10.11

* = isotopic data corrected for 'in situ' U decay (porphyroclast to 620 m.y., mylonite & amphibolite to 280 m.y.)

= calculated model ages and mu values using the method of Stacy and Kramers (1975).

similar from each other, and from the Pb isotopic compositions observed in the porphyroclasts. Both mylonitic alkali feldspar samples are highly radiogenic (Table 3.4), but their μ values are very similar to those obtained from porphyroclasts of their respective protoliths (Table 3.4). The Pb isotopic composition of the alkali feldspar from the mylonite UM 419 is considerably more radiogenic than that of the alkali feldspar porphyroclast from the gray gneiss protolith, which indicates that the alkali feldspar in the mylonite re-equilibrated during mylonitization. By contrast, the isotopic composition of Pb in UM 872 is markedly less radiogenic than that of the alkali feldspar porphyroclast from the pink gneiss. This could be explained by the re-equilibration of UM 872, during mylonitization, with a source of Pb having a less radiogenic composition than the Pb from the alkali feldspar in the pink gneiss. A possible source of such Pb is the gray augen gneiss itself, or fluids which equilibrated with the gray augen gneiss prior to interacting with the pink gneiss in the mylonite zone. This also concurs with oxygen isotope data (Stakes, pers. comm. 1990), which indicates that quartz and magnetite from UM 872 has an oxygen isotopic signature intermediate to quartz and magnetite from the pink granitic gneiss and the gray augen gneiss.

Rockfish Valley Fault Zone

The U-Pb isotopic data for zircons from the charnockitic rocks of the Pedlar Massif were originally presented in Sinha and Bartholomew (1984). For this study, their raw isotopic data was reprocessed using PBDAT (Ludwig 1988), and are listed in table 3. New U-Pb isotopic data were collected on three size fractions (+ 100, + 200, -200) obtained from the Pedlar-derived retrograde mylonites of the Rockfish Valley Fault Zone These data (Table 3.3) suggest that the zircon U-Pb isotopic system remained relatively undisturbed during retrograde mylonitization during the Paleozoic. Specifically, the $^{207}Pb/^{206}Pb$ ages of zircons from the mylonite and the charnockite protolith are consistently Grenvillian.

The three size fractions of zircons from the Rockfish Valley Fault Zone contain approximately the same amount of Pb and U (Table 3.3, Figure 3.14). However, Pb and U concentrations of the zircons from the mylonite zone are distinctly lower than those observed in zircons from the charnockite protolith. The isotopic data from the three size fractions obtained from the mylonite, combined with the data from the charnockite yield a well-constrained upper intercept age of 1033 (+3/-3) m.y. and a lower intercept of 40 (+52/-52) m.y. which is, within error, essentially 0 m.y. in age (Figure 3.15). The upper intercept age is in close agreement with the whole rock Rb-Sr age of 1021 m.y., obtained by Pettingill et al. (1984). Note, however, that the data points representing the charnockite zircons and two of the three mylonite fractions are tightly clustered (Figure 3.15). When combined with the data from the reversely discordant +100 ultramylonite zircons, the result is a chord that is essentially based on two points. Thus, the significance of the upper intercept age is debatable, despite the low errors and excellent correlation with Rb-Sr whole rock isochron ages (Pettingill et al. 1984). More significant is the very close correspondence of the $^{207}Pb/^{206}Pb$ ages of the zircons from the charnockite and the retrograde ultramylonite, which indicates that the zircon U-Pb system remained closed during the greenschist-grade event. This stands in marked contrast to the behavior of the zircon U-Pb system in the ductilely deformed, amphibolite-grade gneisses and mylonites of the Hope Valley Shear Zone, where Pb loss and U-gain are clearly related to late Paleozoic deformation and metamorphism.

It is also interesting to note that, while two of the zircon fractions from the ultramylonite are no more discordant than the zircons from the charnockite protolith, the +100 fraction from the mylonite is, in fact, reversely discordant. Reverse discordance may be caused by laboratory procedures (Aleinikoff 1985), or by geological processes (Williams et al. 1984). We see no evidence to attribute the reverse discordance to analytical problems, and instead suggest that its cause is related to geological factors. There are several possible geologic causes for reverse discordance, and distinctions between them is made here on a purely speculative basis. Selective leaching of U from inclusions within zircon grains is unlikely because inclusions are relatively uncommon in the zircons from the mylonite zone, and because there is no evidence for surface pitting or corrosion apparent in SEM images (Figure 3.7b). BSE images of several zircon grains revealed no high Z-number in-

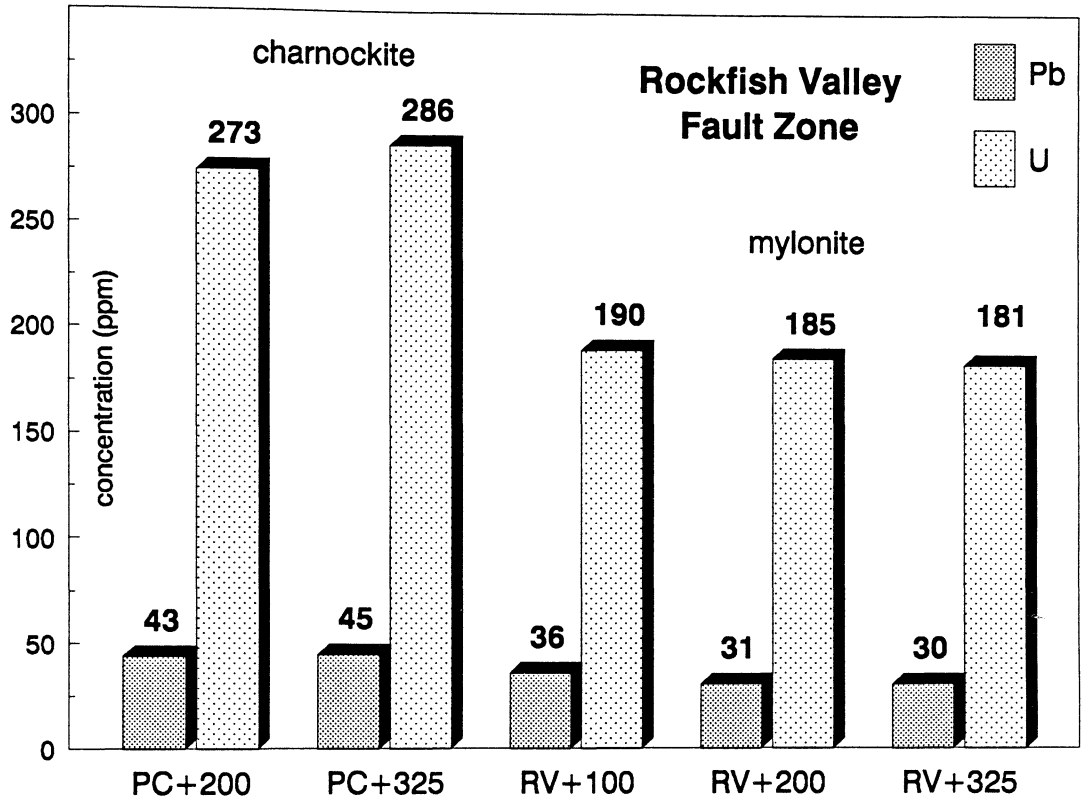


Figure 3.14. U and Pb concentrations of zircon separates from the charnockite and the Rockfish Valley Fault Zone mylonite: Note the consistently lower Pb and U concentrations of the fractions taken from the ultramylonite.

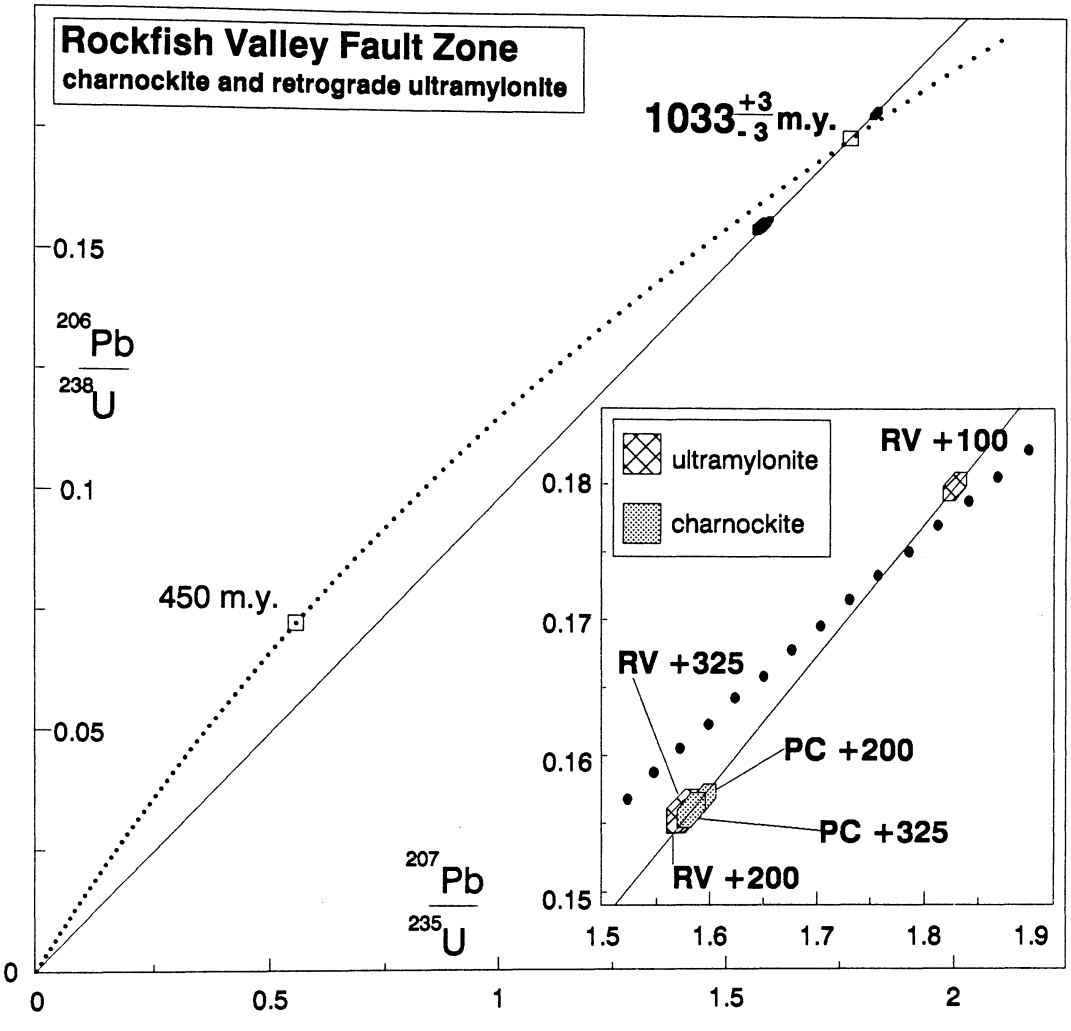


Figure 3.15. Zircon U-Pb isotopic data from the Rockfish Valley Fault Zone mylonite and the charnockite protolith: Note that none of the zircon data from the mylonite is rotated towards the age of mylonitization (≃450 m.y.). All errors represent 2σ uncertainties.

cluded phases, and although no comprehensive analysis of zircon inclusions was undertaken, it is extremely unlikely that only one size fraction of zircons from a single sample would contain such inclusions.

Despite the problems associated with reverse discordance, the zircon U-Pb isotopic data from the charnockite of the Pedlar Massif, and the ultramylonites derived from it, demonstrate unequivocally that the geochemical and physical processes associated with mylonitization do not necessarily result in preferential Pb loss or U gain. The critical factor in the preservation of $^{207}Pb/^{206}Pb$ ages in the mylonites of the Rockfish Valley Fault Zone was the apparent inability of the fluids associated with the deformation and hydration of the retrograde mylonitic assemblage to leach radiogenic Pb, even from severely α-damaged regions of zircon grains. In this case, the brittle failure of zircons during simple shear also did not facilitate Pb-loss, as observed in other mylonitic rocks (Lindh and Schoberg 1988; Wayne and Sinha 1988). Thus, it is apparent that geochronologic information on the timing of movement is not always recorded by the zircon U-Pb system, despite intense physical degradation.

Isotopic stability of zircon in shear zones

Several lines of evidence limit the mechanism and extent of zircon corrosion and reprecipitation in the Ponaganset gneiss. First, the corrosion was probably not caused by a magmatic process such as resorption of pre-existing zircon, because U-Pb isotopic data obtained from the Ponaganset gneiss zircons reveal no trace of an inherited component. Furthermore, whole-rock Rb-Sr isotopic data (Wayne and Sinha 1988, 1989) from both gneiss units yield latest Precambrian to ealy Cambrian ages. While the Rb-Sr ages are somewhat younger than those obtained from the zircon U-Pb data (as would be expected from intensely metamorphosed gneisses), they rule out the possibility of a magmatic origin for the zircon overgrowths in the pink gneiss. Thus, the zircon-

consuming reaction(s) most likely occurred during the Late Paleozoic amphibolite-grade metamorphic event. Second, the fluid phase presumably responsible for zircon corrosion did not cause pervasive resetting of whole-rock Rb-Sr systematics in the gneisses, even on a centimeter scale (Wayne and Sinha 1988, 1989a). This can not be said of certain portions of the mylonite zones, where Rb-Sr whole rock data obtained from thin slabs yield Permian ages (Wayne and Sinha 1988b, 1989a). Third, the corrosion and reprecipitation of zircon in the pink granitic gneiss and UM 872 were spatially restricted. This is evident from the mixture of uncorroded, corroded and overgrowth-bearing zircon in all size fractions from the pink gneiss, and from the occurrence of partially overgrown and variably corroded zircon grains. Furthermore, grain-to-grain chemical variation is typical of zircon overgrowths from the pink gneiss, which supports local control on the availability, mobility, and/or partitioning behavior of high field strength elements (HFSE) during zircon growth.

As noted previously, the pink gneiss contains abundant accessory fluorite, and one possible cause of the observed corrosion and reprecipitation of zircon in the pink gneiss is the enrichment of HF in the vapor phase during metamorphism. To depict the relationships between some of the fluorite-bearing assemblages observed in the pink gneiss and the ratio of μ_{HF} to μ_{H_2O} of the coexisting fluid, a Schreinemakers diagram (Figure 3.16) was constructed in $\mu_{HF} - \mu_{H_2O}$ space which represents a succession of divariant metamorphic reactions related to the univariant assemblage PLAG + AM + BI + DI + FLT + KSP + Q + V, assuming variable An content of plagioclase, but constant P-T and Fe/(Fe+Mg) ratio in the ferromagnesian silicates. The vapor phase is composed of HF and H_2O exclusively. This diagram suggests that, under these idealized conditions, the presence of fluorite is consistent with relatively high μ_{HF} to μ_{H_2O} ratios in the coexisting fluid. The narrow width of the stability fields for each of the assemblages in μ_{HF} vs. μ_{H_2O} space suggests that the observed amphibole- and biotite-bearing assemblages (coexisting with plagioclase of a given An content) could arise at constant P-T and Fe/(Fe+Mg), by small incremental changes in μ_{HF} or μ_{H_2O} However, the pink gneiss sample from which zircons were obtained for this study contained no clinopyroxene, but did contain biotite, hastingsite and Ca-Mn-rich garnet. While it is possible that the garnet (instead of clinopyroxene) participated in HF-buffering reactions, it is also

likely that HF fugacity was not buffered by the pink gneiss for two reasons: 1) the Fe/(Fe + Mg) ratio of the mafic minerals throughout the pink granitic gneiss is variable, and 2) there is no conclusive evidence that $P_{fluid} = P_{total}$ during metamorphism. In the latter case, HF fugacities would be unconstrained and subject to local variations. In light of the extremely high F fugacities (rather than HF fugacity: see Bohlen and Essene 1979) required for the breakdown of zircon, the concept of unconstrained, locally variable HF fugacity may be more appropriate for the Ponaganset gneiss.

The pink granitic gneiss also contains an extensive network of largely crosscutting quartz veins, some of which are associated with macroscopic accumulations of fluorite. The vein system could be related to fluids evolved from the Ponaganset gneiss during metamorphism, or could be associated with an influx of fluorine-rich fluids during metamorphism. In either case, it is possible that the interaction of these fluids is responsible for the corrosion and reprecipitaton of zircon. If the corrosion occurred after the main phase of the deformation, it may have been restricted to regions adjacent to zones of relatively late-stage brittle failure and hydrothermal alteration. Similar quartz veins, some of which contain fluorite, also occur in the gray gneiss but zircon corrosion was not documented from the gray gneiss. The lack of zircon corrosion in the gray gneiss could be explained by the ability of Mg-rich biotite to scavenge fluorine from a coexisting fluid phase. This was demonstrated experimentally by Munoz and Eugster (1969), who showed that fluorine was strongly partitioned into phlogopite in equilibrium with fluids in which HF fugacity was buffered to extremely low values, over a range of T and f_{O_2}. Studies of natural and experimental F-OH exchange in biotite (summarized in Munoz 1984) also demonstrate a positive correlation between the phlogopite content of biotite and fluorine content. Microprobe analyses of biotites from the Ponaganset gneiss (Wayne 1990) indicate that the average ratio of Mg to total octahedral cations (Mg/OCT) ratio of biotites in the gray augen gneiss is significantly higher (0.44 to 0.47) than those from the pink granitic gneiss (0.27 to 0.39). Thus, biotites in the gray augen gneiss are somewhat more efficient scavengers of fluorine from a coexisting fluid phase than the biotites in the pink gneiss.

Biotites from the gray gneiss typically contain 1.0 to 1.8 wt.% F. and the fluorine content of biotites from the pink gneiss falls in the range 1.0 to 1.5 wt.% F. Log (H_2O/HF) fugacity ratios

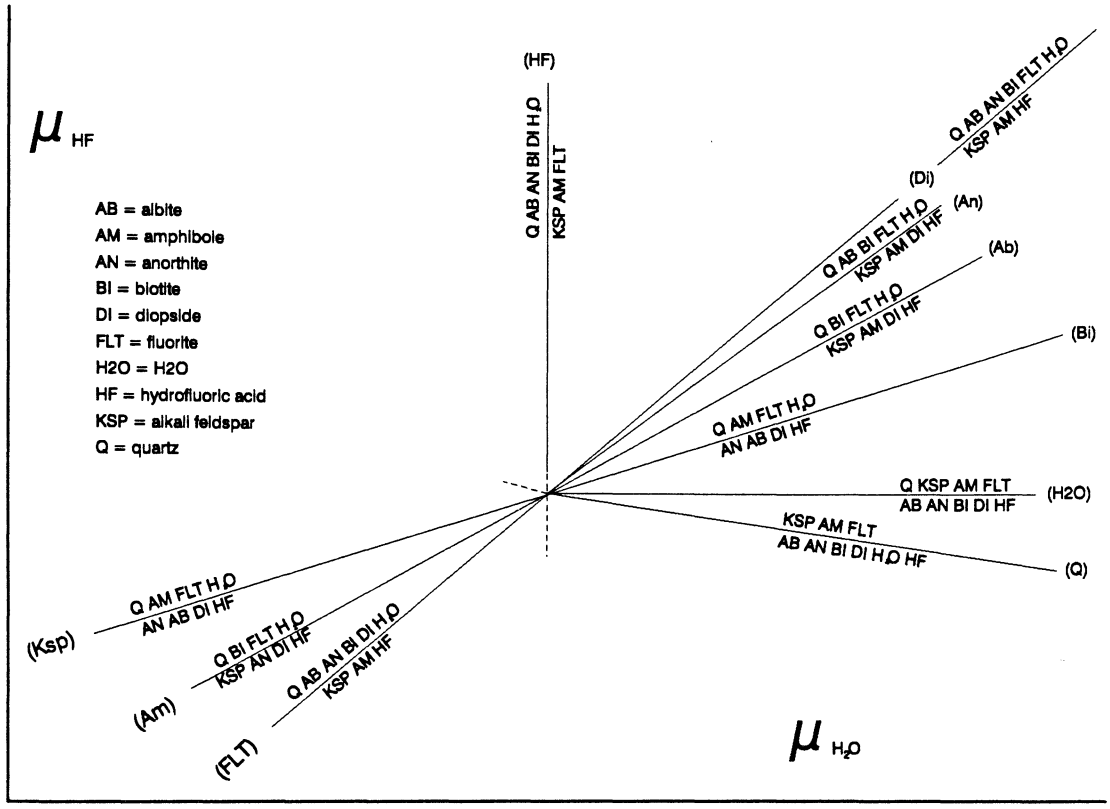


Figure 3.16. **Idealized chemical potential diagram in μ_{H2O} - μ_{HF} space:** This diagram depicts a succession of divariant assemblages observed in the pink gneiss which could potentially buffer f_{HF} at constant P-T (assuming $P_{fluid} = P_{total}$) and constant $Fe^{2+}/(Fe^{2+} + Mg)$ for all ferromagnesian silicates. Plagioclase composition may vary, although this diagram represents a reaction topology drawn in a plane of constant X_{An}. Fluorite-bearing assemblages occur in equilibrium with fluids of relatively high μ_{HF}. Note also that the angular relationships of the curves has been altered slightly in order to specify the phases participating in the reactions.

of biotite from the Ponaganset gneiss calculated using the equations of Munoz (1984) and assuming T = 600°C suggest that, in general, f_{H_2O}/f_{HF} is slightly higher in the gray gneiss (4.04 to 4.18) than in the pink gneiss (3.98 to 3.89). One group of biotites adjacent to a quartz ribbon within the pink gneiss yielded the higher values (3.98), which suggests that some F could have exchanged with late-stage fluids. The differences in f_{H_2O}/f_{HF} between the two units implies that an actual gradient in f_{HF} (or f_{H_2O}) existed between the two units, with the higher relative f_{HF} in the fluorite-bearing pink gneiss. This hypothesis assumes that Fe-rich biotite in the pink gneiss and the less Fe-rich biotite in the gray ceased exchanging F with the metamorphic fluid at the same point along the P-T path of the Ponaganset gneiss. If this is not the case, the gradient recorded by the present-day biotite F contents may actually be significantly "smeared out" due to continued halogen exchange during cooling, and the compositional dependence for the closure of the halogen exchange reactions.

The magnitude of Pb loss incurred as the result of leaching by metamorphic fluids is difficult to evaluate. Because the overgrowths are U-rich, the accumulation of large amounts of radiogenic Pb as the result of U decay in the overgrowths tends to mask the subtler differences in Pb concentration caused by leaching. Experimental studies of U and Pb loss from non-metamict zircon due to interaction with a 2M NaCl solution (Sinha, et al. 1989, and in prep.) suggests that coupled U and Pb loss and extensive zircon corrosion may occur at amphibolite-grade conditions, over relatively short time periods (approximately one month) at relatively high fluid/solid ratios (>1). Although the zircons from the pink granitic gneiss appear to be more extensively corroded than the experimentally treated zircons, the surface features of the experimentally corroded zircons are strikingly similar to those of the zircons from the pink granitic gneiss.

Like zircon corrosion, the formation of metamorphic zircon also appears to be lithologically controlled in the Ponaganset gneiss, Metamorphic zircon occurs primarily in the pink granitic gneiss (as rims on pre-existing grains) and in the mylonites derived from the pink gneiss (both as rims and as discrete new grains). A minor amount of U-rich metamorphic zircon grew in the mylonites derived from the gray gneiss, and none grew in the gray gneiss itself. This suggests that there existed fundamental differences in the geochemical evolution of the gneisses and the mylonites derived from them.

In terms of mass balance, zircon growth during metamorphism requires the breakdown of a Zr-bearing phase and the transport of the Zr cations to the sites of new growth. Alternatively, Zr enrichment (and perhaps new growth of zircon) can occur during mylonitization as a consequence of residual accumulation due to volume loss, provided that Zr behaves as an immobile element. In fact, the residual enrichment mechanism is a highly effective model for explaining the net increase of Zr, Nb, Ti, and other immobile high field strength elements (HFSE) in a number of retrograde shear zones (O'Hara 1988; O'Hara and Blackburn 1988; Dickin 1988) where volume loss during fluid-rock interaction may exceed 50%.

Unlike the shear zones investigated in the studies of O'Hara 1988, O'Hara and Blackburn 1988, and others, the portion of the Hope Valley Shear Zone examined in this study incurred negligable volume losses as the result of mineral reactions during deformation (Wayne 1990). There is also little evidence for the operation of hydration reactions or silica loss on the scale commonly observed in retrograde shear zones (Sinha, et al 1986; O'Hara and Blackburn 1988). The possibility of fluid flow during mylonitization in the Hope Valley Shear Zone cannot be ruled out due to the lack of hydrated, phyllosilicate-rich assemblages. In fact, the observed U-Pb isotopic patterns and the growth of metamorphic zircon require the participation of a fluid phase during the deformation and metamorphism of the Ponaganset gneiss.

In both gneiss units the abundance patterns of HFSE, specifically Zr, are converse to those observed in many retrograde shear zones (e.g. Winchester and Max 1984; O'Hara and Blackburn 1988). Zirconium concentrations (Table 3.5) in the gray gneiss range from 190 to 280 ppm, while the mylonites derived from the gray gneiss contain only 80 to 90 ppm. Similarly, Zr depletion occurs in the mylonites derived from the pink gneiss (50 to 60 ppm) relative to the pink gneiss itself (80 to 170 ppm). The net loss of Zr from the mylonitized gneisses, whether truly the result of Zr transport out of the system or merely an artifact of the comparative enrichment of major elements (namely Si and Na), is strong evidence against the formation of zircon overgrowths via residual enrichment (e.g. Dickin 1988).

As van Breemen et al (1986) point out, the formation of zircon during a metamorphic episode requires the breakdown of a Zr-bearing phase. Besides zircon, such phases are absent from the

Table 3.5. Concentrations (in ppm) of zirconium in whole rock samples from the Ponaganset gneiss.

Gray gneiss	Zr (ppm)	Pink Gneiss	Zr (ppm)
GG452	280	PG649	110
GG419	190	PG872-A5	80
Ultramylonite		PG872-B4	120
UM419-A	80	PG419	170
UM419-B	80	Ultramylonite	
UM431-A	90	UM872-A1	50
UM431-B	90	UM872-B1	50
		UM880	60

Ponaganset gneiss. Extensive corrosion of zircon is apparent in the pink granitic gneiss, and therefore it seems likely that zircon itself acted as a source for Zr cations during metamorphism. The enrichment of U, and perhaps Th, Y, and REE in the overgrowths relative to the cores may be related to the redistribution of these elements during metamorphism (e.g. Dostal and Capedri 1978) from grain boundaries, cleavage planes and fractures. Alternatively, the introduction of incompatible elements may have occurred in conjunction with the formation of late-stage hydrothermal viens.

In the Rockfish Valley Fault Zone, Paleozoic greenschist-grade mylonitization had a pronounced effect on zircon morphology and zoning patterns, but the U-Pb isotopic system remained essentially undisturbed. This is exemplified by the preservation of the Grenville $^{207}Pb/^{206}Pb$ ages in the zircons from the mylonite. Unlike the zircons from the Ponaganset gneiss, the zircons from the Rockfish Valley Fault Zone underwent a process which did not cause preferential Pb-loss or U-gain, and resulted in the preservation of primary igneous ages, despite the apparent loss of original igneous zoning features. Thus, recrystallization is probably not responsible for the diffuse nature of zoning in the zircons from the ultramylonite of the Rockfish Valley Fault Zone

All zircon fractions from the Rockfish Valley Fault Zone have experienced nearly identical degrees of Pb and U loss relative to zircons from the charnockite. While this may simply reflect primary heterogeneities in the U and Pb content of the different zircon populations, the observed lack of U-Th rich zones in zircons from the ultramylonite corresponds to the consistently lower U and Pb contents obtianed via mass spectrometry. Typically, loss of radiogenic Pb occurs with little or no attendant U-loss, or even (as in the case of the Ponaganset gneiss) U-gain. Preferential Pb loss is attributed to chemical processes, such as leaching via interaction with a fluid phase or the formation of U-poor overgrowths. In fact, no preferential loss of radiogenic Pb occurred in the zircons from the greenschist-grade ultramylonites of the Rockfish Valley Fault Zone. Instead, U and Pb were removed simultaneously during mylonitization via purely mechanical processes, such as fracturing and comminution of individual zircon grains in the ductilely deforming matrix. In this scenario, weaker, highly α-damaged regions of individual zircon grains are preferentially destroyed while more competent (or more homogenous) grains, or portions of grains, resist breakage.

Summary

The two examples (the Ponaganset gneiss and the Rockfish Valley Fault Zone) presented here represent two extreme cases of the many complex processes which may, or may not, facilitate the redistribution of Pb and U isotopes in zircon during metamorphism and deformation. In the Ponaganset gneiss, the degree of disruption of the zircon U-Pb system during amphibolite-grade mylonitization and recrystallization is correlated to rock type: the gray gneiss contains very few corroded grains or overgrown grains, whereas the pink gneiss zircons are commonly corroded and/or overgrown. Therefore, the isotopic and geochemical evolution of the two contiguous quartzofeldspathic units was distinct despite their similar metamorphic history. In the mylonites derived from these rocks, the extent of metamorphic resetting is greater than in the gneisses, but is not complete, which suggests that a significant proportion of igneous zircon is preserved despite extensive new growth and corrosion. The abundance of corrosion features and obvious metamorphic overgrowths requires that HFSE, such as Zr, Y and Hf, were mobilized during metamorphism. This implies that the fluid phase present in the Ponaganset gneiss during ductile deformation and mylonitization must have contained significant amounts of fluorine, or other species which are able to dissolve zircon (e.g. Caruba et al. 1974) and form Zr (and/or alkali-Zr) complexes in solution. Again, the most compelling evidence for the existence of a fluorine-rich fluid during the metamorphism of the Ponaganset gneiss is the association between fluorite-bearing assemblages and the high degree of zircon corrosion and overgrowth formation in the pink granitic gneiss, and in the mylonites derived from the pink gneiss (e.g. UM 872).

By contrast, the zircons from the retrograde ultramylonites of the Rockfish Valley Fault Zone did not record the age of mylonitization, despite extensive fracturing and physical disaggregation.

Thus, it is not possible to predict whether the zircon Pb-U system has recorded the age of mylonitization from physical criteria (e.g. grain size reduction) alone. Evidently, the fluids present during the formation of ductile deformation zones in the Rockfish Valley Fault Zone did not chemically interact with the zircon, and the original igneous Pb-U signature was preserved. The consistently lower concentrations of U and Pb in the zircons from the ultramylonites of the Rockfish Valley Fault Zone can be explained by the physical removal of relatively U-rich, metamict zircon domains as the result of brittle failure and comminution. Resistant, low-U, low-Pb portions of zircon grains remained intact, and were concentrated in the larger size fractions.

Such "passive" behavior of the zircon Pb-U system has also been observed in other retrograde mylonites, such as the Brevard Fault Zone (the $\simeq$ 270 m.y. event only: Sinha et al. 1988) and the Bitterroot mylonite zone (Chase et al. 1983). This generalization cannot be extended to include all retrograde mylonites, as perturbation of the zircon U-Pb system as the result of greenschist-grade mylonitization has been documented by Gehrels and Saleeby (1987), Lancelot et al. (1983), and Lindh and Schoberg (1988). In two of these three examples (Lancelot et al. 1983; Lindh and Schoberg 1988), corrosion of the zircon from the mylonites was observed. It seems, therefore, that discordance in zircons from mylonitic rocks is related to zircon corrosion regardless of their metamorphic grade.

References

Aaberg, G. and Bollmark, B. (1985) Retention of U and Pb in zircons from shocked granite in the Siljan impact structure, Sweden. Earth Planet. Sci. Lett., v. 74, p. 347-349.

Albee, A.L. and Ray, L. (1970) Correction factors for electron-probe microanalysis of silicates, oxides, carbonates, phosphates and sulphates. Analytical Chem., 42, 1408-1414.

Aleinikoff, J.N. (1985) Isotopic and morphologic evidence for the age of the Fordham Gneiss., Am. J. Sci. 285, 459-479.

Allison, I. and LaTour, T.E. (1977) Brittle deformation of hornblende in a mylonite: a direct geometrical analogue of ductile deformation by translation gliding., Can. J. Earth Sci., 14, 1953-1958.

Bartholomew, M.J., Gathright, T.M. and Henika, W.S. (1981) A tectonic model for the Blue Ridge of Central Virginia. Am. J. Sci., 281, 1164-1183.

Bence, A.E. and A.L. Albee, (1968) Empirical correction factors for the electron microanalysis of silicates and oxides. J. Geol., 76, 382-403, 1968.

Black, L.P., Williams, I.S. and Compston, W. (1986) Four zircon ages from one rock: the history of a 3930-Ma-old granulite from Mount Sones, Enderby Land, Antarctica. Contrib. Mineral. Petrol., 94, 427-437.

Bohlen, S.R. and Essene, E.J. (1978) The significance of metamorphic fluorite in the Adirondacks. Geochim. Cosmochim. Acta, v. 42, p. 1669-1678.

Boullier, A.M. (1980) A preliminary study on the behavior of brittle minerals in a ductile matrix: example of zircon and feldspars. J. Struct. Geol, v. 2, p. 211-217.

Boullier, A.M. and Bouchez, J-L. (1978) Le quartz en rubans dans les mylonites., Bull. Soc. Geol. France, 7, 253-262.

van Breemen, O., Henderson, J.B., Loveridge, W.D., and Thompson, P.H. (1986) U-Pb zircon and monazite geochronology and zircon morphology of granulites and granite from the Thelon Tectonic Zone, Healey Lake and Artillery Lake map areas, N.W.T.; in Current Research, Part A, Geological Survey of Canada, Paper 87-1A, 783-801.

Brodie, K.H. and Rutter, E.H. (1985) On the relationship between deformation and metamorphism, with special reference to the behavior of basic rocks. *In* Thompson, A.B. and Rubie, D.C. (eds.), Metamorphic Reactions: Kinetics, Textures and Deformation, Springer-Verlag Press, p. 138-179.

Caruba, R. , Mano, J. , Dars, R. and Turco, G. (1974) Corrosions experimentales de cristaux de zircons et comparaison avec des corrosions naturelles de zircons de granites albitises. Tsch. Min. Pet. Mitt., 21, 33-46.

Chakoumakos, B.C., T. Murakami, G.R. Lumpkin, R.C. Ewing, (1988) Alpha-decay--induced fracturing in zircon: the transition from the crystalline to the metamict state. Science, 236, 1556-1559.

Chase, R.B., Bickford, M.E. and Arruda, C.E. (1983) Tectonic implications of tertiary intrusion and shearing within the Bitterroot dome, northeastern Idaho batholith. Jour. Geol., v. 91, p. 462-470.

Clinard, F.W. and L.W. Hobbs (1986) Radiation effects in non-metals., in: Physics of Radiation Effects in Crystals, Johnson, R.A. and Orlov, A.N., eds., Elsevier Science Publishers, Amsterdam., 387-469.

Dallmeyer, R.D. (1975) Incremental $^{39}Ar/^{40}Ar$ ages of biotite and hornblende from retrograde basement gneisses of the southern Blue Ridge and their bearing on the age of Paleozoic metamorphism., Am. J. Sci., 276, 444-460.

Dallmeyer, R.D. (1982) $^{39}Ar/^{40}Ar$ ages from the Narragansett Basin and southern Rhode Island basement terrane: Their bearing on the extent and timing of Alleghanian tectonothermal events in New England. Geol. Soc. Am. Bull., 93, 1118-1130.

Dallmeyer, R.D., Hermes, O.D. and Gil-Ibarguchi, J.I. (1990) $^{39}Ar/^{40}Ar$ mineral ages from the Scituate Granite, Rhode Island: implications for late Paleozoic tectonothermal activity in New England. Jour. Metamorphic Geol., 8, 145-157.

Davis, G.L., Hart, S.R. and Tilton, G.R. (1968) Some effects of contact metamorphism on zircon ages., Earth Planet. Sci. Lett., 5, 27-34.

Dickin, A.P. (1988) Evidence for limited REE leaching from the Roffna gneiss, Switzerland--a discussion of the paper by Vocke et al. (1987; CMP 95; 145-154). Contrib. Min. Pet., v. 99, p. 273-275.

Dostal, J. and Capedri, S. (1978) Uranium in metamorphic rocks., Contrib. Mineral. Petrol., 66, 409-414.

Duchesne, J.C., Caruba, R. and Iacconi, P. (1987) Zircon in charnockitic rocks from Rogaland (southwest Norway): petrogenetic implications. Lithos, 20, 357-368.

Etheridge, M.A., Wall, V.J. and Cox, S.F. (1984) High fluid pressures during regional metamorphism and deformation: implications for mass transport and deformation mechanisms. Jour. Geophys. Res., 89, 4344-4358.

Gehrels, G.E., Saleeby, J.B. and Berg, H.C. (1987) Geology of Annette, Gravina, and Duke Islands, southeastern Alaska. Can. J. Earth Sci., 24, 866-881.

Gehrels, G.E. and Saleeby, J.B. (1987) Geology of southern Prince of Wales Island, southeastern Alaska. Geol. Soc. Am. Bull.,98, 123-137.

Getty, S.R. and Gromet, L.P. (1988) Alleghanian polyphase deformation of the Hope Valley Shear Zone, southeastern New England. Tectonics, 7, 1325-1338.

Getty, S.R. and Gromet, L.P. (1989) Late Paleozoic extension and doming of the basement-cover contact at the Willimantic Dome, eastern Connecticut. *In* Geol. Soc. Am. Abst. with Prog., v. 21, p. A69.

Gilotti, J. A. (1989) Reaction progress during mylonitization of basaltic dikes along the Sarv thrust, Swedish Caledonides., Contrib. Mineral. Petrol., 101, 30-45.

Grauert B (1974) U-Pb systematics in heterogeneous zircon populations from the Precambrian basement of the Maryland Piedmont. Earth Planet Sci Lett:238-248.

Gromet, L.P. (1989) Avalonian terranes and late Paleozoic tectonism in southeastern New England; Constraints and problems. Geol. Soc. Am., Special Paper 230, 193-211.

Gromet, L.P. and Getty, S.R. (1989) Direct dating of deformational fabrics in high-grade rocks using a microstructural-geochronological approach. Geol. Soc. Am. Abst. with Prog., v. 21, p. A227.

Gromet, L.P. and O'Hara, K.D. (1985) The Hope Valley Shear Zone -- a major late Paleozoic ductile shear zone in southeastern New England. *In* Guidebook for fieldtrips in Connecticut and adjacent areas of New York and Rhode Island, NEIGC 77th Annual Meeting, State Geol. Nat. Hist. Survey of Conn. Guidebook 6, p. 277-295.

Gulson, B.L. and T.E. Krogh, (1975) Evidence of multiple intrusion, possible resetting of U-Pb ages, and new crystallization of zircons in the post-tectonic intrusions ('Rapakivi Granites') and gneisses from South Greenland. Geochim. Cosmochim. Acta, 39, 65-82.

Hart, S.R., G.L. Davis, R.H. Steiger and G.R. Tilton (1968) A comparison of the isotopic mineral age variations and petrologic changes induced by contact metamorphism. In E.I. Hamilton and R.M. Farquhar, eds., Radiometric Dating for Geologists, p. 73-110.

Hermes, O.D. and Zartman, R.E. (1985) Late Proterozoic and Devonian plutonic terrane within the Avalon zone of Rhode Island. Geol. Soc. Am. Bull., 96, 272-282.

Kerrich, R., Fyfe, W.S., Gorman, B.E. and Allison, I. (1977) Local modification of rock chemistry by deformation, Contrib. Min. Pet., v. 65, p. 183-190.

Kerrich, R., T.E. LaTour and L. Willmore (1984) Fluid participation in deep fault zones: evidence from geological, geochemical and $^{18}O/^{16}O$ relations, J. Geophys. Res., 89-B6, 4331-4343.

Knipe, R.J. and Wintsch, R.P. (1985) Heterogenous deformation, foliation development and metamorphic processes in a polyphase mylonite, in: *In* Thompson, A.B. and Rubie, D.C. (eds.), Metamorphic Reactions: Kinetics, Textures and Deformation, Springer-Verlag Press, p. 180-210.

Kovach, A., Hurley, P.M., and Fairbairn, H.W. (1977) Rb-Sr whole rock age determinations of the Dedham granodiorite, eastern Massachusetts., Am. Jour. Sci., 277, 905-912.

Krogh, T.E. (1973) A low contamination method for hydrothermal decomposition of zircon and extraction of U and Pb for isotopic age determinations. Geochim. Cosmochim. Acta, 37, 485-494.

Krogh, T.E. and G.L. Davis (1972) The effect of regional metamorphism on U-Pb systems in zircon and a comparison with Rb-Sr systems in the same whole rock and its constituent minerals. Carnegie Inst. of Washington Yearbook, 72, 601-610.

Lancelot, J.R., Boullier, A.M., Maluski, H., and Ducrot, J. (1983) Deformation and related radiochronology in a late Pan-African mylonite shear zone, Adrar des Iforas, Mali. Contrib. Min. Pet., v. 82, p. 312-326.

Lindh, A. and Schoberg, H. (1988) A tentative study of the U-Pb isotope system in zircon from the Mylonite Zone, southeast Norway. Geol. Foren. Stockholm Forh., 110, 15-20.

Lloyd, G.E. (1987) Atomic number and crystallographic contrast images with the SEM: a review of backscattered electron techniques., Min. Mag., 51, 3-19.

Ludwig, K.R. (1980) Calculation of uncertainties of U-Pb isotope data., Earth Planet. Sci. Lett., 46, 212-220.

Ludwig, K.R. (1988) PBDAT for MS-DOS: A computer program for IBM-PC compatibles for processing raw Pb-U-Th isotope data, Version 1.00. U.S.G.S. Open-File Report 88-542.

Mitra, G. (1978) Ductile deformation zones and mylonites: the mechanical processes involved in the deformation of crystalline basement rocks, Amer. Jour. Sci., v. 278, p. 1057-1084.

Munoz, J.L. (1984) F-OH and Cl-OH exchange in micas with applications to hydrothermal ore deposits. *In* Bailey, S.W. (ed.) Micas, Reviews in Mineralogy, Min. Soc. Amer., Washington, D.C., p. 469-494.

Munoz, J.L. and Eugster, H.P. (1969) Experimental control of fluorine reactions in hydrothermal systems., Am. Min., 54, 943-959.

O'Hara, K. (1988) Fluid flow and volume loss during mylonitization: an origin for phyllonite in an overthrust setting, North Carolina, U.S.A. Tectonophys., 156, p. 21-36.

O'Hara, K. and Blackburn, W.H. (1989) Volume-loss model for trace element enrichment in mylonites., Geology, 17

O'Hara, K. and Gromet, L.P. (1983) Textural and Rb-Sr isotopic evidence for late Paleozoic mylonitization within the Honey Hill fault zone, southeastern Connecticut. Amer. Jour. Sci., 283, 762-779.

O'Hara, K. and Gromet, L.P. (1985) Two distinct late Precambrian (Avalonian) terranes in southeastern New England and their Paleozoic juxtaposition. Amer. Jour. Sci., v. 285, p. 673-709.

O'Nions, R.K. and Baadsgaard, H. (1971) A radiometric study of polymetamorphism in the Bamble Region, Norway. Contr. Min. Pet., v. 34, 1-21.

Paterson, B.A., Stephens, W.E. and Herd, D.A. (1989) Zoning in granitoid accessory minerals as revealed by backscattered electron imagery., Min. Mag., 53, 55-61.

Peterman, Z.E., Zartman, R.E. and Sims, P.K. (1980) Tonalitic gneiss of early Archean age from northern Michigan., Geol. Soc. Am. Special Paper 182, 125-134.

Pettingill, H.S., Sinha, A.K. and Tatsumoto, M. (1984) Age and origin of anorthosites, charnockites and granulites in the central Virginia Blue Ridge: Nd and Sr isotopic evidence. Contr. Min. Pet., v. 85, p. 279-291.

Phair, G., Stern, T.W., and Gottfreid, D. (1971) Boulder Creek Batholith, Colorado Part III. Fingerprinting discordant zircon ages in a complex intrusion. Geol. Soc. Am. Bull.

Rubin, J.N., Henry, C.D. and Price, J.G. (1989) Hydrothermal zircon and zircon overgrowths, Sierra Blanca Peaks, Texas., Am. Min., 74, 865-869.

Scharer, U. (1978) Rock deformation and zircon-sphene U-Pb dating, in: Short Papers of the Fourth International Conference, Geochronology, Cosmochronology, Isotope Geology 1978, U.S.G.S. Open-File Report 78-701., 380-382.

Simpson, C. (1985) Deformation of granitic rocks across the brittle-ductile transition, Jour. Struct. Geol., v. 7, p. 503-511.

Simpson, C. (1986) Fabric development in brittle-to-ductile shear zones., Pure Appl. Geoph., 124, 269-288.

Simpson, C. and Wintsch, R.P. (1989) Evidence for deformation-induced K-feldspar replacement by myrmekite, J. Meta. Geol., v. 7, p. 261-275.

Sinha, A.K. and Glover, L. (1978) U-Pb systematics of zircons during dynamic metamorphism. Contrib. Min. Petrol., v. 66, p. 305-310.

Sinha, A.K., and Bartholomew, M. (1984) Evolution of the Grenville terrane in central Virginia Appalachians. Geol. Soc. Amer. Spec. Paper 194, p. 175-186.

Sinha, A.K., Hewitt, D.A. and Rimstidt, J.D. (1986) Fluid interaction and element mobility in the development of ultramylonites. Geol., v. 14, p. 883-886.

Sinha, A.K., Hewitt, D.A., Rimstidt, J.D. (1988) Metamorphic petrology and strontium isotope geochemistry associated with the development of mylonites: an example from the Brevard fault zone. Amer. Jour. Sci., v. 288A, p. 115-147.

Sinha, A.K., D.A. Hewitt, and D.M. Wayne (1989) Hydrothermal stability of zircon: experimental and isotopic studies. In: Zircons and fluids: An experimental investigation with applications for radioactive waste disposal. Progress Report prepared for the U.S. Dept. of Energy, Contract No. DE-FGO5-88 ER 13951-1. Virginia Polytechnic Institute and State University, Dept. of Geological Sciences, Blacksburg, VA 24061., p.2-9.

Stacy, J.S. and Kramers, J.D. (1975) Approximation of terrestrial lead isotope evolution by a two-stage model., Earth Planet. Sci. Lett., 26, 207-221.

Steiger, R.H. and Jaeger, E. (1977) Subcommission on geochronology: Convention on the use of decay constants in geo- and cosmo- chronology. Earth Planet. Sci. Lett., 36, 359-362.

Stern, R.J, Kroner A., Manton, W.I., Reichsmann, T., Mansour, M. and Hussein, I.M. (1989) Geochronolgy of the late Precambrian Hamisana shear zone, Red Sea Hills, Sudan and Egypt. Jour. Geol. Soc., London, 146, 1017-1029.

Wayne, D.M. (1990) Petrogenesis and isotopic systematics of mylonites., unpub. PhD. dissert., Virginia Polytechnic Institute and State University., 151 p.

Wayne D.M. and Sinha, A.K. (1988a) Physical and chemical response of zircons to deformation. Contrib. Min. Pet., v. 98, p. 109-121.

Wayne, D.M. and A.K. Sinha (1988b) Mosaic equilibrium in ultramylonites: constraints on isotopic dating of shear zones. In: Abstracts with Programs, Geological Society of America 1988 Annual Meeting, Denver, CO., A331.

Wayne, D.M. and A.K. Sinha (1989a) Isotopic and mineralogic data from the Hope Valley Shear Zone (HVSZ) in south-central Massachusetts. In: Abstracts with Programs, Geological Society of America 1989 Annual Meeting, Northeast Section, New Brunswick, NJ.,74.

Wayne, D.M. and A.K. Sinha (1989b) Differential response of the zircon U-Pb system across a lithologic boundary: an example from southern New England. In: Abstracts with Programs, Geological Society of America 1989 Annual Meeting, St.Louis, MO.,A226.

White, S.H., Burrows, S.E., Carreras, J., Shaw, N.D., and Humphreys, F.J. (1980) On mylonites in ductile shear zones. J. Struct. Geol. 2, 175-187.

Williams, I.S., W. Compston, L.P. Black, T.R. Ireland and J.J. Foster (1984) Unsupported radiogenic Pb in zircon: a cause of anomalously high Pb-Pb, U-Pb and Th-Pb ages. Contrib. Mineral. Petrol., 88, 322-327.

Winchester, J.A. and Max, M.D. (1984) Element mobility associated with syn-metamorphic shear zones near Scotchport, NW Mayo, Ireland., J. Meta. Geol., 2, 1-11.

Wintsch, R.P. and Aleinikoff, J.N. (1987) U-Pb isotopic and geologic evidence for late Paleozoic anatexis, deformation, and accretion of the late Proterozoic Avalon terrane, southcentral Connecticut., Am. J. Sci., 287, 107-126.

Zartman, R.E. and Hermes, O.D. (1987) Archean inheritance in zircon from late Paleozoic granites from the Avalon zone of southeastern New England: an African connection. Earth Planet. Sci. Lett., 82, 305-315.

Zartman, R.E., Hermes, O.D., Pease, M.H. (1988) Zircon crystallization ages and subsequent isotopic disturbance events in gneissic rocks of eastern Connecticut and western Rhode Island. Amer. Jour. Sci., v. 288, p. 376-402.

Zartman, R.E., Naylor, R.S. (1984) Structural implications of some radiometric ages of igneous rocks in southeastern New England. Geol. Soc. Amer. Bull., v. 95, p. 522-539.

Explanation of Appendices

Standard Analyses

During the period of microprobe analysis, natural and synthetic standards which were not part of the calibration package were analyzed repeatedly to monitor analytical precision and accuracy. The results of these analyses are presented in Appendix A. The following standards were used; Kakanui hornblende, Cl-biotite from Lemhi County, Idaho (see Solberg and Speer 1982), Tiburon albite, Ingamells' K-feldspar, synthetic clinopyroxene Di_{85} Jd_{15}, and titanite from Groschener, Swiss Alps, National Museum of Natural History #26731. All standard deviations in Appendix A are reported at the 2σ level, and the number of individual analyses is listed at the top of each data column. STD denotes the average values obtained from the microprobe analyses. WET denotes the wet chemical analyses of the same standard or, in the case of the synthetic materials, the composition of the starting mixture.

For the analysis of minerals from the Hope Valley Shear Zone, all standard deviations are reported at the 1σ level. "Distance" refers to the approximate distance of the analysis spot (in cm) from the top of the transect, starting with the least-deformed gray gneiss in both the 419 and the S-1 transects.

Feldspar Analyses

AB, AN and KSP denote the contents of the albite, anorthite and K-feldspar components normalized to 100%. The cation formulas are not normalized.

Biotite Analyses

In all samples, Cl was not detected, and the totals have been adjusted for the presence of F only. OH content was estimated by difference (4- # of F atoms p.f.u.). "Mg/OCT" refers to the number of Mg atoms per formula unit divided by the total number of VI atoms. X_{sid} and X_{ann} refer to the mole fraction of the siderophyllite and annite components, calculated using the formulas given in Munoz (1984). "X(F/OH)" is the log ratio of F to F + OH, "IV(F)" is the fluorine intercept value (see Munoz 1984), and "F-rat" is the calculated log fugacity ratio of H_2O to HF (see Munoz 1984). "Cations" refers to the sum of the cation charges per 2 formula units and "a(PHL)" refers to the approximate fluorphlogopite activity calculated using the formula given by Nordstrom and Munoz (1986).

Amphibole Analyses

As with biotite, Cl was analyzed and not detected. Therefore OH was estimated by difference (2-# of F atoms p.f.u.). Fe^{3+}, Na^{A} and Na^{M4} represent the 'average' values obtained using the amphibole recalculation program RECAMP (Spear and Kimball 1984). a_{Tr} is the estimated tremolite activity calculated using the formula given in Holland and Richardson (1979). The values FeMg, FeAl, MgCa, pl, ed, and tk are the magnitudes of the $FeMg_{-1}$, $Fe^{3+}Al_{1-}$, $MgCa_{-1}$,

plagioclase, edenite and tschermakite exchange vectors calculated using the component transformations given in Thompson et al. (1982).

Clinopyroxene Analyses

MgCa, tk, ed, and pl are the magnitudes of the $MgCa_{-1}$, tschermakite, edenite and plagioclase exchange vectors calculated on the basis of the component transformations given by Ferry 1984.

Appendix A - MICROPROBE STANDARD ANALYSES

	Kakanui Hornblende (112)	*STD*	Kak.Hbd. WET	Lemhi Biotite (54)	*STD*	Lem.Bio. WET
SiO2	40.29	*0.36*	40.37	33.52	*0.36*	33.09
Al2O3	14.28	*0.15*	14.90	17.62	*0.26*	17.65
TiO2	4.80	*0.14*	4.75	1.44	*0.11*	1.30
MgO	13.05	*0.26*	12.80	3.00	*0.09*	2.83
FeO	10.72	*0.24*	10.92	31.67	*0.47*	31.40
MnO	0.12	*0.02*	0.10	0.11	*0.02*	0.04
CaO	10.24	*0.09*	10.30	0.08	*0.01*	0.10
Na2O	2.61	*0.12*	2.60	0.14	*0.04*	0.13
K2O	2.03	*0.03*	2.05	8.80	*0.15*	9.04
BaO				0.12	*0.05*	0.90
F	0.18	*0.05*	0.15	0.20	*0.05*	0.23
Cl				1.12	*0.03*	1.11
total	98.32	*0.65*	98.85	97.80	*0.82*	97.01
- (F+Cl)	98.24	*0.64*	98.79	97.46	*0.82*	96.66
Si	5.914	0.034		5.322	0.030	
Al(IV)	2.086	0.034		2.678	0.030	
Al(VI)	0.384	0.032		0.619	0.036	
Ti	0.529	0.014		0.172	0.012	
Fe2+	1.089	0.056		4.206	0.057	
Mn	0.015	0.003		0.014	0.003	
Mg	2.854	0.057		0.709	0.019	
Ca	1.611	0.015		0.014	0.001	
Na	0.744	0.034		0.043	0.013	
K	0.380	0.006		1.782	0.030	
Fe3+	0.244	0.055		-	-	
F	0.083	0.023		0.099	0.025	
Na (M4)	0.332	0.023		-	-	
Na (a)	0.414	0.029		-	-	

	Tiburon Albite		Tib. AB	Ingamells Kspar		Ing. Ksp
	(52)	*STD*	WET	(58)	*STD*	WET
SiO2	68.45	*0.60*	68.73	64.08	*0.63*	64.39
Al2O3	19.55	*0.23*	19.44	18.64	*0.18*	18.58
FeO				0.03	*0.01*	0.03
CaO	0.00	*0.01*	0.04	0.03	*0.01*	0.00
Na2O	11.47	*0.40*	11.70	1.04	*0.08*	1.14
K2O	0.01	*0.01*	0.10	14.44	*0.22*	14.92
BaO				0.84	*0.10*	0.82
total	99.48	*0.81*	100.01	99.10	*0.75*	99.88
Si	2.998	0.011		2.984	0.009	
Al	1.010	0.012		1.023	0.010	
Ca	0.000	-		0.001	0.001	
Na	0.978	0.026		0.094	0.008	
K	0.001	0.002		0.858	0.014	

	Syn. Di85-Jd15		Di-Jd	Titanite #26731 *		Titanite
	(30)	*STD*	WET	(53)	*STD*	WET
SiO2	56.27	*0.63*	56.08	30.35	*0.27*	30.61
Al2O3	3.78	*0.06*	3.78	0.07	*0.01*	0.09
TiO2				39.06	*0.86*	39.43
MgO	15.96	*0.29*	15.83			
FeO	0.05	*0.01*	0.00	0.90	*0.14*	1.03
CaO	22.17	*0.16*	22.02	28.78	*0.22*	28.57
Na2O	2.22	*0.11*	2.31			
total	100.45	*0.86*	100.02	99.20	*1.01*	99.74
Si	1.997	0.009		1.001	0.011	
Al	0.158	0.003		0.003	0.001	
Ca	0.843	0.008		1.017	0.008	
Na	0.153	0.008		-	-	
Mg	0.844	0.012		-	-	
Fe	0.001	-		0.022	0.004	
Ti	-	-		0.968	0.014	

* (also contains 0.04+/-0.01 F)

Appendix B - PLAGIOCLASE ANALYSES - 419 & S-1 Transects

Plagioclase - Gray Gneiss 419									Average	Std.Dev.
Sample #	C4	C5	R12	C13	16 IN AM 27		C46	R46	Gneiss	(8)
SiO2	60.9	62.82	64.15	63.72	64.51	64.01	64.59	63.85	63.57	1.13
Al2O3	24.53	22.41	22.43	22.81	22.33	22.65	21.99	22.26	22.68	0.74
CaO	3.45	3.63	3.45	3.66	3.4	3.52	3.06	3.51	3.46	0.17
Na2O	8.87	9.46	9.47	9.31	9.13	9.65	10.17	9.87	9.49	0.38
K2O	0.36	0.3	0.3	0.28	0.17	0.23	0.3	0.28	0.28	0.05
FeO	0.09	0.08	0.13	0.08	0.05	0.16	0.11	0.09	0.10	0.03
total	98.2	98.7	99.93	99.86	99.59	100.22	100.22	99.86	99.57	0.69
AB	80.5	81.1	81.8	80.8	82.1	82.2	84.3	82.3	81.89	1.11
AN	17.3	17.2	16.4	17.5	16.9	16.5	14.1	16.2	16.51	1.01
KSP	2.2	1.7	1.7	1.6	1	1.3	1.6	1.6	1.59	0.32
Si	2.74	2.814	2.834	2.818	2.851	2.822	2.848	2.828	2.819	0.032
Al	1.301	1.183	1.168	1.189	1.163	1.177	1.142	1.162	1.186	0.046
Ca	0.166	0.174	0.163	0.173	0.161	0.166	0.145	0.167	0.164	0.008
Na	0.774	0.822	0.811	0.798	0.782	0.825	0.869	0.848	0.816	0.030
K	0.021	0.017	0.017	0.016	0.01	0.013	0.017	0.016	0.016	0.003
Fe	0.004	0.003	0.005	0.003	0.002	0.006	0.004	0.003	0.004	0.001
distance	0.5	0.5	0.5	0.5	0.5	0.5	0.5	0.5		

Plagioclase - U-6 419									Average	Std.Dev.
Sample #	84	94	C95	106	76	77	78	79	419U6	(8)
SiO2	65.07	66.17	66.15	65.95	63.68	64.36	64.4	63.89	64.80	1.01
Al2O3	21.99	21.42	21.51	21.69	22.25	22.37	22.27	22.49	22.03	0.37
CaO	2.79	2.17	2.44	2.48	2.63	2.64	2.55	2.63	2.54	0.16
Na2O	9.81	9.24	9.55	9.96	9.91	9.74	9.66	9.7	9.73	0.22
K2O	0.2	0.14	0.11	0.22	0.16	0.18	0.2	0.25	0.18	0.04
FeO	0.11	0.07	0.04	0.08	0.16	0.1	0.13	0.17	0.11	0.04
total	99.97	99.21	99.8	100.38	98.79	99.39	99.21	99.13	99.40	0.52
AB	85.4	87.8	87	86.8	86.39	86.10	86.28	85.73	86.47	0.68
AN	13.5	11.3	12.3	11.9	12.70	12.87	12.58	12.83	12.46	0.60
KSP	1.1	0.9	0.6	1.2	0.91	1.03	1.14	1.44	1.05	0.22
Si	2.865	2.914	2.904	2.886	2.84	2.848	2.854	2.838	2.865	0.028
Al	1.141	1.111	1.113	1.119	1.169	1.167	1.163	1.177	1.148	0.026
Ca	0.132	0.102	0.115	0.116	0.126	0.125	0.121	0.125	0.120	0.008
Na	0.837	0.789	0.813	0.845	0.857	0.836	0.83	0.835	0.834	0.021
K	0.011	0.008	0.006	0.012	0.009	0.01	0.011	0.014	0.010	0.002
Fe	0.004	0.003	0.001	0.003	0.006	0.004	0.005	0.006	0.004	0.002
distance	1.5	1.5	1.5	1.5	1.5	1.5	1.5	1.5		

Plagioclase - 419 U-5 Protomylonite

Sample #	112	116	117	118	119	44	45	46	48	49
SiO2	65.1	65.98	66.56	66.5	66.34	64.44	65.1	64.64	64.48	64.1
Al2O3	21.64	21.6	21.42	21.64	21.62	22.39	22.13	21.94	22.46	22.34
CaO	2.3	2.52	2.47	2.56	2.3	2.72	2.34	2.29	2.72	2.94
Na2O	9.86	10.33	10.4	10.31	10.4	9.83	10.26	10.06	10.11	9.85
K2O	0.17	0.1	0.23	0.26	0.05	0.31	0.21	0.2	0.18	0.24
FeO	0.08	0.04	0.06	0.06	0.03	0.12	0.15	0.12	0	0.06
total	99.15	100.57	101.14	101.33	100.74	99.81	100.19	99.25	99.95	99.53
AB	87.7	87.5	87.3	86.7	88.9	85.21	87.75	87.80	86.23	84.60
AN	11.3	11.8	11.4	11.9	10.8	13.07	11.04	11.08	12.77	14.00
KSP	1	0.6	1.3	1.4	0.3	1.72	1.20	1.12	1.00	1.40
Si	2.883	2.886	2.897	2.888	2.892	2.845	2.861	2.864	2.842	2.839
Al	1.129	1.113	1.099	1.107	1.111	1.165	1.146	1.146	1.166	1.166
Ca	0.109	0.118	0.115	0.119	0.107	0.129	0.11	0.109	0.128	0.14
Na	0.847	0.876	0.878	0.868	0.879	0.841	0.874	0.864	0.864	0.846
K	0.01	0.006	0.013	0.014	0.003	0.017	0.012	0.011	0.01	0.014
Fe	0.003	0.001	0.002	0.002	0.001	0.004	0.006	0.004	0	0.002
distance	4.5	4.5	4.5	4.5	4.5	4.5	4.5	4.5	4.5	4.5

Plagioclase - 419 U-5 Protomylonite

							CORE(Hi-An)
Sample #	55	56	57	C120	PROTO	(14)	R-COR47
SiO2	65.12	64.37	64.25	65.83	65.20	0.85	63.32
Al2O3	22.22	22.37	22.4	21.55	21.98	0.37	22.42
CaO	2.4	2.52	2.65	2.43	2.51	0.19	3.41
Na2O	10.14	9.94	10.04	10.5	10.15	0.22	9.71
K2O	0.2	0.24	0.23	0.1	0.19	0.07	0.28
FeO	0.09	0.09	0.12	-0.02	0.07	0.05	0.5
total	100.17	99.53	99.69	100.39	100.10	0.65	99.64
AB	87.44	86.50	86.10	88.2	86.99	1.13	82.46
AN	11.45	12.08	12.60	11.3	11.90	0.88	15.96
KSP	1.11	1.42	1.30	0.6	1.11	0.37	1.58
Si	2.859	2.847	2.841	2.886	2.866	0.021	2.814
Al	1.15	1.166	1.167	1.113	1.139	0.025	1.174
Ca	0.113	0.119	0.126	0.114	0.118	0.009	0.162
Na	0.863	0.852	0.861	0.893	0.865	0.014	0.837
K	0.011	0.014	0.013	0.006	0.011	0.004	0.016
Fe	0.003	0.003	0.004	0	0.003	0.002	0.019
distance	4.5	4.5	4.5	4.5			4.5

Patron,

Page 233 is omitted from enumeration.

Plagioclase 419 Mylonite U-4								Average	Std.Dev.	Rim
Sample #	123	84	85	86	88	92	93	UM419U4	(7)	87
SiO2	65.68	64.24	64.24	64.24	64.43	65.64	64.45	64.70	0.61	66.13
Al2O3	21.14	22.46	22.33	22.32	22.08	22.3	22.31	22.13	0.42	20.96
CaO	2.3	2.45	2.53	2.54	2.3	2.26	2.35	2.39	0.11	0.85
Na2O	10.08	9.98	10.11	10.08	10.26	9.95	10.04	10.07	0.09	11.08
K2O	0.22	0.18	0.18	0.21	0.2	0.16	0.16	0.19	0.02	0.11
FeO	0.09	0.13	0.18	0.09	0.1	0.11	0.07	0.11	0.03	0
total	99.51	99.44	99.57	99.48	99.37	100.42	99.38	99.60	0.34	99.13
AB	87.7	87.17	86.96	86.67	88.02	88.00	87.77	87.47	0.49	95.38
AN	11.1	11.81	12.04	12.12	10.88	11.06	11.31	11.48	0.47	4.02
KSP	1.2	1.02	1.00	1.20	1.10	0.94	0.92	1.05	0.11	0.60
Si	2.9	2.843	2.843	2.845	2.855	2.869	2.852	2.858	0.019	2.922
Al	1.1	1.171	1.164	1.165	1.153	1.149	1.163	1.152	0.022	1.091
Ca	0.109	0.116	0.12	0.121	0.109	0.106	0.111	0.113	0.005	0.04
Na	0.863	0.856	0.867	0.865	0.882	0.843	0.861	0.862	0.011	0.949
K	0.012	0.01	0.01	0.012	0.011	0.009	0.009	0.010	0.001	0.006
Fe	0.003	0.005	0.007	0.003	0.004	0.004	0.003	0.004	0.001	0
distance	7.5	7.5	7.5	7.5	7.5	7.5	7.5			7.5

Plagioclase 419 Mylonite U-3								
Sample #	120	122	123	125	126	127	129	130
SiO2	64.47	64.64	65.39	64.48	65.15	64.45	64.88	64.66
Al2O3	21.9	21.7	21.96	21.8	21.59	21.87	21.83	21.69
CaO	1.99	2	1.94	2.18	1.86	2.1	1.94	2.03
Na2O	10.27	10.29	10.46	10.43	10.47	10.41	10.12	10.21
K2O	0.18	0.21	0.15	0.13	0.16	0.21	0.15	0.2
FeO	0.02	0.17	0.09	0.05	0.12	0.03	0.05	0.08
total	98.83	99.01	99.99	99.07	99.35	99.07	98.97	98.87
AB	89.39	89.22	90.00	89.00	90.25	88.89	89.07	90.34
AN	9.60	9.57	9.19	10.31	8.84	9.92	9.82	8.67
KSP	1.01	1.21	0.81	0.69	0.90	1.19	1.11	1.00
Si	2.867	2.872	2.874	2.864	2.882	2.862	2.874	2.872
Al	1.148	1.136	1.137	1.141	1.125	1.145	1.136	1.137
Ca	0.095	0.095	0.091	0.104	0.088	0.1	0.097	0.087
Na	0.885	0.886	0.891	0.898	0.898	0.896	0.88	0.907
K	0.01	0.012	0.008	0.007	0.009	0.012	0.011	0.01
Fe	0.001	0.006	0.003	0.002	0.004	0.001	0.003	0.002
distance	11	11	11	11	11	11	11	11

Plagioclase 419	Mylonite U-3 A				Mylonite U-3 B			Average	Std.Dev.
Sample #	173	177	U-3 A	(11)	188	190	181	U-3 B	(3)
SiO2	66.13	66.15	64.99	0.61	65.84	66.58	66.14	66.19	0.30
Al2O3	21.44	21.1	21.67	0.24	21.14	20.81	20.74	20.90	0.17
CaO	2.21	2.13	2.01	0.13	1.96	1.96	1.8	1.91	0.08
Na2O	10.59	10.2	10.34	0.14	10.41	10.4	10.52	10.44	0.05
K2O	0.19	0.18	0.17	0.03	0.13	0.15	0.15	0.14	0.01
FeO	0.04	0.07	0.07	0.04	0.09	0.05	0.05	0.06	0.02
total	100.6	99.83	99.25	0.63	99.57	99.95	99.4	99.64	0.23
AB	88.6	88.8	89.47	0.66	90	89.8	90.6	90.1	0.34
AN	10.3	10.2	9.54	0.62	9.4	9.3	8.6	9.1	0.36
KSP	1.1	1	0.99	0.15	0.7	0.8	0.8	0.8	0.05
Si	2.893	2.911	2.88	0.01	2.904	2.923	2.921	2.916	0.009
Al	1.105	1.094	1.13	0.02	1.099	1.077	1.079	1.085	0.010
Ca	0.104	0.1	0.10	0.01	0.093	0.092	0.085	0.090	0.004
Na	0.898	0.87	0.89	0.01	0.89	0.885	0.901	0.892	0.007
K	0.011	0.01	0.01	0.00	0.007	0.008	0.008	0.008	0.000
Fe	0.001	0.003	0.00	0.00	0.003	0.002	0.002	0.002	0.000
distance	11	11			11.75	11.75	11.75		

Plagioclase - Amphibolite 419 GG-AM Contact					Average	Std.Dev.
Sample #	206	216	225	226	Matrix	(4)
SiO2	66.68	66.57	66.22	66.48	66.49	0.17
Al2O3	20.39	20.98	20.74	21.19	20.83	0.30
CaO	1.38	1.96	1.83	1.89	1.77	0.23
Na2O	10.94	10.41	10.56	10.74	10.66	0.20
K2O	0.13	0.18	0.16	0.15	0.16	0.02
FeO	0.19	0.16	0.21	0.26	0.21	0.04
total	99.71	100.26	99.72	100.71	100.10	0.42
AB	92.7	89.6	90.5	90.4	90.80	1.15
AN	6.5	9.3	8.6	8.7	8.28	1.06
KSP	0.7	1	0.9	0.8	0.85	0.11
Si	2.934	2.916	2.918	2.904	2.918	0.011
Al	1.057	1.083	1.077	1.091	1.077	0.013
Ca	0.065	0.092	0.086	0.088	0.083	0.010
Na	0.933	0.884	0.902	0.909	0.907	0.018
K	0.007	0.01	0.009	0.008	0.009	0.001
Fe	0.007	0.006	0.008	0.009	0.008	0.001
distance	12.5	12.5	12.5	12.5		

Plag. - Amphibolite 419			Average	Std.Dev.	
Sample #	238	240	Matrix	(2)	284
SiO2	66.02	66.2	66.11	0.09	66.88
Al2O3	20.87	20.85	20.86	0.01	20.83
CaO	1.95	1.9	1.93	0.02	1.5
Na2O	10.63	10.43	10.53	0.10	10.04
K2O	0.16	0.18	0.17	0.01	0.13
FeO	0.19	0.15	0.17	0.02	0.05
total	99.82	99.71	99.77	0.05	99.43
AB	89.9	89.8	89.85	0.05	91.6
AN	9.1	9.1	9.10	ERR	7.6
KSP	0.9	1.1	1.00	0.10	0.7
Si	2.91	2.915	2.913	0.002	2.941
Al	1.084	1.082	1.083	0.001	1.08
Ca	0.092	0.09	0.091	0.001	0.071
Na	0.909	0.89	0.900	0.009	0.856
K	0.009	0.011	0.010	0.001	0.007
Fe	0.007	0.006	0.007	0.000	0.002
distance	14.75	14.75			16

Plagioclase - Amphibolite 419							Average	Std.Dev.
Sample #	298	306	307	311	312	349	Matrix	(6)
SiO2	66.75	66.6	66.8	66.12	67.01	66.07	66.56	0.35
Al2O3	21.24	21.1	20.81	21	20.62	20.73	20.92	0.22
CaO	1.83	1.85	1.74	1.85	1.34	1.79	1.73	0.18
Na2O	10.36	10.45	10.56	10.44	10.76	10.55	10.52	0.13
K2O	0.19	0.21	0.19	0.22	0.13	0.21	0.19	0.03
FeO	0.23	0.23	0.28	0.19	0.21	0.1	0.21	0.05
total	100.6	100.44	100.38	99.82	100.07	99.45	100.13	0.40
AB	90	90	90.6	90	92.9	90.3	90.63	1.04
AN	8.8	8.8	8.3	8.8	6.4	8.5	8.27	0.86
KSP	1.1	1.2	1.1	1.2	0.7	1.2	1.08	0.18
Si	2.913	2.913	2.924	2.909	2.935	2.917	2.919	0.009
Al	1.092	1.087	1.073	1.089	1.064	1.079	1.081	0.010
Ca	0.086	0.087	0.082	0.087	0.063	0.085	0.082	0.009
Na	0.877	0.886	0.896	0.89	0.914	0.903	0.894	0.012
K	0.011	0.012	0.011	0.012	0.007	0.012	0.011	0.002
Fe	0.008	0.008	0.01	0.007	0.008	0.004	0.008	0.002
distance	17.5	17.5	17.5	17.5	17.5	17.5		

Plagioclase - CPX-AB Layer L2-1							Average	Std.Dev.
Sample #	643	644	R647	C648	571	632	CPX-AB	(6)
SiO2	68.13	67.45	66.28	67.16	67.9	65.44	67.06	0.94
Al2O3	19.99	20.03	21.16	19.88	20.09	21.4	20.43	0.61
CaO	0.64	0.39	0.8	0.52	0.69	0.31	0.56	0.17
Na2O	10.89	11.2	10.79	10.74	10.08	10.49	10.70	0.35
K2O	0.12	0.16	0.15	0.17	0.14	0.06	0.13	0.04
FeO	0.14	0.17	0.09	0.13	0.23	0.06	0.14	0.05
total	99.91	99.4	99.27	98.6	99.13	97.76	99.01	0.68
AB	96.1	97.1	95.2	96.2	95.5	98.1	96.37	0.98
AN	3.1	1.8	3.9	2.6	3.6	1.6	2.77	0.86
KSP	0.7	1	0.8	1	0.9	0.3	0.78	0.24
Si	2.978	2.967	2.921	2.974	2.982	2.919	2.957	0.026
Al	1.03	1.038	1.099	1.037	1.04	1.125	1.062	0.037
Ca	0.03	0.018	0.038	0.025	0.032	0.015	0.026	0.008
Na	0.923	0.955	0.922	0.922	0.858	0.907	0.915	0.029
K	0.007	0.01	0.008	0.01	0.008	0.003	0.008	0.002
Fe	0.005	0.006	0.004	0.005	0.008	0.002	0.005	0.002
distance	18.5	18.5	18.5	18.5	18.5	18.5		

Plagioclase - Amphibolite 419						Average	Std.Dev.
Sample #	C576	R578	C579	C580	R581	Matrix	(5)
SiO2	65.5	67.07	66.75	66.46	66.23	66.40	0.53
Al2O3	21.63	20.79	20.88	20.85	20.55	20.94	0.36
CaO	1.49	1.12	1.61	1.68	1.34	1.45	0.20
Na2O	8.95	9.82	9.24	9.23	9.56	9.36	0.30
K2O	0.2	0.2	0.22	0.22	0.15	0.20	0.03
FeO	0.15	0.09	0.13	0.14	0.12	0.13	0.02
total	97.92	99.09	98.83	98.58	97.95	98.47	0.47
AB	90.3	92.9	90	89.6	91.9	90.94	1.25
AN	8.3	5.9	8.7	9	7.1	7.80	1.15
KSP	1.3	1.2	1.4	1.4	1	1.26	0.15
Si	2.914	2.951	2.945	2.94	2.949	2.940	0.013
Al	1.134	1.078	1.085	1.087	1.078	1.092	0.021
Ca	0.071	0.053	0.076	0.08	0.064	0.069	0.010
Na	0.772	0.838	0.79	0.792	0.825	0.803	0.024
K	0.011	0.011	0.012	0.012	0.009	0.011	0.001
Fe	0.006	0.003	0.005	0.005	0.004	0.005	0.001
distance	20	20	20	20	20		

CPX-AB Myl. L-3 Cores					Average	Std.Dev.
Sample #	595	C651	C652	669	CPX-AB	(4)
SiO2	67.32	66.99	66.81	66.51	66.91	0.29
Al2O3	19.73	20.1	20.34	20.42	20.15	0.27
CaO	0.52	0.65	0.83	0.95	0.74	0.16
Na2O	9.6	10.44	10.32	11.56	10.48	0.70
K2O	0.17	0.17	0.18	0.16	0.17	0.01
FeO	0.16	0.17	0.2	0.06	0.15	0.05
total	97.5	98.52	98.68	99.66	98.59	0.77
AB	95.8	95.6	94.8	94.8	95.25	0.46
AN	2.9	3.3	4.2	4.3	3.68	0.59
KSP	1.2	1.1	1.1	0.9	1.08	0.11
Si	2.998	2.967	2.956	2.933	2.964	0.023
Al	1.036	1.049	1.061	1.061	1.052	0.010
Ca	0.025	0.031	0.039	0.045	0.035	0.008
Na	0.829	0.897	0.885	0.988	0.900	0.057
K	0.01	0.01	0.01	0.009	0.010	0.000
Fe	0.006	0.006	0.007	0.002	0.005	0.002
distance	23	23	23	23		

Cpx-Ab Mylonite L-3 Rims				Average	Std.Dev.
Sample #	R653	R650	R?594	Rims	(3)
SiO2	66.09	65.5	65.69	65.76	0.25
Al2O3	21.25	20.92	21.03	21.07	0.14
CaO	1.77	1.76	1.84	1.79	0.04
Na2O	10.26	10.4	9.27	9.98	0.50
K2O	0.18	0.18	0.17	0.18	0.00
FeO	0.15	0.15	0.16	0.15	0.00
total	99.7	98.91	98.16	98.92	0.63
AB	90.4	90.4	89.1	89.97	0.61
AN	8.6	8.5	9.8	8.97	0.59
KSP	1	1	1.1	1.03	0.05
Si	2.909	2.908	2.923	2.913	0.007
Al	1.102	1.094	1.103	1.100	0.004
Ca	0.083	0.084	0.088	0.085	0.002
Na	0.876	0.895	0.8	0.857	0.041
K	0.01	0.01	0.01	0.010	ERR
Fe	0.006	0.006	0.006	0.006	ERR
distance	23	23	23		

Cpx-Ab Mylonite E3A				Average	Std.Dev.
Sample #	491	493	495	Myl.	(3)
SiO2	66.9	66.67	67.61	67.06	0.40
Al2O3	20.46	20.35	20.23	20.35	0.09
CaO	0.61	1.05	0.87	0.84	0.18
Na2O	11.08	10.85	11.38	11.10	0.22
K2O	0.14	0.16	0.16	0.15	0.01
FeO	0.17	0.15	0.03	0.12	0.06
total	99.36	99.23	100.28	99.62	0.47
AB	96.1	94	95.1	95.07	0.86
AN	2.9	5.1	4	4.00	0.90
KSP	0.8	0.9	0.9	0.87	0.05
Si	2.946	2.945	2.955	2.949	0.004
Al	1.062	1.059	1.042	1.054	0.009
Ca	0.029	0.05	0.041	0.040	0.009
Na	0.946	0.929	0.964	0.946	0.014
K	0.008	0.009	0.009	0.009	0.000
Fe	0.006	0.006	0.001	0.004	0.002
distance	23.5	23.5	23.5		

419 Pink Gneiss Plagioclase			Average	Std.Dev.			Average	Std.Dev.	RIM
Sample #	518	677		(2)	693	696		(2)	668
SiO2	65.97	65.2	65.59	0.38	65.65	65.66	65.66	0.01	66.74
Al2O3	20.98	21.1	21.04	0.06	21.02	21.15	21.09	0.06	20.41
CaO	1.73	1.58	1.66	0.07	1.56	1.82	1.69	0.13	0.83
Na2O	10.21	11.38	10.80	0.58	10.43	11.2	10.82	0.39	11.73
K2O	0.13	0.22	0.18	0.04	0.15	0.15	0.15	0.00	0.17
FeO	0.08	0.13	0.11	0.02	0.15	0.07	0.11	0.04	0.09
total	99.1	99.61	99.36	0.25	98.96	100.05	99.51	0.54	99.97
AB	90.8	91.8	91.30	0.50	91.6	91	91.30	0.30	95.4
AN	8.5	7	7.75	0.75	7.6	8.2	7.90	0.30	3.7
KSP	0.7	1.1	0.90	0.20	0.8	0.8	0.80	0.00	0.9
Si	2.918	2.887	2.903	0.015	2.908	2.893	2.901	0.007	2.933
Al	1.093	1.101	1.097	0.004	1.097	1.098	1.098	0.000	1.061
Ca	0.082	0.075	0.079	0.004	0.074	0.086	0.080	0.006	0.039
Na	0.876	0.977	0.927	0.050	0.896	0.957	0.927	0.031	0.999
K	0.007	0.012	0.010	0.003	0.008	0.008	0.008	0.000	0.01
Fe	0.003	0.005	0.004	0.001	0.006	0.003	0.005	0.001	0.003
distance	24.25	24.25			28	28			24.25

419 Pink Gneiss Plagioclase		L5 1,2			Average	Std.Dev.	ALTERED
Sample #	710	R712	723	R725		(4)	705
SiO2	65.83	66.55	66.29	66.46	66.43	0.39	67.04
Al2O3	21.1	20.53	21.15	21.06	20.83	0.35	20.3
CaO	1.89	1.49	1.9	1.58	1.57	0.33	1.01
Na2O	10.46	10.92	11.29	11.38	10.91	0.39	10.49
K2O	0.17	0.16	0.18	0.18	0.15	0.04	0.08
FeO	0.07	0.02	0.24	0.12	0.10	0.08	0.03
total	99.52	99.67	101.05	100.78	99.99	0.79	98.95
AB	90	92.2	90.6	91.94	91.83	1.53	94.43
AN	9	6.9	8.4	7.05	7.27	1.38	5.02
KSP	1	0.9	0.9	0.96	0.85	0.19	0.47
Si	2.905	2.931	2.893	2.903	2.918	0.024	2.958
Al	1.097	1.065	1.088	1.084	1.078	0.015	1.056
Ca	0.089	0.07	0.089	0.074	0.074	0.015	0.048
Na	0.895	0.932	0.955	0.964	0.929	0.029	0.897
K	0.01	0.009	0.01	0.01	0.009	0.002	0.005
Fe	0.003	0.001	0.009	0.004	0.004	0.003	0.001
distance	29.75	29.75	29.75	29.75			29.75

419 Pink Gneiss Plagioclase			Micro. Myl. L-6					Average	Std.Dev.
Sample #	108	111	112	114	115	117	118	Myl.	(7)
SiO2	64.68	63.79	64.61	65.37	65.16	65.72	64.73	64.87	0.58
Al2O3	21.74	21.7	21.68	21.82	21.66	21.72	21.88	21.74	0.07
CaO	2.08	2.04	2.06	1.83	1.92	1.77	2.06	1.97	0.12
Na2O	9.92	10.18	10	10.25	10.01	10.15	10.2	10.10	0.11
K2O	0.16	0.16	0.18	0.13	0.19	0.1	0.16	0.15	0.03
FeO	0.13	0.08	0.08	0	0.02	0.11	0.1	0.07	0.04
total	98.71	97.95	98.61	99.4	98.96	99.57	99.13	98.90	0.50
AB	88.79	89.22	88.88	90.32	89.40	90.68	89.13	89.49	0.67
AN	10.28	9.87	10.09	8.96	9.46	8.69	9.96	9.62	0.56
KSP	0.93	0.91	1.03	0.72	1.14	0.63	0.91	0.90	0.16
Si	2.877	2.863	2.877	2.884	2.887	2.892	2.87	2.879	0.009
Al	1.139	1.148	1.137	1.135	1.131	1.126	1.143	1.137	0.007
Ca	0.099	0.098	0.098	0.087	0.091	0.083	0.098	0.093	0.006
Na	0.855	0.886	0.863	0.877	0.86	0.866	0.877	0.869	0.010
K	0.009	0.009	0.01	0.007	0.011	0.006	0.009	0.009	0.002
Fe	0.005	0.003	0.003	0	0.001	0.004	0.004	0.003	0.002
distance	32	32	32	32	32	32	32		

419 Pink Gneiss Plagioclase			Average	Std.Dev.	Rim n/t KSP
Sample #	R736	C739		(2)	R737
SiO2	66.54	65.71	66.13	0.42	67.59
Al2O3	21.02	21.4	21.21	0.19	19.66
CaO	1.9	2.05	1.97	0.08	0.15
Na2O	10.96	10.82	10.89	0.07	12.16
K2O	0.14	0.21	0.18	0.03	0.16
FeO	0.05	0.08	0.07	0.01	0.1
total	100.61	100.27	100.44	0.17	99.82
AB	90.65	89.5	90.08	0.57	98.34
AN	8.68	9.3	8.99	0.31	0.67
KSP	0.76	1.2	0.98	0.22	0.9
Si	2.909	2.887	2.898	0.011	2.97
Al	1.083	1.108	1.096	0.012	1.018
Ca	0.089	0.096	0.093	0.003	0.007
Na	0.929	0.922	0.926	0.003	1.036
K	0.008	0.012	0.010	0.002	0.01
Fe	0.002	0.003	0.003	0.001	0.004
distance	36	36			36

419 Pink Gneiss Plagioclase					Average	Std.Dev.		Rim
Sample #	746	763	764	C766		(4)		R765
SiO2	65.73	66.32	66.08	65.51	65.91	0.31		67.65
Al2O3	20.96	20.86	21.45	21.14	21.10	0.22		20.09
CaO	2.21	1.77	2.33	2.26	2.14	0.22		1
Na2O	10.23	11.26	10.93	10.77	10.80	0.37		11.4
K2O	0.22	0.16	0.25	0.23	0.22	0.03		0.13
FeO	0.02	0.04	0.1	0.09	0.06	0.03		0.02
total	99.37	100.41	101.14	100	100.23	0.64		100.29
AB	88	91.1	88.2	88.5	88.95	1.25		94.76
AN	10.6	7.9	10.4	10.3	9.80	1.10		4.59
KSP	1.3	1	1.3	1.2	1.20	0.12		0.71
Si	2.905	2.907	2.882	2.888	2.896	0.011		2.957
Al	1.091	1.078	1.102	1.098	1.092	0.009		1.035
Ca	0.105	0.083	0.109	0.107	0.101	0.010		0.047
Na	0.876	0.957	0.924	0.921	0.920	0.029		0.966
K	0.013	0.01	0.014	0.013	0.013	0.001		0.007
Fe	0.001	0.001	0.004	0.003	0.002	0.001		0.001
distance	41	41	41	41				41

419 Pink Gneiss Plagioclase			Average	Std.Dev.					Average	Std.Dev.
Sample #	830	838		(2)	854	862	863	864		(4)
SiO2	66.38	65.72	66.05	0.33	65.51	67.41	65.01	65.47	65.85	0.92
Al2O3	21.5	21.05	21.28	0.22	21.5	21.33	21.31	21.33	21.37	0.08
CaO	2.13	2.12	2.13	0.00	2.38	2.22	2.54	2.4	2.39	0.11
Na2O	11.11	10.39	10.75	0.36	10.25	10.33	10.47	10.02	10.27	0.16
K2O	0.18	0.18	0.18	0.00	0.2	0.17	0.18	0.2	0.19	0.01
FeO	0.04	0.05	0.05	0.00	0.21	0.03	0.07	0.04	0.09	0.07
total	101.34	99.51	100.43	0.92	100.05	101.49	99.58	99.46	100.15	0.81
AB	89.5	89	89.25	0.25	87.7	88.5	87.4	87.3	87.73	0.47
AN	9.5	10	9.75	0.25	11.2	10.5	11.7	11.6	11.25	0.47
KSP	1	1	1.00	0.00	1.1	0.9	1	1.1	1.03	0.08
Si	2.886	2.902	2.894	0.008	2.881	2.915	2.878	2.893	2.892	0.015
Al	1.102	1.095	1.099	0.004	1.114	1.087	1.112	1.111	1.106	0.011
Ca	0.099	0.1	0.100	0.001	0.112	0.103	0.12	0.114	0.112	0.006
Na	0.937	0.89	0.914	0.023	0.874	0.866	0.899	0.858	0.874	0.015
K	0.01	0.01	0.010	0.000	0.011	0.009	0.01	0.011	0.010	0.001
Fe	0.001	0.002	0.002	0.001	0.008	0.001	0.003	0.001	0.003	0.003
distance	46	46			50.5	50.5	50.5	50.5		

419 Pink Gneiss Plagioclase				Average	Std.Dev.				Average	Std.Dev.
Sample #	887	888	889		(3)	890	900	904		(3)
SiO2	65.88	65.36	65.48	65.57	0.22	64.8	65.48	65.1	65.13	0.28
Al2O3	21.93	22.1	21.52	21.85	0.24	21.73	21.23	21.09	21.35	0.27
CaO	2.65	2.67	2.72	2.68	0.03	2.88	2.44	2.35	2.56	0.23
Na2O	10.88	10.69	10.3	10.62	0.24	10.27	10.47	10.59	10.44	0.13
K2O	0.24	0.19	0.22	0.22	0.02	0.27	0.17	0.15	0.20	0.05
FeO	0.11	0.14	0.2	0.15	0.04	0.14	0.28	0.08	0.17	0.08
total	101.69	101.15	100.44	101.09	0.51	100.09	100.07	99.36	99.84	0.34
AB	87	86.9	86.2	86.70	0.36	85.2	87.7	88.4	87.10	1.37
AN	11.7	12	12.6	12.10	0.37	13.2	11.3	10.9	11.80	1.00
KSP	1.2	1.1	1.2	1.17	0.05	1.5	1	0.8	1.10	0.29
Si	2.862	2.855	2.876	2.864	0.009	2.858	2.886	2.887	2.877	0.013
Al	1.123	1.137	1.113	1.124	0.010	1.129	1.102	1.102	1.111	0.013
Ca	0.123	0.125	0.128	0.125	0.002	0.136	0.115	0.112	0.121	0.011
Na	0.916	0.905	0.877	0.899	0.016	0.878	0.895	0.912	0.895	0.014
K	0.013	0.011	0.012	0.012	0.001	0.015	0.01	0.008	0.011	0.003
Fe	0.004	0.005	0.007	0.005	0.001	0.005	0.01	0.003	0.006	0.003
distance	53	53	53			55	55	55		

419 Pink Gneiss Plagioclase			Rims	Average	Std.Dev.
Sample #	894	911	912	RIMS	(3)
SiO2	65.56	67.43	67.45	66.81	0.89
Al2O3	21.09	20.87	20.83	20.93	0.11
CaO	2.04	1.25	1.4	1.56	0.34
Na2O	10.86	11.85	11.67	11.46	0.43
K2O	0.16	0.16	0.1	0.14	0.03
FeO	0.03	0.07	0.1	0.07	0.03
total	99.74	101.63	101.55	100.97	0.87
AB	89.8	93.7	93.2	92.23	1.73
AN	9.3	5.5	6.2	7.00	1.65
KSP	0.9	0.8	0.6	0.77	0.12
Si	2.894	2.92	2.923	2.912	0.013
Al	1.097	1.065	1.063	1.075	0.016
Ca	0.096	0.058	0.065	0.073	0.017
Na	0.929	0.995	0.98	0.968	0.028
K	0.009	0.009	0.006	0.008	0.001
Fe	0.001	0.003	0.004	0.003	0.001
distance	55	55	55		

419 Pink Gneiss Plagioclase			L14		Average	Std.Dev.	RIM	RIM	Average	Std.Dev.
Sample #	921	922	931	933		(4)	919	920		(2)
SiO2	65.57	65.1	64.64	65.39	65.18	0.35	66.71	66.29	66.50	0.21
Al2O3	21.96	21.98	21.73	21.52	21.80	0.19	21.09	21.33	21.21	0.12
CaO	3.02	2.71	2.98	3.06	2.94	0.14	1.63	1.93	1.78	0.15
Na2O	10.3	10.78	10.51	10.46	10.51	0.17	11.67	11.39	11.53	0.14
K2O	0.25	0.23	0.25	0.27	0.25	0.01	0.18	0.19	0.19	0.01
FeO	0.05	0.08	0.12	0.04	0.07	0.03	0.03	0.03	0.03	0.00
total	101.15	100.88	100.23	100.74	100.75	0.33	101.31	101.16	101.24	0.07
AB	84.9	86.7	85.2	84.8	85.40	0.76	91.9	90.3	91.10	0.80
AN	13.7	12	13.4	13.7	13.20	0.70	7.1	8.5	7.80	0.70
KSP	1.4	1.2	1.3	1.4	1.33	0.08	0.9	1	0.95	0.05
Si	2.86	2.852	2.852	2.867	2.858	0.006	2.901	2.89	2.896	0.005
Al	1.129	1.135	1.13	1.112	1.127	0.009	1.081	1.096	1.089	0.007
Ca	0.141	0.127	0.141	0.144	0.138	0.007	0.076	0.091	0.084	0.007
Na	0.871	0.916	0.899	0.889	0.894	0.016	0.984	0.963	0.974	0.010
K	0.014	0.013	0.014	0.015	0.014	0.001	0.01	0.011	0.011	0.000
Fe	0.002	0.003	0.004	0.001	0.003	0.001	0.001	0.001	0.001	ERR
distance	57	57	57	57			57	57		

419 Pink Gneiss Plagioclase			PG419				
Sample #	13	14	15	16	21	22	25
SiO2	64.67	64.72	64.59	64.36	64.18	63.95	64.22
Al2O3	22.81	22.12	22.48	22.42	22.76	22.76	22.57
CaO	2.98	2.96	2.61	2.75	3.02	3.06	2.84
Na2O	9.68	9.78	10.51	9.92	9.82	9.83	9.71
K2O	0.28	0.23	0.14	0.17	0.19	0.23	0.22
FeO	0.19	0.09	0.19	0.12	0.1	0.05	0.05
total	100.61	99.9	100.52	99.74	100.07	99.88	99.61
AB	84.05	84.53	87.23	85.84	84.49	84.20	85.07
AN	14.31	14.16	11.99	13.14	14.40	14.50	13.70
KSP	1.64	1.31	0.78	1.01	1.11	1.30	1.23
Si	2.833	2.853	2.836	2.842	2.828	2.824	2.838
Al	1.177	1.149	1.163	1.166	1.182	1.184	1.175
Ca	0.14	0.14	0.123	0.13	0.143	0.145	0.134
Na	0.822	0.836	0.895	0.849	0.839	0.842	0.832
K	0.016	0.013	0.008	0.01	0.011	0.013	0.012
Fe	0.007	0.003	0.007	0.004	0.004	0.002	0.002
distance	+70	+70	+70	+70	+70	+70	+70

419 Pink Gneiss Plagioclase			PG419					Average	Std.Dev.
Sample #	26	30	31	32	33	35	36		(15)
SiO2	64.62	63.76	64.32	64.14	64.17	64.02	64.46	64.30	0.28
Al2O3	22.61	22.81	22.45	22.88	22.79	22.76	22.78	22.64	0.20
CaO	2.87	2.98	2.84	3.07	3.05	2.83	3.01	2.92	0.13
Na2O	9.81	9.74	9.81	9.43	9.61	9.88	9.69	9.80	0.23
K2O	0.16	0.25	0.23	0.28	0.26	0.26	0.28	0.23	0.04
FeO	0.09	0.12	0.1	0.05	0.15	0.23	0.1	0.12	0.05
total	100.16	99.66	99.75	99.85	100.03	99.98	100.32	100.01	0.30
AB	85.31	84.36	85.11	83.35	83.78	85.01	83.93	84.73	0.95
AN	13.78	14.23	13.58	14.99	14.69	13.48	14.45	13.96	0.74
KSP	0.92	1.41	1.32	1.65	1.53	1.51	1.63	1.31	0.27
Si	2.841	2.822	2.84	2.829	2.828	2.825	2.831	2.834	0.008
Al	1.171	1.19	1.168	1.189	1.184	1.184	1.179	1.176	0.011
Ca	0.135	0.141	0.134	0.145	0.144	0.134	0.142	0.138	0.006
Na	0.836	0.836	0.84	0.806	0.821	0.845	0.825	0.837	0.019
K	0.009	0.014	0.013	0.016	0.015	0.015	0.016	0.013	0.003
Fe	0.003	0.004	0.004	0.002	0.006	0.008	0.004	0.004	0.002
distance	+70	+70	+70	+70	+70	+70	+70		

S-1 Transect - Plagioclase UG-1				Average	Std.Dev.	S-1 Transect UG-2				
Sample #	4 IN	AMP 12	17	Gray Gn.	(3)	38	39	28	29	RIM 31
SiO2	64.79	65.12	64.96	64.96	0.13	64.45	65.89	66.61	65.35	64.87
Al2O3	22.08	22.26	21.62	21.99	0.27	21.49	21.94	21.99	21.87	21.46
CaO	3.53	3.25	2.99	3.26	0.22	3.32	3.49	3.11	3.28	3.34
Na2O	7.99	8.67	8.57	8.41	0.30	8.11	7.79	8.88	9.09	9.03
K2O	0.24	0.26	0.22	0.24	0.02	0.28	0.29	0.27	0.21	0.26
FeO	0.06	0.22	0.07	0.12	0.07	0.05	0.07	0.11	0.21	0.08
total	98.69	99.78	98.43	98.97	0.58	97.7	99.47	100.97	100.01	99.04
AB	79	81.5	82.7	81.07	1.54	80.1	78.6	82.3	82.4	81.7
AN	19.3	16.7	15.9	17.30	1.45	18.1	19.5	16	16.4	16.7
KSP	1.1	1.7	1.3	1.37	0.25	1.8	1.9	1.7	1.3	1.6
Si	2.873	2.865	2.889	2.876	0.010	2.889	2.894	2.891	2.872	2.879
Al	1.154	1.154	1.133	1.147	0.010	1.135	1.135	1.125	1.133	1.122
Ca	0.168	0.153	0.142	0.154	0.011	0.159	0.164	0.145	0.154	0.159
Na	0.687	0.739	0.739	0.722	0.025	0.705	0.663	0.747	0.775	0.777
K	0.014	0.015	0.012	0.014	0.001	0.016	0.016	0.015	0.012	0.015
Fe	0.002	0.008	0.003	0.004	0.003	0.002	0.003	0.004	0.008	0.003
Distance	1.05	1.55	2.3			3.35	3.35	3.75	4.4	4.4

S-1 Transect UG-2 Plagioclase				Average	Std.Dev.
Sample #	CORE 32	25	20	Gray Gn.	(8)
SiO2	64.43	65.53	65.25	65.30	0.69
Al2O3	21.34	20.97	21.73	21.60	0.33
CaO	3.22	2.86	2.99	3.20	0.19
Na2O	8.85	8.63	8.61	8.62	0.43
K2O	0.33	0.24	0.3	0.27	0.03
FeO	0.06	0.11	0.07	0.10	0.05
total	98.23	98.34	98.95	99.09	0.99
AB	81.6	83.2	82.3	81.53	1.39
AN	16.4	15.2	15.8	16.76	1.30
KSP	2	1.6	1.9	1.73	0.21
Si	2.881	2.915	2.888	2.889	0.012
Al	1.125	1.099	1.133	1.126	0.011
Ca	0.154	0.136	0.142	0.152	0.009
Na	0.767	0.744	0.739	0.740	0.036
K	0.019	0.014	0.017	0.016	0.002
Fe	0.002	0.004	0.003	0.004	0.002
Distance	5.6	5.8	5.8		

S-1 Transect - Plagioclase	UG-3				Average	Std.Dev.
Sample #	42	46	48	51	Gray Gn.	(4)
SiO2	66.05	66	65.96	66.09	66.03	0.05
Al2O3	21.62	21.79	21.9	21.66	21.74	0.11
CaO	3.1	2.99	2.81	2.82	2.93	0.12
Na2O	7.77	7.83	8.39	9.02	8.25	0.50
K2O	0.3	0.2	0.26	0.3	0.27	0.04
FeO	0.06	0.05	0.11	0.08	0.08	0.02
total	98.9	98.86	99.43	99.97	99.29	0.45
AB	80.3	81.5	82.9	83.7	82.10	1.30
AN	17.7	17.2	15.3	14.4	16.15	1.35
KSP	2.1	1.3	1.7	1.9	1.75	0.30
Si	2.912	2.91	2.899	2.896	2.904	0.007
Al	1.123	1.132	1.134	1.119	1.127	0.006
Ca	0.146	0.141	0.132	0.132	0.138	0.006
Na	0.664	0.669	0.715	0.766	0.704	0.041
K	0.017	0.011	0.015	0.017	0.015	0.002
Fe	0.002	0.002	0.004	0.003	0.003	0.001
Distance	8.5	9.2	9.5	9.9		

S-1 Transect	UG-4 Protomylonite				Average	Std.Dev.
Sample #	RIM 53	CORE 54	57	64	P-Myl.	(4)
SiO2	65.89	66.17	65.96	65.71	65.93	0.16
Al2O3	22.05	21.7	21.4	21.82	21.74	0.23
CaO	3.21	2.87	2.21	2.9	2.80	0.36
Na2O	8.36	8.22	8.68	7.83	8.27	0.31
K2O	0.28	0.3	0.38	0.18	0.29	0.07
FeO	0.06	0.06	0.04	0.04	0.05	0.01
total	99.85	99.32	98.67	98.48	99.08	0.54
AB	81	82.2	85.5	81.9	82.65	1.70
AN	17.2	15.8	12.1	16.7	15.45	2.00
KSP	1.8	2	2.4	1.2	1.85	0.43
Si	2.887	2.908	2.919	2.906	2.905	0.012
Al	1.138	1.124	1.116	1.137	1.129	0.009
Ca	0.151	0.135	0.105	0.137	0.132	0.017
Na	0.71	0.701	0.745	0.671	0.707	0.026
K	0.016	0.017	0.021	0.01	0.016	0.004
Fe	0.002	0.002	0.001	0.001	0.002	0.001
Distance	11.2	11.2	12.1	13.75		

S-1 Transect Plagioclase LG-4				Average	Std.Dev.	LG-3 Pink Gneiss			
Sample #	CORE 83	81	78	Mylonite	(3)	69	118	113	111
SiO2	67.6	66.11	65.8	66.50	0.79	66.62	64.23	64.57	65.42
Al2O3	19.61	20.69	21.54	20.61	0.79	21.43	21.84	21.54	22.31
CaO	0.61	1.86	2.84	1.77	0.91	2.57	2.91	2.48	2.99
Na2O	10.02	9.55	8.23	9.27	0.76	7.77	8.99	8.95	8.18
K2O	0.17	0.17	0.22	0.19	0.02	0.2	0.23	0.27	0.23
FeO	0.09	0.02	0.06	0.06	0.03	0.16	0.07	0.11	0.07
total	98.1	98.4	98.69	98.40	0.24	98.75	98.27	97.92	99.2
AB	95.7	89.3	82.7	89.23	5.31	83.4	83.6	85.2	81.9
AN	3.2	9.6	15.8	9.53	5.14	15.2	14.9	13.1	16.5
KSP	1.1	1.1	1.5	1.23	0.19	1.4	1.5	1.6	1.5
Si	2.997	2.935	2.91	2.947	0.037	2.933	2.868	2.887	2.881
Al	1.025	1.082	1.123	1.077	0.040	1.112	1.149	1.135	1.158
Ca	0.029	0.088	0.135	0.084	0.043	0.121	0.139	0.119	0.141
Na	0.861	0.822	0.706	0.796	0.066	0.663	0.778	0.776	0.698
K	0.01	0.01	0.013	0.011	0.001	0.011	0.014	0.015	0.013
Fe	0.003	0.001	0.002	0.002	0.001	0.006	0.003	0.004	0.003
Distance	14.4	14.4	15.25			16.3	18.2	18.6	18.6

S-1 Transect LG-3 Pink Gneiss						
Sample #					Average	Std.Dev.
SiO2	108	99	91	84	Pink Gn.	(8)
Al2O3	64.84	64.11	65.72	65.19	65.09	0.78
CaO	22.7	21.85	21.49	21.39	21.82	0.44
Na2O	3.54	2.93	2.42	2.8	2.83	0.34
K2O	7.8	9.07	9.6	8.46	8.60	0.61
FeO	0.27	0.31	0.25	0.29	0.26	0.03
total	0.09	0.08	0.08	0.08	0.09	0.03
	99.24	98.35	99.56	98.21	98.69	0.55
AB						
AN	78.4	83.3	86.4	83	83.15	2.21
KSP	19.7	14.8	12.1	15.2	15.19	2.13
	1.8	1.9	1.5	1.8	1.63	0.17
Si						
Al	2.857	2.865	2.895	2.902	2.886	0.023
Ca	1.179	1.15	1.116	1.123	1.140	0.022
Na	0.167	0.14	0.115	0.134	0.135	0.016
K	0.666	0.786	0.82	0.73	0.740	0.055
Fe	0.015	0.018	0.014	0.016	0.014	0.002
Distance	0.004	0.003	0.003	0.003	0.004	0.001
	18.6	19.2	20.3	20.3		

S-1 Transect Plagioclase LG-2 Pink					Average	Std.Dev.
Sample #	140	136	128	126	Pink Gn.	(4)
SiO2	63.59	64.93	64.93	64.35	64.45	0.55
Al2O3	21.84	21.33	21.47	21.78	21.61	0.21
CaO	3.08	2.39	2.44	2.76	2.67	0.28
Na2O	8.79	8.79	8.44	8.33	8.59	0.21
K2O	0.3	0.27	0.29	0.23	0.27	0.03
FeO	0.08	0.07	0.13	0.07	0.09	0.02
total	97.68	97.78	97.7	97.52	97.67	0.09
AB	82.3	85.4	84.4	83.3	83.85	1.16
AN	15.9	12.8	13.5	15.2	14.35	1.25
KSP	1.8	1.7	2	1.5	1.75	0.18
Si	2.86	2.902	2.903	2.883	2.887	0.018
Al	1.157	1.124	1.131	1.15	1.141	0.013
Ca	0.148	0.114	0.117	0.132	0.128	0.014
Na	0.766	0.762	0.732	0.724	0.746	0.018
K	0.017	0.015	0.017	0.013	0.016	0.002
Fe	0.003	0.003	0.005	0.003	0.004	0.001
Distance	21.6	23.1	23.1	24		

S-1 Transect LG-1 Pink Gneiss				Average	Std.Dev.	Altered
Sample #	122	147	143	Pink Gn.	(3)	60
SiO2	63.99	65.24	65.13	64.79	0.57	68.96
Al2O3	21.79	21.56	21.22	21.52	0.23	19.53
CaO	2.98	2.31	2.17	2.49	0.35	0.21
Na2O	8.74	9.53	9.15	9.14	0.32	9.49
K2O	0.18	0.26	0.31	0.25	0.05	0.14
FeO	0.05	0.08	0.06	0.06	0.01	0.02
total	97.73	98.98	98.04	98.25	0.53	98.35
AB	83.2	86.8	86.7	85.57	1.67	97.8
AN	15.7	11.7	11.4	12.93	1.96	1.2
KSP	1.1	1.6	2	1.57	0.37	1
Si	2.87	2.89	2.907	2.889	0.015	3.032
Al	1.152	1.125	1.116	1.131	0.015	1.012
Ca	0.143	0.11	0.104	0.119	0.017	0.01
Na	0.76	0.819	0.792	0.790	0.024	0.809
K	0.01	0.015	0.018	0.014	0.003	0.008
Fe	0.002	0.003	0.002	0.002	0.000	0.001
Distance	25.2	26.55	27.4			

Appendix C - K-FELDSPAR ANALYSES - 419 & S-1 Transects

Ponaganset Gray Gneiss 419 K-Feldspar

Sample #	9	10	11	17	41	45	47	48	49
SiO2	63.69	63.84	64.39	64.41	64.39	64.27	64.52	64.2	63.61
Al2O3	18.26	18.53	18.56	18.63	18.45	18.48	18.57	18.45	18.47
CaO	0.04	0.04	0.03	0.03	0.03	0.03	0.02	0.02	0.04
Na2O	0.82	0.82	0.9	0.68	0.75	0.79	0.89	0.86	0.76
K2O	14.98	15	15.08	15.29	15.34	15.19	15.19	15.23	15.24
BaO	0.33	0.35	0.36	0.36	0.24	0.38	0.39	0.34	0.37
FeO	0.07	0.06	0.09	0.15	0.06	0.15	0.05	0.04	0.05
total	98.19	98.64	99.41	99.55	99.26	99.29	99.63	99.14	98.54
sample	9	10	11	17	41	45	47	48	49
AB	7.6	7.6	8.2	6.3	6.9	7.3	8.1	7.9	7
AN	0.2	0.2	0.1	0.1	0.1	0.1	0.1	0.1	0.2
KSP	91.5	91.5	90.9	92.9	92.6	91.8	91.1	91.4	92.1
Si	2.993	2.985	2.988	2.987	2.993	2.989	2.989	2.989	2.983
Al	1.011	1.021	1.015	1.018	1.01	1.013	1.014	1.012	1.021
Ca	0.002	0.002	0.001	0.001	0.001	0.001	0.001	0.001	0.002
Na	0.075	0.074	0.081	0.061	0.068	0.072	0.08	0.078	0.069
K	0.898	0.895	0.893	0.904	0.909	0.901	0.898	0.904	0.912
Ba	0.006	0.007	0.007	0.007	0.004	0.007	0.007	0.006	0.007
Fe	0.003	0.002	0.003	0.006	0.002	0.006	0.002	0.002	0.002

GG419 K-S Average Std.Dev.			GG419 419 Transect U-6 K-Spar					Average Std.Dev.	
Sample #	GG419	(9)	43 Rim	76	77	R?85	93	107	419U-6	(6)
SiO2	64.15	0.32	64.14	65.43	65.15	65.32	65.34	64.95	65.24	0.17
Al2O3	18.49	0.10	18.55	18.49	18.63	18.6	18.46	18.66	18.57	0.08
CaO	0.03	0.01	0.03	0.03	0.02	0.02	0.02	0.04	0.03	0.01
Na2O	0.81	0.07	0.44	0.81	0.81	0.55	0.67	0.81	0.73	0.11
K2O	15.17	0.12	15.73	15.28	15.34	15.46	15.39	15.32	15.36	0.06
BaO	0.35	0.04	0.23	0.19	0.17	0.21	0.2	0.21	0.20	0.01
FeO	0.08	0.04	0.04	0.1	0.1	0.08	0.1	0.1	0.10	0.01
total	99.07	0.47	99.16	100.33	100.22	100.24	100.18	100.09	100.21	0.08
sample										
AB	7.43	0.58	4.05	7.4	7.4	5.1	6.2	7.4	6.70	0.93
AN	0.13	0.05	0.15	0.1	0.1	0.1	0.1	0.2	0.12	0.04
KSP	91.76	0.63	95.36	92.2	92.2	94.4	93.3	92	92.82	0.91
Si	2.988	0.003	2.987	3.002	2.996	3.001	3.004	2.992	2.999	0.004
Al	1.015	0.004	1.018	1	1.01	1.007	1	1.013	1.006	0.005
Ca	0.001	0.000	0.001	0.001	0.001	0.001	0.001	0.002	0.001	0.000
Na	0.073	0.006	0.04	0.072	0.072	0.049	0.06	0.072	0.065	0.009
K	0.902	0.006	0.934	0.894	0.9	0.906	0.902	0.9	0.900	0.004
Ba	0.006	0.001	0.004	0.003	0.003	0.004	0.004	0.004	0.004	0.000
Fe	0.003	0.002	0.002	0.004	0.004	0.003	0.004	0.004	0.004	0.000

Ponaganset 419 U-5 Protomylonite K-Spar								Average Protomyl.	Std.Dev. (7)
Sample #	R113	R114	R115	50	52	53	54		
SiO2	64.11	64.4	65.57	63.8	63.73	63.55	63.11	64.04	0.73
Al2O3	17.99	18.31	18.49	19.04	19.14	19.15	19.18	18.76	0.45
CaO	0.04	0.03	0.04	0.02	0.01	0	0.01	0.02	0.01
Na2O	0.64	0.84	0.65	0.76	0.66	0.63	0.66	0.69	0.07
K2O	15.05	14.73	15.16	15.61	15.86	16.13	15.93	15.50	0.48
BaO	0.09	0.12	0.15	n.a.	n.a.	n.a.	n.a.	0.12	0.02
FeO	0.07	0.06	0.1	0.08	0.08	0.04	0.13	0.08	0.03
total	97.99	98.49	100.16	99.31	99.48	99.5	99.02	99.14	0.66
AB	6	8	4.1	6.84	5.91	5.62	5.93	6.06	1.10
AN	0.2	0.1	0.2	0.10	0.00	0.00	0.10	0.10	0.08
KSP	93.6	91.7	93.4	93.06	94.09	94.38	93.97	93.46	0.83
Si	3.009	3.003	3.009	2.965	2.961	2.958	2.951	2.979	0.024
Al	0.995	1.006	1	1.043	1.048	1.05	1.057	1.028	0.025
Ca	0.002	0.001	0.002	0.001	0	0	0.001	0.001	0.001
Na	0.058	0.076	0.058	0.068	0.059	0.057	0.06	0.062	0.007
K	0.901	0.876	0.887	0.925	0.94	0.957	0.95	0.919	0.029
Ba	0.002	0.002	0.003	n.a.	n.a.	n.a.	n.a.	0.002	0.000
Fe	0.003	0.002	0.004	0.003	0.003	0.002	0.005	0.003	0.001

419 Transect K-Feldspar - Mylonite						
Sample #	82	83	124	125	174	175
SiO2	63.68	63.47	64.45	65.07	64.41	64.18
Al2O3	19.22	19.06	18.09	18.16	18.22	18.18
CaO	0	0.03	0.03	0.03	0.02	0.02
Na2O	0.86	0.8	0.7	0.49	0.9	0.81
K2O	15.49	15.67	15.01	15.41	15.06	15.06
BaO	n.a.	n.a.	0.01	0.11	0.23	0.09
FeO	0.03	0.08	0.11	0.11	0.08	0.05
total	99.28	99.11	98.4	99.38	98.92	98.39
sample						
AB	7.74	7.16	6.6	4.6	8.3	7.5
AN	0.00	0.10	0.2	0.1	0.1	0.1
KSP	92.26	92.74	93.2	95.1	91.2	92.2
Si	2.96	2.96	3.01	3.015	3.002	3.002
Al	1.053	1.047	0.996	0.991	1.001	1.002
Ca	0	0.001	0.002	0.001	0.001	0.001
Na	0.077	0.072	0.063	0.044	0.081	0.073
K	0.918	0.932	0.894	0.911	0.895	0.899
Ba	n.a.	n.a.	0	0.002	0.004	0.002
Fe	0.001	0.003	0.004	0.004	0.003	0.002

419 Transect K-Feldspar - Mylonite Continued					Avg.	Std.Dev.
Sample #	178	179	182	121	UM419	(10)
SiO2	63.97	64.07	64.52	63.06	64.09	0.55
Al2O3	18.27	18.29	18.46	19.02	18.50	0.41
CaO	0.03	0.02	0.04	0.02	0.02	0.01
Na2O	0.75	0.67	0.83	0.69	0.75	0.11
K2O	15.36	15.41	15.25	15.73	15.35	0.24
BaO	0.11	0.05	0.08	n.a	0.10	0.06
FeO	0.08	0.03	0.12	0.08	0.08	0.03
total	98.57	98.54	99.3	98.6	98.85	0.37
sample						
AB	6.9	6.2	7.7	6.27	6.90	1.00
AN	0.2	0.1	0.2	0.10	0.12	0.06
KSP	92.7	93.6	92	93.63	92.86	1.03
Si	2.995	2.996	2.993	2.958	2.989	0.020
Al	1.008	1.008	1.009	1.051	1.017	0.023
Ca	0.002	0.001	0.002	0.001	0.001	0.001
Na	0.068	0.061	0.075	0.063	0.068	0.010
K	0.917	0.919	0.902	0.941	0.913	0.015
Ba	0.002	0.001	0.001	n.a	0.002	0.001
Fe	0.003	0.001	0.005	0.003	0.003	0.001

K-Feldspar 419 Transect - Amphibolite 11-13 Cm									Std.Dev.
Sample #	189	203	204	205	217	223	224	11-13 Cm	(7)
SiO2	64.5	64.25	64.69	64.25	64.99	64.12	64.58	64.48	0.28
Al2O3	18.31	18.23	18.5	18.56	18.22	18.6	18.58	18.43	0.16
CaO	0.04	0.04	0.03	0.03	0.05	0.03	0.04	0.04	0.01
Na2O	0.88	1.05	0.99	0.99	0.82	0.96	0.98	0.95	0.07
K2O	15.07	14.66	14.84	14.82	15.12	14.79	14.9	14.89	0.15
BaO	0.07	0.2	0.12	0.09	0.1	0.13	0.17	0.13	0.04
FeO	0.09	0.13	0.14	0.12	0.15	0.14	0.12	0.13	0.02
total	98.96	98.56	99.31	98.86	99.45	98.77	99.37	99.04	0.31
AB	8.1	9.8	9.2	9.2	7.6	9	9.1	8.86	0.69
AN	0.2	0.2	0.1	0.2	0.2	0.1	0.2	0.17	0.05
KSP	91.6	89.6	90.5	90.4	92	90.7	90.3	90.73	0.76
Si	3	2.999	2.995	2.989	3.008	2.987	2.991	2.996	0.007
Al	1.003	1.003	1.009	1.017	0.994	1.021	1.014	1.009	0.009
Ca	0.002	0.002	0.001	0.002	0.002	0.001	0.002	0.002	0.000
Na	0.079	0.095	0.089	0.089	0.074	0.087	0.089	0.086	0.007
K	0.894	0.873	0.876	0.879	0.892	0.879	0.88	0.882	0.007
Ba	0.001	0.004	0.002	0.002	0.002	0.002	0.003	0.002	0.001
Fe	0.004	0.005	0.005	0.005	0.006	0.005	0.005	0.005	0.001

K-Feldspar 419 Amphibolite 14-17.5 Cm									Average	Std.Dev.
Sample #	239	283	309	310	313	350	351	352	14-17.5cm	(8)
SiO2	64.79	64.71	64.73	64.4	65.04	64.22	64.42	64.32	64.58	0.26
Al2O3	18.74	18.34	18.22	18.27	18.35	18.22	18.33	18.21	18.34	0.16
CaO	0.05	0.05	0.06	0.04	0.05	0.05	0.05	0.05	0.05	0.00
Na2O	0.76	0.8	0.68	0.84	0.67	0.83	0.74	0.8	0.77	0.06
K2O	15.03	14.87	15.29	15.23	15.35	15.08	15.17	15.07	15.14	0.15
BaO	0.09	0.2	0.27	0.22	0.18	0.33	0.2	0.1	0.20	0.07
FeO	0.15	0.1	0.19	0.12	0.18	0.07	0.1	0.09	0.13	0.04
total	99.61	99.07	99.44	99.12	99.82	98.8	99.01	98.64	99.19	0.38
AB	7.1	7.5	6.3	7.7	6.2	7.6	6.9	7.4	7.09	0.54
AN	0.2	0.2	0.3	0.2	0.2	0.2	0.2	0.3	0.23	0.04
KSP	90.3	91.9	92.9	91.7	93.3	91.5	92.5	92.1	92.03	0.87
Si	2.991	3.003	3.001	2.996	3.003	2.997	2.997	3.002	2.999	0.004
Al	1.02	1.003	0.996	1.002	0.998	1.002	1.005	1.001	1.003	0.007
Ca	0.002	0.002	0.003	0.002	0.002	0.002	0.002	0.003	0.002	0.000
Na	0.068	0.072	0.061	0.076	0.06	0.075	0.067	0.072	0.069	0.006
K	0.885	0.88	0.904	0.904	0.904	0.898	0.9	0.897	0.897	0.009
Ba	0.002	0.004	0.005	0.004	0.003	0.006	0.004	0.002	0.004	0.001
Fe	0.006	0.004	0.007	0.005	0.007	0.003	0.004	0.004	0.005	0.001

K-Spar CPX-AB	Mylo	L2-1	L2-1	L3-1	L3-1	L3-1
Sample #	570	645	646	596	597	598
SiO2	64.21	63.91	63.72	63.04	63.71	64.46
Al2O3	18.8	18.46	18.4	18.48	18.55	18.52
CaO	0.09	0.04	0.04	0.07	0.09	0.07
Na2O	0.21	0.2	0.21	0.13	0.13	0.49
K2O	16.12	16	15.54	16.24	16.19	15.54
BaO	0.23	0.17	0.59	0.17	0.11	0.29
FeO	0.19	0.05	0.08	0.2	0.2	0.14
total	99.85	98.83	98.58	98.33	98.98	99.51
AB	1.9	1.8	2	1.2	1.2	4.6
AN	0.4	0.3	0.2	0.4	0.5	0.3
KSP	97.2	97.5	96.7	98.1	98.1	94.6
Si	2.977	2.988	2.991	2.973	2.979	2.991
Al	1.027	1.017	1.018	1.027	1.022	1.013
Ca	0.004	0.003	0.002	0.004	0.005	0.003
Na	0.019	0.018	0.019	0.012	0.012	0.045
K	0.953	0.955	0.93	0.977	0.966	0.92
Ba	0.004	0.003	0.011	0.003	0.002	0.005
Fe	0.007	0.002	0.003	0.008	0.008	0.005

CPX-Ab	L3-1	E3A	Average	Std.Dev.	E3A	L2-2
Sample #	649	492	Cpx-Ab	(8)	LG KSP494	577
SiO2	63.86	63.96	63.86	0.39	63.98	64.57
Al2O3	18.61	18.75	18.57	0.13	18.68	18.47
CaO	0.06	0.05	0.06	0.02	0.05	0.05
Na2O	0.31	0.42	0.26	0.12	0.72	0.7
K2O	15.88	15.89	15.93	0.25	15.52	15.5
BaO	0.23	0.2	0.25	0.14	0.24	0.24
FeO	0.13	0.19	0.15	0.05	0.1	0.19
total	99.08	99.46	99.08	0.48	99.29	99.72
AB	2.9	3.9	2.44	1.17	6.6	6.4
AN	0.3	0.2	0.33	0.10	0.2	0.2
KSP	96.4	95.5	96.76	1.16	92.8	93
Si	2.982	2.976	2.982	0.007	2.977	2.991
Al	1.024	1.028	1.022	0.005	1.024	1.008
Ca	0.003	0.002	0.003	0.001	0.002	0.002
Na	0.028	0.038	0.024	0.011	0.065	0.063
K	0.946	0.943	0.949	0.017	0.921	0.916
Ba	0.004	0.004	0.005	0.003	0.004	0.004
Fe	0.005	0.007	0.006	0.002	0.004	0.007

419 Transect K-Feldspar Pink Gneiss (w/CPX) (24-29.5 cm)									Average	Std.Dev.
Sample #	508	515	516	517	666	667	675	676	PG(Cpx)	(8)
SiO2	63.61	63.31	63.81	64.02	63.95	63.91	63.9	63.59	63.74	0.22
Al2O3	18.77	18.77	18.45	18.68	18.3	18.61	18.38	18.54	18.55	0.16
CaO	0.07	0.05	0.04	0.05	0.03	0.02	0.04	0.03	0.04	0.01
Na2O	0.96	0.78	0.82	0.83	0.84	0.65	0.76	0.46	0.77	0.13
K2O	15.13	15.24	15.17	15.22	15.22	15.42	15.41	15.73	15.30	0.18
BaO	0.17	0.23	0.22	0.13	0.19	0.13	0.16	0.22	0.17	0.05
FeO	0.09	0.08	0.12	0.08	0.09	0.09	0.06	0.07	0.09	0.02
total	98.8	98.46	98.63	99.01	98.62	98.83	98.71	98.64	98.66	0.20
AB	8.74	7.2	7.5	7.6	7.8	6	6.9	4.2	7.08	1.24
AN	0.35	0.3	0.2	0.2	0.2	0.1	0.2	0.2	0.23	0.07
KSP	90.6	92.1	91.9	92	91.7	93.7	92.5	95.1	92.37	1.23
Si	2.969	2.973	2.986	2.981	2.991	2.983	2.987	2.981	2.982	0.006
Al	1.033	1.032	1.017	1.025	1.009	1.024	1.013	1.024	1.022	0.008
Ca	0.004	0.003	0.002	0.002	0.002	0.001	0.002	0.002	0.002	0.001
Na	0.087	0.071	0.074	0.075	0.077	0.059	0.069	0.042	0.070	0.012
K	0.901	0.913	0.905	0.904	0.908	0.919	0.919	0.941	0.913	0.011
Ba	0.003	0.004	0.004	0.002	0.003	0.002	0.003	0.004	0.003	0.001
Fe	0.004	0.003	0.005	0.003	0.004	0.004	0.002	0.003	0.004	0.001

419 Transect Pink Gneiss (AM Only) K-Spar (30-32 cm)								Average	Std.Dev.
Sample #	695	697	698	699	706	724	R726	PinkGn.	(7)
SiO2	64.04	63.45	63.73	64.2	65.36	64.94	64.89	64.29	0.67
Al2O3	18.17	18.36	18.59	18.46	18.29	18.41	18.42	18.38	0.13
CaO	0.05	0.03	0.05	0.02	0.03	0.02	0.04	0.03	0.01
Na2O	0.53	0.28	0.22	0.8	0.86	0.82	0.89	0.59	0.26
K2O	15.64	16.03	16.08	15.39	15.11	15.3	15.17	15.59	0.36
BaO	0.15	0.25	0	0.09	0.08	0.2	0.22	0.13	0.08
FeO	0.1	0.09	0.17	0.09	0.09	0.24	0.12	0.13	0.06
total	98.68	98.49	98.84	99.05	99.82	99.93	99.75	99.14	0.55
AB	4.9	2.57	2.03	7.3	8	7.5	8.2	5.38	2.39
AN	0.3	0.15	0.26	0.1	0.1	0.1	0.2	0.17	0.08
KSP	94.5	96.81	97.73	92.4	91.8	92	91.2	94.21	2.35
Si	2.996	2.984	2.981	2.989	3.01	2.997	2.998	2.993	0.010
Al	1.002	1.018	1.025	1.013	0.992	1.001	1.003	1.009	0.011
Ca	0.003	0.002	0.003	0.001	0.001	0.001	0.002	0.002	0.001
Na	0.048	0.026	0.02	0.072	0.077	0.073	0.08	0.053	0.023
K	0.933	0.962	0.959	0.914	0.887	0.901	0.894	0.926	0.028
Ba	0.003	0.005	0	0.002	0.001	0.004	0.004	0.003	0.002
Fe	0.004	0.004	0.007	0.004	0.003	0.009	0.005	0.005	0.002

419 Transect Pink Gneiss (AM Only) K-Spar					(33-35cm) Average	Std.Dev.		Turbid	
Sample #	735R	738	740	109	119	(33-35CM)	(5)	707	711R
SiO2	64.69	64.2	64.48	62.5	63.16	63.81	0.84	63.33	63.99
Al2O3	18.11	18.11	18.58	19.03	18.96	18.56	0.40	18.24	18.48
CaO	0.02	0.04	0.06	0.02	0.01	0.03	0.02	0.02	0.05
Na2O	0.53	0.75	0.82	0.48	0.67	0.65	0.13	0.21	0.22
K2O	15.78	15.47	15.42	15.91	15.87	15.69	0.21	16	15.63
BaO	0.1	0.15	0.13	n.a.	n.a.	0.13	0.02	0.14	0.08
FeO	0.11	0.05	0.07	0	0	0.05	0.04	0.07	0.05
total	99.34	98.77	99.56	97.94	98.67	98.86	0.57	98.01	98.5
AB	4.9	6.8	7.5	4.38	6.03	5.92	1.16	1.95	2.09
AN	0.1	0.2	0.3	0.10	0.10	0.16	0.08	0.1	0.26
KSP	94.8	92.7	92	95.52	93.87	93.78	1.30	97.69	97.5
Si	3.007	3	2.988	2.953	2.961	2.982	0.021	2.989	2.993
Al	0.992	0.997	1.014	1.06	1.047	1.022	0.027	1.015	1.018
Ca	0.001	0.002	0.003	0.001	0.001	0.002	0.001	0.001	0.003
Na	0.048	0.068	0.074	0.044	0.061	0.059	0.011	0.019	0.02
K	0.935	0.922	0.911	0.959	0.949	0.935	0.017	0.963	0.932
Ba	0.002	0.003	0.002	n.a.	n.a.	0.001	0.001	0.003	0.001
Fe	0.004	0.002	0.003	0	0	0.003	0.001	0.003	0.002

419 Transect Pink Gneiss (AM Only) K-Spar						Average	Std.Dev.	Turbid
Sample #	747	761C	762C	767R	768C	36-38 cm	(5)	748
SiO2	64.74	64.07	64.2	64.31	63.99	64.26	0.26	63.71
Al2O3	18.35	18.25	18.94	18.39	17.97	18.38	0.32	18.24
CaO	0.03	0.03	0.04	0.02	0.03	0.03	0.01	0.04
Na2O	0.74	0.76	0.53	0.45	0.78	0.65	0.14	0.28
K2O	15.2	15.32	15.56	15.66	15.07	15.36	0.22	16.01
BaO	0.25	0.2	0.23	0.2	0.22	0.22	0.02	0.19
FeO	0.07	0.07	0.1	0.08	0.05	0.07	0.02	0.04
total	99.38	98.7	99.6	99.11	98.11	98.98	0.53	98.51
AB	6.8	7	4.9	4.2	7.2	6.02	1.23	2.58
AN	0.1	0.2	0.2	0.1	0.2	0.16	0.05	0.2
KSP	92.6	92.4	94.5	95.3	92.1	93.38	1.28	96.87
Si	3.001	2.995	2.975	2.996	3.006	2.995	0.011	2.993
Al	1.002	1.005	1.034	1.01	0.995	1.009	0.013	1.01
Ca	0.001	0.002	0.002	0.001	0.002	0.002	0.000	0.002
Na	0.066	0.069	0.048	0.041	0.071	0.059	0.012	0.026
K	0.899	0.914	0.92	0.931	0.903	0.913	0.012	0.959
Ba	0.005	0.004	0.004	0.004	0.004	0.004	0.000	0.003
Fe	0.003	0.003	0.004	0.003	0.002	0.003	0.001	0.002

419 Trans PG KSP (Bi+Am)				Average	Std.Dev.	50 cm		
Sample #	828	829	839	45 cm	(3)	860	861T	865R
SiO2	64.94	64.96	64.79	64.90	0.08	64.05	64.04	64.3
Al2O3	18.68	18.51	18.25	18.48	0.18	18.19	18.26	18.32
CaO	0.03	0.03	0.03	0.03	0.00	0.03	0.03	0.01
Na2O	0.54	0.64	0.77	0.65	0.09	0.77	0.4	0.52
K2O	15.43	15.23	14.96	15.21	0.19	14.9	15.03	15.02
BaO	0.22	0.11	0.14	0.16	0.05	0.23	0.13	0.11
FeO	0.08	0.05	0.1	0.08	0.02	0.08	0.03	0.06
total	99.92	99.53	99.04	99.50	0.36	98.25	97.92	98.34
AB	5	5.9	7.2	6.03	0.90	7.2	3.87	5
AN	0.1	0.1	0.1	0.10	ERR	0.2	0.16	0.1
KSP	94.5	93.7	92.4	93.53	0.87	92.1	95.71	94.7
Si	2.995	3.001	3.007	3.001	0.005	3.001	3.006	3.004
Al	1.015	1.008	0.999	1.007	0.007	1.004	1.01	1.008
Ca	0.001	0.001	0.001	0.001	ERR	0.002	0.002	0.001
Na	0.048	0.057	0.069	0.058	0.009	0.07	0.036	0.047
K	0.908	0.898	0.886	0.897	0.009	0.89	0.9	0.895
Ba	0.004	0.002	0.003	0.003	0.001	0.004	0.002	0.002
Fe	0.003	0.002	0.004	0.003	0.001	0.003	0.001	0.002

419 Trans PG KSP	Average	Std.Dev.	419 Trans PG KSP (Bi+Am)		52-59 cm (L12-L14)			
Sample #	866C PG 50 cm	(4)	891	893C	895	899	906	910
SiO2	64.10	0.12	64.83	64.61	64.43	64.82	64.71	64.61
Al2O3	18.27	0.05	18.41	17.95	17.95	18.09	18.32	18.45
CaO	0.02	0.01	0.03	0.03	0.04	0.03	0.04	0.03
Na2O	0.52	0.16	0.85	0.54	0.84	0.99	0.63	1.03
K2O	15.06	0.14	14.82	15.09	14.78	14.66	15.14	14.59
BaO	0.24	0.14	0.16	0.1	0.25	0.09	0.13	0.17
FeO	0.05	0.02	0.09	0.05	0.06	0.1	0.07	0.05
total	98.24	0.20	99.19	98.37	98.35	98.78	99.04	98.93
AB	4.89	1.44	7.9	5.1	7.9	9.3	5.9	9.7
AN	0.14	0.04	0.1	0.2	0.2	0.1	0.2	0.1
KSP	94.48	1.42	91.6	94.4	91.4	90.4	93.6	89.9
Si	3.002	0.003	3.003	3.018	3.012	3.013	3.006	2.999
Al	1.008	0.002	1.005	0.988	0.989	0.991	1.003	1.009
Ca	0.002	0.001	0.001	0.002	0.002	0.001	0.002	0.001
Na	0.047	0.014	0.076	0.049	0.076	0.089	0.057	0.093
K	0.900	0.009	0.876	0.899	0.881	0.869	0.897	0.864
Ba	0.004	0.003	0.003	0.002	0.005	0.002	0.002	0.003
Fe	0.002	0.001	0.003	0.002	0.002	0.004	0.003	0.002

419 Trans PG KSP (Bi+Am)	52-59 cm (L12-L14)						Average	Std.Dev.
Sample #	917	918	924	925	932	934	52-59 cm	(12)
SiO2	65.22	65.4	64.67	64.8	65.16	64.82	64.84	0.27
Al2O3	18.27	18.67	18.25	18.58	18.2	18.25	18.28	0.21
CaO	0.02	0.03	0.03	0.06	0.03	0.03	0.03	0.01
Na2O	0.89	0.78	0.8	1.38	1.13	0.77	0.89	0.22
K2O	14.78	15.12	15.04	14.62	14.48	15.05	14.85	0.22
BaO	0.09	0.15	0.13	0.12	0.14	0.15	0.14	0.04
FeO	0.07	0.03	0.05	0.02	0.03	0.05	0.06	0.02
total	99.34	100.18	98.97	99.58	99.17	99.12	99.09	0.48
AB	8.4	7.2	7.4	12.48	10.5	7.2	8.25	1.93
AN	0.1	0.1	0.2	0.3	0.1	0.2	0.16	0.06
KSP	91.3	92.4	92.1	87	89.1	92.3	91.29	1.91
Si	3.013	3	3.004	2.99	3.013	3.008	3.007	0.008
Al	0.994	1.009	0.999	1.01	0.992	0.998	0.999	0.008
Ca	0.001	0.001	0.002	0.003	0.001	0.002	0.002	0.001
Na	0.08	0.069	0.072	0.123	0.101	0.069	0.080	0.019
K	0.871	0.885	0.892	0.861	0.854	0.891	0.878	0.014
Ba	0.002	0.003	0.002	0.002	0.003	0.003	0.003	0.001
Fe	0.003	0.001	0.002	0.001	0.002	0.002	0.002	0.001

419 Pink Gneiss	+70 cm (reference pink gneiss)							Average	Std.Dev.
Sample #	9	10	23	24	27	28	29	PG419	(7)
SiO2	64.25	64.76	63.14	63.42	64.09	63.58	63.71	63.85	0.51
Al2O3	19.35	19.25	19.14	19.18	19.13	18.95	19.17	19.17	0.11
CaO	0.03	0.02	0.07	0.01	0.01	0.01	0.02	0.02	0.02
Na2O	0.85	0.81	0.55	0.55	0.76	0.75	0.73	0.71	0.11
K2O	15.5	15.5	15.91	15.81	15.76	15.7	15.78	15.71	0.14
BaO	n.a.	n.a.	n.a.	n.a.	n.a.	n.a.	n.a.	n.a.	n.a.
FeO	0.07	0.06	0.06	0.11	0	0	0.06	0.05	0.04
total	100.05	100.4	98.87	99.08	99.75	98.99	99.47	99.52	0.54
AB	7.69	7.35	4.98	5.05	6.81	6.79	6.59	6.46	0.98
AN	0.10	0.10	0.40	0.00	0.00	0.00	0.10	0.10	0.13
OR	92.21	92.55	94.62	94.95	93.19	93.21	93.31	93.44	0.94
Si	2.962	2.971	2.955	2.958	2.967	2.967	2.96	2.963	0.005
Al	1.051	1.041	1.056	1.054	1.043	1.042	1.049	1.048	0.006
Ca	0.001	0.001	0.004	0	0	0	0.001	0.001	0.001
Na	0.076	0.072	0.05	0.05	0.068	0.068	0.066	0.064	0.010
K	0.911	0.907	0.95	0.941	0.93	0.934	0.935	0.930	0.014
Ba	n.a.	n.a.	n.a.	n.a.	n.a.	n.a.	n.a.	n.a.	n.a.
Fe	0.003	0.002	0.002	0.004	0	0	0.002	0.002	0.001

S-1 Transect K-Feldspars			Avg.	Std.Dev.	Gray Gneiss UG-2			Avg.	Std.Dev.
Sample #	5	13	GG-UG1	(2)	36	33	21	GG-UG2	(3)
SiO2	65.28	64.53	64.905	0.37	64.39	65.66	65.36	65.137	0.54
Al2O3	18.36	18.06	18.210	0.15	17.74	18.27	18.38	18.130	0.28
CaO	0.03	0.05	0.040	0.01	0.03	0.05	0.04	0.040	0.01
Na2O	0.67	0.89	0.780	0.11	1.41	0.9	0.64	0.983	0.32
K2O	15.44	14.96	15.200	0.24	15.16	14.96	15.41	15.177	0.18
BaO	0	0	0.000	0.00	0.66	0	0	0.220	0.31
FeO	0.12	0.06	0.090	0.03	0.04	0.05	0.05	0.047	0.00
total	99.9	98.55	99.225	0.67	99.43	99.89	99.88	99.733	0.21
AB	6.2	8.2	7.200	1.000	12.3	8.3	5.91	8.837	2.636
AN	0.1	0.2	0.150	0.050	0.2	0.2	0.2	0.200	0.000
KSP	93.2	91.1	92.150	1.050	87.1	91	93.54	90.547	2.649
Si	3.004	3.007	3.006	0.002	3.005	3.013	3.007	3.008	0.003
Al	0.996	0.992	0.994	0.002	0.976	0.988	0.996	0.987	0.008
Ca	0.001	0.002	0.002	0.001	0.002	0.002	0.002	0.002	0.000
Na	0.06	0.08	0.070	0.010	0.128	0.08	0.057	0.088	0.030
K	0.906	0.889	0.898	0.008	0.903	0.876	0.904	0.894	0.013
Ba	0.005	0.005	0.005	0.000	0.004	0.005	0.003	0.004	0.001
Fe	0.005	0.002	0.004	0.001	0.002	0.002	0.002	0.002	0.000

S-1 Transect K-Feldspars			Avg.	Std.Dev.	Gray Gn. Protomyl. UG4				Avg.	Std.Dev.
Sample #	41	45	GG-UG3	(2)	55	56	59	63	Proto UG4	(4)
SiO2	66.1	65.94	66.020	0.08	66.13	65.68	65.73	64.97	65.628	0.42
Al2O3	18.35	18.54	18.445	0.10	18.33	18.37	18.33	18.32	18.338	0.02
CaO	0.03	0.04	0.035	0.00	0.03	0.03	0.03	0.04	0.033	0.00
Na2O	0.82	0.81	0.815	0.00	0.78	0.65	0.78	0.55	0.690	0.10
K2O	15.32	15.3	15.310	0.01	15.26	15.63	15.38	15.65	15.480	0.17
BaO	0	0	0.000	0.00	0	0.01	0	0	0.003	0.00
FeO	0.05	0.05	0.050	0.00	0.05	0.06	0.04	0.05	0.050	0.01
total	100.67	100.68	100.675	0.01	100.58	100.43	100.29	99.58	100.220	0.38
AB	7.4	7.4	7.400	0.000	7.2	5.9	7.1	5	6.300	0.908
AN	0.1	0.2	0.150	0.050	0.2	0.1	0.1	0.2	0.150	0.050
KSP	92.1	91.9	92.000	0.100	92.2	93.6	92.5	94.5	93.200	0.914
Si	3.013	3.007	3.010	0.003	3.016	3.008	3.01	3.004	3.010	0.004
Al	0.986	0.996	0.991	0.005	0.986	0.991	0.99	0.998	0.991	0.004
Ca	0.001	0.002	0.002	0.001	0.002	0.001	0.001	0.002	0.002	0.000
Na	0.072	0.072	0.072	0.000	0.069	0.058	0.069	0.049	0.061	0.008
K	0.891	0.89	0.891	0.000	0.888	0.913	0.898	0.923	0.906	0.013
Ba	0.003	0.004	0.004	0.001	0.004	0.003	0.003	0.003	0.003	0.000
Fe	0.002	0.002	0.002	0.000	0.002	0.002	0.002	0.002	0.002	0.000

S-1 Transect K-Feldspars			LG4 Myl.	Avg.	Std.Dev.	LG3 Pink Gneiss			Avg.	Std.Dev.
Sample #	80	77	72	LG4 Myl.	(3)	116	102	92	PG LG3	(3)
SiO2	65.07	65.7	65.64	65.470	0.28	64.3	63.84	64.95	64.363	0.46
Al2O3	18.26	18.32	18.34	18.307	0.03	18.37	18.19	18.68	18.413	0.20
CaO	0.03	0.04	0.04	0.037	0.00	0.04	0.03	0.03	0.033	0.00
Na2O	0.91	0.73	0.84	0.827	0.07	1.03	0.78	0.93	0.913	0.10
K2O	15.25	15.68	15.34	15.423	0.19	15.68	15.67	14.02	15.123	0.78
BaO	0.02	0.01	0	0.010	0.01	0.03	0.01	0.01	0.017	0.01
FeO	0.06	0.06	0.05	0.057	0.00	0.07	0.05	0.05	0.057	0.01
total	99.6	100.54	100.25	100.130	0.39	99.52	98.57	98.67	98.920	0.43
AB	8.3	6.6	7.7	7.533	0.704	9.1	7	9.1	8.400	0.990
AN	0.1	0.2	0.2	0.167	0.047	0.2	0.2	0.1	0.167	0.047
KSP	91.2	92.9	91.7	91.933	0.713	90.4	92.3	90.3	91.000	0.920
Si	3.003	3.008	3.009	3.007	0.003	2.985	2.989	3.003	2.992	0.008
Al	0.993	0.988	0.991	0.991	0.002	1.005	1.004	1.018	1.009	0.006
Ca	0.001	0.002	0.002	0.002	0.000	0.002	0.002	0.001	0.002	0.000
Na	0.082	0.065	0.075	0.074	0.007	0.093	0.071	0.083	0.082	0.009
K	0.898	0.916	0.897	0.904	0.009	0.928	0.936	0.827	0.897	0.050
Ba	0.004	0.003	0.004	0.004	0.000	0.004	0.005	0.005	0.005	0.000
Fe	0.002	0.002	0.002	0.002	0.000	0.003	0.002	0.002	0.002	0.000

S-1 Transect K-Feldspars			Pink Gn. LG2 & LG1			Avg.	Std.Dev.	Turbid
Sample #	134	153	151	148	145	LG1 (4)	LG1 (4)	14
SiO2	64.16	63.68	63.73	63.89	63.85	63.788	0.09	64.72
Al2O3	18.35	18.4	18.21	18.56	18.37	18.385	0.12	18.32
CaO	0.03	0.04	0.04	0.05	0.04	0.043	0.00	0.04
Na2O	0.74	0.73	0.79	0.75	0.95	0.805	0.09	0.11
K2O	15.86	16	15.98	15.92	15.79	15.923	0.08	16.46
BaO	0	0.01	0	0.01	0.01	0.008	0.00	0
FeO	0.07	0.21	0.08	0.06	0.06	0.103	0.06	0.07
total	99.21	99.07	98.83	99.24	99.07	99.053	0.15	99.72
	LG 2	LG 1	LG 1	LG 1	LG 1			
AB	6.6	6.4	7	6.7	8.3	7.100	0.725	1
AN	0.1	0.2	0.2	0.2	0.2	0.200	0.000	0.2
KSP	92.9	93.1	92.5	92.7	91.3	92.400	0.671	98.49
Si	2.987	2.976	2.983	2.977	2.98	2.979	0.003	2.998
Al	1.007	1.013	1.004	1.019	1.01	1.012	0.005	1
Ca	0.001	0.002	0.002	0.002	0.002	0.002	0.000	0.002
Na	0.067	0.066	0.072	0.068	0.086	0.073	0.008	0.01
K	0.942	0.954	0.954	0.946	0.94	0.949	0.006	0.973
Ba	0.004	0.003	0.003	0.004	0.002	0.003	0.001	0.003
Fe	0.003	0.008	0.003	0.002	0.002	0.004	0.002	0.003

Appendix D - BIOTITE ANALYSES - 419 & S-1 Transects

419 Gray Gneiss Biotites						Average	Std.Dev.
Sample #	2	3	14	15	40	GG419	(5)
SiO2	37.14	37.14	37.13	37.31	36.85	37.11	0.15
Al2O3	14.18	14.13	14.39	14.44	14.93	14.41	0.28
TiO2	1.48	1.49	1.53	1.54	1.54	1.52	0.03
FeO	21.09	20.92	20.91	20.88	21.07	20.97	0.09
MgO	11.2	11.12	11.24	11.17	10.97	11.14	0.09
MnO	0.69	0.67	0.68	0.65	0.55	0.65	0.05
CaO	0.05	0.06	0.06	0.06	0.09	0.06	0.01
K2O	9.36	9.42	9.5	9.53	9.29	9.42	0.09
BaO	0.04	0.12	0.04	0.06	0.08	0.07	0.03
Na2O	0.1	0.11	0.08	0.08	0.08	0.09	0.01
F	1.27	1.23	1.31	1.21	1.23	1.25	0.04
H2O	3.28	3.3	3.28	3.33	3.31	3.30	0.02
total	99.88	99.71	100.15	100.26	99.99	100.00	0.19
-(F)	99.35	99.19	99.60	99.75	99.47	99.47	0.19
Si	5.648	5.661	5.628	5.649	5.592	5.636	0.024
AlIV	2.352	2.339	2.372	2.351	2.408	2.364	0.024
AlVI	0.189	0.199	0.198	0.224	0.262	0.214	0.026
Ti	0.169	0.171	0.174	0.175	0.176	0.173	0.003
Fe	2.682	2.666	2.651	2.643	2.674	2.663	0.014
Mn	0.089	0.086	0.087	0.083	0.071	0.083	0.006
Mg	2.539	2.526	2.539	2.52	2.481	2.521	0.021
Ca	0.008	0.01	0.01	0.01	0.016	0.011	0.003
Na	0.029	0.033	0.024	0.023	0.024	0.027	0.004
K	1.815	1.831	1.837	1.84	1.798	1.824	0.016
Ba	0.003	0.007	0.002	0.004	0.005	0.004	0.002
F	0.611	0.593	0.628	0.584	0.59	0.601	0.016
Mg/OCT	0.448	0.447	0.449	0.446	0.438	0.446	0.004
X sid	0.110	0.117	0.116	0.132	0.156	0.126	0.016
X ann	0.442	0.436	0.435	0.422	0.406	0.428	0.013
Xf/OH	-0.744	-0.759	-0.730	-0.767	-0.762	-0.752	0.014
IV(F)	1.633	1.646	1.619	1.649	1.629	1.635	0.011
F-rat	4.038	4.051	4.024	4.055	4.035	4.041	0.011
cations	43.377	43.396	43.357	43.404	43.398	43.386	0.017
Mg/Mg+Fe	0.486	0.487	0.489	0.488	0.481	0.486	0.003
a (PHL)	0.001573	0.001474	0.001679	0.001425	0.001347	0.001500	0.000116
distance	0.5	0.5	0.5	0.5	0.5		

419 U6 Biotites								Average	Std.Dev.
Sample #	70	71	72	73	74	82	83	U-6	(7)
SiO2	37.08	36.71	36.55	37.03	36.56	37.37	37.77	37.01	0.42
Al2O3	14.53	14.6	14.34	14.81	14.44	14.32	14.21	14.46	0.19
TiO2	1.36	1.52	1.4	1.69	1.68	1.46	1.43	1.51	0.12
FeO	21.41	21.68	21.28	20.54	21.24	20.49	20.26	20.99	0.50
MgO	12.06	11.82	12.18	11.84	11.74	11.71	11.99	11.91	0.16
MnO	0.56	0.63	0.51	0.57	0.67	0.66	0.62	0.60	0.05
CaO	0	0	0.01	0	0.02	0.06	0.08	0.02	0.03
K2O	9.66	9.65	9.39	9.81	9.49	9.5	9.38	9.55	0.15
BaO	n.a.	n.a.	n.a.	n.a.	n.a.	0.11	0.07	0.09	0.02
Na2O	0.06	0	0.02	0.02	0.02	0.08	0.09	0.04	0.03
F	1.05	1.19	1.08	0.87	1.04	1.31	1.19	1.10	0.13
H2O	3.44	3.36	3.39	3.52	3.41	3.29	3.37	3.40	0.07
total	101.21	101.16	100.15	100.7	100.31	100.36	100.46	100.62	0.39
-(F)	100.77	100.66	99.70	100.33	99.87	99.81	99.96	100.16	0.40
Si	5.582	5.538	5.558	5.589	5.557	5.641	5.682	5.592	0.048
AlIV	2.418	2.462	2.442	2.411	2.443	2.359	2.318	2.408	0.048
AlVI	0.16	0.133	0.128	0.224	0.143	0.188	0.201	0.168	0.034
Ti	0.154	0.172	0.16	0.192	0.192	0.166	0.162	0.171	0.014
Fe	2.696	2.735	2.706	2.593	2.7	2.587	2.549	2.652	0.068
Mn	0.071	0.08	0.066	0.073	0.086	0.084	0.079	0.077	0.007
Mg	2.706	2.658	2.761	2.664	2.66	2.635	2.688	2.682	0.039
Ca	0	0	0.002	0	0.003	0.01	0.013	0.004	0.005
Na	0.018	0	0.006	0.006	0.006	0.023	0.026	0.012	0.009
K	1.855	1.857	1.821	1.889	1.84	1.829	1.8	1.842	0.027
Ba	n.a.	n.a.	n.a.	n.a.	n.a.	0.007	0.004	0.006	0.001
F	0.5	0.568	0.519	0.415	0.5	0.625	0.566	0.528	0.062
Mg/OCT	0.468	0.460	0.474	0.464	0.460	0.466	0.473	0.466	0.005
X sid	0.088	0.074	0.069	0.125	0.080	0.106	0.112	0.093	0.020
X ann	0.444	0.466	0.456	0.411	0.460	0.428	0.415	0.440	0.020
Xf/OH	-0.845	-0.781	-0.827	-0.936	-0.845	-0.732	-0.783	-0.818	0.060
IV(F)	1.760	1.691	1.753	1.839	1.754	1.641	1.699	1.731	0.059
F-rat	4.166	4.096	4.159	4.244	4.159	4.047	4.105	4.136	0.059
cations	43.497	43.428	43.479	43.584	43.498	43.367	43.425	43.476	0.064
Mg/Mg+Fe	0.501	0.493	0.505	0.507	0.496	0.505	0.513	0.503	0.006
a (PHL)	0.001294	0.001575	0.001450	0.000867	0.001215	0.001854	0.001595	0.001407	0.000294
distance	1.5	1.5	1.5	1.5	1.5	1.5	1.5		

419 U-5 (Protomyl.) Biotites						Average	Std.Dev.
Sample #	63	65	66	67	68	U-5	(5)
SiO2	37.34	37.54	37.54	37.58	37.27	37.45	0.12
Al2O3	15.01	14.62	14.83	14.83	14.77	14.81	0.13
TiO2	1.38	1.42	1.71	1.7	1.74	1.59	0.16
FeO	20.6	20.78	20.86	20.46	20.21	20.58	0.23
MgO	12.11	12.23	12.13	12.02	11.79	12.06	0.15
MnO	0.63	0.54	0.53	0.55	0.5	0.55	0.04
CaO	0.02	0.01	0.01	0	0	0.01	0.01
K2O	9.62	9.71	9.61	9.7	9.7	9.67	0.04
BaO	n.a.	n.a.	n.a.	n.a.	n.a.	-	-
Na2O	0.08	0.06	0.05	0.06	0.03	0.06	0.02
F	0.82	1.05	1.18	1.07	0.93	1.01	0.12
H2O	3.57	3.47	3.43	3.47	3.5	3.49	0.05
total	101.18	101.43	101.88	101.44	100.44	101.27	0.47
-(F)	100.83	100.99	101.38	100.99	100.05	100.85	0.44
Si	5.602	5.616	5.584	5.61	5.621	5.607	0.013
AlIV	2.398	2.384	2.416	2.39	2.379	2.393	0.013
AlVI	0.255	0.193	0.183	0.219	0.246	0.219	0.028
Ti	0.156	0.16	0.191	0.191	0.197	0.179	0.017
Fe	2.585	2.6	2.595	2.554	2.549	2.577	0.021
Mn	0.08	0.068	0.067	0.07	0.064	0.070	0.005
Mg	2.708	2.727	2.689	2.675	2.651	2.690	0.026
Ca	0.003	0.002	0.002	0	0	0.001	0.001
Na	0.023	0.017	0.014	0.017	0.009	0.016	0.005
K	1.841	1.853	1.823	1.847	1.866	1.846	0.014
Ba	n.a.	n.a.	n.a.	n.a.	n.a.	-	-
F	0.389	0.497	0.555	0.505	0.444	0.478	0.057
Mg/OCT	0.468	0.474	0.470	0.469	0.465	0.469	0.003
X sid	0.140	0.106	0.102	0.122	0.138	0.122	0.015
X ann	0.391	0.420	0.429	0.409	0.397	0.409	0.012
Xf/OH	-0.968	-0.848	-0.793	-0.840	-0.904	-0.867	0.039
IV(F)	1.872	1.767	1.707	1.749	1.804	1.777	0.035
F-rat	4.277	4.172	4.113	4.154	4.210	4.182	0.035
cations	43.607	43.499	43.440	43.493	43.550	43.518	0.039
Mg/Mg+Fe	0.512	0.512	0.509	0.512	0.510	0.511	0.001
a (PHL)	0.000781	0.001313	0.001538	0.001274	0.000970	0.001175	0.000268
distance	4.5	4.5	4.5	4.5	4.5		

419 Pink Gneiss L-10 Biotites				Average	Std.Dev.
Sample #	824	825	827	L-10	(3)
SiO2	38.59	38.61	38.04	38.41	0.26
Al2O3	13.96	13.9	13.79	13.88	0.07
TiO2	1.37	1.43	1.47	1.42	0.04
FeO	21.11	20.91	21.31	21.11	0.16
MgO	11.29	11.07	11.11	11.16	0.10
MnO	1.08	0.98	1.12	1.06	0.06
CaO	0.06	0.08	0.09	0.08	0.01
K2O	9.31	9.25	8.91	9.16	0.18
BaO	0.1	0.12	0.14	0.12	0.02
Na2O	0.06	0.01	0.07	0.05	0.03
F	1.47	1.47	1.35	1.43	0.06
H2O	3.27	3.26	3.29	3.27	0.01
total	101.67	101.09	100.69	101.15	0.40
-(F)	101.05	100.47	100.12	100.55	0.38
Si	5.745	5.773	5.73	5.749	0.018
AlIV	2.255	2.227	2.27	2.251	0.018
AlVI	0.195	0.222	0.178	0.198	0.018
Ti	0.153	0.161	0.167	0.160	0.006
Fe	2.63	2.615	2.684	2.643	0.030
Mn	0.136	0.124	0.143	0.134	0.008
Mg	2.505	2.467	2.494	2.489	0.016
Ca	0.01	0.013	0.015	0.013	0.002
Na	0.017	0.003	0.02	0.013	0.007
K	1.768	1.764	1.712	1.748	0.026
Ba	0.006	0.007	0.008	0.007	0.001
F	0.692	0.695	0.643	0.677	0.024
Mg/OCT	0.446	0.441	0.440	0.442	0.002
X sid	0.115	0.133	0.105	0.118	0.011
X ann	0.439	0.426	0.455	0.440	0.012
Xf/OH	-0.679	-0.677	-0.718	-0.691	0.019
IV(F)	1.565	1.554	1.599	1.572	0.019
F-rat	3.970	3.959	4.004	3.978	0.019
cations	43.301	43.302	43.352	43.318	0.024
Mg/Mg+Fe	0.488	0.485	0.482	0.485	0.003
a (PHL)	0.001906	0.001836	0.001570	0.001771	0.000144
distance	46	46	46		

419 Pink Gn. Bio. L-12 (Qtz. Vein)					Average	Std.Dev.
Sample #	855	856	857	858	L-12 (QV)	(4)
SiO2	37.2	36.68	36.24	36.85	36.74	0.35
Al2O3	14.85	14.96	14.85	14.91	14.89	0.05
TiO2	1.12	1.06	0.98	1.02	1.05	0.05
FeO	23.92	24.6	25.04	24.34	24.48	0.41
MgO	8.48	8.02	7.75	8.15	8.10	0.26
MnO	1.03	1.18	1.08	1.16	1.11	0.06
CaO	0.07	0.08	0.12	0.08	0.09	0.02
K2O	9.26	9.17	8.94	9.05	9.11	0.12
BaO	0.03	0.12	0.13	0.14	0.11	0.04
Na2O	0.06	0.04	0	0.04	0.04	0.02
F	0.84	1.09	0.91	1.15	1.00	0.13
H2O	3.47	3.32	3.37	3.3	3.37	0.07
total	100.33	100.32	99.41	100.19	100.06	0.38
-(F)	99.98	99.86	99.03	99.71	99.64	0.37
Si	5.713	5.655	5.656	5.674	5.675	0.023
AlIV	2.287	2.345	2.344	2.326	2.326	0.023
AlVI	0.401	0.373	0.387	0.379	0.385	0.010
Ti	0.129	0.123	0.115	0.118	0.121	0.005
Fe	3.072	3.172	3.268	3.135	3.162	0.071
Mn	0.134	0.154	0.143	0.151	0.146	0.008
Mg	1.941	1.843	1.803	1.87	1.864	0.050
Ca	0.012	0.013	0.02	0.013	0.015	0.003
Na	0.018	0.012	0	0.012	0.011	0.007
K	1.814	1.805	1.78	1.777	1.794	0.016
Ba	0.002	0.007	0.008	0.008	0.006	0.002
F	0.408	0.531	0.449	0.56	0.487	0.061
Mg/OCT	0.342	0.325	0.315	0.331	0.328	0.010
X sid	0.278	0.266	0.278	0.269	0.273	0.005
X ann	0.380	0.409	0.407	0.401	0.399	0.012
Xf/OH	-0.945	-0.815	-0.898	-0.788	-0.858	0.063
IV(F)	1.680	1.534	1.604	1.513	1.579	0.065
F-rat	4.085	3.940	4.010	3.919	3.985	0.065
cations	43.586	43.461	43.541	43.426	43.504	0.063
Mg/Mg+Fe	0.387	0.367	0.356	0.374	0.371	0.011
a (PHL)	0.000315	0.000452	0.000299	0.000519	0.000396	0.000092
distance	50.5	50.5	50.5	50.5		

419 Pink Gneiss Biotite L-13				Average	Std.Dev.
Sample #	896	897	898	L-13	(3)
SiO2	37.33	37.21	37.4	37.31	0.08
Al2O3	13.91	14.46	14.55	14.31	0.28
TiO2	1.26	1.18	1.23	1.22	0.03
FeO	22.71	22.08	21.56	22.12	0.47
MgO	9.38	9.59	9.6	9.52	0.10
MnO	1.23	1.2	1.21	1.21	0.01
CaO	0.07	0.06	0.07	0.07	0.00
K2O	9.14	9.1	8.76	9.00	0.17
BaO	0.11	0.02	0.07	0.07	0.04
Na2O	0.07	0.06	0.08	0.07	0.01
F	1.74	1.02	1.18	1.31	0.31
H2O	3.03	3.37	3.3	3.23	0.15
total	99.98	99.35	99.01	99.45	0.40
-(F)	99.25	98.92	98.51	98.89	0.30
Si	5.705	5.72	5.738	5.721	0.013
AlIV	2.295	2.28	2.262	2.279	0.013
AlVI	0.21	0.34	0.369	0.306	0.069
Ti	0.145	0.136	0.142	0.141	0.004
Fe	2.902	2.839	2.766	2.836	0.056
Mn	0.159	0.156	0.159	0.158	0.001
Mg	2.137	2.2	2.195	2.177	0.029
Ca	0.011	0.01	0.012	0.011	0.001
Na	0.021	0.018	0.024	0.021	0.002
K	1.782	1.784	1.714	1.760	0.033
Ba	0.007	0.001	0.004	0.004	0.002
F	0.841	0.496	0.573	0.637	0.148
Mg/OCT	0.385	0.388	0.390	0.388	0.002
X sid	0.139	0.220	0.239	0.200	0.043
X ann	0.476	0.392	0.371	0.413	0.045
Xf/OH	-0.575	-0.849	-0.777	-0.723	0.116
IV(F)	1.387	1.647	1.573	1.525	0.109
F-rat	3.793	4.053	3.978	3.931	0.109
cations	43.150	43.498	43.423	43.357	0.150
Mg/Mg+Fe	0.424	0.437	0.442	0.434	0.008
a (PHL)	0.001755	0.000668	0.000852	0.001092	0.000475

419 Pink Gneiss Biotite L-14					Average	Std.Dev.	Pink Gneiss 419 (reference)		
Sample #	913	914	915	916	L-14	(4)	5	6	7
SiO2	38.03	37.55	37.27	36.46	37.33	0.57	35.46	35.8	35.71
Al2O3	14.47	14.42	14.77	14.38	14.51	0.15	15.55	15.46	15.32
TiO2	1.33	1.31	1.44	1.24	1.33	0.07	1.92	1.84	1.94
FeO	22.99	22.78	23.28	23.57	23.16	0.30	27.1	27.11	26.77
MgO	9.41	9.36	9.16	9.46	9.35	0.11	6.36	6.41	6.39
MnO	1.27	1.27	1.36	1.2	1.28	0.06	1.23	1.28	1.33
CaO	0.07	0.07	0.09	0.13	0.09	0.02	0.06	0.09	0.06
K2O	9.2	9.04	9.13	8.23	8.90	0.39	9.25	9.11	9.37
BaO	0.02	0.05	0.06	0.1	0.06	0.03	n.a.	n.a.	n.a.
Na2O	0.08	0.09	0.09	0.13	0.10	0.02	0.06	0.02	0.03
F	1.65	1.53	1.24	0.89	1.33	0.29	1.14	0.96	1.12
H2O	3.15	3.17	3.31	3.41	3.26	0.11	3.29	3.39	3.3
total	101.67	100.64	101.2	99.2	100.68	0.93	101.42	101.47	101.34
-(F)	100.98	100.00	100.68	98.83	100.12	0.83	100.94	101.07	100.87
Si	5.706	5.696	5.651	5.648	5.675	0.026	5.482	5.529	5.521
AlIV	2.294	2.304	2.349	2.352	2.325	0.026	2.518	2.471	2.479
AlVI	0.265	0.273	0.289	0.273	0.275	0.009	0.314	0.342	0.311
Ti	0.15	0.149	0.164	0.144	0.152	0.007	0.223	0.214	0.226
Fe	2.885	2.89	2.952	3.053	2.945	0.068	3.503	3.501	3.461
Mn	0.161	0.163	0.175	0.157	0.164	0.007	0.161	0.167	0.174
Mg	2.104	2.116	2.07	2.184	2.119	0.041	1.465	1.475	1.472
Ca	0.011	0.011	0.015	0.022	0.015	0.004	0.01	0.015	0.01
Na	0.023	0.026	0.026	0.039	0.029	0.006	0.018	0.006	0.009
K	1.761	1.751	1.766	1.626	1.726	0.058	1.824	1.794	1.848
Ba	0.001	0.003	0.004	0.006	0.004	0.002	n.a.	n.a.	n.a.
F	0.783	0.734	0.595	0.436	0.637	0.135	0.557	0.469	0.548
Mg/OCT	0.378	0.378	0.366	0.376	0.375	0.005	0.259	0.259	0.261
X sid	0.177	0.182	0.194	0.176	0.182	0.007	0.246	0.266	0.244
X ann	0.445	0.440	0.440	0.449	0.443	0.004	0.495	0.475	0.495
Xf/OH	-0.614	-0.648	-0.758	-0.912	-0.723	0.116	-0.791	-0.877	-0.799
IV(F)	1.411	1.445	1.538	1.707	1.515	0.115	1.441	1.523	1.453
F-rat	3.816	3.850	3.943	4.113	3.920	0.115	3.847	3.928	3.858
cations	43.209	43.254	43.398	43.552	43.353	0.134	43.436	43.527	43.449
Mg/Mg+Fe	0.422	0.423	0.412	0.417	0.418	0.004	0.295	0.296	0.298
a (PHL)	0.001435	0.001274	0.000787	0.000457	0.000988	0.000389	0.000247	0.000177	0.000247
distance	57	57	57	57			62	62	62

Pink Gneiss 419 (reference)							Average	Std.Dev.
Sample #	8	11	12	19	20	34	PG419	(9)
SiO2	35.84	36.46	36.52	36.26	36.06	36.64	36.08	0.39
Al2O3	15.48	15.15	15.29	15.38	15.32	15.47	15.38	0.12
TiO2	1.86	1.95	2.04	1.77	1.95	1.81	1.90	0.08
FeO	26.41	26.37	26.13	26.41	26.84	26.72	26.65	0.32
MgO	6.73	6.77	6.92	6.55	6.64	6.69	6.61	0.18
MnO	1.3	1.3	1.19	1.3	1.28	1.28	1.28	0.04
CaO	0.05	0.04	0.04	0.01	0.01	0.01	0.04	0.03
K2O	9.2	9.36	9.41	9.5	9.56	9.36	9.35	0.13
BaO	n.a.	n.a.	n.a.	n.a.	n.a.	n.a.	-	-
Na2O	0.06	0.02	0.01	0.06	0.06	0.04	0.04	0.02
F	1.11	0.93	1.06	1.03	1.15	1.05	1.06	0.07
H2O	3.32	3.43	3.38	3.37	3.32	3.4	3.36	0.05
total	101.36	101.78	101.99	101.64	102.19	102.47	101.74	0.38
-(F)	100.89	101.39	101.54	101.21	101.71	102.03	101.29	0.38
Si	5.521	5.594	5.577	5.575	5.526	5.581	5.545	0.036
AlIV	2.479	2.406	2.423	2.425	2.474	2.419	2.455	0.036
AlVI	0.332	0.333	0.329	0.362	0.293	0.357	0.330	0.021
Ti	0.215	0.225	0.234	0.205	0.225	0.207	0.219	0.009
Fe	3.403	3.383	3.337	3.396	3.44	3.404	3.425	0.052
Mn	0.17	0.169	0.154	0.169	0.166	0.165	0.166	0.005
Mg	1.545	1.548	1.575	1.501	1.517	1.519	1.513	0.036
Ca	0.008	0.007	0.007	0.002	0.002	0.002	0.007	0.004
Na	0.018	0.006	0.003	0.018	0.018	0.012	0.012	0.006
K	1.808	1.832	1.833	1.863	1.869	1.818	1.832	0.023
Ba	n.a.	n.a.	n.a.	n.a.	n.a.	n.a.	-	-
F	0.541	0.451	0.512	0.501	0.557	0.506	0.516	0.036
Mg/OCT	0.273	0.274	0.280	0.266	0.269	0.269	0.268	0.007
X sid	0.255	0.256	0.252	0.282	0.227	0.277	0.256	0.018
X ann	0.472	0.470	0.468	0.451	0.504	0.455	0.476	0.017
Xf/OH	-0.806	-0.896	-0.833	-0.844	-0.791	-0.839	-0.830	0.033
IV(F)	1.470	1.561	1.506	1.495	1.457	1.494	1.488	0.033
F-rat	3.875	3.966	3.911	3.901	3.862	3.899	3.893	0.033
cations	43.455	43.545	43.482	43.498	43.442	43.490	43.480	0.033
Mg/Mg+Fe	0.312	0.314	0.321	0.307	0.306	0.309	0.306	0.008
a (PHL)	0.000273	0.000195	0.000264	0.000223	0.000283	0.000230	0.000238	0.000033
distance	62	62	62	62	62	62		

S-1 Transect	Gray Gn. UG-1		Avg.	Std.Dev.	S-1 Trans.	Gray G. UG-2		Avg.	Std.Dev.
Sample #	16	18	UG-1	(2)	27	24	22	UG-2	(3)
SiO2	37.59	38.52	38.06	0.46	38.81	38.13	38.17	38.37	0.31
Al2O3	13.91	14.00	13.96	0.05	14.01	13.74	13.92	13.89	0.11
TiO2	1.27	1.27	1.27	0.00	1.14	1.06	1.32	1.17	0.11
FeO	20.50	20.83	20.67	0.16	20.80	20.43	21.20	20.81	0.31
MgO	10.81	10.64	10.73	0.08	11.08	10.55	10.55	10.73	0.25
MnO	0.78	0.79	0.79	0.01	0.80	0.85	0.84	0.83	0.02
CaO	0.07	0.05	0.06	0.01	0.06	0.10	0.04	0.07	0.02
K2O	9.47	9.74	9.61	0.14	9.48	9.24	9.75	9.49	0.21
BaO	0.08	0.08	0.08	0.00	0.12	0.12	0.06	0.10	0.03
Na2O	0.05	0.04	0.05	0.00	0.04	0.05	0.05	0.05	0.00
F	1.93	1.85	1.89	0.04	1.74	1.72	1.84	1.77	0.05
H2O	2.96	3.06	3.01	0.05	3.13	3.05	3.05	3.08	0.04
total	99.42	100.87	100.15	0.72	101.21	99.04	100.79	100.35	0.94
- (F)	98.61	100.09	99.35	0.74	100.48	98.32	100.02	99.60	0.93
Si	5.708	5.768	5.738	0.030	5.783	5.804	5.737	5.775	0.028
AlIV	2.292	2.232	2.262	0.030	2.217	2.196	2.263	2.225	0.028
AlVI	0.198	0.238	0.218	0.020	0.242	0.269	0.202	0.238	0.028
Ti	0.145	0.143	0.144	0.001	0.128	0.121	0.149	0.133	0.012
Fe	2.603	2.608	2.606	0.003	2.592	2.601	2.665	2.619	0.032
Mn	0.100	0.100	0.100	0.000	0.101	0.110	0.108	0.106	0.004
Mg	2.447	2.375	2.411	0.036	2.461	2.394	2.363	2.406	0.041
Ca	0.011	0.008	0.010	0.002	0.010	0.016	0.006	0.011	0.004
Na	0.015	0.012	0.014	0.002	0.012	0.015	0.015	0.014	0.001
K	1.834	1.860	1.847	0.013	1.802	1.794	1.871	1.822	0.035
Ba	0.005	0.005	0.005	0.000	0.007	0.007	0.004	0.006	0.001
F	0.927	0.876	0.902	0.025	0.820	0.833	0.875	0.843	0.023
Mg/OCT	0.445	0.435	0.440	0.005	0.446	0.436	0.431	0.437	0.006
X sid	0.120	0.147	0.133	0.014	0.145	0.165	0.126	0.146	0.016
X ann	0.435	0.418	0.427	0.008	0.409	0.399	0.444	0.417	0.019
Xf/OH	-0.520	-0.552	-0.536	0.016	-0.589	-0.580	-0.553	-0.574	0.015
IV(F)	1.404	1.418	1.411	0.007	1.467	1.443	1.419	1.443	0.019
F-rat	3.810	3.823	3.816	0.007	3.872	3.848	3.824	3.848	0.019
Mg/Mg+Fe	0.485	0.477	0.481	0.004	0.487	0.479	0.470	0.479	0.007
a (PHL)	0.003296	0.002743	0.003019	0.000277	0.002593	0.002456	0.002705	0.002585	0.000102
CATIONS	43.063	43.118	43.091	0.027	43.177	43.160	43.117	43.151	0.025
distance	3.6	3.6			5.7	6.7	7.1		

S-1 Trans. Gray Gn. UG-3						Avg.	Std.Dev.
Sample #	40	43	44	47	49	UG-3	(5)
SiO2	38.71	38.97	38.70	38.89	38.31	38.72	0.23
Al2O3	14.38	14.40	13.93	14.30	14.01	14.20	0.20
TiO2	1.35	1.30	1.21	1.10	1.32	1.26	0.09
FeO	20.44	20.07	20.81	20.86	20.59	20.55	0.29
MgO	10.77	10.58	10.81	10.84	10.70	10.74	0.09
MnO	0.90	0.94	0.93	0.97	0.94	0.94	0.02
CaO	0.09	0.12	0.10	0.10	0.06	0.09	0.02
K2O	9.62	9.62	9.56	9.65	9.69	9.63	0.04
BaO	0.10	0.09	0.11	0.07	0.11	0.10	0.01
Na2O	0.05	0.05	0.04	0.04	0.10	0.06	0.02
F	1.78	1.89	1.97	1.84	1.88	1.87	0.06
H2O	3.12	3.07	3.02	3.10	3.03	3.07	0.04
total	101.31	101.10	101.19	101.76	100.74	101.22	0.33
- (F)	100.56	100.30	100.36	100.99	99.95	100.43	0.34
Si	5.757	5.790	5.769	5.765	5.744	5.765	0.015
AlIV	2.243	2.210	2.231	2.235	2.256	2.235	0.015
AlVI	0.276	0.311	0.216	0.263	0.219	0.257	0.036
Ti	0.151	0.146	0.136	0.123	0.149	0.141	0.010
Fe	2.542	2.494	2.595	2.586	2.582	2.560	0.038
Mn	0.113	0.118	0.117	0.122	0.119	0.118	0.003
Mg	2.387	2.343	2.402	2.395	2.391	2.384	0.021
Ca	0.014	0.019	0.016	0.016	0.010	0.015	0.003
Na	0.014	0.014	0.012	0.011	0.029	0.016	0.007
K	1.825	1.823	1.818	1.825	1.853	1.829	0.012
Ba	0.006	0.005	0.006	0.004	0.006	0.005	0.001
F	0.837	0.888	0.929	0.863	0.891	0.882	0.031
Mg/OCT	0.436	0.433	0.439	0.436	0.438	0.437	0.002
X sid	0.170	0.195	0.133	0.162	0.135	0.159	0.023
X ann	0.393	0.372	0.428	0.402	0.427	0.405	0.021
Xf/OH	-0.577	-0.545	-0.519	-0.561	-0.543	-0.549	0.019
IV(F)	1.440	1.398	1.393	1.425	1.415	1.414	0.017
F-rat	3.846	3.803	3.799	3.830	3.820	3.819	0.017
Mg/Mg+Fe	0.484	0.484	0.481	0.481	0.481	0.482	0.002
a (PHL)	0.002492	0.002656	0.003119	0.002678	0.002879	0.002765	0.000216
CATIONS	43.152	43.102	43.063	43.128	43.095	43.108	0.030
distance	9.8	9.8	9.8	10.7	10.9		

S-1 GG-->Myl. Trans. Bio.			UG-4			Avg.	Std.Dev.
Sample #	52	58	62	66	67	UG-4	(5)
SiO2	38.88	37.87	38.42	37.78	36.61	37.91	0.76
Al2O3	14.90	14.38	14.72	14.30	14.74	14.61	0.23
TiO2	1.53	1.38	1.48	1.47	1.14	1.40	0.14
FeO	20.14	21.29	20.21	20.34	21.68	20.73	0.63
MgO	10.53	10.46	10.54	9.77	10.77	10.41	0.34
MnO	0.97	1.01	1.04	0.91	1.06	1.00	0.05
CaO	0.05	0.04	0.05	0.11	0.09	0.07	0.03
K2O	9.75	9.72	9.77	9.08	7.83	9.23	0.75
BaO	0.11	0.11	0.10	0.09	0.09	0.10	0.01
Na2O	0.04	0.06	0.04	0.07	0.08	0.06	0.02
F	1.76	1.90	1.92	1.52	1.44	1.71	0.20
H2O	3.16	3.03	3.05	3.14	3.17	3.11	0.06
total	101.82	101.25	101.34	98.58	98.70	100.34	1.40
- (F)	101.08	100.45	100.53	97.94	98.09	99.62	1.33
Si	5.744	5.672	5.711	5.778	5.609	5.703	0.059
AlIV	2.256	2.328	2.289	2.222	2.391	2.297	0.059
AlVI	0.337	0.212	0.289	0.354	0.271	0.293	0.050
Ti	0.170	0.155	0.165	0.170	0.131	0.158	0.015
Fe	2.488	2.667	2.512	2.601	2.778	2.609	0.106
Mn	0.121	0.128	0.131	0.118	0.138	0.127	0.007
Mg	2.319	2.335	2.335	2.227	2.460	2.335	0.074
Ca	0.008	0.006	0.008	0.020	0.015	0.011	0.005
Na	0.011	0.017	0.012	0.021	0.024	0.017	0.005
K	1.837	1.857	1.852	1.771	1.530	1.769	0.124
Ba	0.006	0.006	0.006	0.005	0.005	0.006	0.000
F	0.822	0.900	0.903	0.735	0.698	0.812	0.084
Mg/OCT	0.427	0.425	0.430	0.407	0.426	0.423	0.008
X sid	0.213	0.133	0.182	0.230	0.161	0.183	0.035
X ann	0.360	0.442	0.389	0.363	0.413	0.394	0.031
Xf/OH	-0.587	-0.537	-0.535	-0.648	-0.675	-0.594	0.057
IV(F)	1.430	1.395	1.388	1.465	1.528	1.439	0.051
F-rat	3.835	3.801	3.794	3.870	3.933	3.845	0.051
Mg/Mg+Fe	0.482	0.467	0.482	0.461	0.470	0.472	0.008
a (PHL)	0.002216	0.002724	0.002745	0.001517	0.001568	0.002154	0.000534
CATIONS	43.167	43.086	43.086	43.254	43.292	43.177	0.085
distance	12.5	13.45	14.4	15	15		

S-1 Trans. Mylonite LG-4			Avg.	Std.Dev.
Sample #	79	76	LG-4	(2)
SiO2	38.13	38.65	38.39	0.26
Al2O3	15.21	14.27	14.74	0.47
TiO2	1.35	1.44	1.40	0.00
FeO	20.43	20.78	20.61	0.17
MgO	10.30	10.77	10.54	0.23
MnO	1.03	0.95	0.99	0.04
CaO	0.12	0.07	0.10	0.03
K2O	9.33	9.76	9.55	0.22
BaO	0.08	0.08	0.08	0.00
Na2O	0.11	0.04	0.08	0.04
F	1.63	2.02	1.83	0.20
H2O	3.18	3.02	3.10	0.08
total	100.90	101.85	101.38	0.48
- (F)	100.21	101.00	100.61	0.39
Si	5.694	5.725	5.710	0.015
AlIV	2.306	2.275	2.291	0.015
AlVI	0.371	0.216	0.294	0.078
Ti	0.152	0.160	0.156	0.004
Fe	2.551	2.574	2.563	0.012
Mn	0.130	0.119	0.125	0.006
Mg	2.293	2.378	2.336	0.042
Ca	0.019	0.011	0.015	0.004
Na	0.032	0.011	0.022	0.010
K	1.777	1.844	1.811	0.034
Ba	0.005	0.005	0.005	0.000
F	0.770	0.946	0.858	0.088
Mg/OCT	0.417	0.437	0.427	0.010
X sid	0.236	0.134	0.184	0.051
X ann	0.347	0.430	0.389	0.041
Xf/OH	-0.623	-0.509	-0.564	0.057
IV(F)	1.450	1.380	1.413	0.035
F-rat	3.855	3.785	3.818	0.035
Mg/Mg+Fe	0.473	0.480	0.477	0.003
a (PHL)	0.001811	0.003172	0.002492	0.000681
CATIONS	43.220	43.042	43.131	0.089
distance	15.7	16.1		

Appendix E - AMPHIBOLE ANALYSES - 419 & S-1 Transects

Gray Gneiss 419

Sample#	20	21	22	23	24	25	26	28	29	30
SiO2	40.01	40.29	40.01	39.66	40.33	39.95	39.82	39.84	40.23	40.39
Al2O3	11.33	11.52	11.81	11.61	11.4	11.46	11.38	11.42	11.47	11.09
TiO2	0.37	0.46	0.57	0.33	0.49	0.5	0.46	0.46	0.43	0.48
MgO	7.22	7.07	7.02	7.02	7.11	7.16	7.13	6.94	7.19	7.22
FeO	22.54	22.94	23.04	22.84	22.81	22.83	22.69	22.8	23.03	22.42
MnO	0.86	0.95	0.91	0.99	0.9	0.93	0.87	0.87	0.91	0.96
CaO	11.42	11.42	11.44	11.42	11.43	11.34	11.38	11.32	11.43	11.29
Na2O	1.77	1.67	1.81	1.58	1.83	1.84	1.84	1.93	1.93	1.95
K2O	1.71	1.71	1.78	1.65	1.72	1.68	1.71	1.73	1.68	1.7
F	0.62	0.58	0.7	0.53	0.58	0.61	0.55	0.63	0.54	0.61
H2O	1.6	1.64	1.58	1.64	1.64	1.61	1.63	1.6	1.65	1.61
total	99.45	100.25	100.67	99.27	100.24	99.91	99.46	99.54	100.49	99.72
- (F)	99.19	100.01	100.38	99.05	100.00	99.65	99.23	99.27	100.26	99.46
Si	6.26	6.257	6.195	6.228	6.265	6.23	6.238	6.24	6.242	6.297
Al IV	1.74	1.743	1.805	1.772	1.735	1.77	1.762	1.76	1.758	1.703
Al VI	0.348	0.366	0.349	0.376	0.352	0.336	0.341	0.347	0.341	0.335
Ti	0.044	0.054	0.066	0.039	0.057	0.059	0.054	0.054	0.05	0.056
Fe 2+	2.287	2.278	2.312	2.186	2.349	2.275	2.31	2.393	2.307	2.377
Mn	0.114	0.125	0.119	0.132	0.118	0.124	0.115	0.115	0.12	0.127
Mg	1.684	1.637	1.62	1.643	1.646	1.664	1.665	1.62	1.663	1.678
Ca	1.914	1.9	1.898	1.923	1.902	1.895	1.91	1.899	1.9	1.886
Na	0.537	0.503	0.543	0.481	0.551	0.556	0.559	0.586	0.581	0.589
K	0.341	0.339	0.352	0.33	0.341	0.334	0.344	0.346	0.332	0.338
Fe 3+	0.641	0.677	0.651	0.78	0.595	0.679	0.64	0.576	0.657	0.533
F	0.307	0.285	0.343	0.263	0.285	0.301	0.272	0.312	0.265	0.301
Na M4	0.053	0.062	0.061	0.053	0.059	0.064	0.056	0.06	0.062	0.066
Na TOT	0.534	0.5	0.54	0.477	0.548	0.551	0.554	0.583	0.574	0.587
Na A	0.481	0.438	0.479	0.424	0.489	0.487	0.498	0.523	0.512	0.521
Fe3+/FeT	0.219	0.229	0.220	0.263	0.202	0.230	0.217	0.194	0.222	0.183
Mg/Mg+Fe	0.424	0.418	0.412	0.429	0.412	0.422	0.419	0.404	0.419	0.414
a(TR)	0.000071	0.000076	0.000049	0.000083	0.000061	0.000063	0.000057	0.000041	0.000056	0.000058
K/K+Na	0.415	0.436	0.424	0.438	0.411	0.407	0.409	0.398	0.393	0.393
M	15.91	15.879	15.91	15.89	15.911	15.922	15.938	15.936	15.951	15.919
FeMg	2.357	2.349	2.365	2.279	2.41	2.34	2.371	2.454	2.377	2.448
FeAl	0.729	0.785	0.783	0.858	0.709	0.797	0.748	0.684	0.757	0.645
MgCa	0.118	0.137	0.117	0.156	0.117	0.137	0.125	0.105	0.138	0.106
PL	0.053	0.062	0.061	0.053	0.059	0.064	0.056	0.06	0.062	0.066
ED	0.91	0.879	0.91	0.89	0.911	0.922	0.938	0.936	0.951	0.919
TK	0.883	0.926	0.956	0.935	0.883	0.912	0.88	0.884	0.869	0.85
distance	0.5	0.5	0.5	0.5	0.5	0.5	0.5	0.5	0.5	0.5

Gray Gneiss 419						Average	Std. Dev.
Sample#	30	31	32	33	34	GRAY419	(14)
SiO2	40.39	40	40.29	40.43	40.76	40.14	0.28
Al2O3	11.09	11.19	11.17	11.05	11.09	11.36	0.21
TiO2	0.48	0.42	0.5	0.49	0.43	0.46	0.06
MgO	7.22	7.59	7.41	7.41	7.41	7.21	0.18
FeO	22.42	22.3	22.48	22.35	22.47	22.68	0.24
MnO	0.96	0.87	0.94	0.93	0.92	0.92	0.04
CaO	11.29	11.46	11.31	11.38	11.39	11.39	0.05
Na2O	1.95	1.7	2	1.89	1.86	1.83	0.11
K2O	1.7	1.7	1.61	1.72	1.66	1.70	0.04
F	0.61	0.69	0.62	0.68	0.78	0.62	0.07
H2O	1.61	1.57	1.61	1.58	1.55	1.61	0.03
total	99.72	99.49	99.94	99.91	100.32	99.90	0.42
- (F)	99.46	99.20	99.68	99.62	99.99	99.64	0.41
Si	6.297	6.246	6.269	6.286	6.303	6.254	0.028
Al IV	1.703	1.754	1.731	1.714	1.697	1.746	0.028
Al VI	0.335	0.305	0.316	0.313	0.326	0.339	0.019
Ti	0.056	0.049	0.059	0.057	0.05	0.053	0.007
Fe 2+	2.377	2.166	2.297	2.32	2.314	2.298	0.060
Mn	0.127	0.115	0.124	0.122	0.12	0.121	0.005
Mg	1.678	1.769	1.718	1.717	1.708	1.674	0.041
Ca	1.886	1.917	1.885	1.896	1.887	1.901	0.011
Na	0.589	0.515	0.603	0.57	0.558	0.552	0.033
K	0.338	0.339	0.319	0.341	0.327	0.337	0.008
Fe 3+	0.533	0.723	0.609	0.572	0.58	0.637	0.063
F	0.301	0.341	0.305	0.334	0.381	0.307	0.032
Na M4	0.066	0.052	0.067	0.061	0.064	0.060	0.005
Na TOT	0.587	0.509	0.6	0.567	0.554	0.548	0.033
Na A	0.521	0.457	0.533	0.506	0.49	0.488	0.031
Fe3+/FeT	0.183	0.250	0.210	0.198	0.200	0.217	0.021
Mg/Mg+Fe	0.414	0.450	0.428	0.425	0.425	0.421	0.010
a(TR)	0.000058	0.000103	0.000065	0.000070	0.000083	0.000067	0.000015
K/K+Na	0.393	0.426	0.374	0.403	0.400	0.409	0.017
M	15.919	15.898	15.93	15.908	15.87	15.912	0.022
FeMg	2.448	2.232	2.362	2.385	2.384	2.365	0.056
FeAl	0.645	0.821	0.727	0.686	0.68	0.743	0.058
MgCa	0.106	0.127	0.123	0.101	0.098	0.122	0.016
PL	0.066	0.052	0.067	0.061	0.064	0.060	0.005
ED	0.919	0.898	0.93	0.908	0.87	0.912	0.022
TK	0.85	0.908	0.868	0.867	0.891	0.894	0.029
distance	0.5	0.5	0.5	0.5	0.5		

419-U6								Average	Std. Dev.
Sample #	79	80	81	87	88	90	91	U6	(7)
SiO2	41.32	40.93	41.37	40.51	41.88	42.15	41.98	41.45	0.55
Al2O3	11.32	11.43	10.9	10.41	10.31	10.65	10.79	10.83	0.39
TiO2	0.49	0.48	0.51	0.42	0.51	0.41	0.43	0.46	0.04
MgO	7.85	7.91	8.12	7.98	8.33	8.37	8.41	8.14	0.22
FeO	21.94	22	21.81	21.45	21.43	21.5	21.35	21.64	0.25
MnO	0.89	0.93	0.84	0.86	0.92	0.89	0.9	0.89	0.03
CaO	11.52	11.43	11.3	11.26	11.27	11.53	11.49	11.40	0.11
Na2O	1.83	1.78	1.87	1.7	1.86	1.49	1.53	1.72	0.14
K2O	1.68	1.67	1.68	1.63	1.55	1.63	1.58	1.63	0.05
F	0.49	0.47	0.7	0.5	0.62	0.6	0.67	0.58	0.09
H2O	1.71	1.71	1.6	1.65	1.64	1.66	1.63	1.66	0.04
total	101.04	100.74	100.7	98.37	100.32	100.88	100.76	100.40	0.85
- (F)	100.83	100.54	100.41	98.16	100.06	100.63	100.48	100.16	0.84
Si	6.326	6.293	6.343	6.372	6.431	6.43	6.407	6.372	0.050
Al IV	1.674	1.707	1.657	1.628	1.569	1.57	1.593	1.628	0.050
Al VI	0.368	0.364	0.313	0.302	0.297	0.344	0.346	0.333	0.027
Ti	0.058	0.055	0.059	0.05	0.059	0.047	0.049	0.054	0.005
Fe 2+	2.239	2.145	2.203	2.167	2.202	2.102	2.071	2.161	0.055
Mn	0.115	0.121	0.109	0.115	0.121	0.115	0.116	0.116	0.004
Mg	1.791	1.813	1.856	1.871	1.907	1.903	1.913	1.865	0.044
Ca	1.89	1.883	1.856	1.898	1.854	1.884	1.878	1.878	0.015
Na	0.543	0.531	0.556	0.518	0.554	0.441	0.453	0.514	0.044
K	0.328	0.327	0.329	0.327	0.304	0.317	0.307	0.320	0.010
Fe 3+	0.553	0.659	0.58	0.631	0.537	0.621	0.635	0.602	0.043
F	0.237	0.229	0.339	0.249	0.301	0.289	0.323	0.281	0.040
Na M4	0.066	0.072	0.082	0.063	0.083	0.069	0.072	0.072	0.007
Na TOT	0.54	0.526	0.552	0.515	0.552	0.438	0.45	0.510	0.044
Na A	0.474	0.454	0.47	0.452	0.469	0.369	0.378	0.438	0.042
Fe3+/FeT	0.198	0.235	0.208	0.226	0.196	0.228	0.235	0.218	0.016
Mg/Mg+Fe	0.444	0.458	0.457	0.463	0.464	0.475	0.480	0.463	0.011
a(TR)	0.000119	0.000131	0.000143	0.000180	0.000214	0.000303	0.000298	0.000199	0.000071
K/K+Na	0.409	0.419	0.412	0.420	0.393	0.462	0.448	0.423	0.022
M	15.885	15.898	15.861	15.879	15.835	15.774	15.768	15.843	0.049
FeMg	2.296	2.211	2.253	2.232	2.264	2.17	2.138	2.223	0.051
FeAl	0.669	0.769	0.698	0.731	0.655	0.715	0.733	0.710	0.037
MgCa	0.124	0.157	0.12	0.136	0.123	0.132	0.13	0.132	0.012
PL	0.066	0.072	0.082	0.063	0.083	0.069	0.072	0.072	0.007
ED	0.885	0.898	0.861	0.879	0.835	0.774	0.768	0.843	0.049
TK	0.855	0.881	0.878	0.812	0.817	0.865	0.897	0.858	0.030
distance	1.5	1.5	1.5	1.5	1.5	1.5	1.5		

419-U5								Average	Std.Dev
Sample #	99	100	102	103	104	105	42	419-U5	(7)
SiO2	42.7	41.41	41.29	41.85	42.05	42.06	41.61	41.85	0.44
Al2O3	9.84	10.68	10.72	10.78	10.2	10.44	10.41	10.44	0.31
TiO2	0.36	0.44	0.52	0.46	0.49	0.55	0.47	0.47	0.06
MgO	8.7	8.42	8.25	8.41	8.29	8.41	8.45	8.42	0.13
FeO	20.72	21.51	21.83	21.74	21.56	21.39	22.55	21.61	0.51
MnO	0.93	0.93	0.95	0.84	0.91	0.91	0.86	0.90	0.04
CaO	11.39	11.32	11.39	11.29	11.29	11.38	11.17	11.32	0.07
Na2O	1.71	1.77	1.72	1.89	1.63	1.69	1.77	1.74	0.08
K2O	1.41	1.68	1.68	1.68	1.61	1.57	1.49	1.59	0.10
F	0.51	0.61	0.63	0.69	0.53	0.64	0.46	0.58	0.08
H2O	1.7	1.64	1.63	1.62	1.68	1.64	1.73	1.66	0.04
total	99.97	100.41	100.61	101.25	100.24	100.68	100.97	100.59	0.40
- (F)	99.76	100.15	100.34	100.96	100.02	100.41	100.78	100.35	0.39
Si	6.548	6.364	6.345	6.373	6.463	6.429	6.385	6.415	0.066
Al IV	1.452	1.636	1.655	1.627	1.537	1.571	1.615	1.585	0.066
Al VI	0.326	0.298	0.286	0.307	0.311	0.309	0.268	0.301	0.018
Ti	0.042	0.051	0.06	0.053	0.057	0.063	0.054	0.054	0.006
Fe 2+	2.151	2.092	2.109	2.162	2.175	2.149	2.032	2.124	0.046
Mn	0.121	0.121	0.124	0.108	0.12	0.118	0.112	0.118	0.005
Mg	1.988	1.931	1.89	1.909	1.901	1.916	1.933	1.924	0.030
Ca	1.871	1.864	1.875	1.842	1.859	1.864	1.837	1.859	0.013
Na	0.508	0.527	0.512	0.558	0.486	0.501	0.527	0.517	0.021
K	0.276	0.329	0.329	0.326	0.316	0.306	0.292	0.311	0.019
Fe 3+	0.492	0.653	0.676	0.592	0.578	0.571	0.824	0.627	0.098
F	0.247	0.301	0.306	0.332	0.258	0.309	0.223	0.282	0.037
Na M4	0.074	0.08	0.075	0.09	0.082	0.078	0.1	0.083	0.009
Na TOT	0.505	0.524	0.508	0.554	0.483	0.498	0.519	0.513	0.021
Na A	0.431	0.444	0.433	0.464	0.401	0.42	0.419	0.430	0.019
Fe3+/FeT	0.186	0.238	0.243	0.215	0.210	0.210	0.289	0.227	0.031
Mg/Mg+Fe	0.480	0.480	0.473	0.469	0.466	0.471	0.488	0.475	0.007
a(TR)	0.000419	0.000206	0.000190	0.000179	0.000279	0.000267	0.000266	0.000258	0.000076
K/K+Na	0.390	0.426	0.432	0.413	0.441	0.421	0.411	0.419	0.015
M	15.775	15.866	15.861	15.857	15.803	15.797	15.879	15.834	0.038
FeMg	2.23	2.162	2.173	2.217	2.238	2.204	2.09	2.188	0.048
FeAl	0.576	0.755	0.796	0.698	0.692	0.697	0.932	0.735	0.102
MgCa	0.12	0.146	0.145	0.131	0.142	0.126	0.223	0.148	0.032
PL	0.074	0.08	0.075	0.09	0.082	0.078	0.1	0.083	0.009
ED	0.775	0.866	0.861	0.857	0.803	0.797	0.879	0.834	0.038
TK	0.751	0.85	0.869	0.86	0.816	0.852	0.836	0.833	0.037
distance	3	3	3	3	3	3	3		

Mylonite 419					Average	Std.Dev
Sample #	108	109	110	111	U4A Myl.	(4)
SiO2	42.02	42.11	41.80	40.59	41.63	0.61
Al2O3	11.18	10.29	10.44	10.43	10.58	0.35
TiO2	0.53	0.45	0.43	0.44	0.46	0.04
MgO	8.33	8.14	8.33	7.80	8.15	0.22
FeO	22.45	21.62	21.63	21.89	21.90	0.34
MnO	0.96	0.94	0.91	0.82	0.91	0.05
CaO	11.34	11.16	11.28	11.14	11.23	0.08
Na2O	1.96	1.85	1.64	1.71	1.79	0.12
K2O	1.66	1.49	1.49	1.56	1.55	0.07
F	0.52	0.60	0.71	0.62	0.61	0.07
H2O	1.72	1.65	1.60	1.60	1.64	0.05
total	102.67	100.30	100.26	98.60	100.46	1.45
- (F)	102.45	100.05	99.96	98.34	100.20	1.47
Si	6.335	6.466	6.42	6.372	6.398	0.049
Al IV	1.665	1.534	1.58	1.628	1.602	0.049
Al VI	0.321	0.328	0.309	0.301	0.315	0.010
Ti	0.06	0.052	0.05	0.052	0.054	0.004
Fe 2+	2.132	2.247	2.091	2.2	2.168	0.060
Mn	0.123	0.122	0.118	0.109	0.118	0.006
Mg	1.872	1.863	1.907	1.825	1.867	0.029
Ca	1.832	1.836	1.856	1.874	1.850	0.017
Na	0.573	0.551	0.488	0.52	0.533	0.032
K	0.319	0.292	0.292	0.312	0.304	0.012
Fe 3+	0.673	0.516	0.668	0.653	0.628	0.065
F	0.248	0.296	0.345	0.308	0.299	0.035
Na M4	0.099	0.092	0.084	0.075	0.088	0.009
Na TOT	0.568	0.548	0.484	0.518	0.530	0.032
Na A	0.469	0.456	0.4	0.443	0.442	0.026
Fe3+/FeT	0.240	0.187	0.242	0.229	0.224	0.022
Mg/Mg+Fe	0.468	0.453	0.477	0.453	0.463	0.010
a(TR)	0.000151	0.000220	0.000286	0.000172	0.000208	0.000052
K/K+Na	0.405	0.390	0.422	0.413	0.408	0.012
M	15.905	15.807	15.779	15.846	15.834	0.047
FeMg	2.195	2.317	2.159	2.257	2.232	0.060
FeAl	0.793	0.62	0.768	0.757	0.735	0.067
MgCa	0.181	0.128	0.143	0.14	0.148	0.020
PL	0.099	0.092	0.084	0.075	0.088	0.009
ED	0.905	0.807	0.779	0.846	0.834	0.047
TK	0.859	0.819	0.885	0.857	0.855	0.024
distance	4.5	4.5	4.5	4.5		

Mylonite 419					Average	Std.Dev			Average	Std.Dev
Sample #	121	122	126	127	U4B Myl.	(4)	128	129	U4C Myl.	(2)
SiO2	42.09	41.67	42.63	41.84	42.06	0.36	41.39	41.33	41.36	0.03
Al2O3	10.52	10.39	9.66	10.18	10.19	0.33	10.38	10.45	10.42	0.03
TiO2	0.48	0.45	0.46	0.44	0.46	0.01	0.44	0.43	0.44	0.01
MgO	8.18	8.17	8.14	7.82	8.08	0.15	7.72	7.77	7.75	0.02
FeO	22.02	21.87	21.41	21.90	21.80	0.23	22.22	21.78	22.00	0.22
MnO	0.98	1.00	1.16	1.20	1.09	0.10	1.09	1.03	1.06	0.03
CaO	11.23	11.14	10.96	10.97	11.08	0.11	10.96	11.10	11.03	0.07
Na2O	1.87	1.86	1.86	1.95	1.89	0.04	1.95	1.82	1.89	0.06
K2O	1.55	1.55	1.37	1.60	1.52	0.09	1.56	1.60	1.58	0.02
F	0.67	0.61	0.58	0.53	0.60	0.05	0.56	0.52	0.54	0.02
H2O	1.63	1.64	1.66	1.67	1.65	0.02	1.65	1.67	1.66	0.01
total	101.22	100.35	99.89	100.10	100.39	0.51	99.92	99.50	99.71	0.21
- (F)	100.94	100.09	99.65	99.88	100.14	0.49	99.68	99.28	99.48	0.20
Si	6.418	6.415	6.562	6.464	6.465	0.059	6.417	6.424	6.421	0.003
Al IV	1.582	1.585	1.438	1.536	1.535	0.059	1.583	1.576	1.580	0.003
Al VI	0.307	0.3	0.314	0.318	0.310	0.007	0.314	0.338	0.326	0.012
Ti	0.055	0.052	0.053	0.051	0.053	0.001	0.051	0.05	0.051	0.000
Fe 2+	2.204	2.179	2.28	2.311	2.244	0.054	2.287	2.271	2.279	0.008
Mn	0.127	0.13	0.151	0.157	0.141	0.013	0.143	0.136	0.140	0.003
Mg	1.859	1.875	1.867	1.801	1.851	0.029	1.784	1.8	1.792	0.008
Ca	1.834	1.837	1.807	1.816	1.824	0.012	1.821	1.848	1.835	0.013
Na	0.553	0.555	0.555	0.584	0.562	0.013	0.586	0.548	0.567	0.019
K	0.301	0.304	0.269	0.315	0.297	0.017	0.309	0.317	0.313	0.004
Fe 3+	0.588	0.617	0.465	0.504	0.544	0.061	0.576	0.543	0.560	0.016
F	0.323	0.297	0.282	0.259	0.290	0.023	0.275	0.256	0.266	0.009
Na M4	0.094	0.094	0.107	0.103	0.100	0.006	0.102	0.087	0.095	0.007
Na TOT	0.588	0.553	0.553	0.581	0.569	0.016	0.583	0.544	0.564	0.019
Na A	0.494	0.459	0.446	0.478	0.469	0.018	0.481	0.457	0.469	0.012
Fe3+/FeT	0.211	0.221	0.169	0.179	0.195	0.021	0.201	0.193	0.197	0.004
Mg/Mg+Fe	0.458	0.463	0.450	0.438	0.452	0.009	0.438	0.442	0.440	0.002
a(TR)	0.000164	0.000197	0.000284	0.000149	0.000198	0.000052	0.000134	0.000157	0.000146	0.000012
K/K+Na	0.379	0.398	0.376	0.397	0.388	0.010	0.391	0.410	0.400	0.009
M	15.828	15.849	15.761	15.857	15.824	0.038	15.871	15.851	15.861	0.010
FeMg	2.276	2.257	2.378	2.417	2.332	0.067	2.379	2.357	2.368	0.011
FeAl	0.698	0.721	0.571	0.606	0.649	0.062	0.678	0.643	0.661	0.018
MgCa	0.14	0.153	0.13	0.142	0.141	0.008	0.155	0.138	0.147	0.008
PL	0.094	0.094	0.107	0.103	0.100	0.006	0.102	0.087	0.095	0.007
ED	0.828	0.849	0.761	0.857	0.824	0.038	0.871	0.851	0.861	0.010
TK	0.848	0.83	0.784	0.782	0.811	0.029	0.814	0.812	0.813	0.001
distance	7.5	7.5	7.5	7.5			9.5	9.5		

Mylonite 419								Average	Std.Dev.
Sample #	R166	R167	C168	C169	C170	176	180	U3A Myl.	(7)
SiO2	42.42	42.78	41.35	42.44	42.47	41.08	41.91	42.06	0.59
Al2O3	9.36	9.04	10.21	9.67	9.19	10.52	9.80	9.68	0.50
TiO2	0.42	0.46	0.58	0.37	0.39	0.43	0.44	0.44	0.06
MgO	8.56	8.53	8.02	8.33	8.60	7.77	8.15	8.28	0.29
FeO	21.87	21.92	22.69	22.28	22.06	22.54	22.37	22.25	0.29
MnO	0.93	1.00	0.94	0.96	0.90	0.96	0.87	0.94	0.04
CaO	11.43	11.25	11.33	11.48	11.44	11.03	11.24	11.31	0.15
Na2O	1.56	1.70	1.82	1.61	1.57	1.97	1.78	1.72	0.14
K2O	1.36	1.33	1.56	1.36	1.29	1.76	1.51	1.45	0.15
F	0.56	0.51	0.49	0.46	0.52	0.54	0.48	0.51	0.03
H2O	1.66	1.69	1.70	1.72	1.68	1.66	1.70	1.69	0.02
total	100.13	100.21	100.69	100.68	100.11	100.26	100.25	100.33	0.23
- (F)	99.89	100.00	100.48	100.49	99.89	100.03	100.05	100.12	0.24
Si	6.53	6.581	6.38	6.513	6.543	6.367	6.473	6.484	0.076
Al IV	1.47	1.419	1.62	1.487	1.457	1.633	1.527	1.516	0.076
Al VI	0.228	0.219	0.237	0.261	0.211	0.288	0.256	0.243	0.025
Ti	0.049	0.053	0.067	0.043	0.045	0.05	0.051	0.051	0.007
Fe 2+	2.098	2.179	2.191	2.138	2.084	2.284	2.223	2.171	0.065
Mn	0.121	0.13	0.123	0.125	0.117	0.126	0.114	0.122	0.005
Mg	1.964	1.956	1.844	1.905	1.975	1.795	1.876	1.902	0.063
Ca	1.885	1.854	1.873	1.888	1.888	1.832	1.86	1.869	0.020
Na	0.466	0.507	0.544	0.479	0.469	0.592	0.533	0.513	0.043
K	0.267	0.261	0.307	0.266	0.253	0.348	0.297	0.286	0.031
Fe 3+	0.692	0.619	0.707	0.693	0.729	0.616	0.641	0.671	0.042
F	0.273	0.248	0.239	0.223	0.253	0.265	0.234	0.248	0.016
Na M4	0.071	0.086	0.078	0.07	0.07	0.097	0.084	0.079	0.009
Na TOT	0.461	0.505	0.54	0.473	0.463	0.587	0.529	0.508	0.043
Na A	0.39	0.419	0.462	0.403	0.393	0.49	0.445	0.429	0.035
Fe3+/FeT	0.248	0.221	0.244	0.245	0.259	0.212	0.224	0.236	0.016
Mg/Mg+Fe	0.484	0.473	0.457	0.471	0.487	0.440	0.458	0.467	0.015
a(TR)	0.000455	0.000436	0.000173	0.000368	0.000495	0.000099	0.000242	0.000325	0.000142
K/K+Na	0.406	0.384	0.399	0.398	0.392	0.415	0.400	0.399	0.009
M	15.77	15.778	15.893	15.798	15.771	15.931	15.851	15.827	0.060
FeMg	2.17	2.256	2.247	2.22	2.156	2.36	2.286	2.242	0.065
FeAl	0.79	0.725	0.841	0.779	0.819	0.716	0.743	0.773	0.044
MgCa	0.152	0.156	0.169	0.165	0.161	0.159	0.161	0.160	0.005
PL	0.071	0.086	0.078	0.07	0.07	0.097	0.084	0.079	0.009
ED	0.77	0.778	0.893	0.798	0.771	0.931	0.851	0.827	0.060
TK	0.771	0.727	0.805	0.759	0.756	0.799	0.76	0.768	0.025
distance	11	11	11	11	11	11	11		

Mylonite 419			Average	Std.Dev.
Sample #	131	134	U3B Myl.	(2)
SiO2	41.12	41.68	41.40	0.28
Al2O3	9.51	9.72	9.62	0.11
TiO2	0.46	0.41	0.44	0.02
MgO	8.84	9.10	8.97	0.13
FeO	22.89	21.14	22.02	0.88
MnO	0.70	0.72	0.71	0.01
CaO	10.68	11.17	10.93	0.24
Na2O	1.70	1.66	1.68	0.02
K2O	1.27	1.40	1.34	0.06
F	0.49	0.38	0.44	0.06
H2O	1.68	1.74	1.71	0.03
total	99.34	99.12	99.23	0.11
- (F)	99.13	98.96	99.05	0.09
Si	6.419	6.473	6.446	0.027
Al IV	1.581	1.527	1.554	0.027
Al VI	0.169	0.252	0.211	0.041
Ti	0.054	0.048	0.051	0.003
Fe 2+	2.006	1.928	1.967	0.039
Mn	0.093	0.095	0.094	0.001
Mg	2.057	2.107	2.082	0.025
Ca	1.786	1.859	1.823	0.036
Na	0.515	0.5	0.508	0.007
K	0.253	0.277	0.265	0.012
Fe 3+	0.937	0.781	0.859	0.078
F	0.242	0.187	0.215	0.027
Na M4	0.084	0.089	0.087	0.002
Na TOT	0.508	0.493	0.501	0.007
Na A	0.424	0.404	0.414	0.010
Fe3+/FeT	0.318	0.288	0.303	0.015
Mg/Mg+Fe	0.506	0.522	0.514	0.008
a(TR)	0.000406	0.000535	0.000471	0.000065
K/K+Na	0.374	0.407	0.390	0.017
M	15.87	15.847	15.859	0.011
FeMg	2.045	1.975	2.010	0.035
FeAl	1.045	0.877	0.961	0.084
MgCa	0.316	0.211	0.263	0.052
PL	0.084	0.089	0.087	0.002
ED	0.87	0.847	0.858	0.012
TK	0.795	0.769	0.782	0.013
distance	11.5	11.5		

GG-AM Contact - Cores			Average	Std.Dev.	Amphibolite - Cores				
Sample #	184	187	Cores	(2)	194	198	199	200	229
SiO2	42.03	41.81	41.92	0.11	43.57	43.5	42.4	42.55	43.79
Al2O3	9.75	10.22	9.99	0.23	9	9.48	9.52	9.35	9.26
TiO2	0.48	0.44	0.46	0.02	0.38	0.37	0.48	0.44	0.37
MgO	8.81	8.09	8.45	0.36	10.15	9.8	9.47	9.73	9.96
FeO	21.48	22.02	21.75	0.27	20.06	20.71	20.57	20.57	20.35
MnO	0.73	0.76	0.75	0.02	0.64	0.65	0.62	0.66	0.61
CaO	11.26	11.2	11.23	0.03	11.35	11.52	11.21	11.42	11.46
Na2O	1.92	1.83	1.88	0.05	1.91	1.82	1.9	1.74	1.9
K2O	1.48	1.5	1.49	0.01	1.31	1.44	1.46	1.45	1.3
F	0.52	0.51	0.52	0.01	0.6	0.71	0.67	0.58	0.53
H2O	1.68	1.68	1.68	0.00	1.67	1.64	1.62	1.67	1.72
total	100.14	100.06	100.10	0.04	100.64	101.64	99.92	100.16	101.25
-(F)	99.92	99.85	99.88	0.04	100.39	101.34	99.64	99.92	101.03
Si	6.467	6.451	6.459	0.008	6.596	6.504	6.498	6.51	6.596
Al IV	1.533	1.549	1.541	0.008	1.404	1.496	1.502	1.49	1.404
Al VI	0.235	0.309	0.272	0.037	0.203	0.176	0.217	0.195	0.239
Ti	0.056	0.051	0.054	0.003	0.043	0.041	0.055	0.051	0.042
Fe 2+	2.136	2.252	2.194	0.058	1.946	1.989	2.027	1.924	1.998
Mn	0.095	0.099	0.097	0.002	0.082	0.082	0.08	0.086	0.078
Mg	2.021	1.86	1.941	0.080	2.29	2.183	2.163	2.219	2.236
Ca	1.856	1.851	1.854	0.002	1.841	1.846	1.841	1.872	1.849
Na	0.573	0.547	0.560	0.013	0.561	0.528	0.565	0.516	0.555
K	0.29	0.295	0.293	0.002	0.253	0.275	0.285	0.283	0.25
Fe 3+	0.607	0.571	0.589	0.018	0.578	0.6	0.595	0.684	0.549
F	0.253	0.249	0.251	0.002	0.292	0	0.325	0.281	0.252
Na M4	0.084	0.086	0.085	0.001	0.091	0.082	0.091	0.077	0.087
Na TOT	0.517	0.545	0.531	0.014	0.558	0.527	0.562	0.511	0.553
Na A	0.433	0.459	0.446	0.013	0.467	0.445	0.471	0.434	0.466
Fe3+/FeT	0.221	0.202	0.212	0.010	0.229	0.232	0.227	0.262	0.216
Mg/Mg+Fe	0.486	0.452	0.469	0.017	0.541	0.523	0.516	0.536	0.528
a (TR)	0.000259	0.000138	0.000199	0.000061	0.000573	0.000411	0.000299	0.000482	0.000534
K/K+Na	0.401	0.391	0.396	0.005	0.351	0.382	0.377	0.395	0.349
M	15.869	15.835	15.852	0.017	15.797	15.72	15.828	15.83	15.796
FeMg	2.175	2.3	2.238	0.062	1.985	2.03	2.052	1.959	2.034
FeAl	0.719	0.673	0.696	0.023	0.664	0.682	0.705	0.786	0.633
MgCa	0.15	0.142	0.146	0.004	0.142	0.071	0.137	0.159	0.142
PL	0.084	0.086	0.085	0.001	0.091	0.082	0.091	0.077	0.087
ED	0.869	0.835	0.852	0.017	0.797	0.72	0.828	0.83	0.796
TK	0.748	0.8	0.774	0.026	0.698	0.858	0.765	0.737	0.695
distance	11.75	11.75			12.5	12.5	12.5	12.5	12.5

Amph. Cores		Average	Std.Dev.	Amph. Cores		Average	Std.Dev.
Sample #	230	Cores	(6)	234	235	Cores	(2)
SiO2	43.17	43.16	0.52	42.86	42.56	42.71	0.15
Al2O3	9.37	9.33	0.17	9.52	9.58	9.55	0.03
TiO2	0.52	0.43	0.06	0.43	0.55	0.49	0.06
MgO	9.71	9.80	0.21	9.53	9.33	9.43	0.10
FeO	20.71	20.50	0.23	20.88	21.21	21.05	0.16
MnO	0.68	0.64	0.02	0.55	0.56	0.56	0.00
CaO	11.41	11.40	0.10	11.2	11.21	11.21	0.01
Na2O	1.88	1.86	0.06	1.98	1.87	1.93	0.05
K2O	1.47	1.41	0.07	1.5	1.48	1.49	0.01
F	0.59	0.61	0.06	0.53	0.55	0.54	0.01
H2O	1.68	1.67	0.03	1.7	1.68	1.69	0.00
total	101.19	100.80	0.62	100.68	100.58	100.63	0.05
-(F)	100.94	100.54	0.61	100.46	100.35	100.40	0.05
Si	6.531	6.539	0.041	6.523	6.496	6.510	0.014
Al IV	1.469	1.461	0.041	1.477	1.504	1.491	0.013
Al VI	0.202	0.205	0.019	0.23	0.22	0.225	0.005
Ti	0.059	0.049	0.007	0.049	0.064	0.057	0.007
Fe 2+	2.02	1.984	0.037	2.07	2.056	2.063	0.007
Mn	0.087	0.083	0.003	0.071	0.072	0.072	0.000
Mg	2.19	2.214	0.042	2.162	2.123	2.143	0.020
Ca	1.85	1.850	0.011	1.826	1.833	1.830	0.003
Na	0.554	0.547	0.018	0.584	0.553	0.569	0.016
K	0.284	0.272	0.015	0.293	0.288	0.291	0.002
Fe 3+	0.584	0.598	0.042	0.571	0.631	0.601	0.030
F	0.282	0.239	0.109	0.255	0.266	0.261	0.006
Na M4	0.087	0.086	0.005	0.099	0.097	0.098	0.001
Na TOT	0.55	0.544	0.018	0.581	0.55	0.566	0.015
Na A	0.463	0.458	0.013	0.482	0.453	0.468	0.014
Fe3+/FeT	0.224	0.232	0.015	0.216	0.235	0.226	0.009
Mg/Mg+Fe	0.520	0.527	0.009	0.511	0.508	0.509	0.001
a (TR)	0.000367	0.000444	0.000095	0.000251	0.000285	0.000268	0.000017
K/K+Na	0.380	0.372	0.017	0.378	0.389	0.383	0.005
M	15.83	15.800	0.039	15.856	15.84	15.848	0.008
FeMg	2.048	2.018	0.034	2.092	2.064	2.078	0.014
FeAl	0.702	0.695	0.047	0.669	0.759	0.714	0.045
MgCa	0.142	0.132	0.028	0.153	0.166	0.159	0.006
PL	0.087	0.086	0.005	0.099	0.097	0.098	0.001
ED	0.83	0.800	0.039	0.856	0.84	0.848	0.008
TK	0.726	0.747	0.055	0.72	0.761	0.741	0.021
distance	12.5			13.75	13.75	13.750	

Amphibolite - Cores							Average	Std.Dev.
Sample #	279	280	288	289	290	295	Cores	(6)
SiO2	43.45	43.18	44.5	44.39	43.34	44.88	43.96	0.66
Al2O3	9.22	9.22	8.59	8.41	9.08	8.09	8.77	0.43
TiO2	0.53	0.53	0.44	0.29	0.41	0.48	0.45	0.08
MgO	9.27	9.01	9.63	9.72	9.23	10.1	9.49	0.36
FeO	21.28	21.74	20.88	20.34	21.03	20.44	20.95	0.48
MnO	0.54	0.57	0.54	0.52	0.54	0.59	0.55	0.02
CaO	11.41	11.25	11.23	11.5	11.4	11.24	11.34	0.10
Na2O	1.83	1.73	1.74	1.58	1.71	1.8	1.73	0.08
K2O	1.41	1.45	1.32	1.13	1.39	1.14	1.31	0.13
F	0.51	0.43	0.53	0.41	0.54	0.43	0.48	0.05
H2O	1.72	1.75	1.72	1.76	1.69	1.77	1.74	0.03
total	101.17	100.86	101.12	100.05	100.36	100.96	100.75	0.41
-(F)	100.96	100.68	100.90	99.88	100.13	100.78	100.55	0.40
Si	6.583	6.579	6.709	6.75	6.609	6.761	6.665	0.077
Al IV	1.417	1.421	1.291	1.25	1.391	1.239	1.335	0.077
Al VI	0.229	0.234	0.234	0.257	0.242	0.197	0.232	0.018
Ti	0.06	0.061	0.05	0.033	0.048	0.054	0.051	0.009
Fe 2+	2.162	2.162	2.145	2.082	2.145	2.065	2.127	0.039
Mn	0.069	0.074	0.069	0.067	0.07	0.075	0.071	0.003
Mg	2.093	2.048	2.164	2.203	2.098	2.268	2.146	0.074
Ca	1.852	1.836	1.814	1.874	1.863	1.814	1.842	0.023
Na	0.538	0.511	0.509	0.466	0.506	0.526	0.509	0.022
K	0.272	0.282	0.254	0.219	0.27	0.219	0.253	0.025
Fe 3+	0.518	0.587	0.476	0.488	0.523	0.494	0.514	0.036
F	0.244	0.207	0.253	0.197	0.26	0.205	0.228	0.025
Na M4	0.085	0.095	0.104	0.074	0.079	0.105	0.090	0.012
Na TOT	0.534	0.506	0.506	0.463	0.502	0.521	0.505	0.022
Na A	0.449	0.411	0.402	0.389	0.423	0.416	0.415	0.019
Fe3+/FeT	0.193	0.214	0.182	0.190	0.196	0.193	0.195	0.010
Mg/Mg+Fe	0.492	0.486	0.502	0.514	0.494	0.523	0.502	0.013
a (TR)	0.000372	0.000356	0.000631	0.001036	0.000466	0.000932	0.000632	0.000266
K/K+Na	0.377	0.407	0.387	0.360	0.390	0.345	0.378	0.020
M	15.793	15.795	15.715	15.689	15.765	15.712	15.745	0.041
FeMg	2.171	2.175	2.164	2.116	2.167	2.086	2.147	0.033
FeAl	0.638	0.709	0.576	0.554	0.619	0.602	0.616	0.050
MgCa	0.131	0.166	0.138	0.13	0.126	0.153	0.141	0.014
PL	0.085	0.095	0.104	0.074	0.079	0.105	0.090	0.012
ED	0.793	0.795	0.715	0.689	0.765	0.712	0.745	0.041
TK	0.709	0.721	0.68	0.635	0.705	0.632	0.680	0.035
distance	14.75	14.75	14.75	14.75	14.75	14.75		

Amphibolite - Cores								Average	Std.Dev.
Sample #	304	305	308	338	339	353	354	Cores	(7)
SiO2	43.26	43.43	43.63	44.07	43.61	43.06	42.87	43.42	0.37
Al2O3	9.16	9.07	9.15	8.96	8.8	9.16	9.69	9.14	0.26
TiO2	0.47	0.45	0.47	0.49	0.5	0.53	0.58	0.50	0.04
MgO	9.52	9.6	9.21	9.03	9.16	9.19	9.32	9.29	0.19
FeO	20.93	20.86	20.88	21.82	21.9	21.41	20.93	21.25	0.43
MnO	0.56	0.57	0.52	0.59	0.57	0.59	0.58	0.57	0.02
CaO	11.26	11.32	11.5	11.41	11.43	11.17	11.33	11.35	0.10
Na2O	1.95	1.89	1.74	1.81	1.76	2.09	1.85	1.87	0.11
K2O	1.48	1.41	1.32	1.37	1.36	1.45	1.61	1.43	0.09
F	0.49	0.49	0.35	0.52	0.45	0.49	0.48	0.47	0.05
H2O	1.72	1.72	1.79	1.73	1.75	1.72	1.73	1.74	0.02
total	100.8	100.81	100.56	101.8	101.29	100.86	100.97	101.01	0.38
-(F)	100.59	100.60	100.41	101.58	101.10	100.65	100.77	100.82	0.37
Si	6.575	6.594	6.637	6.642	6.619	6.561	6.515	6.592	0.042
Al IV	1.425	1.406	1.363	1.358	1.381	1.439	1.485	1.408	0.042
Al VI	0.216	0.216	0.277	0.233	0.193	0.206	0.25	0.227	0.026
Ti	0.054	0.051	0.054	0.056	0.057	0.061	0.066	0.057	0.005
Fe 2+	2.123	2.091	2.193	2.255	2.173	2.214	2.118	2.167	0.054
Mn	0.072	0.073	0.067	0.075	0.073	0.076	0.075	0.073	0.003
Mg	2.157	2.172	2.088	2.029	2.072	2.087	2.111	2.102	0.046
Ca	1.834	1.841	1.874	1.843	1.859	1.824	1.845	1.846	0.015
Na	0.575	0.556	0.513	0.529	0.518	0.617	0.545	0.550	0.034
K	0.287	0.273	0.256	0.263	0.263	0.282	0.312	0.277	0.018
Fe 3+	0.522	0.541	0.448	0.482	0.585	0.499	0.525	0.515	0.041
F	0.24	0.235	0.168	0.248	0.216	0.236	0.231	0.225	0.025
Na M4	0.094	0.091	0.073	0.089	0.083	0.1	0.089	0.088	0.008
Na TOT	0.57	0.553	0.511	0.525	0.512	0.614	0.542	0.547	0.034
Na A	0.476	0.462	0.438	0.436	0.429	0.514	0.453	0.458	0.027
Fe3+/FeT	0.197	0.206	0.170	0.176	0.212	0.184	0.199	0.192	0.015
Mg/Mg+Fe	0.504	0.510	0.488	0.474	0.488	0.485	0.499	0.492	0.011
a (TR)	0.000309	0.000403	0.000491	0.000377	0.000437	0.000184	0.000260	0.000352	0.000099
K/K+Na	0.376	0.371	0.369	0.376	0.380	0.354	0.408	0.376	0.015
M	15.84	15.814	15.77	15.765	15.793	15.866	15.847	15.814	0.036
FeMg	2.141	2.113	2.206	2.274	2.189	2.229	2.127	2.183	0.054
FeAl	0.63	0.643	0.556	0.594	0.699	0.621	0.657	0.629	0.042
MgCa	0.144	0.144	0.127	0.13	0.153	0.143	0.145	0.141	0.008
PL	0.094	0.091	0.073	0.089	0.083	0.1	0.089	0.088	0.008
ED	0.84	0.814	0.77	0.765	0.793	0.866	0.847	0.814	0.036
TK	0.679	0.683	0.666	0.682	0.671	0.673	0.727	0.683	0.019
distance	16.75	16.75	16.75	16.75	16.75	16.75	16.75		

CPX-AB Mylonite					Average	Std.Dev.
Sample #	566	567	637	639	CPX-AB	(4)
SiO2	42.57	42.78	42.95	43.72	43.01	0.43
Al2O3	9.71	9.55	9.52	8.88	9.42	0.32
TiO2	0.43	0.39	0.37	0.35	0.39	0.03
MgO	8.79	8.99	8.96	9.43	9.04	0.24
FeO	21.49	21.53	21.81	21.56	21.60	0.13
MnO	0.54	0.64	0.63	0.59	0.60	0.04
CaO	11.39	11.53	11.33	11.72	11.49	0.15
Na2O	1.71	1.66	1.98	1.45	1.70	0.19
K2O	1.67	1.5	1.41	1.18	1.44	0.18
F	0.6	0.53	0.52	0.58	0.56	0.03
H2O	1.66	1.7	1.71	1.69	1.69	0.02
total	100.56	100.8	101.19	101.15	100.93	0.26
-(F)	100.31	100.58	100.97	100.91	100.69	0.27
Si	6.51	6.526	6.532	6.619	6.547	0.042
Al IV	1.49	1.474	1.468	1.381	1.453	0.042
Al VI	0.259	0.243	0.238	0.203	0.236	0.020
Ti	0.049	0.045	0.042	0.04	0.044	0.003
Fe 2+	2.204	2.107	2.182	1.992	2.121	0.083
Mn	0.07	0.083	0.081	0.076	0.078	0.005
Mg	2.003	2.044	2.033	2.128	2.052	0.046
Ca	1.866	1.885	1.846	1.901	1.875	0.021
Na	0.507	0.491	0.584	0.426	0.502	0.056
K	0.328	0.292	0.274	0.228	0.281	0.036
Fe 3+	0.53	0.618	0.573	0.713	0.609	0.068
F	0.29	0.256	0.25	0.278	0.269	0.016
Na M4	0.076	0.07	0.089	0.062	0.074	0.010
Na TOT	0.503	0.487	0.581	0.422	0.498	0.057
Na A	0.427	0.417	0.492	0.36	0.424	0.047
Fe3+/FeT	0.194	0.227	0.208	0.264	0.223	0.026
Mg/Mg+Fe	0.476	0.492	0.482	0.517	0.492	0.015
a (TR)	0.000235	0.000356	0.000220	0.000811	0.000406	0.000240
K/K+Na	0.434	0.412	0.358	0.388	0.398	0.028
M	15.816	15.808	15.853	15.707	15.796	0.054
FeMg	2.225	2.145	2.221	2.028	2.155	0.080
FeAl	0.628	0.708	0.657	0.793	0.697	0.063
MgCa	0.115	0.14	0.149	0.152	0.139	0.015
PL	0.076	0.07	0.089	0.062	0.074	0.010
ED	0.816	0.808	0.853	0.707	0.796	0.054
TK	0.75	0.736	0.704	0.736	0.731	0.017
distance	17.75	17.75	17.75	17.75		

Amphibolite - Cores					Average	Std.Dev.
Sample #	575	582	583	585	Cores	(4)
SiO2	43.9	43.35	43.45	43.3	43.50	0.24
Al2O3	8.82	9.2	9.19	9.22	9.11	0.17
TiO2	0.42	0.48	0.32	0.4	0.41	0.06
MgO	10.02	10	9.91	9.92	9.96	0.05
FeO	20.52	20.66	20.69	20.52	20.60	0.08
MnO	0.58	0.65	0.6	0.59	0.61	0.03
CaO	11.38	11.37	11.26	11.39	11.35	0.05
Na2O	1.76	1.52	1.69	1.76	1.68	0.10
K2O	1.29	1.36	1.35	1.41	1.35	0.04
F	0.6	0.44	0.44	0.52	0.50	0.07
H2O	1.69	1.76	1.75	1.72	1.73	0.03
total	100.98	100.79	100.65	100.75	100.79	0.12
-(F)	100.73	100.60	100.46	100.53	100.58	0.10
Si	6.63	6.575	6.597	6.569	6.593	0.024
Al IV	1.37	1.425	1.403	1.431	1.407	0.024
Al VI	0.199	0.219	0.241	0.217	0.219	0.015
Ti	0.048	0.055	0.037	0.046	0.047	0.006
Fe 2+	1.972	1.83	1.907	1.945	1.914	0.053
Mn	0.074	0.083	0.077	0.076	0.078	0.003
Mg	2.255	2.261	2.243	2.243	2.251	0.008
Ca	1.841	1.848	1.832	1.851	1.843	0.007
Na	0.515	0.447	0.497	0.521	0.495	0.029
K	0.248	0.263	0.261	0.273	0.261	0.009
Fe 3+	0.602	0.759	0.692	0.636	0.672	0.060
F	0.287	0.211	0.211	0.249	0.240	0.032
Na M4	0.091	0.093	0.1	0.088	0.093	0.004
Na TOT	0.51	0.44	0.491	0.515	0.489	0.030
Na A	0.419	0.347	0.391	0.427	0.396	0.031
Fe3+/FeT	0.234	0.293	0.266	0.246	0.260	0.022
Mg/Mg+Fe	0.533	0.553	0.540	0.536	0.541	0.007
a (TR)	0.000715	0.000823	0.000672	0.000561	0.000693	0.000094
K/K+Na	0.372	0.431	0.400	0.390	0.398	0.022
M	15.754	15.765	15.787	15.808	15.779	0.021
FeMg	1.998	1.858	1.947	1.975	1.945	0.053
FeAl	0.698	0.869	0.766	0.728	0.765	0.065
MgCa	0.15	0.207	0.197	0.163	0.179	0.023
PL	0.091	0.093	0.1	0.088	0.093	0.004
ED	0.754	0.765	0.787	0.808	0.779	0.021
TK	0.707	0.753	0.716	0.711	0.722	0.018
distance	19.25	19.25	19.25	19.25		

Amphibolite - Cores			Lowermost Amph.			Average	Std.Dev.
Sample #	590	592	659	660	661	Cores	(5)
SiO2	42.21	42.87	42.46	42.26	42.17	42.39	0.26
Al2O3	9.39	9.27	9.17	9.37	9.64	9.37	0.16
TiO2	0.46	0.48	0.53	0.5	0.49	0.49	0.02
MgO	8.26	8.46	8.24	8.18	8.17	8.26	0.10
FeO	22.06	21.96	21.83	22.15	21.87	21.97	0.12
MnO	1.44	1.51	1.46	1.33	1.45	1.44	0.06
CaO	11.43	11.53	11.22	11.5	11.58	11.45	0.13
Na2O	1.46	1.43	1.92	1.61	1.77	1.64	0.19
K2O	1.5	1.42	1.36	1.41	1.39	1.42	0.05
F	0.58	0.41	0.49	0.53	0.42	0.49	0.06
H2O	1.66	1.76	1.7	1.68	1.74	1.71	0.04
total	100.45	101.1	100.38	100.52	100.69	100.63	0.26
-(F)	100.21	100.93	100.17	100.30	100.51	100.42	0.28
Si	6.504	6.554	6.542	6.509	6.487	6.519	0.025
Al IV	1.496	1.446	1.458	1.491	1.513	1.481	0.025
Al VI	0.209	0.224	0.207	0.21	0.234	0.217	0.010
Ti	0.053	0.055	0.061	0.058	0.057	0.057	0.003
Fe 2+	2.076	2.049	2.228	2.154	2.168	2.135	0.065
Mn	0.188	0.196	0.191	0.174	0.189	0.188	0.007
Mg	1.897	1.93	1.892	1.878	1.873	1.894	0.020
Ca	1.887	1.889	1.852	1.898	1.908	1.887	0.019
Na	0.439	0.424	0.574	0.481	0.528	0.489	0.056
K	0.295	0.279	0.267	0.277	0.273	0.278	0.009
Fe 3+	0.739	0.727	0.566	0.674	0.62	0.665	0.065
F	0.283	0.198	0.239	0.258	0.204	0.236	0.032
Na M4	0.07	0.071	0.086	0.064	0.058	0.070	0.009
Na TOT	0.433	0.42	0.57	0.477	0.522	0.484	0.056
Na A	0.363	0.349	0.484	0.413	0.464	0.415	0.053
Fe3+/FeT	0.263	0.262	0.203	0.238	0.222	0.238	0.023
Mg/Mg+Fe	0.477	0.485	0.459	0.466	0.463	0.470	0.010
a (TR)	0.000368	0.000473	0.000270	0.000323	0.000264	0.000339	0.000077
K/K+Na	0.448	0.444	0.356	0.401	0.370	0.404	0.038
M	15.783	15.773	15.838	15.804	15.85	15.810	0.030
FeMg	2.211	2.19	2.358	2.27	2.3	2.266	0.061
FeAl	0.845	0.837	0.688	0.79	0.734	0.779	0.060
MgCa	0.162	0.181	0.145	0.148	0.141	0.155	0.015
PL	0.07	0.071	0.086	0.064	0.058	0.070	0.009
ED	0.783	0.773	0.838	0.804	0.85	0.810	0.030
TK	0.783	0.744	0.706	0.751	0.721	0.741	0.026
distance	22.25	22.25	22.25	22.25	22.25		

Amph. Rims - GG-AM. Contact Average Std.Dev. Amphibolite - Rims										
Sample #	183	185	Rims	(2)	196	201	202	207	209	219
SiO2	42.56	42.58	42.57	0.01	42.83	43.53	43.4	43.61	44.57	46.17
Al2O3	9.39	9.67	9.53	0.14	9.38	8.64	8.86	8.92	8.11	7.53
TiO2	0.4	0.54	0.47	0.07	0.45	0.43	0.49	0.47	0.36	0.32
MgO	9.01	8.96	8.99	0.02	9.53	10.09	9.9	10.01	10.61	11.21
FeO	21.28	21.54	21.41	0.13	20.58	19.61	19.89	19.81	19.47	18.94
MnO	0.74	0.84	0.79	0.05	0.64	0.61	0.65	0.62	0.67	0.61
CaO	11.22	11.39	11.31	0.08	11.21	11.31	11.34	11.24	11.55	11.49
Na2O	1.93	1.76	1.85	0.08	1.88	1.78	1.68	1.92	1.68	1.69
K2O	1.48	1.47	1.48	0.00	1.41	1.26	1.27	1.33	1.16	1.01
F	0.6	0.65	0.63	0.02	0.6	0.55	0.55	0.7	0.66	0.63
H2O	1.65	1.64	1.65	0.00	1.66	1.68	1.69	1.63	1.66	1.7
total	100.26	101.04	100.65	0.39	100.17	99.49	99.72	100.26	100.5	101.3
-(F)	100.01	100.77	100.39	0.38	99.92	99.26	99.49	99.97	100.22	101.03
Si	6.524	6.483	6.504	0.021	6.541	6.654	6.627	6.615	6.721	6.858
Al IV	1.476	1.517	1.497	0.021	1.459	1.346	1.373	1.385	1.279	1.142
Al VI	0.221	0.218	0.220	0.002	0.229	0.21	0.221	0.211	0.163	0.176
Ti	0.046	0.062	0.054	0.008	0.052	0.049	0.056	0.054	0.042	0.036
Fe 2+	2.146	2.076	2.111	0.035	2.035	1.976	1.965	2.027	1.899	1.891
Mn	0.096	0.108	0.102	0.006	0.083	0.079	0.084	0.08	0.086	0.077
Mg	2.061	2.033	2.047	0.014	2.169	2.299	2.253	2.263	2.385	2.482
Ca	1.843	1.858	1.851	0.008	1.834	1.852	1.855	1.827	1.868	1.829
Na	0.574	0.52	0.547	0.027	0.557	0.528	0.497	0.565	0.491	0.487
K	0.289	0.285	0.287	0.002	0.275	0.246	0.247	0.257	0.223	0.191
Fe 3+	0.568	0.648	0.608	0.040	0.578	0.517	0.559	0.478	0.545	0.455
F	0.291	0.313	0.302	0.011	0.29	0.266	0.266	0.336	0.315	0.296
Na M4	0.089	0.083	0.086	0.003	0.094	0.085	0.084	0.095	0.076	0.095
Na TOT	0.569	0.516	0.543	0.027	0.554	0.526	0.494	0.563	0.49	0.485
Na A	0.48	0.433	0.457	0.023	0.46	0.441	0.41	0.468	0.414	0.39
Fe3+/FeT	0.209	0.238	0.224	0.014	0.221	0.207	0.221	0.191	0.223	0.194
Mg/Mg+Fe	0.490	0.495	0.492	0.002	0.516	0.538	0.534	0.528	0.557	0.568
a(TR)	0.000227	0.000283	0.000255	0.000028	0.000359	0.000778	0.000769	0.000521	0.001323	0.002128
K/K+Na	0.376	0.397	0.386	0.011	0.374	0.358	0.376	0.354	0.350	0.329
M	15.844	15.808	15.826	0.018	15.812	15.756	15.737	15.762	15.702	15.624
FeMg	2.196	2.122	2.159	0.037	2.066	2.006	1.993	2.053	1.943	1.932
FeAl	0.66	0.772	0.716	0.056	0.682	0.615	0.671	0.586	0.629	0.527
MgCa	0.138	0.145	0.141	0.004	0.146	0.13	0.138	0.113	0.12	0.117
PL	0.089	0.083	0.086	0.003	0.094	0.085	0.084	0.095	0.076	0.095
ED	0.844	0.808	0.826	0.018	0.812	0.756	0.737	0.762	0.702	0.624
TK	0.721	0.792	0.757	0.036	0.741	0.675	0.72	0.718	0.653	0.613
distance	11.75	11.75	11.750		12.5	12.5	12.5	12.5	12.5	12.5

Amphibolite - Rims				Average	Std.Dev.	Actinolitic Rims			Average	Std.Dev.
Sample #	220	227	228	Rims	(9)	208	210	221	Actinolit	(3)
SiO2	44.46	45.16	44.58	44.26	0.97	51.08	50.19	48.02	49.76	1.29
Al2O3	8.46	8.15	8.32	8.49	0.51	3.56	3.81	6.29	4.55	1.23
TiO2	0.34	0.34	0.48	0.41	0.06	0.09	0.1	0.19	0.13	0.04
MgO	10.27	10.75	10.56	10.33	0.48	12.98	13.03	12.05	12.69	0.45
FeO	19.77	19.38	19.54	19.67	0.42	16.38	16.85	17.63	16.95	0.52
MnO	0.59	0.63	0.64	0.63	0.02	0.58	0.62	0.63	0.61	0.02
CaO	11.19	11.51	11.49	11.37	0.13	12.05	12.2	11.79	12.01	0.17
Na2O	1.41	1.72	1.82	1.73	0.14	0.76	0.81	1.33	0.97	0.26
K2O	1.09	1.09	1.16	1.20	0.12	0.42	0.45	0.76	0.54	0.15
F	0.38	0.57	0.47	0.57	0.09	0.41	0.39	0.54	0.45	0.07
H2O	1.78	1.72	1.75	1.70	0.04	1.83	1.84	1.76	1.81	0.04
total	99.74	101.02	100.81	100.33	0.59	100.25	100.35	100.99	100.53	0.33
-(F)	99.58	100.78	100.61	100.10	0.58	100.08	100.18	100.76	100.34	0.30
Si	6.753	6.761	6.711	6.693	0.089	7.495	7.395	7.08	7.323	0.177
Al IV	1.247	1.239	1.289	1.307	0.089	0.505	0.605	0.92	0.677	0.177
Al VI	0.268	0.199	0.187	0.207	0.029	0.111	0.057	0.173	0.114	0.047
Ti	0.039	0.038	0.054	0.047	0.007	0.01	0.011	0.021	0.014	0.005
Fe 2+	1.848	1.905	1.942	1.943	0.060	1.828	1.719	1.803	1.783	0.047
Mn	0.077	0.08	0.082	0.081	0.003	0.072	0.077	0.079	0.076	0.003
Mg	2.325	2.399	2.369	2.327	0.088	2.839	2.862	2.648	2.783	0.096
Ca	1.821	1.846	1.853	1.843	0.015	1.894	1.926	1.864	1.895	0.025
Na	0.415	0.499	0.531	0.508	0.042	0.216	0.231	0.383	0.277	0.075
K	0.211	0.208	0.223	0.231	0.025	0.079	0.085	0.143	0.102	0.029
Fe 3+	0.639	0.509	0.503	0.531	0.053	0.183	0.351	0.366	0.300	0.083
F	0.183	0.27	0.224	0.272	0.044	0.19	0.182	0.252	0.208	0.031
Na M4	0.105	0.087	0.085	0.090	0.008	0.056	0.043	0.075	0.058	0.013
Na TOT	0.41	0.497	0.529	0.505	0.043	0.216	0.231	0.38	0.276	0.074
Na A	0.305	0.41	0.444	0.416	0.046	0.16	0.188	0.305	0.218	0.063
Fe3+/FeT	0.257	0.211	0.206	0.215	0.019	0.091	0.170	0.169	0.143	0.037
Mg/Mg+Fe	0.557	0.557	0.550	0.545	0.016	0.608	0.625	0.595	0.609	0.012
a(TR)	0.001532	0.001450	0.001072	0.001104	0.000529	0.023475	0.021498	0.006068	0.017014	0.007782
K/K+Na	0.409	0.337	0.334	0.358	0.024	0.331	0.311	0.319	0.320	0.008
M	15.643	15.683	15.744	15.718	0.057	15.232	15.319	15.48	15.344	0.103
FeMg	1.886	1.947	1.97	1.977	0.055	1.89	1.785	1.861	1.845	0.044
FeAl	0.717	0.585	0.611	0.625	0.055	0.203	0.373	0.408	0.328	0.090
MgCa	0.196	0.13	0.137	0.136	0.023	0.043	0.077	0.09	0.070	0.020
PL	0.105	0.087	0.085	0.090	0.008	0.056	0.043	0.075	0.058	0.013
ED	0.643	0.683	0.744	0.718	0.057	0.232	0.319	0.48	0.344	0.103
TK	0.709	0.643	0.63	0.678	0.043	0.329	0.329	0.515	0.391	0.088
distance	12.5	12.5	12.5			12.5	12.5	12.5		

Amphibolite - Rims						Average	Std.Dev.	Amphibolite - Rims		
Sample #	231	232	233	236	241	Rims	(5)	275	276	278
SiO2	43.72	43.7	44.01	43.4	43.75	43.72	0.19	44.77	43.33	44.51
Al2O3	8.74	8.96	7.88	9.39	8.99	8.79	0.50	8.68	9.27	8.61
TiO2	0.44	0.4	0.39	0.47	0.48	0.44	0.04	0.27	0.51	0.3
MgO	10.04	9.84	10.27	9.95	9.99	10.02	0.14	9.82	9.24	9.67
FeO	20.18	20.6	19.33	20.23	20.44	20.16	0.44	20.78	21.42	20.63
MnO	0.57	0.53	0.51	0.53	0.55	0.54	0.02	0.51	0.52	0.54
CaO	11.61	11.39	11.21	11.37	11.39	11.39	0.13	11.76	11.53	11.72
Na2O	1.61	1.86	1.59	1.9	1.82	1.76	0.13	1.46	1.7	1.49
K2O	1.27	1.32	1.07	1.38	1.32	1.27	0.11	1.11	1.29	1.12
F	0.54	0.54	0.51	0.64	0.61	0.57	0.05	0.42	0.58	0.44
H2O	1.7	1.7	1.69	1.66	1.68	1.69	0.01	1.78	1.69	1.76
total	100.42	100.84	98.46	100.92	101.02	100.33	0.96	101.36	101.08	100.79
-(F)	100.19	100.61	98.25	100.65	100.76	100.09	0.94	101.18	100.84	100.60
Si	6.633	6.616	6.77	6.557	6.602	6.636	0.072	6.724	6.568	6.723
Al IV	1.367	1.384	1.23	1.443	1.398	1.364	0.072	1.276	1.432	1.277
Al VI	0.196	0.214	0.198	0.228	0.201	0.207	0.012	0.26	0.224	0.256
Ti	0.05	0.046	0.045	0.053	0.054	0.050	0.004	0.03	0.058	0.034
Fe 2+	1.947	2.042	1.947	1.996	1.996	1.986	0.036	2.014	2.102	2.062
Mn	0.073	0.068	0.066	0.068	0.07	0.069	0.002	0.065	0.067	0.069
Mg	2.273	2.22	2.355	2.24	2.247	2.267	0.047	2.198	2.088	2.177
Ca	1.887	1.847	1.847	1.84	1.842	1.853	0.017	1.892	1.873	1.897
Na	0.474	0.546	0.474	0.557	0.533	0.517	0.036	0.425	0.5	0.436
K	0.246	0.255	0.21	0.266	0.254	0.246	0.019	0.213	0.249	0.216
Fe 3+	0.596	0.55	0.525	0.547	0.569	0.557	0.024	0.576	0.596	0.527
F	0.259	0.263	0.248	0.306	0.291	0.273	0.022	0.199	0.278	0.21
Na M4	0.067	0.088	0.087	0.091	0.09	0.085	0.009	0.066	0.075	0.062
Na TOT	0.469	0.543	0.47	0.554	0.53	0.513	0.036	0.423	0.496	0.434
Na A	0.402	0.455	0.383	0.463	0.44	0.429	0.031	0.357	0.421	0.372
Fe3+/FeT	0.234	0.212	0.212	0.215	0.222	0.219	0.008	0.222	0.221	0.204
Mg/Mg+Fe	0.539	0.521	0.547	0.529	0.530	0.533	0.009	0.522	0.498	0.514
a(TR)	0.000924	0.000543	0.001454	0.000459	0.000601	0.000796	0.000364	0.001150	0.000482	0.001058
K/K+Na	0.380	0.359	0.354	0.365	0.366	0.365	0.009	0.374	0.372	0.367
M	15.742	15.788	15.667	15.795	15.766	15.752	0.046	15.673	15.757	15.674
FeMg	1.97	2.064	1.968	2.011	2.012	2.005	0.035	2.049	2.111	2.097
FeAl	0.696	0.642	0.615	0.653	0.677	0.657	0.028	0.636	0.712	0.595
MgCa	0.135	0.14	0.136	0.132	0.137	0.136	0.003	0.143	0.135	0.125
PL	0.067	0.088	0.087	0.091	0.09	0.085	0.009	0.066	0.075	0.062
ED	0.742	0.788	0.667	0.795	0.766	0.752	0.046	0.673	0.757	0.674
TK	0.692	0.684	0.65	0.739	0.722	0.697	0.031	0.669	0.75	0.665
distance	13.75	13.75	13.75	13.75	13.75			14.75	14.75	14.75

Amphibolite - Rims				Average	Std.Dev.	Amphibolite - Rims			Average	Std.Dev.
Sample #	286	287	293	Rims	(6)	300	301	340	Rims	(3)
SiO2	44.84	44.33	44.07	44.31	0.51	43.81	44.32	43.77	43.97	0.25
Al2O3	8.26	8.42	8.76	8.67	0.32	8.79	8.54	8.75	8.69	0.11
TiO2	0.36	0.46	0.49	0.40	0.09	0.41	0.43	0.39	0.41	0.02
MgO	9.86	9.61	9.5	9.62	0.21	9.69	9.69	9.25	9.54	0.21
FeO	20.22	20.49	20.68	20.70	0.37	20.79	20.81	21.31	20.97	0.24
MnO	0.55	0.56	0.54	0.54	0.02	0.59	0.57	0.6	0.59	0.01
CaO	11.54	11.24	11.2	11.50	0.21	11.41	11.22	11.44	11.36	0.10
Na2O	1.61	1.7	1.78	1.62	0.12	1.78	1.87	1.66	1.77	0.09
K2O	1.13	1.14	1.25	1.17	0.07	1.26	1.24	1.24	1.25	0.01
F	0.4	0.39	0.45	0.45	0.06	0.39	0.56	0.49	0.48	0.07
H2O	1.78	1.77	1.74	1.75	0.03	1.78	1.7	1.73	1.74	0.03
total	100.55	100.11	100.46	100.73	0.41	100.7	100.95	100.63	100.76	0.14
-(F)	100.38	99.95	100.27	100.54	0.40	100.54	100.71	100.42	100.56	0.12
Si	6.775	6.74	6.688	6.703	0.066	6.651	6.694	6.659	6.668	0.019
Al IV	1.225	1.26	1.312	1.297	0.066	1.349	1.306	1.341	1.332	0.019
Al VI	0.246	0.249	0.255	0.248	0.012	0.223	0.215	0.228	0.222	0.005
Ti	0.041	0.053	0.056	0.045	0.011	0.047	0.049	0.045	0.047	0.002
Fe 2+	2.099	2.127	2.15	2.092	0.044	2.061	2.135	2.133	2.110	0.034
Mn	0.07	0.072	0.069	0.069	0.002	0.076	0.073	0.077	0.075	0.002
Mg	2.221	2.178	2.149	2.169	0.042	2.193	2.181	2.098	2.157	0.042
Ca	1.868	1.831	1.821	1.864	0.029	1.856	1.816	1.865	1.846	0.021
Na	0.472	0.501	0.524	0.476	0.036	0.524	0.548	0.49	0.521	0.024
K	0.218	0.221	0.242	0.227	0.014	0.244	0.239	0.241	0.241	0.002
Fe 3+	0.443	0.464	0.462	0.511	0.059	0.558	0.482	0.559	0.533	0.036
F	0.191	0.188	0.216	0.214	0.030	0.187	0.267	0.236	0.230	0.033
Na M4	0.076	0.096	0.101	0.079	0.014	0.085	0.103	0.08	0.089	0.010
Na TOT	0.468	0.498	0.522	0.474	0.036	0.519	0.545	0.486	0.517	0.024
Na A	0.392	0.402	0.421	0.394	0.024	0.434	0.442	0.406	0.427	0.015
Fe3+/FeT	0.174	0.179	0.177	0.196	0.020	0.213	0.184	0.208	0.202	0.013
Mg/Mg+Fe	0.514	0.506	0.500	0.509	0.008	0.516	0.505	0.496	0.506	0.008
a(TR)	0.001097	0.000813	0.000585	0.000864	0.000258	0.000639	0.000578	0.000602	0.000606	0.000024
K/K+Na	0.357	0.355	0.365	0.365	0.007	0.360	0.351	0.372	0.361	0.009
M	15.678	15.696	15.728	15.701	0.031	15.782	15.738	15.736	15.752	0.021
FeMg	2.128	2.146	2.163	2.116	0.037	2.09	2.159	2.165	2.138	0.034
FeAl	0.525	0.57	0.574	0.602	0.059	0.652	0.58	0.649	0.627	0.033
MgCa	0.12	0.143	0.141	0.134	0.009	0.158	0.135	0.14	0.144	0.010
PL	0.076	0.096	0.101	0.079	0.014	0.085	0.103	0.08	0.089	0.010
ED	0.678	0.696	0.728	0.701	0.031	0.782	0.738	0.736	0.752	0.021
TK	0.623	0.66	0.685	0.675	0.038	0.652	0.671	0.685	0.669	0.014
distance	14.75	14.75	14.75			16.75	16.75	16.75		

CPX-AB Myl. - Rims				Average	Std.Dev.	19.25cm
Sample #	636	638	521	Rims	(3)	583
SiO2	44.59	45.11	44.02	44.57	0.45	43.45
Al2O3	8.22	8.26	8.26	8.25	0.02	9.19
TiO2	0.21	0.34	0.35	0.30	0.06	0.32
MgO	9.65	9.64	9.87	9.72	0.11	9.91
FeO	21.16	20.8	21	20.99	0.15	20.69
MnO	0.65	0.58	0.59	0.61	0.03	0.6
CaO	11.74	11.57	11.66	11.66	0.07	11.26
Na2O	1.59	1.48	1.5	1.52	0.05	1.69
K2O	1.08	1.1	1.12	1.10	0.02	1.35
F	0.55	0.52	0.43	0.50	0.05	0.44
H2O	1.71	1.74	1.76	1.74	0.02	1.75
total	101.15	101.14	100.56	100.95	0.28	100.65
-(F)	100.92	100.92	100.38	100.74	0.25	100.46
Si	6.731	6.783	6.691	6.735	0.038	6.597
Al IV	1.269	1.217	1.309	1.265	0.038	1.403
Al VI	0.194	0.247	0.171	0.204	0.032	0.241
Ti	0.024	0.038	0.04	0.034	0.007	0.037
Fe 2+	2.069	2.114	1.956	2.046	0.066	1.907
Mn	0.083	0.074	0.076	0.078	0.004	0.077
Mg	2.171	2.161	2.236	2.189	0.033	2.243
Ca	1.899	1.864	1.899	1.887	0.016	1.832
Na	0.465	0.431	0.442	0.446	0.014	0.497
K	0.208	0.211	0.217	0.212	0.004	0.261
Fe 3+	0.584	0.488	0.686	0.586	0.081	0.692
F	0.263	0.247	0.207	0.239	0.024	0.211
Na M4	0.061	0.078	0.064	0.068	0.007	0.1
Na TOT	0.463	0.429	0.438	0.443	0.014	0.491
Na A	0.402	0.351	0.374	0.376	0.021	0.391
Fe3+/FeT	0.220	0.188	0.26	0.223	0.030	0.266
Mg/Mg+Fe	0.512	0.505	0.533	0.517	0.012	0.540
a(TR)	0.000994	0.001105	0.001139	0.001079	0.000061	0.000671
K/K+Na	0.341	0.375	0.367	0.361	0.015	0.400
M	15.697	15.628	15.723	15.683	0.040	15.787
FeMg	2.128	2.15	1.992	2.090	0.070	1.947
FeAl	0.632	0.564	0.766	0.654	0.084	0.766
MgCa	0.125	0.122	0.165	0.137	0.020	0.197
PL	0.061	0.078	0.064	0.068	0.007	0.1
ED	0.697	0.628	0.723	0.683	0.040	0.787
TK	0.633	0.667	0.65	0.650	0.014	0.716
distance	17.75	17.75	17.75			19.25

Amph. Rims Lower Contact					Average	Std.Dev.
Sample #	591	593	658	662	Rims	(4)
SiO2	43.07	42.27	43.41	42.77	42.88	0.42
Al2O3	8.93	9.72	8.77	8.85	9.07	0.38
TiO2	0.45	0.33	0.37	0.32	0.37	0.05
MgO	8.68	8.16	8.79	8.68	8.58	0.25
FeO	21.69	22.2	21.74	21.82	21.86	0.20
MnO	1.42	1.44	1.51	1.42	1.45	0.04
CaO	11.34	11.4	11.29	11.53	11.39	0.09
Na2O	1.6	1.47	1.88	1.82	1.69	0.17
K2O	1.26	1.4	1.22	1.26	1.29	0.07
F	0.43	0.42	0.51	0.62	0.50	0.08
H2O	1.74	1.74	1.71	1.65	1.71	0.04
total	100.61	100.55	101.2	100.74	100.78	0.25
-(F)	100.43	100.37	100.99	100.48	100.57	0.24
Si	6.599	6.507	6.612	6.559	6.569	0.041
Al IV	1.401	1.493	1.388	1.441	1.431	0.041
Al VI	0.211	0.271	0.186	0.158	0.207	0.042
Ti	0.052	0.038	0.042	0.037	0.042	0.006
Fe 2+	2.058	2.048	2.107	2.101	2.079	0.026
Mn	0.184	0.188	0.196	0.184	0.188	0.005
Mg	1.982	1.872	1.996	1.984	1.959	0.050
Ca	1.861	1.88	1.842	1.894	1.869	0.020
Na	0.475	0.439	0.555	0.541	0.503	0.048
K	0.246	0.275	0.237	0.246	0.251	0.014
Fe 3+	0.693	0.775	0.64	0.675	0.696	0.050
F	0.208	0.204	0.246	0.301	0.240	0.039
Na M4	0.084	0.077	0.093	0.065	0.080	0.010
Na TOT	0.47	0.435	0.55	0.538	0.498	0.048
Na A	0.386	0.358	0.457	0.473	0.419	0.048
Fe3+/FeT	0.252	0.275	0.233	0.243	0.251	0.015
Mg/Mg+Fe	0.491	0.478	0.486	0.486	0.485	0.005
a(TR)	0.000428	0.000290	0.000333	0.000319	0.000343	0.000052
K/K+Na	0.389	0.434	0.341	0.342	0.377	0.038
M	15.762	15.786	15.801	15.82	15.792	0.021
FeMg	2.19	2.198	2.261	2.248	2.224	0.031
FeAl	0.797	0.851	0.724	0.749	0.780	0.049
MgCa	0.18	0.192	0.167	0.139	0.170	0.020
PL	0.084	0.077	0.093	0.065	0.080	0.010
ED	0.762	0.786	0.801	0.82	0.792	0.021
TK	0.723	0.784	0.68	0.686	0.718	0.041
distance	22.25	22.25	22.25	22.25		

CPX-AB mylonite @ PG-AM. Contact				Average	Std.Dev.
Sample #	487	490	497	mylonite	(3)
SiO2	43.58	43.05	43.04	43.22	0.25
Al2O3	8.38	8.85	8.89	8.71	0.23
TiO2	0.42	0.38	0.42	0.41	0.02
MgO	8.92	8.68	8.74	8.78	0.10
FeO	21.55	21.6	22.01	21.72	0.21
MnO	1.62	1.5	1.59	1.57	0.05
CaO	11.41	11.42	11.41	11.41	0.00
Na2O	1.75	1.72	1.63	1.70	0.05
K2O	1.15	1.23	1.25	1.21	0.04
F	0.38	0.38	0.42	0.39	0.02
H2O	1.77	1.76	1.75	1.76	0.01
total	100.93	100.57	101.15	100.88	0.24
- (F)	100.77	100.41	100.97	100.72	0.23
Si	6.658	6.607	6.577	6.614	0.033
AlIV	1.342	1.393	1.423	1.386	0.033
AlVI	0.166	0.207	0.18	0.184	0.017
Ti	0.048	0.044	0.048	0.047	0.002
Fe2+	2.063	2.08	1.998	2.047	0.035
Mn	0.21	0.195	0.207	0.204	0.006
Mg	2.031	1.985	1.991	2.002	0.020
Ca	1.868	1.878	1.868	1.871	0.005
Na	0.518	0.512	0.483	0.504	0.015
K	0.224	0.241	0.244	0.236	0.009
Fe3+	0.661	0.663	0.781	0.702	0.056
F	0.184	0.184	0.203	0.190	0.009
Na M4	0.081	0.076	0.083	0.080	0.003
Na TOT	0.513	0.506	0.478	0.499	0.015
Na A	0.432	0.43	0.395	0.419	0.017
Fe3+/FeT	0.243	0.242	0.281	0.255	0.018
Mg/Mg+Fe	0.496	0.488	0.499	0.495	0.005
a (TR)	0.000493	0.000393	0.000414	0.000434	0.000043
K/K+Na	0.341	0.359	0.382	0.361	0.017
M	15.789	15.805	15.8	15.798	0.007
FeMg	2.225	2.231	2.157	2.204	0.034
FeAl	0.757	0.751	0.877	0.795	0.058
MgCa	0.179	0.174	0.205	0.186	0.014
PL	0.081	0.076	0.083	0.080	0.003
ED	0.789	0.805	0.8	0.798	0.007
TK	0.634	0.664	0.706	0.668	0.030
distance	23	23	23		

Am. from coarse CPX-QTZ boudins					Average	Std.Dev.
Sample #	499	500	501	502	boudin	(4)
SiO2	44.33	43.61	44.76	44.35	44.26	0.41
Al2O3	8.08	7.99	8.07	8.03	8.04	0.04
TiO2	0.31	0.35	0.29	0.29	0.31	0.02
MgO	9.38	9.31	9.81	9.57	9.52	0.19
FeO	20.96	20.83	20.35	20.46	20.65	0.25
MnO	1.71	1.65	1.67	1.66	1.67	0.02
CaO	11.21	11.07	11.44	11.27	11.25	0.13
Na2O	1.81	1.72	1.57	1.61	1.68	0.09
K2O	1.14	1.11	1.06	1.06	1.09	0.03
F	0.46	0.44	0.38	0.44	0.43	0.03
H2O	1.75	1.73	1.79	1.75	1.76	0.02
total	101.14	99.81	101.19	100.49	100.66	0.56
- (F)	100.95	99.62	101.03	100.30	100.48	0.57
Si	6.725	6.708	6.758	6.749	6.735	0.020
AlIV	1.275	1.292	1.242	1.251	1.265	0.020
AlVI	0.169	0.156	0.193	0.188	0.177	0.015
Ti	0.035	0.04	0.033	0.034	0.036	0.003
Fe2+	2.008	1.959	1.877	1.921	1.941	0.048
Mn	0.22	0.215	0.214	0.214	0.216	0.002
Mg	2.121	2.134	2.208	2.171	2.159	0.034
Ca	1.822	1.824	1.851	1.837	1.834	0.012
Na	0.532	0.513	0.46	0.475	0.495	0.029
K	0.221	0.218	0.204	0.206	0.212	0.007
Fe3+	0.628	0.693	0.665	0.658	0.661	0.023
F	0.221	0.214	0.181	0.212	0.207	0.015
Na M4	0.104	0.104	0.091	0.097	0.099	0.005
Na TOT	0.527	0.508	0.456	0.471	0.491	0.028
Na A	0.423	0.404	0.365	0.374	0.392	0.023
Fe3+/FeT	0.238	0.261	0.262	0.255	0.254	0.009
Mg/Mg+Fe	0.514	0.521	0.541	0.531	0.527	0.010
a (TR)	0.000666	0.000713	0.001069	0.000930	0.000845	0.000163
K/K+Na	0.343	0.350	0.359	0.355	0.352	0.006
M	15.756	15.752	15.705	15.704	15.729	0.025
FeMg	2.193	2.134	2.058	2.101	2.122	0.049
FeAl	0.698	0.773	0.731	0.726	0.732	0.027
MgCa	0.181	0.197	0.19	0.186	0.188	0.006
PL	0.104	0.104	0.091	0.097	0.099	0.005
ED	0.756	0.752	0.705	0.704	0.729	0.025
TK	0.623	0.644	0.628	0.644	0.635	0.009
distance	23.5	23.5	23.5	23.5		

Pink Gneiss							Average	Std.Dev.
Sample #	663	664	665	670	671	673	gneiss	(6)
SiO2	43.18	44.3	44.69	43.21	42.62	43.49	43.71	0.67
Al2O3	8.59	8.19	7.72	8.55	9.21	8.45	8.38	0.41
TiO2	0.4	0.35	0.39	0.36	0.49	0.4	0.37	0.05
MgO	8.98	9.38	9.66	9.12	8.92	9.03	9.19	0.34
FeO	20.82	19.94	20.41	20.63	20.63	20.44	20.82	0.56
MnO	1.57	1.57	1.59	1.53	1.55	1.65	1.60	0.06
CaO	11.35	11.42	11.16	11.42	11.23	11.29	11.32	0.12
Na2O	1.73	1.81	2.08	1.63	1.88	1.73	1.74	0.13
K2O	1.21	1.16	1.01	1.19	1.27	1.17	1.15	0.08
F	0.39	0.34	0.52	0.38	0.43	0.4	0.41	0.04
H2O	1.75	1.8	1.72	1.76	1.73	1.75	1.75	0.02
total	99.97	100.26	100.95	99.78	99.96	99.8	100.46	0.54
- (F)	99.81	100.12	100.73	99.62	99.78	99.63	100.29	0.52
Si	6.642	6.752	6.768	6.651	6.558	6.685	6.676	0.071
AlIV	1.358	1.248	1.232	1.349	1.442	1.315	1.324	0.071
AlVI	0.198	0.223	0.145	0.202	0.228	0.215	0.202	0.028
Ti	0.046	0.04	0.044	0.042	0.057	0.046	0.046	0.005
Fe2+	2.043	2.104	2.088	1.991	2.034	2.057	2.053	0.037
Mn	0.205	0.203	0.204	0.199	0.202	0.215	0.205	0.005
Mg	2.059	2.131	2.18	2.092	2.046	2.069	2.096	0.046
Ca	1.87	1.865	1.811	1.883	1.851	1.859	1.857	0.023
Na	0.516	0.535	0.611	0.486	0.561	0.516	0.538	0.040
K	0.237	0.226	0.195	0.234	0.249	0.229	0.228	0.017
Fe3+	0.611	0.424	0.484	0.638	0.599	0.551	0.551	0.075
F	0.19	0.164	0.249	0.185	0.209	0.194	0.199	0.026
Na M4	0.078	0.078	0.106	0.072	0.088	0.083	0.084	0.011
Na TOT	0.512	0.533	0.608	0.481	0.556	0.51	0.533	0.040
Na A	0.434	0.455	0.502	0.409	0.468	0.427	0.449	0.030
Fe3+/FeT	0.230	0.168	0.188	0.243	0.227	0.211	0.211	0.026
Mg/Mg+Fe	0.502	0.503	0.511	0.512	0.501	0.501	0.505	0.005
a (TR)	0.000494	0.000666	0.000684	0.000597	0.000354	0.000558	0.000559	0.000112
K/K+Na	0.353	0.332	0.280	0.364	0.347	0.349	0.338	0.028
M	15.785	15.751	15.762	15.767	15.827	15.757	15.775	0.026
FeMg	2.202	2.267	2.248	2.148	2.179	2.226	2.212	0.040
FeAl	0.703	0.504	0.572	0.722	0.713	0.643	0.643	0.081
MgCa	0.162	0.125	0.145	0.164	0.166	0.153	0.152	0.014
PL	0.078	0.078	0.106	0.072	0.088	0.083	0.084	0.011
ED	0.785	0.751	0.762	0.767	0.827	0.757	0.775	0.026
TK	0.651	0.575	0.576	0.654	0.703	0.641	0.633	0.045
distance	24.5	24.5	24.5	24.5	24.5	24.5		

Pink Gneiss					Average	Std.Dev.
Sample #	708	709	716	717	gneiss	(4)
SiO2	41.96	43.03	43.92	42.94	42.96	0.69
Al2O3	9.95	8.99	8.35	9.55	9.21	0.60
TiO2	0.39	0.46	0.41	0.28	0.39	0.07
MgO	7.69	8.52	8.86	7.96	8.26	0.46
FeO	22.36	21.34	20.87	21.55	21.53	0.54
MnO	1.55	1.54	1.64	1.51	1.56	0.05
CaO	11.24	11.11	11.17	11.22	11.19	0.05
Na2O	1.99	1.9	1.75	1.95	1.90	0.09
K2O	1.75	1.32	1.26	1.39	1.43	0.19
F	0.51	0.64	0.39	0.47	0.50	0.09
H2O	1.69	1.64	1.76	1.72	1.70	0.04
total	101.08	100.49	100.38	100.54	100.62	0.27
- (F)	100.87	100.22	100.22	100.34	100.41	0.23
Si	6.455	6.591	6.715	6.587	6.587	0.092
AlIV	1.545	1.409	1.285	1.413	1.413	0.092
AlVI	0.258	0.214	0.219	0.314	0.251	0.040
Ti	0.045	0.053	0.047	0.032	0.044	0.008
Fe2+	2.346	2.186	2.152	2.336	2.255	0.087
Mn	0.202	0.2	0.212	0.196	0.203	0.006
Mg	1.763	1.945	2.019	1.82	1.887	0.101
Ca	1.853	1.823	1.831	1.844	1.838	0.012
Na	0.594	0.564	0.519	0.58	0.564	0.028
K	0.343	0.258	0.246	0.272	0.280	0.038
Fe3+	0.515	0.536	0.501	0.418	0.493	0.045
F	0.248	0.31	0.189	0.228	0.244	0.044
Na M4	0.085	0.099	0.097	0.088	0.092	0.006
Na TOT	0.592	0.562	0.516	0.578	0.562	0.029
Na A	0.507	0.463	0.419	0.49	0.470	0.033
Fe3+/FeT	0.180	0.197	0.189	0.152	0.179	0.017
Mg/Mg+Fe	0.429	0.471	0.484	0.438	0.455	0.023
a (TR)	0.000075	0.000277	0.000488	0.000172	0.000253	0.000153
K/K+Na	0.404	0.358	0.370	0.357	0.372	0.019
M	15.919	15.779	15.746	15.812	15.814	0.065
FeMg	2.503	2.333	2.317	2.5	2.413	0.088
FeAl	0.605	0.642	0.595	0.482	0.581	0.060
MgCa	0.129	0.134	0.15	0.116	0.132	0.012
PL	0.085	0.099	0.097	0.088	0.092	0.006
ED	0.919	0.779	0.746	0.812	0.814	0.065
TK	0.711	0.729	0.636	0.689	0.691	0.035
distance	29.25	29.25	29.25	29.25		

Pink Gneiss - beg. of CPX Absent Zone					Average	Std.Dev.
Sample #	718	719	720	721	gneiss	(4)
SiO2	41.57	41.85	41.75	41.81	41.75	0.11
Al2O3	10.28	9.81	10.44	9.71	10.06	0.31
TiO2	0.35	0.44	0.44	0.54	0.44	0.07
MgO	7.37	7.73	7.34	7.26	7.43	0.18
FeO	22.22	22.26	22.65	22.14	22.32	0.20
MnO	1.65	1.64	1.63	1.61	1.63	0.01
CaO	11.31	11.25	11.21	11.26	11.26	0.04
Na2O	1.88	1.81	2.11	1.94	1.94	0.11
K2O	1.55	1.58	1.71	1.58	1.61	0.06
F	0.51	0.74	0.63	0.58	0.62	0.08
H2O	1.68	1.58	1.64	1.64	1.64	0.04
total	100.37	100.69	101.55	100.07	100.67	0.55
- (F)	100.16	100.38	101.28	99.83	100.41	0.52
Si	6.434	6.45	6.398	6.489	6.443	0.033
AlIV	1.566	1.55	1.602	1.511	1.557	0.033
AlVI	0.309	0.232	0.283	0.265	0.272	0.028
Ti	0.041	0.051	0.051	0.063	0.052	0.008
Fe2+	2.312	2.242	2.4	2.463	2.354	0.084
Mn	0.216	0.214	0.212	0.212	0.214	0.002
Mg	1.7	1.776	1.679	1.68	1.709	0.040
Ca	1.876	1.858	1.84	1.872	1.862	0.014
Na	0.564	0.541	0.627	0.584	0.579	0.032
K	0.306	0.311	0.334	0.313	0.316	0.011
Fe3+	0.548	0.612	0.492	0.404	0.514	0.076
F	0.25	0.361	0.305	0.285	0.300	0.040
Na M4	0.073	0.081	0.089	0.071	0.079	0.007
Na TOT	0.561	0.537	0.625	0.582	0.576	0.032
Na A	0.488	0.456	0.536	0.511	0.498	0.029
Fe3+/FeT	0.192	0.214	0.170	0.141	0.179	0.027
Mg/Mg+Fe	0.424	0.442	0.412	0.406	0.421	0.014
a (TR)	0.000086	0.000122	0.000046	0.000075	0.000083	0.000027
K/K+Na	0.385	0.405	0.384	0.380	0.389	0.010
M	15.872	15.837	15.918	15.856	15.871	0.030
FeMg	2.487	2.405	2.561	2.612	2.516	0.078
FeAl	0.63	0.714	0.594	0.53	0.617	0.066
MgCa	0.126	0.127	0.117	0.087	0.114	0.016
PL	0.073	0.081	0.089	0.071	0.079	0.007
ED	0.872	0.837	0.918	0.856	0.871	0.030
TK	0.767	0.794	0.773	0.726	0.765	0.025
distance	30.25	30.25	30.25	30.25	30.250	

Pink Gneiss - L6 Mylonite						Average	Std.Dev.
Sample #	106	107	110	113	116	419L6 my	(5)
SiO2	40.93	39.18	40.37	40.6	39.82	40.18	0.62
Al2O3	9.92	11.03	10.28	9.84	10.48	10.31	0.43
TiO2	0.41	0.46	0.36	0.45	0.43	0.42	0.04
MgO	7.67	7.15	7.63	7.79	7.28	7.50	0.25
FeO	23.06	23.96	22.77	22.73	23.37	23.18	0.45
MnO	1.72	1.7	1.72	1.74	1.74	1.72	0.01
CaO	11	10.8	11.18	10.92	11	10.98	0.12
Na2O	1.66	1.73	1.57	1.61	1.78	1.67	0.08
K2O	1.37	1.83	1.37	1.54	1.63	1.55	0.17
F	0.53	0.55	0.41	0.49	0.49	0.49	0.05
H2O	1.66	1.63	1.7	1.67	1.66	1.66	0.02
total	99.93	100.02	99.36	99.38	99.68	99.67	0.27
- (F)	99.71	99.79	99.19	99.17	99.47	99.47	0.25
Si	6.391	6.173	6.344	6.379	6.273	6.312	0.081
AlIV	1.609	1.827	1.656	1.621	1.727	1.688	0.081
AlVI	0.216	0.221	0.248	0.201	0.218	0.221	0.015
Ti	0.048	0.055	0.043	0.053	0.051	0.050	0.004
Fe2+	2.009	1.997	1.944	1.982	2.064	1.999	0.039
Mn	0.227	0.227	0.229	0.232	0.232	0.229	0.002
Mg	1.785	1.679	1.787	1.824	1.709	1.757	0.054
Ca	1.84	1.823	1.882	1.838	1.856	1.848	0.020
Na	0.503	0.528	0.478	0.49	0.544	0.509	0.024
K	0.273	0.368	0.275	0.309	0.327	0.310	0.035
Fe3+	0.957	1.102	0.997	0.958	0.966	0.996	0.055
F	0.262	0.274	0.204	0.243	0.244	0.245	0.024
Na M4	0.101	0.112	0.081	0.102	0.093	0.098	0.010
Na TOT	0.495	0.519	0.47	0.483	0.535	0.500	0.024
Na A	0.394	0.407	0.39	0.381	0.442	0.403	0.021
Fe3+/FeT	0.323	0.356	0.339	0.326	0.319	0.332	0.013
Mg/Mg+Fe	0.470	0.457	0.479	0.479	0.453	0.468	0.011
a (TR)	0.000159	0.000053	0.000155	0.000161	0.000073	0.000121	0.000047
K/K+Na	0.409	0.475	0.414	0.448	0.425	0.434	0.024
M	15.858	16	15.883	15.887	15.967	15.919	0.055
FeMg	2.188	2.169	2.13	2.161	2.245	2.179	0.038
FeAl	1.053	1.212	1.083	1.064	1.068	1.096	0.059
MgCa	0.242	0.281	0.248	0.25	0.24	0.252	0.015
PL	0.101	0.112	0.081	0.102	0.093	0.098	0.010
ED	0.858	1	0.883	0.887	0.967	0.919	0.055
TK	0.852	0.939	0.854	0.836	0.853	0.867	0.037
distance	32	32	32	32	32		

Pink Gneiss									Average	Std.Dev.
Sample #	727	728	729	730	731	732	733	734	gneiss	(8)
SiO2	40.67	40.18	40.54	40.59	41.68	41.16	40.17	39.79	40.60	0.56
Al2O3	10.8	10.82	10.67	10.88	10.44	10.29	11.17	11.17	10.78	0.29
TiO2	0.41	0.44	0.5	0.32	0.42	0.37	0.34	0.51	0.41	0.06
MgO	7.02	6.99	7.24	7.43	7.4	7.45	7.12	6.86	7.19	0.21
FeO	22.45	23.19	22.69	22.91	22.61	22.83	23.15	23.22	22.88	0.27
MnO	1.91	1.72	1.69	1.57	1.63	1.58	1.61	1.61	1.67	0.10
CaO	11.33	11.06	11.2	11.03	11.33	11.1	11.08	11.03	11.15	0.12
Na2O	1.9	2.04	1.98	1.81	1.73	2.15	1.89	1.88	1.92	0.12
K2O	1.76	2.11	1.85	1.87	1.6	1.55	2.09	1.97	1.85	0.19
F	0.5	0.43	0.5	0.67	0.66	0.69	0.73	0.62	0.60	0.10
H2O	1.68	1.7	1.68	1.6	1.62	1.59	1.57	1.6	1.63	0.05
total	100.43	100.68	100.54	100.68	101.12	100.76	100.92	100.26	100.67	0.25
- (F)	100.22	100.50	100.33	100.40	100.84	100.47	100.61	100.00	100.42	0.24
Si	6.329	6.275	6.309	6.294	6.402	6.368	6.235	6.224	6.305	0.058
AlIV	1.671	1.725	1.691	1.706	1.598	1.632	1.765	1.776	1.696	0.057
AlVI	0.309	0.266	0.266	0.282	0.292	0.244	0.278	0.283	0.278	0.018
Ti	0.048	0.052	0.059	0.037	0.049	0.043	0.04	0.06	0.049	0.008
Fe2+	2.301	2.305	2.293	2.161	2.25	2.295	2.254	2.284	2.268	0.045
Mn	0.252	0.228	0.223	0.206	0.212	0.207	0.212	0.213	0.219	0.014
Mg	1.628	1.627	1.679	1.717	1.694	1.718	1.647	1.599	1.664	0.042
Ca	1.889	1.851	1.867	1.833	1.865	1.84	1.843	1.848	1.855	0.017
Na	0.573	0.618	0.597	0.544	0.515	0.645	0.572	0.57	0.579	0.038
K	0.349	0.42	0.367	0.37	0.313	0.308	0.414	0.393	0.367	0.039
Fe3+	0.599	0.692	0.653	0.781	0.635	0.639	0.728	0.726	0.682	0.057
F	0.246	0.212	0.246	0.329	0.321	0.338	0.358	0.307	0.295	0.049
Na M4	0.068	0.104	0.079	0.099	0.079	0.092	0.092	0.09	0.088	0.011
Na TOT	0.57	0.611	0.592	0.54	0.514	0.64	0.566	0.565	0.575	0.037
Na A	0.502	0.507	0.513	0.441	0.435	0.548	0.474	0.475	0.487	0.036
Fe3+/FeT	0.207	0.231	0.222	0.265	0.220	0.218	0.244	0.241	0.231	0.017
Mg/Mg+Fe	0.414	0.414	0.423	0.443	0.430	0.428	0.422	0.412	0.423	0.010
a (TR)	0.000042	0.000018	0.000037	0.000062	0.000097	0.000054	0.000027	0.000027	0.000046	0.000024
K/K+Na	0.410	0.453	0.417	0.456	0.418	0.360	0.466	0.453	0.429	0.033
M	15.948	16.059	16.004	15.931	15.825	15.939	15.988	15.976	15.959	0.064
FeMg	2.505	2.481	2.457	2.33	2.413	2.459	2.426	2.437	2.439	0.049
FeAl	0.695	0.796	0.771	0.855	0.733	0.725	0.808	0.846	0.779	0.054
MgCa	0.137	0.17	0.173	0.184	0.132	0.146	0.159	0.165	0.158	0.017
PL	0.068	0.104	0.079	0.099	0.079	0.092	0.092	0.09	0.088	0.011
ED	0.948	1.059	1.004	0.931	0.825	0.939	0.988	0.976	0.959	0.064
TK	0.791	0.77	0.766	0.874	0.852	0.785	0.869	0.89	0.825	0.048
distance	34	34	34	34	34	34	34	34		

Pink Gneiss			Average	Std.Dev.	Pink Gneiss					
Sample #	741	742	gneiss	(2)	744	745	749	750	751	752
SiO2	40.93	39.82	40.55	0.57	40.78	40.59	40.28	40.73	40.24	41.29
Al2O3	10.36	11.15	10.78	0.32	10.81	10.64	10.83	10.96	10.83	10.63
TiO2	0.34	0.45	0.41	0.06	0.38	0.43	0.45	0.45	0.42	0.33
MgO	7.38	6.84	7.17	0.23	6.56	6.82	6.68	6.61	6.83	6.82
FeO	22.53	23.4	22.90	0.31	24.02	23.37	23.61	23.6	23.64	23.32
MnO	1.71	1.65	1.67	0.09	1.68	1.6	1.6	1.69	1.68	1.52
CaO	11.15	11.09	11.14	0.11	11.25	11.16	11.07	11.36	11.02	11.32
Na2O	1.91	1.95	1.92	0.11	1.78	1.81	2.07	1.73	1.99	1.81
K2O	1.71	1.96	1.85	0.18	1.71	1.73	1.92	1.79	1.87	1.7
F	0.74	0.7	0.62	0.10	0.75	0.65	0.87	0.74	0.71	0.7
H2O	1.56	1.57	1.62	0.05	1.56	1.6	1.5	1.57	1.57	1.59
total	100.32	100.58	100.63	0.25	101.28	100.4	100.88	101.23	100.8	101.03
- (F)	100.01	100.29	100.37	0.21	100.96	100.13	100.51	100.92	100.50	100.74
Si	6.358	6.215	6.287	0.071	6.31	6.326	6.261	6.298	6.264	6.377
AlIV	1.642	1.785	1.714	0.071	1.69	1.674	1.739	1.702	1.736	1.623
AlVI	0.254	0.266	0.260	0.006	0.281	0.28	0.244	0.296	0.25	0.312
Ti	0.04	0.053	0.047	0.006	0.044	0.05	0.053	0.052	0.049	0.038
Fe2+	2.252	2.297	2.275	0.022	2.362	2.338	2.428	2.364	2.329	2.41
Mn	0.225	0.218	0.222	0.003	0.22	0.211	0.211	0.221	0.222	0.199
Mg	1.709	1.591	1.650	0.059	1.513	1.584	1.55	1.524	1.585	1.57
Ca	1.856	1.855	1.856	0.000	1.865	1.864	1.843	1.882	1.838	1.873
Na	0.575	0.59	0.583	0.007	0.534	0.547	0.624	0.519	0.601	0.542
K	0.339	0.39	0.365	0.025	0.337	0.344	0.381	0.353	0.371	0.335
Fe3+	0.656	0.733	0.695	0.039	0.723	0.684	0.629	0.668	0.724	0.587
F	0.364	0.346	0.355	0.009	0.367	0.32	0.428	0.362	0.35	0.342
Na M4	0.084	0.086	0.085	0.001	0.08	0.081	0.09	0.069	0.094	0.073
Na TOT	0.573	0.586	0.580	0.006	0.532	0.543	0.621	0.515	0.596	0.538
Na A	0.489	0.5	0.495	0.006	0.452	0.462	0.531	0.446	0.502	0.465
Fe3+/FeT	0.226	0.242	0.234	0.008	0.234	0.226	0.206	0.220	0.237	0.196
Mg/Mg+Fe	0.431	0.409	0.420	0.011	0.390	0.404	0.390	0.392	0.405	0.394
a (TR)	0.000063	0.000022	0.000043	0.000021	0.000039	0.000046	0.000016	0.000038	0.000026	0.000050
K/K+Na	0.409	0.438	0.424	0.014	0.427	0.427	0.418	0.442	0.425	0.419
M	15.906	15.993	15.950	0.043	15.879	15.902	15.963	15.879	15.969	15.866
FeMg	2.437	2.462	2.450	0.012	2.538	2.499	2.586	2.533	2.502	2.571
FeAl	0.736	0.839	0.788	0.052	0.811	0.784	0.735	0.772	0.822	0.663
MgCa	0.136	0.158	0.147	0.011	0.143	0.147	0.115	0.125	0.159	0.116
PL	0.084	0.086	0.085	0.001	0.08	0.081	0.09	0.069	0.094	0.073
ED	0.906	0.993	0.949	0.044	0.879	0.902	0.963	0.879	0.969	0.866
TK	0.82	0.878	0.849	0.029	0.891	0.853	0.866	0.892	0.861	0.83
distance	36	36			41	41	41	41	41	41

Rim - next to Qtz.Vein				Average	Std.Dev.	Core - next to Qtz Vein		
Sample #	753	754	755	rim+GN.	(9)	756C	757C	758C
SiO2	41.27	40.73	40.83	40.75	0.35	39.49	39.66	40.05
Al2O3	10.62	10.49	10.45	10.70	0.16	11.69	11.39	11.19
TiO2	0.48	0.36	0.32	0.40	0.05	0.36	0.43	0.5
MgO	6.72	6.82	6.99	6.76	0.12	6.25	6.54	6.34
FeO	23.58	23.7	22.9	23.53	0.29	24.4	24.08	24.12
MnO	1.65	1.65	1.54	1.62	0.06	1.65	1.59	1.6
CaO	11	11.04	11.09	11.15	0.13	10.99	11.06	10.99
Na2O	1.91	2.01	1.98	1.90	0.11	1.95	2.17	1.99
K2O	1.77	1.63	1.68	1.76	0.09	2.09	1.89	2.11
F	0.85	0.86	0.87	0.78	0.08	0.82	0.84	0.99
H2O	1.53	1.5	1.49	1.55	0.04	1.52	1.5	1.44
total	101.38	100.79	100.14	100.88	0.39	101.21	101.15	101.32
- (F)	101.02	100.43	99.77	100.55	0.39	100.86	100.80	100.90
Si	6.356	6.324	6.357	6.319	0.038	6.15	6.166	6.213
AlIV	1.644	1.676	1.643	1.681	0.038	1.85	1.834	1.787
AlVI	0.284	0.243	0.274	0.274	0.022	0.295	0.253	0.258
Ti	0.056	0.042	0.037	0.047	0.006	0.042	0.05	0.058
Fe2+	2.437	2.362	2.385	2.379	0.036	2.373	2.338	2.455
Mn	0.215	0.217	0.203	0.213	0.008	0.218	0.211	0.21
Mg	1.543	1.578	1.622	1.563	0.032	1.451	1.516	1.466
Ca	1.815	1.836	1.849	1.852	0.020	1.834	1.842	1.827
Na	0.57	0.605	0.598	0.571	0.035	0.589	0.657	0.599
K	0.348	0.323	0.334	0.347	0.018	0.415	0.375	0.417
Fe3+	0.589	0.697	0.587	0.654	0.054	0.781	0.77	0.663
F	0.414	0.422	0.428	0.381	0.039	0.404	0.418	0.486
Na M4	0.103	0.094	0.084	0.085	0.010	0.098	0.105	0.105
Na TOT	0.57	0.602	0.595	0.568	0.035	0.585	0.651	0.597
Na A	0.467	0.508	0.511	0.483	0.029	0.487	0.546	0.492
Fe3+/FeT	0.195	0.228	0.198	0.216	0.016	0.248	0.248	0.213
Mg/Mg+Fe	0.388	0.401	0.405	0.396	0.007	0.379	0.393	0.374
a (TR)	0.000039	0.000038	0.000043	0.000038	0.000010	0.000010	0.000011	0.000011
K/K+Na	0.427	0.389	0.395	0.419	0.016	0.460	0.407	0.459
M	15.857	15.903	15.889	15.901	0.038	15.998	16.012	15.953
FeMg	2.596	2.537	2.551	2.546	0.032	2.549	2.499	2.607
FeAl	0.701	0.781	0.661	0.748	0.057	0.865	0.87	0.779
MgCa	0.124	0.139	0.108	0.131	0.016	0.16	0.138	0.11
PL	0.103	0.094	0.084	0.085	0.010	0.098	0.105	0.105
ED	0.857	0.903	0.889	0.901	0.038	0.998	1.012	0.953
TK	0.89	0.867	0.838	0.865	0.021	0.95	0.927	0.939
distance	41	41	41			41	41	41

	Core - next to Qtz Vein				Pink Gneiss			
Sample #	759C	760C	41CM CORE	(5)	770	771	43CM	(2)
SiO2	39.88	39.51	39.72	0.22	41.07	41.15	41.11	0.04
Al2O3	11.21	10.9	11.28	0.26	10.67	10.97	10.82	0.15
TiO2	0.38	0.49	0.43	0.06	0.35	0.36	0.36	0.01
MgO	6.5	6.4	6.41	0.11	7.17	7.07	7.12	0.05
FeO	24.26	24.06	24.18	0.13	23.22	23.38	23.30	0.08
MnO	1.52	1.48	1.57	0.06	1.6	1.63	1.62	0.01
CaO	11.05	10.95	11.01	0.04	11.23	11.13	11.18	0.05
Na2O	2.1	1.89	2.02	0.10	1.79	1.87	1.83	0.04
K2O	2.01	1.98	2.02	0.08	1.71	1.75	1.73	0.02
F	0.95	0.87	0.89	0.07	0.9	0.79	0.85	0.05
H2O	1.46	1.47	1.48	0.03	1.5	1.56	1.53	0.03
total	101.32	100	101.00	0.50	101.21	101.66	101.44	0.22
- (F)	100.92	99.63	100.62	0.50	100.83	101.33	101.08	0.25
Si	6.192	6.217	6.188	0.026	6.326	6.315	6.321	0.005
AlIV	1.808	1.783	1.812	0.026	1.674	1.685	1.680	0.005
AlVI	0.244	0.238	0.258	0.020	0.263	0.299	0.281	0.018
Ti	0.044	0.058	0.050	0.007	0.041	0.042	0.042	0.001
Fe2+	2.383	2.415	2.393	0.040	2.254	2.282	2.268	0.014
Mn	0.2	0.197	0.207	0.008	0.209	0.212	0.211	0.002
Mg	1.507	1.501	1.488	0.025	1.646	1.617	1.632	0.014
Ca	1.84	1.846	1.838	0.007	1.853	1.83	1.842	0.011
Na	0.632	0.577	0.611	0.029	0.535	0.556	0.546	0.010
K	0.398	0.397	0.400	0.015	0.336	0.343	0.340	0.003
Fe3+	0.748	0.731	0.739	0.042	0.719	0.699	0.709	0.010
F	0.466	0.433	0.441	0.030	0.438	0.388	0.413	0.025
Na M4	0.106	0.088	0.100	0.007	0.084	0.097	0.091	0.006
Na TOT	0.629	0.573	0.607	0.029	0.531	0.554	0.543	0.011
Na A	0.523	0.485	0.507	0.024	0.447	0.457	0.452	0.005
Fe3+/FeT	0.239	0.232	0.236	0.013	0.242	0.234	0.238	0.004
Mg/Mg+Fe	0.387	0.383	0.383	0.007	0.422	0.415	0.418	0.004
a (TR)	0.000011	0.000017	0.000013	0.000003	0.000062	0.000050	0.000057	0.000006
K/K+Na	0.432	0.450	0.442	0.020	0.429	0.429	0.429	0.000
M	15.996	15.96	15.984	0.023	15.856	15.88	15.868	0.012
FeMg	2.539	2.554	2.550	0.035	2.422	2.452	2.437	0.015
FeAl	0.836	0.847	0.839	0.033	0.801	0.783	0.792	0.009
MgCa	0.126	0.14	0.135	0.017	0.132	0.151	0.142	0.010
PL	0.106	0.088	0.100	0.007	0.084	0.097	0.091	0.006
ED	0.996	0.96	0.984	0.023	0.856	0.88	0.868	0.012
TK	0.918	0.911	0.929	0.014	0.902	0.902	0.902	0.000
distance	41	41			43	43		

Pink Gneiss - beg. of BI in Zone								Average gneiss	Std.Dev. (7)
Sample #	831	832	833	834	835	836	837		
SiO2	40.75	41.06	41.02	40.57	41.12	41.19	41.04	40.96	0.21
Al2O3	10.92	10.97	11.09	10.96	10.41	10.45	10.73	10.79	0.25
TiO2	0.46	0.39	0.34	0.36	0.41	0.4	0.42	0.40	0.04
MgO	6.83	6.81	6.82	6.77	7.06	6.83	6.91	6.86	0.09
FeO	24.01	24.06	23.89	23.74	23.76	23.61	23.53	23.80	0.18
MnO	1.55	1.4	1.46	1.46	1.42	1.5	1.44	1.46	0.05
CaO	11.04	11.13	11.12	11	10.96	11.03	11.11	11.06	0.06
Na2O	2	1.9	1.92	1.76	1.99	1.98	1.89	1.92	0.08
K2O	1.85	1.87	1.86	1.85	1.68	1.74	1.65	1.79	0.09
F	0.79	0.78	0.92	0.82	0.77	0.91	0.64	0.80	0.09
H2O	1.55	1.56	1.5	1.53	1.56	1.49	1.62	1.54	0.04
total	101.75	101.93	101.94	100.82	101.14	101.13	100.98	101.38	0.44
- (F)	101.42	101.60	101.55	100.47	100.82	100.75	100.71	101.05	0.40
Si	6.279	6.305	6.291	6.294	6.353	6.358	6.348	6.318	0.031
AlIV	1.721	1.695	1.709	1.706	1.647	1.642	1.652	1.682	0.031
AlVI	0.261	0.29	0.295	0.298	0.248	0.259	0.303	0.279	0.021
Ti	0.053	0.045	0.039	0.042	0.048	0.046	0.049	0.046	0.004
Fe2+	2.37	2.396	2.397	2.325	2.36	2.446	2.361	2.379	0.035
Mn	0.202	0.182	0.19	0.192	0.186	0.196	0.189	0.191	0.006
Mg	1.569	1.559	1.559	1.565	1.626	1.574	1.593	1.578	0.022
Ca	1.823	1.831	1.827	1.828	1.816	1.824	1.841	1.827	0.007
Na	0.597	0.566	0.571	0.529	0.596	0.593	0.567	0.574	0.022
K	0.364	0.366	0.364	0.366	0.331	0.343	0.326	0.351	0.016
Fe3+	0.702	0.675	0.67	0.732	0.69	0.593	0.659	0.674	0.040
F	0.385	0.379	0.446	0.402	0.376	0.444	0.313	0.392	0.042
Na M4	0.102	0.097	0.098	0.099	0.105	0.097	0.092	0.099	0.004
Na TOT	0.593	0.562	0.569	0.526	0.591	0.591	0.563	0.571	0.022
Na A	0.491	0.465	0.471	0.427	0.486	0.494	0.471	0.472	0.021
Fe3+/FeT	0.229	0.220	0.218	0.239	0.226	0.195	0.218	0.221	0.013
Mg/Mg+Fe	0.398	0.394	0.394	0.402	0.408	0.392	0.403	0.399	0.005
a (TR)	0.000029	0.000035	0.000033	0.000042	0.000050	0.000038	0.000051	0.000040	0.000008
K/K+Na	0.426	0.440	0.436	0.462	0.405	0.410	0.409	0.427	0.019
M	15.941	15.91	15.912	15.877	15.901	15.874	15.888	15.900	0.022
FeMg	2.519	2.533	2.548	2.475	2.498	2.596	2.501	2.524	0.037
FeAl	0.808	0.765	0.748	0.816	0.786	0.685	0.757	0.766	0.041
MgCa	0.157	0.147	0.15	0.154	0.158	0.114	0.154	0.148	0.014
PL	0.102	0.097	0.098	0.099	0.105	0.097	0.092	0.099	0.004
ED	0.941	0.91	0.912	0.877	0.901	0.874	0.888	0.900	0.022
TK	0.882	0.882	0.895	0.928	0.851	0.865	0.856	0.880	0.024
distance	46	46	46	46	46	46	46		

Pink Gneiss

Sample #	845	846	847	848	849	850	851	852
SiO2	39.58	40.3	40.22	39.36	39.63	40.11	39.78	40.06
Al2O3	11	10.65	10.66	11.39	11.34	11.02	11.65	10.94
TiO2	0.4	0.32	0.43	0.38	0.43	0.32	0.28	0.36
MgO	5.95	6.22	6.05	5.82	5.91	5.93	5.9	6.2
FeO	24.42	24.37	24.87	25.06	24.89	24.73	24.71	23.82
MnO	1.49	1.62	1.68	1.44	1.59	1.5	1.45	1.55
CaO	11.1	11.03	10.88	10.96	10.93	10.94	10.89	10.98
Na2O	1.54	1.94	2.04	1.92	2.01	1.97	2.02	1.72
K2O	1.75	1.77	1.78	1.83	1.87	1.75	1.85	1.74
F	0.67	0.83	0.88	1.11	0.92	0.83	0.78	0.7
H2O	1.56	1.5	1.48	1.37	1.46	1.5	1.53	1.55
total	99.46	100.55	100.97	100.64	100.98	100.6	100.84	99.62
- (F)	99.18	100.20	100.60	100.17	100.59	100.25	100.51	99.33
Si	6.263	6.301	6.278	6.166	6.189	6.272	6.212	6.304
AlIV	1.737	1.699	1.722	1.834	1.811	1.728	1.788	1.696
AlVI	0.314	0.264	0.239	0.268	0.275	0.303	0.355	0.333
Ti	0.048	0.038	0.05	0.045	0.05	0.038	0.033	0.043
Fe2+	2.392	2.484	2.522	2.477	2.493	2.537	2.504	2.421
Mn	0.2	0.215	0.222	0.191	0.21	0.199	0.192	0.207
Mg	1.403	1.45	1.408	1.359	1.376	1.382	1.373	1.454
Ca	1.882	1.848	1.82	1.839	1.829	1.833	1.822	1.851
Na	0.472	0.588	0.617	0.583	0.609	0.597	0.612	0.525
K	0.353	0.353	0.354	0.366	0.372	0.349	0.368	0.349
Fe3+	0.806	0.684	0.705	0.79	0.738	0.679	0.701	0.691
F	0.335	0.41	0.434	0.55	0.454	0.41	0.385	0.348
Na M4	0.073	0.087	0.102	0.091	0.097	0.094	0.102	0.087
Na TOT	0.466	0.583	0.614	0.579	0.605	0.594	0.607	0.52
Na A	0.393	0.496	0.512	0.488	0.508	0.5	0.505	0.433
Fe3+/FeT	0.252	0.216	0.218	0.242	0.228	0.211	0.219	0.222
Mg/Mg+Fe	0.370	0.369	0.358	0.354	0.356	0.353	0.354	0.375
a (TR)	0.000030	0.000022	0.000015	0.000012	0.000010	0.000016	0.000011	0.000032
K/K+Na	0.473	0.416	0.409	0.429	0.423	0.411	0.422	0.446
M	15.87	15.924	15.937	15.918	15.952	15.917	15.96	15.874
FeMg	2.544	2.661	2.694	2.623	2.653	2.698	2.663	2.585
FeAl	0.902	0.76	0.805	0.88	0.838	0.755	0.767	0.777
MgCa	0.163	0.135	0.146	0.13	0.142	0.138	0.158	0.149
PL	0.073	0.087	0.102	0.091	0.097	0.094	0.102	0.087
ED	0.87	0.924	0.937	0.918	0.952	0.917	0.96	0.874
TK	0.94	0.862	0.887	1.007	0.956	0.905	0.93	0.909
distance	50.5	50.5	50.5	50.5	50.5	50.5	50.5	50.5

Pink Gneiss		Average	Std.Dev.	Pink Gneiss						
Sample #	853	gneiss	(9)	868	869	870	871	872	873	875
SiO2	40.06	39.90	0.31	39.81	39.36	40.04	39.85	39.72	39.35	39.48
Al2O3	10.89	11.06	0.32	10.98	11.27	11.14	11.42	10.95	10.89	11.44
TiO2	0.24	0.35	0.06	0.35	0.34	0.33	0.41	0.36	0.34	0.37
MgO	6.11	6.01	0.13	5.62	5.67	5.58	5.86	5.61	5.54	5.49
FeO	24.68	24.62	0.35	24.85	25.34	25.39	24.77	24.88	25.19	25.49
MnO	1.53	1.54	0.08	1.68	1.58	1.55	1.6	1.62	1.58	1.57
CaO	10.98	10.97	0.06	10.99	10.96	11	10.86	10.88	10.84	10.84
Na2O	1.85	1.89	0.16	1.92	1.85	1.73	1.75	1.99	2.08	2.19
K2O	1.81	1.79	0.04	1.81	1.87	1.85	1.79	1.8	1.81	1.86
F	0.96	0.85	0.13	0.73	1.03	0.63	0.66	0.81	0.96	0.81
H2O	1.44	1.49	0.06	1.54	1.4	1.6	1.59	1.5	1.42	1.51
total	100.55	100.47	0.52	100.28	100.67	100.84	100.56	100.12	100	101.05
- (F)	100.15	100.11	0.47	99.97	100.24	100.57	100.28	99.78	99.60	100.71
Si	6.266	6.250	0.046	6.266	6.178	6.273	6.241	6.26	6.222	6.185
AlIV	1.734	1.750	0.046	1.734	1.822	1.727	1.759	1.74	1.778	1.815
AlVI	0.274	0.292	0.035	0.303	0.262	0.329	0.351	0.293	0.251	0.297
Ti	0.028	0.041	0.007	0.041	0.04	0.039	0.048	0.044	0.04	0.044
Fe2+	2.451	2.476	0.044	2.581	2.478	2.541	2.42	2.604	2.609	2.564
Mn	0.203	0.204	0.010	0.224	0.21	0.206	0.212	0.216	0.212	0.208
Mg	1.424	1.403	0.032	1.319	1.326	1.303	1.368	1.318	1.306	1.282
Ca	1.84	1.840	0.018	1.853	1.843	1.846	1.822	1.837	1.836	1.82
Na	0.561	0.574	0.045	0.586	0.563	0.525	0.531	0.608	0.638	0.665
K	0.361	0.358	0.008	0.363	0.374	0.37	0.358	0.362	0.365	0.372
Fe3+	0.758	0.728	0.045	0.669	0.826	0.755	0.791	0.658	0.706	0.751
F	0.475	0.422	0.062	0.363	0.511	0.312	0.327	0.404	0.48	0.401
Na M4	0.092	0.092	0.008	0.085	0.091	0.092	0.105	0.093	0.094	0.12
Na TOT	0.558	0.570	0.046	0.582	0.56	0.52	0.526	0.604	0.634	0.66
Na A	0.466	0.478	0.038	0.497	0.469	0.428	0.421	0.511	0.54	0.54
Fe3+/FeT	0.236	0.227	0.013	0.206	0.250	0.229	0.246	0.202	0.213	0.227
Mg/Mg+Fe	0.367	0.362	0.008	0.338	0.349	0.339	0.361	0.336	0.334	0.333
a (TR)	0.000021	0.000019	0.000008	0.000012	0.000011	0.000016	0.000021	0.000010	0.000007	0.000005
K/K+Na	0.437	0.429	0.019	0.422	0.444	0.464	0.460	0.415	0.403	0.408
M	15.9	15.917	0.030	15.939	15.922	15.914	15.901	15.94	15.963	16.003
FeMg	2.626	2.639	0.047	2.764	2.648	2.708	2.584	2.776	2.781	2.728
FeAl	0.814	0.811	0.050	0.751	0.906	0.833	0.887	0.746	0.786	0.839
MgCa	0.138	0.144	0.010	0.137	0.142	0.173	0.19	0.133	0.124	0.146
PL	0.092	0.092	0.008	0.085	0.091	0.092	0.105	0.093	0.094	0.12
ED	0.9	0.917	0.030	0.939	0.922	0.914	0.901	0.94	0.963	1.003
TK	0.926	0.925	0.039	0.88	0.991	0.905	0.963	0.893	0.909	0.932
distance	50.5			53	53	53	53	53	53	53

Pink Gneiss									Average	Std.Dev.
Sample #	876	877	878	880	882	883	884	886	gneiss	(15)
SiO2	39.59	39.49	39.47	39.38	39.44	39.41	39.39	39.73	39.57	0.21
Al2O3	11.19	11.18	11.14	11.34	11.37	11.29	11.34	11.25	11.21	0.16
TiO2	0.32	0.37	0.31	0.32	0.36	0.37	0.29	0.32	0.34	0.03
MgO	5.47	5.49	5.56	5.54	5.49	5.52	5.51	5.59	5.57	0.10
FeO	25.54	25.49	25.29	25.39	25.42	25.51	25.45	25.37	25.29	0.25
MnO	1.53	1.55	1.48	1.51	1.55	1.67	1.6	1.63	1.58	0.05
CaO	10.92	10.88	10.89	10.91	10.9	10.9	10.93	10.96	10.91	0.05
Na2O	2.08	2.05	2.14	2.1	2.16	2.11	2.03	1.84	2.00	0.14
K2O	1.89	1.88	1.9	1.91	1.91	1.89	1.88	1.76	1.85	0.05
F	0.88	0.86	0.93	0.82	0.84	0.86	0.82	0.75	0.83	0.10
H2O	1.47	1.48	1.44	1.5	1.49	1.48	1.5	1.54	1.50	0.05
total	100.88	100.72	100.55	100.72	100.93	101.01	100.74	100.74	100.65	0.30
- (F)	100.51	100.36	100.16	100.37	100.58	100.65	100.39	100.42	100.31	0.31
Si	6.21	6.205	6.206	6.189	6.186	6.181	6.191	6.231	6.215	0.031
AlIV	1.79	1.795	1.794	1.811	1.814	1.819	1.809	1.769	1.785	0.031
AlVI	0.279	0.275	0.27	0.29	0.287	0.268	0.291	0.311	0.290	0.025
Ti	0.038	0.044	0.037	0.038	0.042	0.044	0.034	0.038	0.041	0.003
Fe2+	2.621	2.61	2.595	2.574	2.582	2.556	2.572	2.499	2.560	0.054
Mn	0.203	0.206	0.197	0.201	0.206	0.222	0.213	0.218	0.210	0.007
Mg	1.281	1.286	1.303	1.298	1.283	1.29	1.291	1.307	1.304	0.022
Ca	1.835	1.832	1.835	1.837	1.831	1.832	1.841	1.842	1.836	0.008
Na	0.633	0.628	0.652	0.64	0.657	0.642	0.619	0.56	0.610	0.044
K	0.378	0.377	0.381	0.383	0.382	0.378	0.377	0.352	0.371	0.009
Fe3+	0.711	0.719	0.715	0.74	0.731	0.766	0.749	0.798	0.739	0.044
F	0.437	0.427	0.467	0.408	0.422	0.427	0.408	0.372	0.411	0.052
Na M4	0.099	0.098	0.108	0.104	0.113	0.106	0.093	0.093	0.100	0.009
Na TOT	0.629	0.623	0.648	0.634	0.652	0.637	0.615	0.553	0.605	0.044
Na A	0.53	0.525	0.54	0.53	0.539	0.531	0.522	0.46	0.506	0.040
Fe3+/FeT	0.213	0.216	0.216	0.223	0.221	0.231	0.226	0.242	0.224	0.014
Mg/Mg+Fe	0.328	0.330	0.334	0.335	0.332	0.335	0.334	0.343	0.338	0.008
a (TR)	0.000006	0.000006	0.000005	0.000005	0.000005	0.000005	0.000006	0.000014	0.000009	0.000005
K/K+Na	0.416	0.418	0.414	0.419	0.415	0.416	0.419	0.433	0.424	0.017
M	15.979	15.977	15.985	16.001	16.001	15.998	15.987	15.925	15.962	0.034
FeMg	2.786	2.772	2.755	2.737	2.746	2.734	2.751	2.679	2.730	0.054
FeAl	0.787	0.807	0.789	0.816	0.815	0.854	0.817	0.874	0.820	0.045
MgCa	0.133	0.14	0.117	0.141	0.131	0.146	0.15	0.171	0.145	0.019
PL	0.099	0.098	0.108	0.104	0.113	0.106	0.093	0.093	0.100	0.009
ED	0.979	0.977	0.985	1.001	1.001	0.998	0.987	0.925	0.962	0.034
TK	0.91	0.916	0.917	0.914	0.926	0.927	0.915	0.937	0.922	0.026
distance	53	53	53	53	53	53	53	53		

Pink Gneiss					Average	Std.Dev.
Sample #	901	902	907	908	gneiss	(4)
SiO2	39.47	39.59	39.52	39.69	39.57	0.08
Al2O3	11.01	11.14	11.2	11.45	11.20	0.16
TiO2	0.3	0.35	0.39	0.36	0.35	0.03
MgO	5.34	5.4	5.42	5.75	5.48	0.16
FeO	24.91	25.09	25.84	25.21	25.26	0.35
MnO	1.68	1.74	1.86	1.7	1.75	0.07
CaO	10.91	10.84	11.02	10.97	10.94	0.07
Na2O	1.94	1.84	1.71	1.88	1.84	0.08
K2O	1.88	1.87	1.85	1.91	1.88	0.02
F	1.06	0.76	0.6	0.74	0.79	0.17
H2O	1.37	1.52	1.61	1.55	1.51	0.09
total	99.87	100.14	101.02	101.21	100.56	0.57
- (F)	99.42	99.82	100.77	100.90	100.23	0.62
Si	6.236	6.249	6.21	6.198	6.223	0.020
AlIV	1.764	1.751	1.79	1.802	1.777	0.020
AlVI	0.285	0.32	0.284	0.305	0.299	0.015
Ti	0.037	0.042	0.046	0.043	0.042	0.003
Fe2+	2.655	2.576	2.46	2.467	2.540	0.081
Mn	0.225	0.233	0.248	0.225	0.233	0.009
Mg	1.257	1.27	1.269	1.338	1.284	0.032
Ca	1.847	1.833	1.855	1.835	1.843	0.009
Na	0.594	0.563	0.521	0.569	0.562	0.026
K	0.379	0.376	0.371	0.38	0.377	0.003
Fe3+	0.63	0.711	0.894	0.795	0.758	0.098
F	0.53	0.379	0.298	0.365	0.393	0.085
Na M4	0.084	0.097	0.09	0.097	0.092	0.005
Na TOT	0.593	0.56	0.515	0.565	0.558	0.028
Na A	0.509	0.463	0.425	0.468	0.466	0.030
Fe3+/FeT	0.192	0.216	0.267	0.244	0.230	0.028
Mg/Mg+Fe	0.321	0.330	0.340	0.352	0.336	0.011
a (TR)	0.000007	0.000010	0.000013	0.000012	0.000011	0.000002
K/K+Na	0.427	0.448	0.466	0.448	0.447	0.014
M	15.909	15.924	15.948	15.957	15.935	0.019
FeMg	2.843	2.767	2.662	2.649	2.730	0.080
FeAl	0.704	0.795	0.986	0.881	0.842	0.104
MgCa	0.089	0.152	0.201	0.173	0.154	0.041
PL	0.084	0.097	0.09	0.097	0.092	0.005
ED	0.909	0.924	0.948	0.957	0.934	0.019
TK	0.939	0.924	0.932	0.942	0.934	0.007
distance	57	57	57	57		

Pink Gneiss									Average	Std.Dev.
Sample #	927	928	929	930	939	940	941	942	gneiss	(8)
SiO2	39.55	39.71	39.43	39.36	39.94	39.72	39.6	40.18	39.60	0.22
Al2O3	11.58	11.84	11.22	11.64	11.5	11.33	11.46	11.19	11.29	0.21
TiO2	0.39	0.32	0.43	0.4	0.29	0.25	0.34	0.41	0.35	0.04
MgO	5.02	4.96	5.07	5.08	5.31	5.39	5.44	5.06	5.44	0.22
FeO	25.82	25.28	25.85	25.03	25.21	25.42	25.47	25.77	25.34	0.29
MnO	1.84	1.81	1.77	1.74	1.75	1.72	1.73	1.65	1.66	0.10
CaO	10.93	10.99	10.92	10.96	11.05	10.9	11.08	11.03	10.94	0.06
Na2O	1.86	1.84	2.13	2.05	1.56	1.64	1.98	1.73	1.93	0.17
K2O	1.94	1.82	1.8	1.89	1.85	1.89	1.87	1.85	1.86	0.04
F	0.71	0.89	0.96	0.83	0.75	0.85	0.81	0.76	0.82	0.11
H2O	1.55	1.47	1.43	1.49	1.54	1.48	1.51	1.54	1.50	0.06
total	101.19	100.93	101.01	100.47	100.75	100.59	101.29	101.17	100.72	0.37
- (F)	100.89	100.56	100.61	100.12	100.43	100.23	100.95	100.85	100.38	0.33
Si	6.201	6.21	6.19	6.193	6.252	6.237	6.189	6.279	6.219	0.031
AlIV	1.799	1.79	1.81	1.807	1.748	1.763	1.811	1.721	1.781	0.031
AlVI	0.34	0.391	0.265	0.352	0.375	0.334	0.299	0.34	0.337	0.037
Ti	0.046	0.038	0.051	0.047	0.034	0.03	0.04	0.048	0.042	0.007
Fe2+	2.628	2.646	2.681	2.698	2.514	2.498	2.571	2.689	2.616	0.074
Mn	0.244	0.24	0.235	0.232	0.232	0.229	0.229	0.218	0.232	0.007
Mg	1.173	1.156	1.186	1.191	1.239	1.262	1.267	1.179	1.207	0.040
Ca	1.836	1.841	1.837	1.848	1.853	1.834	1.855	1.847	1.844	0.007
Na	0.565	0.558	0.651	0.625	0.473	0.499	0.6	0.524	0.562	0.058
K	0.388	0.363	0.36	0.379	0.369	0.379	0.373	0.369	0.373	0.009
Fe3+	0.731	0.646	0.698	0.585	0.76	0.813	0.735	0.66	0.704	0.067
F	0.352	0.44	0.477	0.413	0.371	0.422	0.4	0.376	0.406	0.038
Na M4	0.095	0.089	0.098	0.089	0.086	0.097	0.085	0.088	0.091	0.005
Na TOT	0.56	0.555	0.647	0.624	0.469	0.495	0.596	0.523	0.559	0.058
Na A	0.465	0.466	0.549	0.535	0.383	0.398	0.511	0.435	0.468	0.057
Fe3+/FeT	0.218	0.196	0.207	0.178	0.232	0.246	0.222	0.197	0.212	0.020
Mg/Mg+Fe	0.309	0.304	0.307	0.306	0.330	0.336	0.330	0.305	0.316	0.013
a (TR)	0.000006	0.000006	0.000003	0.000003	0.000015	0.000014	0.000007	0.000009	0.000008	0.000004
K/K+Na	0.455	0.438	0.396	0.415	0.491	0.488	0.422	0.459	0.445	0.032
M	15.951	15.879	15.964	15.957	15.849	15.878	15.969	15.874	15.915	0.046
FeMg	2.826	2.848	2.865	2.883	2.712	2.697	2.76	2.859	2.806	0.068
FeAl	0.823	0.722	0.8	0.679	0.828	0.873	0.815	0.756	0.787	0.059
MgCa	0.162	0.117	0.116	0.105	0.154	0.166	0.141	0.134	0.137	0.021
PL	0.095	0.089	0.098	0.089	0.086	0.097	0.085	0.088	0.091	0.005
ED	0.951	0.879	0.964	0.957	0.849	0.878	0.969	0.874	0.915	0.046
TK	0.943	1	0.944	0.939	0.985	0.982	0.927	0.935	0.957	0.026
distance	59	59	59	59	59	59	59	59		

S-1 Transect	Amph.Gray Gn. UG-1			Average	Std.Dev.	Gray Gneiss UG-2			Average	Std.Dev.
Sample #	2	10	11	UG-1	(3)	34	30	19	UG-2	(3)
SiO2	40.28	40.54	40.53	40.45	0.12	40.29	40.51	40.53	40.44	0.11
Al2O3	11.49	11.61	11.11	11.40	0.21	11.13	11.17	11.27	11.19	0.06
TiO	0.33	0.34	0.33	0.33	0.00	0.36	0.35	0.39	0.37	0.02
MgO	6.10	6.36	6.25	6.24	0.11	6.04	6.41	6.30	6.25	0.16
FeO	23.80	23.33	23.34	23.49	0.22	23.48	23.37	23.78	23.54	0.17
MnO	1.02	1.10	1.05	1.06	0.03	1.19	1.15	1.19	1.18	0.02
CaO	11.09	10.90	11.07	11.02	0.09	11.12	11.02	11.04	11.06	0.04
Na2O	1.51	1.67	1.55	1.58	0.07	1.76	1.68	1.48	1.64	0.12
K2O	1.95	1.89	1.90	1.91	0.03	1.88	1.88	1.95	1.90	0.03
F	0.91	0.84	0.85	0.87	0.03	0.89	0.92	0.91	0.91	0.01
H2O	1.47	1.51	1.49	1.49	0.02	1.45	1.46	1.47	1.46	0.01
total	99.97	100.11	99.49	99.86	0.27	99.68	99.94	100.33	99.98	0.27
-(F)	99.58	99.75	99.13	99.49	0.26	99.28	99.55	99.94	99.59	0.27
Si	6.289	6.304	6.346	6.313	0.024	6.312	6.316	6.305	6.311	0.005
AlIV	1.711	1.696	1.654	1.687	0.024	1.688	1.684	1.695	1.689	0.005
AlVI	0.403	0.431	0.396	0.410	0.015	0.369	0.368	0.371	0.369	0.001
Ti	0.039	0.04	0.039	0.039	0.000	0.042	0.041	0.046	0.043	0.002
Fe2+	2.515	2.473	2.537	2.508	0.027	2.617	2.489	2.444	2.517	0.073
Mn	0.135	0.145	0.139	0.140	0.004	0.158	0.152	0.157	0.156	0.003
Mg	1.42	1.474	1.459	1.451	0.023	1.413	1.49	1.461	1.455	0.032
Ca	1.855	1.816	1.857	1.843	0.019	1.867	1.841	1.84	1.849	0.012
Na	0.46	0.503	0.471	0.478	0.018	0.535	0.511	0.446	0.497	0.038
K	0.388	0.375	0.379	0.381	0.005	0.378	0.374	0.387	0.380	0.005
Fe3+	0.585	0.552	0.514	0.550	0.029	0.46	0.552	0.638	0.550	0.073
F	0.449	0.413	0.421	0.428	0.015	0.441	0.459	0.448	0.449	0.007
Na M4	0.08	0.101	0.078	0.086	0.010	0.071	0.087	0.09	0.083	0.008
Na TOT	0.457	0.502	0.47	0.476	0.019	0.534	0.508	0.445	0.496	0.037
Na A	0.377	0.401	0.392	0.390	0.010	0.463	0.421	0.355	0.413	0.044
Fe3+/FeT	0.189	0.182	0.168	0.180	0.008	0.149	0.182	0.207	0.179	0.024
Mg/Mg+Fe	0.361	0.373	0.365	0.366	0.005	0.351	0.374	0.374	0.366	0.011
a (TR)	0.000040	0.000045	0.000049	0.000045	0.000004	0.000027	0.000045	0.000051	0.000042	0.000010
K/K+Na	0.507	0.483	0.492	0.494	0.010	0.449	0.470	0.522	0.480	0.030
M	15.800	15.809	15.791	15.800	0.007	15.839	15.818	15.790	15.816	0.020
FeMg	2.611	2.578	2.637	2.609	0.024	2.733	2.600	2.555	2.629	0.076
FeAl	0.663	0.632	0.592	0.629	0.029	0.544	0.634	0.730	0.636	0.076
MgCa	0.097	0.115	0.084	0.099	0.013	0.059	0.092	0.117	0.089	0.024
PL	0.080	0.101	0.078	0.086	0.010	0.071	0.087	0.090	0.083	0.008
ED	0.800	0.809	0.791	0.800	0.007	0.839	0.818	0.790	0.816	0.020
TK	0.991	0.988	0.941	0.973	0.023	0.920	0.953	0.995	0.956	0.031
distance	1.2	1.75	1.75			3.3	4.4	5.5		

S-1 Transect Amph.Pink Gn. LG-3,4									Average	Std.Dev.
Sample #	68	71	120	121	117	103	112	110	LG 3&4	(8)
SiO2	40.55	40.23	39.73	39.92	39.83	39.03	40.02	39.57	39.86	0.42
Al2O3	10.58	10.90	11.09	11.19	11.32	11.03	11.76	11.71	11.20	0.37
TiO	0.39	0.30	0.33	0.38	0.41	0.34	0.32	0.38	0.36	0.04
MgO	6.33	6.30	5.87	6.24	5.35	4.64	5.04	4.81	5.57	0.65
FeO	24.00	23.71	24.99	24.70	25.98	26.21	26.47	26.70	25.35	1.08
MnO	1.20	1.25	1.22	1.32	1.29	1.25	1.32	1.23	1.26	0.04
CaO	10.65	11.13	10.85	10.97	10.89	10.61	11.04	10.99	10.89	0.17
Na2O	1.50	1.55	1.55	1.68	1.58	1.44	1.40	1.34	1.51	0.10
K2O	1.83	1.89	2.02	1.92	1.98	1.93	1.99	2.07	1.95	0.07
F	0.94	1.00	0.95	0.97	0.74	0.75	0.72	0.77	0.86	0.11
H2O	1.44	1.41	1.43	1.44	1.54	1.49	1.56	1.53	1.48	0.05
total	99.43	99.70	100.06	100.75	100.94	98.75	101.67	101.12	100.30	0.92
-(F)	99.03	99.27	99.65	100.34	100.62	98.43	101.36	100.79	99.94	0.94
Si	6.367	6.306	6.251	6.227	6.241	6.267	6.231	6.207	6.262	0.048
AlIV	1.633	1.694	1.749	1.773	1.759	1.733	1.769	1.793	1.738	0.048
AlVI	0.325	0.319	0.306	0.284	0.331	0.354	0.388	0.372	0.335	0.032
Ti	0.046	0.035	0.039	0.045	0.048	0.042	0.037	0.045	0.042	0.004
Fe2+	2.437	2.455	2.479	2.386	2.58	2.71	2.575	2.626	2.531	0.102
Mn	0.16	0.166	0.163	0.174	0.171	0.17	0.174	0.163	0.168	0.005
Mg	1.482	1.472	1.376	1.451	1.25	1.111	1.17	1.125	1.305	0.149
Ca	1.792	1.869	1.828	1.833	1.828	1.825	1.842	1.847	1.833	0.021
Na	0.457	0.471	0.473	0.508	0.48	0.448	0.423	0.408	0.459	0.030
K	0.367	0.378	0.405	0.382	0.396	0.397	0.395	0.414	0.392	0.014
Fe3+	0.699	0.644	0.788	0.813	0.794	0.781	0.836	0.843	0.775	0.065
F	0.467	0.496	0.473	0.479	0.367	0.381	0.355	0.382	0.425	0.055
Na M4	0.116	0.073	0.099	0.096	0.101	0.101	0.095	0.092	0.097	0.011
Na TOT	0.455	0.469	0.469	0.504	0.475	0.444	0.419	0.405	0.455	0.030
Na A	0.339	0.396	0.37	0.408	0.374	0.343	0.324	0.313	0.358	0.032
Fe3+/FeT	0.223	0.208	0.241	0.254	0.235	0.224	0.245	0.243	0.234	0.014
Mg/Mg+Fe	0.378	0.375	0.357	0.378	0.326	0.291	0.312	0.300	0.340	0.034
a (TR)	0.000066	0.000048	0.000030	0.000035	0.000018	0.000012	0.000016	0.000012	0.000030	0.000018
K/K+Na	0.520	0.488	0.523	0.484	0.514	0.536	0.549	0.569	0.523	0.027
M	15.765	15.809	15.857	15.876	15.878	15.838	15.840	15.843	15.838	0.035
FeMg	2.551	2.586	2.603	2.515	2.703	2.838	2.712	2.744	2.657	0.103
FeAl	0.791	0.714	0.866	0.903	0.890	0.865	0.910	0.933	0.859	0.068
MgCa	0.149	0.091	0.151	0.153	0.174	0.168	0.180	0.174	0.155	0.027
PL	0.116	0.073	0.099	0.096	0.101	0.101	0.095	0.092	0.097	0.011
ED	0.765	0.809	0.857	0.876	0.878	0.838	0.840	0.843	0.838	0.035
TK	0.984	0.958	0.991	0.993	0.982	0.996	1.024	1.042	0.996	0.024
distance	16.3	16.3	18	18	18	18.6	18.6	18.6		

S-1 Transect Amph.Pink Gn. LG-2								Average	Std.Dev.
Sample #	139	138	135	130	129	125	123	LG-2	(7)
SiO2	39.13	39.52	39.29	39.50	39.63	39.72	40.19	39.57	0.31
Al2O3	11.16	11.17	11.37	10.95	11.15	11.90	11.17	11.27	0.28
TiO	0.40	0.35	0.34	0.42	0.42	0.31	0.41	0.38	0.04
MgO	4.94	4.78	4.55	5.38	5.08	6.22	6.25	5.31	0.63
FeO	26.43	26.59	27.00	26.03	26.59	24.06	24.43	25.88	1.07
MnO	1.36	1.44	1.29	1.31	1.27	1.40	1.32	1.34	0.06
CaO	10.75	10.82	10.84	10.76	10.77	10.88	10.95	10.82	0.07
Na2O	1.49	1.35	1.50	1.36	1.35	1.44	1.60	1.44	0.09
K2O	2.06	1.97	2.04	1.91	1.92	1.95	1.97	1.97	0.05
F	0.83	0.68	0.77	0.81	0.71	0.91	0.90	0.80	0.08
H2O	1.45	1.54	1.51	1.49	1.54	1.47	1.47	1.50	0.03
total	100.10	100.24	100.52	99.95	100.46	100.28	100.69	100.32	0.24
-(F)	99.73	99.95	100.19	99.60	100.15	99.89	100.30	99.97	0.24
Si	6.21	6.26	6.219	6.253	6.253	6.202	6.261	6.237	0.024
AlIV	1.79	1.74	1.781	1.747	1.747	1.798	1.739	1.763	0.024
AlVI	0.297	0.344	0.34	0.296	0.326	0.391	0.312	0.329	0.031
Ti	0.048	0.042	0.04	0.05	0.05	0.036	0.048	0.045	0.005
Fe2+	2.615	2.619	2.724	2.48	2.546	2.267	2.411	2.523	0.141
Mn	0.183	0.193	0.173	0.176	0.17	0.185	0.174	0.179	0.008
Mg	1.169	1.128	1.074	1.269	1.197	1.448	1.451	1.248	0.139
Ca	1.828	1.836	1.838	1.825	1.821	1.82	1.828	1.828	0.006
Na	0.458	0.415	0.46	0.417	0.413	0.436	0.483	0.440	0.025
K	0.417	0.398	0.412	0.386	0.386	0.388	0.391	0.397	0.012
Fe3+	0.861	0.865	0.818	0.928	0.922	0.848	0.752	0.856	0.056
F	0.417	0.346	0.385	0.406	0.354	0.449	0.443	0.400	0.037
Na M4	0.101	0.098	0.095	0.104	0.108	0.104	0.098	0.101	0.004
Na TOT	0.454	0.41	0.457	0.412	0.408	0.433	0.479	0.436	0.026
Na A	0.353	0.312	0.362	0.308	0.3	0.329	0.381	0.335	0.029
Fe3+/FeT	0.248	0.248	0.231	0.272	0.266	0.272	0.238	0.254	0.015
Mg/Mg+Fe	0.309	0.301	0.283	0.338	0.320	0.390	0.376	0.331	0.037
a (TR)	0.000013	0.000015	0.000008	0.000027	0.000021	0.000044	0.000040	0.000024	0.000013
K/K+Na	0.542	0.561	0.532	0.556	0.563	0.541	0.506	0.543	0.018
M	15.876	15.840	15.879	15.827	15.831	15.819	15.850	15.846	0.022
FeMg	2.750	2.770	2.857	2.606	2.666	2.416	2.537	2.657	0.140
FeAl	0.957	0.949	0.898	1.028	1.022	0.920	0.848	0.946	0.060
MgCa	0.173	0.191	0.169	0.199	0.211	0.175	0.148	0.181	0.019
PL	0.101	0.098	0.095	0.104	0.108	0.104	0.098	0.101	0.004
ED	0.876	0.840	0.879	0.827	0.831	0.819	0.850	0.846	0.022
TK	1.015	0.998	0.997	1.024	1.024	1.083	0.987	1.018	0.030
distance	21.6	21.6	22.9	22.9	22.9	23.9	24.5		

S-1 Transect Amph.Pink Gn. LG-1

Sample #	150	149	146	144	LG-1	(4)
SiO2	39.95	40.12	40.24	39.90	40.05	0.14
Al2O3	11.26	11.34	11.13	10.95	11.17	0.15
TiO	0.40	0.36	0.46	0.41	0.41	0.04
MgO	6.10	6.21	6.53	6.17	6.25	0.16
FeO	24.61	24.48	24.25	24.38	24.43	0.13
MnO	1.23	1.20	1.24	1.40	1.27	0.08
CaO	10.75	10.84	10.68	10.69	10.74	0.06
Na2O	1.63	1.62	1.77	1.61	1.66	0.07
K2O	1.94	1.96	1.94	1.86	1.93	0.04
F	0.89	0.84	0.91	0.89	0.88	0.03
H2O	1.47	1.50	1.47	1.46	1.48	0.01
total	100.25	100.51	100.64	99.75	100.29	0.34
-(F)	99.87	100.15	100.25	99.37	99.91	0.34
Si	6.255	6.26	6.262	6.277	6.264	0.008
AlIV	1.745	1.74	1.738	1.723	1.737	0.008
AlVI	0.332	0.344	0.302	0.306	0.321	0.018
Ti	0.047	0.042	0.054	0.049	0.048	0.004
Fe2+	2.433	2.42	2.379	2.385	2.404	0.023
Mn	0.163	0.159	0.163	0.187	0.168	0.011
Mg	1.423	1.444	1.515	1.447	1.457	0.035
Ca	1.803	1.814	1.781	1.802	1.800	0.012
Na	0.495	0.49	0.534	0.491	0.503	0.018
K	0.387	0.39	0.385	0.373	0.384	0.006
Fe3+	0.767	0.752	0.757	0.799	0.769	0.018
F	0.4	0.414	0.448	0.443	0.426	0.020
Na M4	0.112	0.107	0.123	0.114	0.114	0.006
Na TOT	0.492	0.487	0.529	0.487	0.499	0.018
Na A	0.38	0.38	0.406	0.373	0.385	0.013
Fe3+/FeT	0.240	0.237	0.241	0.251	0.242	0.005
Mg/Mg+Fe	0.369	0.374	0.389	0.378	0.377	0.007
a (TR)	0.000036	0.000039	0.000043	0.000044	0.000040	0.000003
K/K+Na	0.505	0.506	0.487	0.500	0.499	0.008
M	15.850	15.855	15.870	15.839	15.854	0.011
FeMg	2.549	2.537	2.488	2.523	2.524	0.023
FeAl	0.861	0.836	0.865	0.897	0.865	0.022
MgCa	0.165	0.161	0.170	0.173	0.167	0.005
PL	0.112	0.107	0.123	0.114	0.114	0.006
ED	0.850	0.855	0.870	0.839	0.854	0.011
TK	1.007	0.992	0.991	0.998	0.997	0.006
distance	25.00	25	26.5	27.40		

Appendix F - CLINOPYROXENE ANALYSES - 419 Transect

CPX - Amphibolite 419 - Matrix

GrainType	M	M	M	Average	Std.Dev.
Sample #	191	222	192	Matrix	(3)
SiO2	52.07	51.79	51.55	51.80	0.21
Al2O3	0.91	0.91	0.97	0.93	0.03
TiO2	0.11	0.04	0.03	0.06	0.04
FeO	12.63	13.66	12.56	12.95	0.50
MgO	10.54	9.78	10.58	10.30	0.37
MnO	0.75	0.78	0.76	0.76	0.01
CaO	22.17	21.12	22.02	21.77	0.46
Na2O	1.36	1.74	1.42	1.51	0.17
total	100.54	99.82	99.89	100.08	0.32
Si	1.978	1.988	1.973	1.980	0.006
AlIV	0.022	0.012	0.027	0.020	0.006
AlVI	0.019	0.029	0.016	0.021	0.006
Fe	0.401	0.439	0.402	0.414	0.018
Mg	0.597	0.560	0.604	0.587	0.019
Mn	0.024	0.026	0.025	0.025	0.001
Ca	0.903	0.869	0.903	0.892	0.016
Na	0.100	0.130	0.105	0.112	0.013
MgCa	0.048	0.058	0.050	0.052	0.004
TK	0.019	0.029	0.016	0.021	0.006
ED	0.052	0.057	0.058	0.055	0.003
PL	0.048	0.074	0.047	0.056	0.012

CPX - Amphibolite 419 - Porphyroclast

GrainType	PC	PC	PC	PC	PC	PC	Average	Std.Dev.
Sample #	211	212	213	214	215	218	P-Clast	(6)
SiO2	52.09	52.45	51.99	52.69	52.2	52.53	52.33	0.25
Al2O3	0.82	0.79	0.84	0.73	0.83	0.76	0.80	0.04
TiO2	0.04	0.02	0.04	0.02	0.05	0.05	0.04	0.01
FeO	12.34	12.74	12.44	12.08	12.46	12.34	12.40	0.20
MgO	10.85	10.71	10.79	10.98	10.88	10.8	10.84	0.08
MnO	0.7	0.71	0.75	0.79	0.8	0.7	0.74	0.04
CaO	22.54	22.4	22.66	22.84	22.59	22.62	22.61	0.13
Na2O	1.21	1.3	1.16	0.96	1.14	1.11	1.15	0.10
total	100.59	101.12	100.67	101.09	100.95	100.91	100.89	0.20
Si	1.976	1.981	1.973	1.985	1.974	1.984	1.979	0.005
AlIV	0.024	0.019	0.027	0.015	0.026	0.016	0.021	0.005
AlVI	0.013	0.016	0.011	0.017	0.011	0.018	0.014	0.003
Fe	0.392	0.402	0.395	0.381	0.394	0.390	0.392	0.006
Mg	0.614	0.603	0.610	0.617	0.614	0.608	0.611	0.005
Mn	0.022	0.023	0.024	0.025	0.026	0.022	0.024	0.001
Ca	0.916	0.906	0.922	0.922	0.916	0.915	0.916	0.005
Na	0.089	0.095	0.085	0.070	0.084	0.081	0.084	0.008
MgCa	0.045	0.048	0.043	0.042	0.049	0.043	0.045	0.003
TK	0.013	0.016	0.011	0.017	0.011	0.018	0.014	0.003
ED	0.050	0.049	0.050	0.034	0.050	0.040	0.045	0.006
PL	0.039	0.046	0.035	0.036	0.034	0.041	0.039	0.004

CPX - Amphibolite 419 - Matrix

GrainType	M	M	M	M	M	M	M	Average	Std.Dev.
Sample #	274 PALE	277 PALE	285	294	296	297	337	Matrix	(7)
SiO2	52.2	52.39	52.13	52.15	52.68	52.43	52.46	52.35	0.19
Al2O3	1.33	1.35	1.06	1	0.91	0.93	1.07	1.09	0.17
TiO2	0.07	0.05	0.05	0.08	0.05	0.05	0.06	0.06	0.01
FeO	12.84	13.28	13.39	13.02	14.3	14.22	12.76	13.40	0.58
MgO	10.36	10	10.04	10.44	9.51	9.62	10.38	10.05	0.35
MnO	0.63	0.61	0.56	0.59	0.6	0.65	0.68	0.62	0.04
CaO	22.2	21.9	21.36	21.72	20.93	21.07	21.72	21.56	0.42
Na2O	1.34	1.53	1.86	1.49	2.14	1.97	1.71	1.72	0.27
total	100.97	101.11	100.45	100.49	101.12	100.94	100.84	100.85	0.25
Si	1.973	1.980	1.985	1.981	1.998	1.992	1.985	1.985	0.008
AlIV	0.027	0.020	0.015	0.019	0.002	0.008	0.015	0.015	0.008
AlVI	0.032	0.040	0.033	0.026	0.039	0.034	0.032	0.034	0.004
Fe	0.406	0.420	0.426	0.414	0.453	0.452	0.404	0.425	0.019
Mg	0.584	0.563	0.570	0.591	0.537	0.545	0.585	0.568	0.019
Mn	0.020	0.020	0.018	0.019	0.019	0.021	0.022	0.020	0.001
Ca	0.899	0.887	0.871	0.884	0.850	0.858	0.881	0.876	0.016
Na	0.098	0.112	0.137	0.110	0.157	0.145	0.125	0.126	0.020
MgCa	0.049	0.047	0.051	0.057	0.053	0.057	0.048	0.052	0.004
TK	0.032	0.040	0.033	0.026	0.039	0.034	0.032	0.034	0.004
ED	0.046	0.046	0.059	0.051	0.060	0.060	0.054	0.054	0.006
PL	0.052	0.066	0.078	0.059	0.097	0.085	0.071	0.072	0.015

CPX - Amphibolite 419 - Porphyroclast

GrainType	PC	PC	PC	PC	PC	PC	PC	PC	Average	Std.Dev.
Sample #	341	342	343	344	345	346	347	348	P-Clast	(8)
SiO2	52.34	52.31	51.73	51.67	52.08	52.05	52.05	52.01	52.03	0.22
Al2O3	0.95	0.89	0.95	0.89	1.02	0.83	0.87	1.19	0.95	0.11
TiO2	0.06	0.06	0.06	0.03	0.03	0.02	0.03	0.03	0.04	0.02
FeO	12.78	13.11	12.88	12.97	13.11	12.55	12.88	12.94	12.90	0.17
MgO	10.3	10.35	10.3	10.43	10.22	10.57	10.58	10.56	10.41	0.13
MnO	0.65	0.67	0.69	0.71	0.65	0.72	0.68	0.7	0.68	0.02
CaO	22.31	22.32	22.15	22.54	21.99	22.23	22.21	22.02	22.22	0.17
Na2O	1.33	1.29	1.29	1.19	1.37	1.28	1.29	1.44	1.31	0.07
total	100.72	101	100.05	100.43	100.47	100.25	100.59	100.89	100.55	0.30
Si	1.985	1.981	1.978	1.971	1.982	1.982	1.978	1.971	1.979	0.005
AlIV	0.015	0.019	0.022	0.029	0.018	0.018	0.022	0.029	0.022	0.005
AlVI	0.027	0.021	0.021	0.011	0.027	0.019	0.017	0.024	0.021	0.005
Fe	0.405	0.415	0.412	0.414	0.417	0.400	0.409	0.410	0.410	0.005
Mg	0.582	0.584	0.587	0.593	0.580	0.600	0.600	0.596	0.590	0.008
Mn	0.021	0.021	0.022	0.023	0.021	0.023	0.022	0.022	0.022	0.001
Ca	0.906	0.906	0.907	0.921	0.897	0.907	0.904	0.894	0.905	0.008
Na	0.098	0.095	0.096	0.088	0.101	0.095	0.095	0.106	0.097	0.005
MgCa	0.039	0.045	0.045	0.044	0.048	0.045	0.051	0.055	0.047	0.005
TK	0.027	0.021	0.021	0.011	0.027	0.019	0.017	0.024	0.021	0.005
ED	0.043	0.046	0.049	0.053	0.046	0.047	0.050	0.055	0.049	0.004
PL	0.055	0.049	0.047	0.035	0.055	0.048	0.045	0.051	0.048	0.006

CPX - Amphibolite 419 - Matrix

GrainType	M	M	Average	Std.Dev.
Sample #	633	634	Matrix	(2)
SiO2	52.07	51.2	51.64	0.435
Al2O3	0.98	1.15	1.07	0.085
TiO2	0.06	0.13	0.10	0.035
FeO	13.02	13.27	13.15	0.125
MgO	10.39	10.04	10.22	0.175
MnO	0.74	0.64	0.69	0.05
CaO	22.19	21.54	21.87	0.325
Na2O	1.43	1.81	1.62	0.19
total	100.88	99.78	100.33	0.55
Si	1.975	1.968	1.972	0.003
AlIV	0.025	0.032	0.029	0.003
AlVI	0.019	0.020	0.020	0.000
Fe	0.413	0.427	0.420	0.007
Mg	0.588	0.575	0.582	0.006
Mn	0.024	0.021	0.023	0.001
Ca	0.902	0.887	0.895	0.007
Na	0.105	0.135	0.120	0.015
MgCa	0.048	0.052	0.050	0.001
TK	0.019	0.020	0.020	0.000
ED	0.055	0.074	0.064	0.009
PL	0.050	0.061	0.056	0.006

CPX - Amphibolite 419 - Matrix Lower Contact (PG-AM)

GrainType	M	M	M	M	M	M	M	M	Average Matrix	Std.Dev. (8)
Sample #	586	587	588	589	654	655	656	657		
SiO2	51.63	51.3	51.46	51.33	52.03	51.21	50.8	51.15	51.36	0.34
Al2O3	1.04	0.95	0.96	0.91	1.09	1.15	1.11	1.02	1.03	0.08
TiO2	0.07	0.06	0.04	0.05	0.1	0.05	0.1	0.05	0.07	0.02
FeO	13.41	13.4	13.32	13.28	13.41	13.13	14.24	13.98	13.52	0.36
MgO	9.84	9.79	9.69	9.85	9.87	9.78	9.01	9.58	9.68	0.27
MnO	1.74	1.72	1.78	1.62	1.59	1.8	1.8	1.67	1.72	0.08
CaO	21.56	22.52	21.66	22.45	21.53	21.44	21.05	21.2	21.68	0.50
Na2O	1.43	1.14	1.32	1.12	1.67	1.79	1.92	1.72	1.51	0.28
total	100.72	100.88	100.23	100.61	101.29	100.35	100.03	100.37	100.56	0.38
Si	1.972	1.962	1.976	1.966	1.974	1.965	1.967	1.968	1.969	0.004
AlIV	0.028	0.038	0.024	0.034	0.026	0.035	0.033	0.032	0.031	0.004
AlVI	0.019	0.005	0.019	0.007	0.023	0.017	0.017	0.014	0.015	0.006
Fe	0.428	0.429	0.428	0.425	0.425	0.421	0.461	0.450	0.433	0.013
Mg	0.560	0.558	0.555	0.562	0.558	0.559	0.520	0.549	0.553	0.013
Mn	0.056	0.056	0.058	0.053	0.051	0.059	0.059	0.054	0.056	0.003
Ca	0.882	0.923	0.891	0.921	0.875	0.881	0.873	0.874	0.890	0.019
Na	0.106	0.085	0.098	0.083	0.123	0.134	0.144	0.128	0.113	0.021
MgCa	0.070	0.051	0.063	0.051	0.065	0.061	0.063	0.071	0.062	0.007
TK	0.019	0.005	0.019	0.007	0.023	0.017	0.017	0.014	0.015	0.006
ED	0.058	0.059	0.052	0.055	0.063	0.076	0.080	0.073	0.064	0.010
PL	0.048	0.026	0.046	0.028	0.060	0.058	0.064	0.055	0.048	0.013

CPX - Amphibolite 419 - Matrix CPX-AB Myl.

GrainType	M	M	M	M	M	Average	Std.Dev.
Sample #	488	489	496	509	512	Mylonite	(5)
SiO2	51.24	51.26	51.33	50.64	51.1	51.11	0.25
Al2O3	0.87	1.08	1	1.13	1.04	1.02	0.09
TiO2	0.06	0.07	0.05	0.01	0.09	0.06	0.03
FeO	13.39	13.34	15.32	14.08	13.36	13.90	0.76
MgO	10.13	9.97	8.83	9.2	10.01	9.63	0.52
MnO	1.79	1.7	1.89	1.91	1.76	1.81	0.08
CaO	22.24	21.91	20.6	20.83	21.53	21.42	0.62
Na2O	1.27	1.51	2.09	1.9	1.7	1.69	0.29
total	100.99	100.84	101.11	99.7	100.59	100.65	0.50
Si	1.958	1.959	1.972	1.965	1.959	1.963	0.005
AlIV	0.039	0.041	0.028	0.035	0.041	0.037	0.005
AlVI	0.000	0.008	0.017	0.017	0.006	0.010	0.007
Fe	0.428	0.426	0.492	0.457	0.428	0.446	0.026
Mg	0.577	0.568	0.505	0.532	0.572	0.551	0.028
Mn	0.058	0.055	0.061	0.063	0.057	0.059	0.003
Ca	0.911	0.897	0.848	0.867	0.884	0.881	0.022
Na	0.094	0.112	0.156	0.143	0.126	0.126	0.022
MgCa	0.065	0.063	0.080	0.070	0.070	0.070	0.006
TK	-0.003	0.008	0.017	0.017	0.006	0.009	0.008
ED	0.070	0.072	0.084	0.080	0.080	0.077	0.005
PL	0.024	0.040	0.072	0.063	0.046	0.049	0.017

CPX - Amphibolite 419 - Poikiloblast in boudin

GrainType	PKB	PKB	PKB	PKB	PKB	PKB	Average	Std.Dev.
Sample #	503	504	505	506	510	511	Poikil.	(6)
SiO2	51.38	50.31	51.2	50.66	50.47	51.21	50.87	0.41
Al2O3	0.95	0.91	0.91	0.81	0.72	0.86	0.86	0.08
TiO2	0.09	0.04	0.07	0.06	0.03	0.05	0.06	0.02
FeO	13.2	15.1	13.08	13.19	12.74	12.71	13.34	0.81
MgO	9.81	8.84	10.23	9.92	10.26	10.5	9.93	0.54
MnO	1.93	2.01	1.86	1.98	2.01	1.88	1.94	0.06
CaO	21.4	20.64	21.72	22.38	22.55	22.1	21.80	0.65
Na2O	1.5	1.91	1.45	1.01	1.05	1.35	1.38	0.30
total	100.26	99.76	100.52	100.01	99.83	100.66	100.17	0.34
Si	1.973	1.963	1.962	1.957	1.953	1.958	1.961	0.006
AlIV	0.027	0.037	0.038	0.037	0.033	0.039	0.035	0.004
AlVI	0.016	0.004	0.003	0.000	0.000	0.000	0.004	0.006
Fe	0.424	0.493	0.419	0.426	0.412	0.406	0.430	0.029
Mg	0.561	0.514	0.584	0.571	0.592	0.599	0.570	0.028
Mn	0.063	0.066	0.060	0.065	0.066	0.061	0.064	0.002
Ca	0.880	0.863	0.892	0.926	0.935	0.905	0.900	0.025
Na	0.112	0.144	0.108	0.076	0.079	0.100	0.103	0.023
MgCa	0.069	0.081	0.072	0.060	0.056	0.068	0.068	0.008
TK	0.016	0.004	0.003	-0.006	-0.014	-0.003	0.000	0.009
ED	0.061	0.088	0.072	0.062	0.070	0.073	0.071	0.009
PL	0.051	0.056	0.036	0.014	0.009	0.027	0.032	0.017

CPX - Pink Gneiss 419			(E3A-3)		Average	Std.Dev.
Sample #	513	514	564	565	Gneiss	(4)
SiO2	50.4	50.66	51.32	51.36	50.94	0.42
Al2O3	1.05	1.02	1.08	1.09	1.06	0.03
TiO2	0.04	0.03	0.05	0.03	0.04	0.01
FeO	14.4	15.14	14.53	15.53	14.90	0.46
MgO	9.45	8.87	9.33	8.71	9.09	0.31
MnO	1.49	1.32	1.44	1.37	1.41	0.06
CaO	20.96	20.75	21.17	20.93	20.95	0.15
Na2O	1.92	1.93	1.82	1.97	1.91	0.06
total	99.71	99.72	100.74	100.99	100.29	0.58
Si	1.958	1.970	1.969	1.973	1.968	0.006
AlIV	0.042	0.030	0.031	0.027	0.033	0.006
AlVI	0.006	0.017	0.017	0.022	0.016	0.006
Fe	0.468	0.492	0.466	0.499	0.481	0.014
Mg	0.547	0.514	0.533	0.499	0.523	0.018
Mn	0.049	0.043	0.047	0.045	0.046	0.002
Ca	0.872	0.864	0.870	0.861	0.867	0.004
Na	0.145	0.145	0.135	0.147	0.143	0.005
MgCa	0.074	0.070	0.069	0.068	0.070	0.002
TK	0.006	0.017	0.017	0.022	0.016	0.006
ED	0.091	0.079	0.074	0.076	0.080	0.006
PL	0.054	0.066	0.061	0.071	0.063	0.006

CPX - Pink Gneiss 419			(L5-1)	Average	Std.Dev.
Sample #	713	714	715	Gneiss	(3)
SiO2	51.16	51.58	51.31	51.35	0.17
Al2O3	0.92	0.83	0.8	0.85	0.05
TiO2	0.06	0.07	0.04	0.06	0.01
FeO	13.17	12.95	13.29	13.14	0.14
MgO	9.61	9.82	9.7	9.71	0.09
MnO	1.8	1.89	1.62	1.77	0.11
CaO	21.97	22.37	21.7	22.01	0.28
Na2O	1.39	1.18	1.44	1.34	0.11
total	100.08	100.69	99.9	100.22	0.34
Si	1.970	1.972	1.977	1.973	0.003
AlIV	0.030	0.028	0.023	0.027	0.003
AlVI	0.012	0.009	0.014	0.012	0.002
Fe	0.424	0.414	0.428	0.422	0.006
Mg	0.552	0.559	0.557	0.556	0.003
Mn	0.059	0.061	0.053	0.058	0.003
Ca	0.906	0.916	0.896	0.906	0.008
Na	0.104	0.087	0.108	0.100	0.009
MgCa	0.051	0.050	0.054	0.052	0.002
TK	0.012	0.009	0.014	0.012	0.002
ED	0.061	0.053	0.058	0.057	0.003
PL	0.043	0.034	0.050	0.042	0.006

The vita has been removed from the scanned document